Lectures on insulating and conducting quantum spin liquids

Advanced School and Conference on Quantum Matter
International Centre for Theoretical Physics
Trieste, Italy
December 1,2 2025

Subir Sachdev

Lecture notes: sachdev.physics.harvard.edu/talks

Maine Christos
Caltech

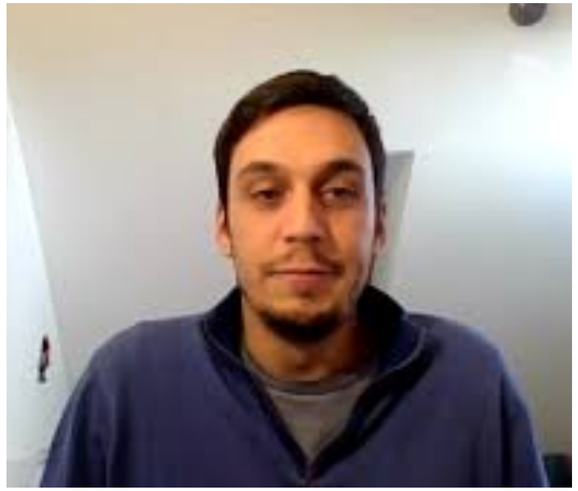

Pietro Bonetti

Alexander
Nikolaenko

Aavishkar Patel
ICTS, Bengaluru

arXiv > cond-mat > arXiv:2508.20164

Condensed Matter > Strongly Correlated Electrons

[Submitted on 27 Aug 2025]

Critical quantum liquids and the cuprate high temperature superconductors

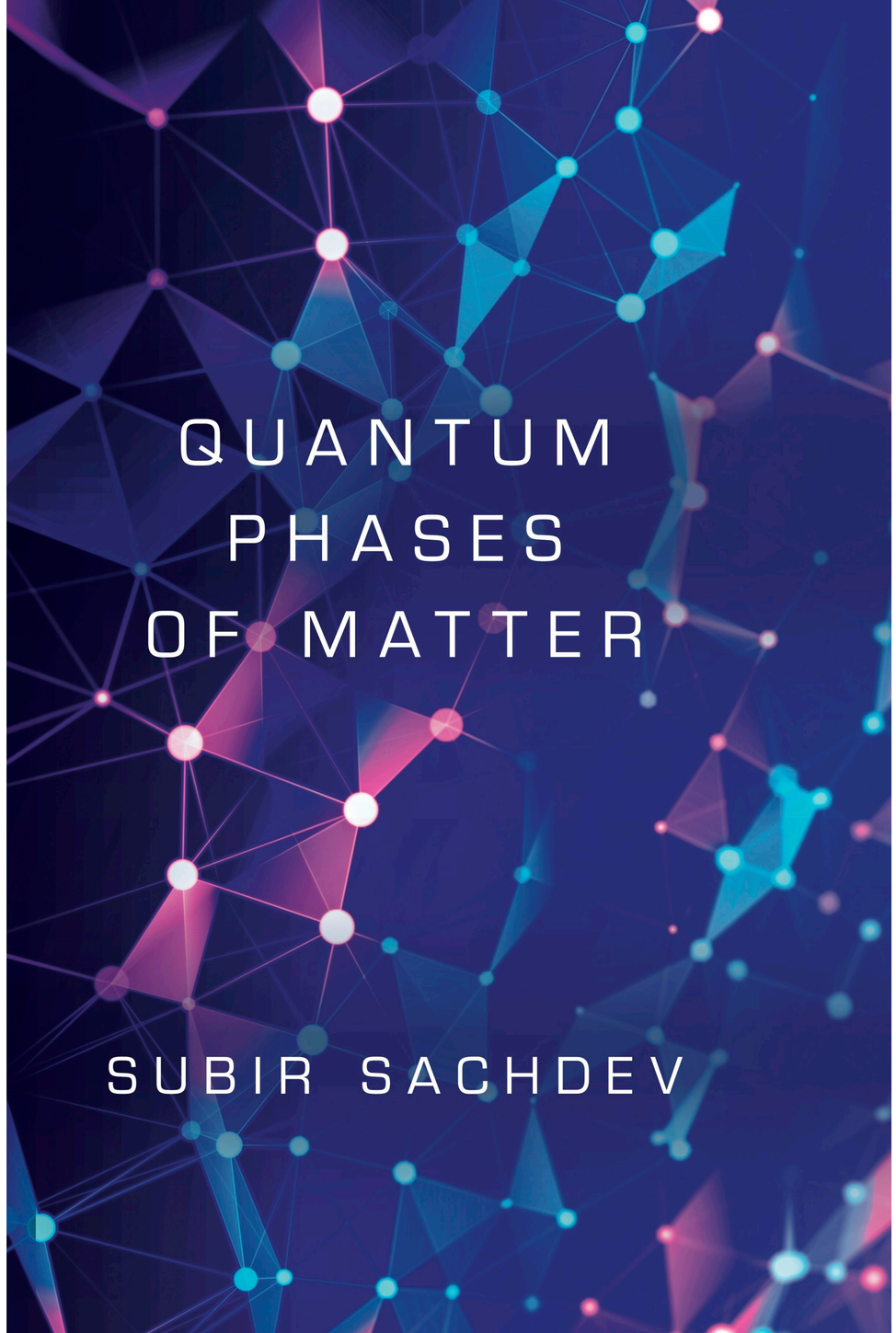

Cambridge University Press
March 2023

The Parton Method

Bosons	Bose partons $\boldsymbol{S} = b^\dagger_\alpha \frac{\boldsymbol{\sigma}_{\alpha\beta}}{2} b_\beta$
Superfluid	Antiferromagnetic order
Paired superfluid	Square lattice: $\mathbb{CP}^1$ model or $SO(5)_1$ WZW model Triangular lattice: $\mathbb{Z}_2$ spin liquid
SPT	Kalmeyer-Laughlin spin liquid

The correspondence between the phases of bosons,
and the phases of spin systems
obtained by expressing the spins in terms of bosonic partons.

The Parton Method

Bosons	Bose partons $\boldsymbol{S} = b^\dagger_\alpha \frac{\boldsymbol{\sigma}_{\alpha\beta}}{2} b_\beta$
Superfluid	Antiferromagnetic order
Paired superfluid	Square lattice: $\mathbb{CP}^1$ model or $SO(5)_1$ WZW model Triangular lattice: $\mathbb{Z}_2$ spin liquid
SPT	Kalmeyer-Laughlin spin liquid

The correspondence between the phases of bosons,
and the phases of spin systems
obtained by expressing the spins in terms of bosonic partons.

Electrons	Fermion partons $\boldsymbol{S} = f^\dagger_\alpha \frac{\boldsymbol{\sigma}_{\alpha\beta}}{2} f_\beta$
Fermi liquid	Bose metal Spinon Fermi surface
BCS superconductor	$\mathbb{Z}_2$ spin liquid
Chern insulator (class A)	Kalmeyer-Laughlin spin liquid
$p_x + ip_y$ superfluid (class D)	ITO-spin liquid with non-abelian Ising anyons (Kitaev honeycomb)
Semi-metals with gapless Dirac spectrum (graphene)	Gapless spin liquid Square lattice: $N_f = 2$ $SU(2)$ QCD or $SO(5)_1$ WZW model Triangular lattice: $N_f = 4$ QED
Complex SYK non-Fermi liquid	SY spin liquid

The correspondence between the phases of fermions, and the phases of spin systems obtained by expressing the spins in terms of fermionic partons.

The Parton Method

Bosons	Bose partons $\boldsymbol{S} = b_\alpha^\dagger \frac{\boldsymbol{\sigma}_{\alpha\beta}}{2} b_\beta$
Superfluid	Antiferromagnetic order
Paired superfluid	Square lattice: $\mathbb{CP}^1$ model or $SO(5)_1$ WZW model Triangular lattice: $\mathbb{Z}_2$ spin liquid
SPT	Kalmeyer-Laughlin spin liquid

The correspondence between the phases of bosons,
and the phases of spin systems
obtained by expressing the spins in terms of bosonic partons.

Electrons	Fermion partons $\boldsymbol{S} = f_\alpha^\dagger \frac{\boldsymbol{\sigma}_{\alpha\beta}}{2} f_\beta$
Fermi liquid	Bose metal Spinon Fermi surface
BCS superconductor	$\mathbb{Z}_2$ spin liquid
Chern insulator (class A)	Kalmeyer-Laughlin spin liquid
$p_x + ip_y$ superfluid (class D)	ITO-spin liquid with non-abelian Ising anyons (Kitaev honeycomb)
Semi-metals with gapless Dirac spectrum (graphene)	Gapless spin liquid Square lattice: $N_f = 2$ $SU(2)$ QCD or $SO(5)_1$ WZW model Triangular lattice: $N_f = 4$ QED
Complex SYK non-Fermi liquid	SY spin liquid

The correspondence between the phases of fermions, and the phases of spin systems obtained by expressing the spins in terms of fermionic partons.

The Parton Method

Fermions	Fermion partons $c = \psi_1\psi_2\psi_3$
ψ_1, ψ_2, ψ_3: IQH	Laughlin and Jain FQH
ψ_3: Fermi liquid ψ_1, ψ_2: IQH	Fermi surface in the half-filled Landau level (HLR)
ψ_3: $p_x + ip_y$ superfluid (class D) ψ_1, ψ_2: IQH	Moore-Read non-abelian FQH

Fractional quantum Hall states obtained by the decomposition of the electron into three fermionic partons.

Abstract

Two of the iconic phases of the hole-doped cuprate materials are the intermediate temperature pseudogap metal and the lower temperature d-wave superconductor. Following the prescient suggestion of P. W. Anderson, there were numerous early theories of these phases as doped quantum spin liquids. However, these theories have had difficulties with two prominent observations: (i) angle-dependent magnetoresistance measurements (ADMR), including observation of the Yamaji effect, present convincing evidence of small hole pockets which can tunnel coherently between square lattice layers, and (ii) the velocities of the nodal Bogoliubov quasiparticles in the d-wave superconductor are highly anisotropic, with $v_F \gg v_\Delta$. These lecture notes review how the fractionalized Fermi Liquid (FL*) state, which dopes quantum spin liquids with gauge-neutral electron-like quasiparticles, resolves both difficulties. Theories of quantum spin liquids employing fractionalization of the electron spin into bosonic and fermionic partons are reviewed. In the early theories, upon doping, the bosonic parton theory leads to a candidate holon metal theory of the pseudogap, while the fermionic parton theory leads to a d-wave superconductor. The construction of the FL* state is described using a quantum dimer model, followed by a more realistic description using the Ancilla Layer Model (ALM). Computations using the ALM resolve the difficulties in both the pseudogap metal and the d-wave superconductor.

1. Spin density wave order in the Hubbard model

2. Bosonic spinon theory of quantum spin liquids

3. Fermionic spinon theory of quantum spin liquids

4. Holon metal from a quantum spin liquid
   with bosonic spinons

5. d-wave superconductior from a quantum spin liquid
   with fermionic spinons

6. Fractionalized Fermi liquids (FL*)

1. Spin density wave order in the Hubbard model

2. Bosonic spinon theory of quantum spin liquids

3. Fermionic spinon theory of quantum spin liquids

4. Holon metal from a quantum spin liquid
   with bosonic spinons

5. d-wave superconductior from a quantum spin liquid
   with fermionic spinons

6. Fractionalized Fermi liquids (FL*)

1. Spin density wave order in the Hubbard model

We consider the onset of magnetism at a non-zero wavevector in a metal, often called a spin density wave (SDW). We will focus on the case where the wavevector of the SDW is $\boldsymbol{K} = (\pi, \pi)$ on the square lattice, and so the ordering has the same symmetry as the Néel state in an insulating antiferromagnet. The main ingredient here will be a bosonic collective mode representing antiferromagnetic spin fluctuations in the metal: this boson is the 'paramagnon'. Near the transition from the Fermi liquid to the antiferromagnetic metal, it is possible to derive a systematic approach to the paramagnon modes of a metal. We begin with an electronic Hubbard model

$$H = \sum_{\boldsymbol{k},\alpha} \varepsilon_{\boldsymbol{k}} c^{\dagger}_{\boldsymbol{k}\alpha} c_{\boldsymbol{k}\alpha} + U \sum_{\boldsymbol{i}} n_{\boldsymbol{i}\uparrow} n_{\boldsymbol{i}\downarrow} \tag{1}$$

where $n_{\boldsymbol{i}\uparrow} \equiv c^{\dagger}_{\boldsymbol{i}\uparrow} c_{\boldsymbol{i}\uparrow}$, and similarly for $n_{\boldsymbol{i}\downarrow}$. Upon using the single-site identity

$$U \left(n_{\boldsymbol{i}\uparrow} - \frac{1}{2} \right) \left(n_{\boldsymbol{i}\downarrow} - \frac{1}{2} \right) = -\frac{2U}{3} \boldsymbol{S}_{\boldsymbol{i}}^2 + \frac{U}{4} \,, \tag{2}$$

(which is easily established from the electron commutation relations) it becomes possible to decouple the 4-fermion term in a particle-hole channel. We decouple the interaction term in

the Hubbard model in (1), by the Hubbard-Stratonovich transformation

$$\exp\left(\frac{2U}{3}\sum_{\boldsymbol{i}}\int d\tau \boldsymbol{S}_{\boldsymbol{i}}^2\right) = \int \mathcal{D}\boldsymbol{\mathcal{P}}_{\boldsymbol{i}}(\tau)\exp\left(-\sum_{\boldsymbol{i}}\int d\tau\left[\frac{3}{8U}\boldsymbol{\mathcal{P}}_{\boldsymbol{i}}^2 - \boldsymbol{\mathcal{P}}_{\boldsymbol{i}}\cdot c_{\boldsymbol{i}\alpha}^\dagger\frac{\boldsymbol{\sigma}_{\alpha\beta}}{2}c_{\boldsymbol{i}\beta}\right]\right) \tag{3}$$

We now have a new field $\boldsymbol{\mathcal{P}}_{\boldsymbol{i}}(\tau)$ which will play the role of the paramagnon field.
The path integral of the Hubbard model can now be written exactly as:

$$\begin{aligned}\mathcal{Z} \;=\; \int \mathcal{D}c_{\boldsymbol{i}\alpha}(\tau)\mathcal{D}\boldsymbol{\mathcal{P}}_{\boldsymbol{i}}(\tau)\exp\Bigg(-\int d\tau\Bigg\{\sum_{\boldsymbol{k},\alpha} c_{\boldsymbol{k}\alpha}^\dagger\left[\frac{\partial}{\partial\tau}+\varepsilon_{\boldsymbol{k}}\right]c_{\boldsymbol{k}\alpha} \\ +\sum_{\boldsymbol{i}}\left[\frac{3}{8U}\boldsymbol{\mathcal{P}}_{\boldsymbol{i}}^2 - \boldsymbol{\mathcal{P}}_{\boldsymbol{i}}\cdot c_{\boldsymbol{i}\alpha}^\dagger\frac{\boldsymbol{\sigma}_{\alpha\beta}}{2}c_{\boldsymbol{i}\beta}\right]\Bigg\}\Bigg)\,.\end{aligned} \tag{4}$$

We can now formally integrate out the electrons, and obtain

$$\frac{\mathcal{Z}}{\mathcal{Z}_0} = \int\prod_{\boldsymbol{i}}\mathcal{D}\boldsymbol{\mathcal{P}}_{\boldsymbol{i}}(\tau)\exp\Big(-\mathcal{S}_{\text{paramagnon}}\left[\boldsymbol{\mathcal{P}}_{\boldsymbol{i}}(\tau)\right]\Big)\,, \tag{5}$$

where $\mathcal{Z}_0$ is the free electron partition function. Close to the onset of SDW order (but still on the non-magnetic side), we can expand the action in powers of $\boldsymbol{\mathcal{P}}$

$$\mathcal{S}_{\text{paramagnon}}\left[\boldsymbol{\mathcal{P}}_{\boldsymbol{i}}(\tau)\right] = \frac{T}{2}\sum_{\boldsymbol{q},\omega_n} |\boldsymbol{\mathcal{P}}(\boldsymbol{q},\omega_n)|^2 \left[\frac{3}{4U} - \frac{\chi_0(\boldsymbol{q},i\omega_n)}{2}\right] + \ldots \tag{6}$$

where $\chi_0(\boldsymbol{q},\omega_n)$ is the frequency-dependent Lindhard susceptibility, given by the particle-hole bubble graph shown in Fig. 1

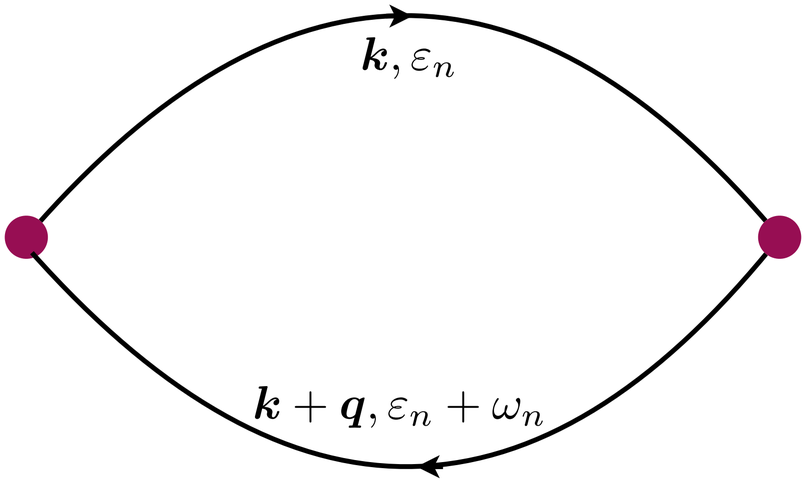

Figure 1: Feynman diagram leading to (7).

$$\chi_0(\boldsymbol{q},i\omega_n) = -\frac{T}{V}\sum_{\boldsymbol{p},\epsilon_n} \frac{1}{(i\epsilon_n - \varepsilon_{\boldsymbol{k}})(i\epsilon_n + i\omega_n - \varepsilon_{\boldsymbol{k}+\boldsymbol{q}})} \tag{7}$$

Performing the sum over frequencies by partial fractions, we obtain

$$\chi_0(\boldsymbol{q}, i\omega_n) = \frac{1}{V}\sum_{\boldsymbol{k}} \frac{f(\varepsilon_{\boldsymbol{k}+\boldsymbol{q}}) - f(\varepsilon_{\boldsymbol{k}})}{i\omega_n + \varepsilon_{\boldsymbol{k}} - \varepsilon_{\boldsymbol{k}+\boldsymbol{q}}}\,, \tag{8}$$

From the structure of the $\mathcal{P}$ propagator, it is clear that $\mathcal{P}$ will first condense at the wavevector $\boldsymbol{q}_{\max}$ at which $\chi_0(\boldsymbol{q}, i\omega = 0)$ is a maximum, and $\boldsymbol{q}_{\max}$ is then the wavevector of the SDW. In the mean field treatment of (6), the appearance of the this condensate requires that U is large enough to obey the 'Stoner criterion':

$$\frac{3}{4U} - \frac{\chi_0(\boldsymbol{q}_{\max}, i\omega = 0)}{2} < 0\,. \tag{9}$$

This wavevector is in turn determined by the dispersion $\varepsilon_{\boldsymbol{k}}$ of the underlying fermions. For simplicitly, we will only consider the case of a SDW with wavevector $\boldsymbol{K} = (\pi, \pi)$. The frequency dependence of $\chi_0(\boldsymbol{q}, i\omega)$ also has an important influence on the dynamics of the paramagnon fluctuations.

1.1. Fermi surface reconstruction

Let us now move into the antiferromagnetic metal phase, where we assume there is a $\mathcal{P}$ condensate at wavevector $\boldsymbol{K} = (\pi, \pi)$

$$\langle \mathcal{P}_{\boldsymbol{i}} \rangle = \eta_{\boldsymbol{i}} \mathcal{N} \hat{\boldsymbol{z}} \,, \tag{10}$$

where the factor

$$\eta_{\boldsymbol{i}} = \pm 1 \tag{11}$$

on the two checkerboard sublattices of the square lattice, and $\mathcal{N}$ measuring the strength of the Néel ordered moment shown in Fig. 2.

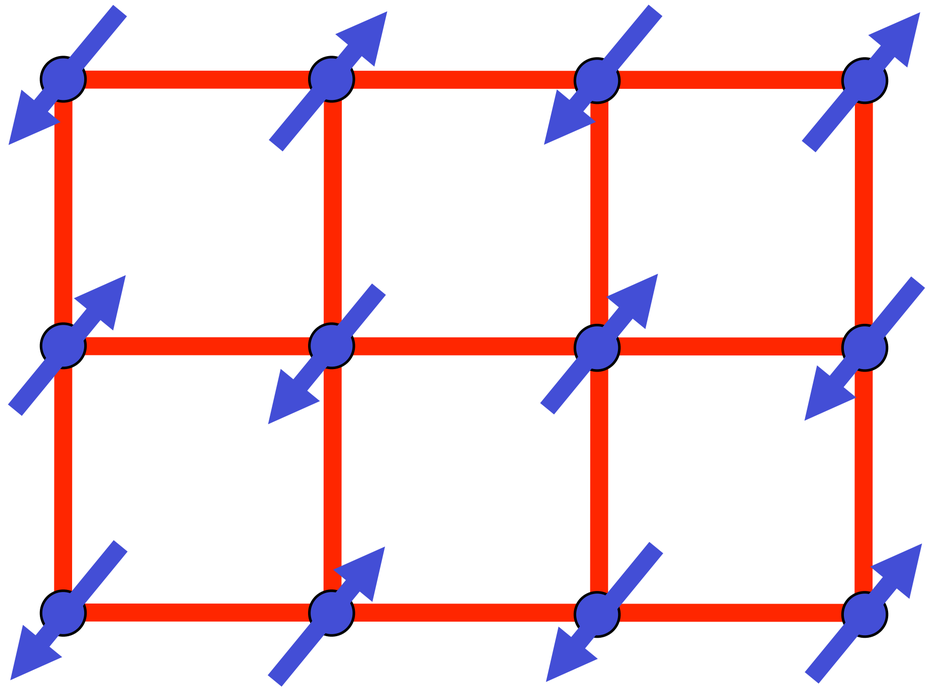

Figure 2: Antiferromagnetic (Néel) order $\mathcal{N}$ of the spin density wave state. This can be an insulator at $p = 0$, provided $\Delta = \mathcal{N}$ is large enough, as shown in Fig. 3. Otherwise, it is a metal with electron and/or hole pocket Fermi surfaces, as shown in Fig. 3-5.

We wish to describe the excitations of this state. One class of excitations are spin waves: these can be obtained by considering transverse fluctuations of $\mathcal{P}$ about the condensate in (10) using the full action in (5). However, there are also low energy fermionic excitations in the antiferromagnetic metal, which are gapped in the insulator. We can determine the spectrum of the fermions by inserting (10) into the Yukawa coupling; using $\eta_{\boldsymbol{i}} = e^{i\boldsymbol{K}\cdot\boldsymbol{r}_{\boldsymbol{i}}}$, with $\boldsymbol{K} = (\pi, \pi)$, we can write the fermion Hamiltonian in momentum space

$$H_{\rm AFM} = \sum_{\boldsymbol{k}} \left[\varepsilon_{\boldsymbol{k}} c^{\dagger}_{\boldsymbol{k}\alpha} c_{\boldsymbol{k}\alpha} - \Delta\, c^{\dagger}_{\boldsymbol{k}\alpha} \sigma^{z}_{\alpha\alpha} c_{\boldsymbol{k}+\boldsymbol{K},\alpha} \right] + \text{constant.} \tag{12}$$

The is the analog of the BCS Hamiltonian for superconductivity, and the analog of the pairing gap is the energy

$$\Delta = \mathcal{N}\,. \tag{13}$$

But, in general, the spectrum of $H_{\rm AFM}$ does not have a gap, as we will see below. As in BCS theory, the value of $\mathcal{N}$ has to be determined self-consistently from the mean-field equations.

Square-lattice Hubbard model with no doping

$\Delta \neq 0$ and large

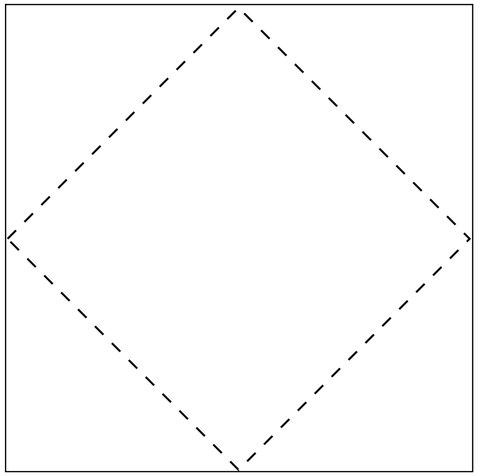

Insulator

$\Delta \neq 0$ and small

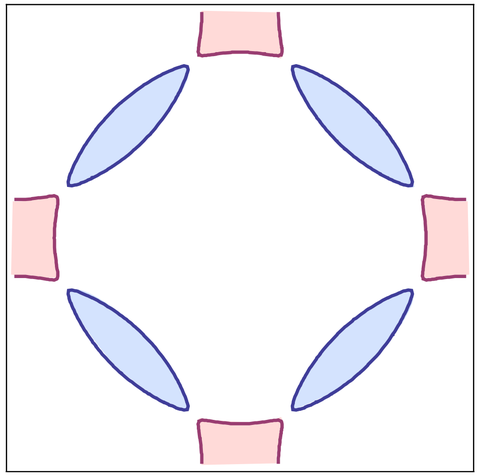

Metal with electron and hole pockets

$\Delta = 0$

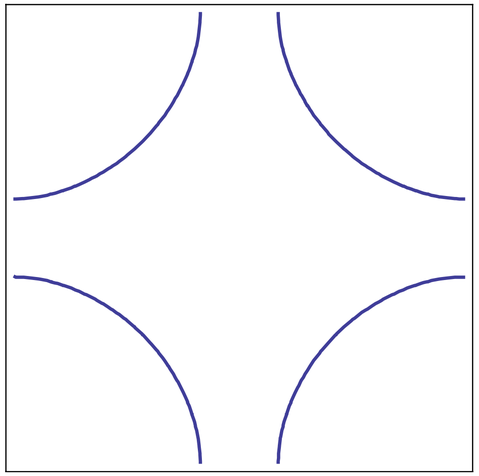

Metal with large Fermi surface

Figure 3: Fermi surfaces of the Néel state at half-fillng, *i.e.* doping $p = 0$. The pockets intersecting the diagonals of the Brillouin zone have both bands in (15) empty and so form hole pockets, while the remaining pockets have both bands occupied and form electron pockets. The dashed line in the insulator shows the boundary of the Brillouin zone of the Néel state

To obtain the fermionic excitation spectrum, we have to perform the analog of the Bogoliubov rotation in BCS theory. This is achieved by writing $H_{\rm AFM}$ in a 2×2 matrix form by using the fact that $2\boldsymbol{K}$ is a reciprocal lattice vector, and so $\varepsilon_{\boldsymbol{k}+2\boldsymbol{K}} = \varepsilon_{\boldsymbol{k}}$; correspondingly, the prime over the summation indicates that it only extends over half the Brillouin zone of the underlying lattice, shown in the left panel of Fig. 3, which is the Brillouin zone of the lattice with Néel order.

$$H_{\rm AFM} = \sum_{\boldsymbol{k}}{}' (c^\dagger_{\boldsymbol{k}\alpha}, c^\dagger_{\boldsymbol{k}+\boldsymbol{K},\alpha}) \begin{pmatrix} \varepsilon_{\boldsymbol{k}} & -\Delta\sigma^z_{\alpha\alpha} \\ -\Delta\sigma^z_{\alpha\alpha} & \varepsilon_{\boldsymbol{k}+\boldsymbol{K}} \end{pmatrix} \begin{pmatrix} c_{\boldsymbol{k}\alpha} \\ c_{\boldsymbol{k}+\boldsymbol{K},\alpha} \end{pmatrix} . \tag{14}$$

It is now easy to diagonalize the 2×2 matrix in (14), and we obtain

$$E_{\boldsymbol{k}\pm} = \frac{\varepsilon_{\boldsymbol{k}} + \varepsilon_{\boldsymbol{k}+\boldsymbol{K}}}{2} \pm \left[\left(\frac{\varepsilon_{\boldsymbol{k}} - \varepsilon_{\boldsymbol{k}+\boldsymbol{K}}}{2} \right)^2 + \Delta^2 \right]^{1/2} \tag{15}$$

The spectrum in (15) is not gapped, or even positive definite. Rather, it is the spectrum of a metal, in which the negative energy states are filled, and bounded by a Fermi surface. The Fermi surfaces so obtained is shown in Figs. 3, 4, 5 for different values of the electron density $1 - p$. Here p is conventionally the hole doping, and electron doping corresponds to $p < 0$. The dispersion $\varepsilon_{\boldsymbol{k}}$ has hoppings $t_{1,2,3}$ to first, second, and third neighbors with $t_{1,3} > 0$ and $t_2 < 0$ as appropriate for the cuprates.

Square-lattice Hubbard model with hole doping

$\Delta \neq 0$
and large

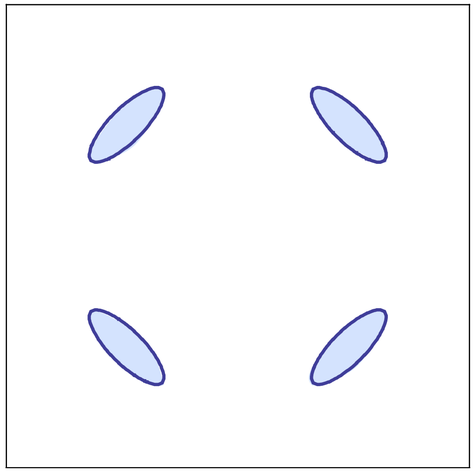

Metal with
hole pockets

$\Delta \neq 0$
and small

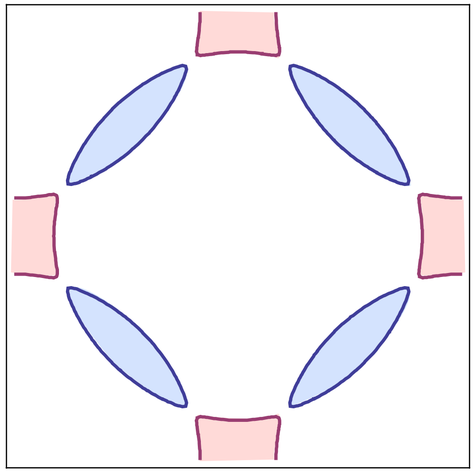

Metal with
electron and
hole pockets

$\Delta = 0$

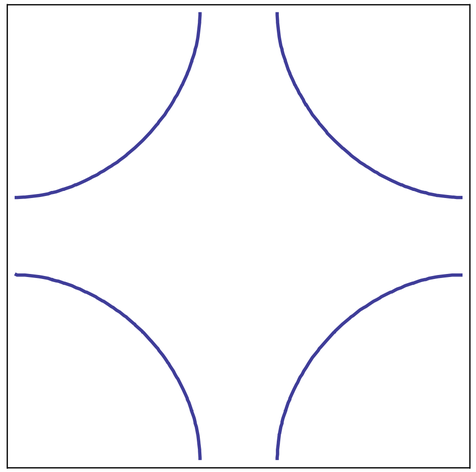

Metal with
“large” Fermi
surface

Figure 4: Fermi surfaces of the Néel state at $p > 0$. The pockets are as in Fig. 3. From (16), the area of each hole pocket on the left (when Δ is large and there are no electron pockets) is $p/4$, in units with the square lattice Brillouin zone having unit area. This follows from the existence of 2 independent hole pockets in the magnetic Brillouin zone, each with a spin degeneracy of 2.

Square-lattice Hubbard model with electron doping

$\Delta \neq 0$ and large

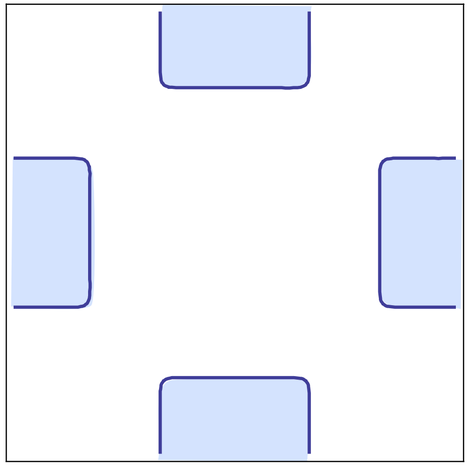

Metal with electron pockets

$\Delta \neq 0$ and small

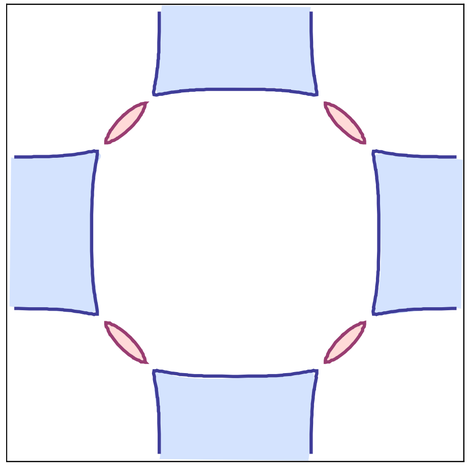

Metal with electron and hole pockets

$\Delta = 0$

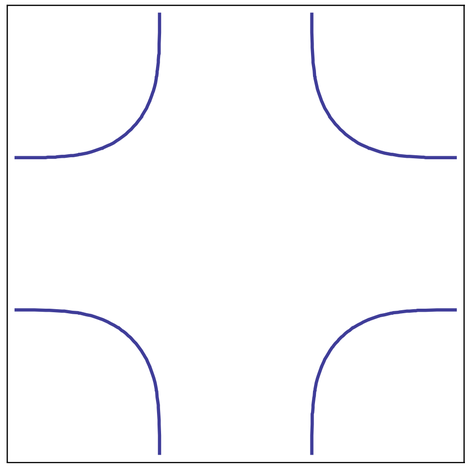

Metal with large Fermi surface

Figure 5: Fermi surfaces of the Néel state at $p < 0$, with pockets as in Figs. 3. From (16), the area of each electron pocket on the left (when Δ is large and there are no hole pockets) is $|p|/2$, in units with the square lattice Brillouin zone having unit area. This follows from the existence of 1 independent electron pocket in the magnetic Brillouin zone with a spin degeneracy of 2.

We observe that the 'large' Fermi surface of the paramagnetic metal has 'reconstructed' into small pocket Fermi surfaces in the SDW state. The excitations of the SDW metal are hole-like quasiparticles on the Fermi surfaces surrounding the hole pockets, and electron-like quasiparticles on the Fermi surfaces surrounding the electron pockets. The spin wave excitations interact rather weakly with the fermionic quasiparticle excitations: this can be see from a somewhat involved computation from the effective action.

Finally, we discuss the fate of the Luttinger relation in this metal. The Luttinger relation connects the volume enclosed by the Fermi surface to the density of electrons, modulo 2 electrons per unit cell. It should be applied in the Brillouin zone of the Néel state, which is half the size of the Brillouin zone of the underlying square lattice, as shown in Fig. 3. In real space, this corresponds to the fact that the unit cell has doubled, and so the density of electrons per unit cell is $2(1-p)$. For spinful electrons, the Luttinger relations measures electron density modulo 2, and so the density appearing in the Luttinger relation is $-2p$. This has to be equated to twice the volumes enclosed by the electron and hole pockets within the

diamond shaped Brillouin zone in Fig. 3. Let $\mathcal{A}_h$ be the area of a single elliptical hole pocket: there are 4 such pockets in the complete Brillouin zone of the square lattice or 2 pockets in the Brillouin zone of the Néel state, as is apparent from Figs. 3, 4, 5. Similarly, let $\mathcal{A}_e$ be the area of a single elliptical electron pocket: there are 2 such pockets in the complete Brillouin zone of the square lattice or 1 pocket in the Brillouin zone of the Néel state. These arguments show that the Luttinger relation becomes

$$2 \times \frac{1}{(2\pi)^2/2} \times (-2\mathcal{A}_h + \mathcal{A}_e) = -2p\,. \tag{16}$$

On the left hand side, the first factor is the spin degeneracy, and the second factor is the inverse of the volume of the Brillouin zone of the Néel state. To reiterate, this is the conventional Luttinger relation applied after accounting for the doubling of the unit cell, and it determines a linear constraint on the areas of the electron and hole pockets.

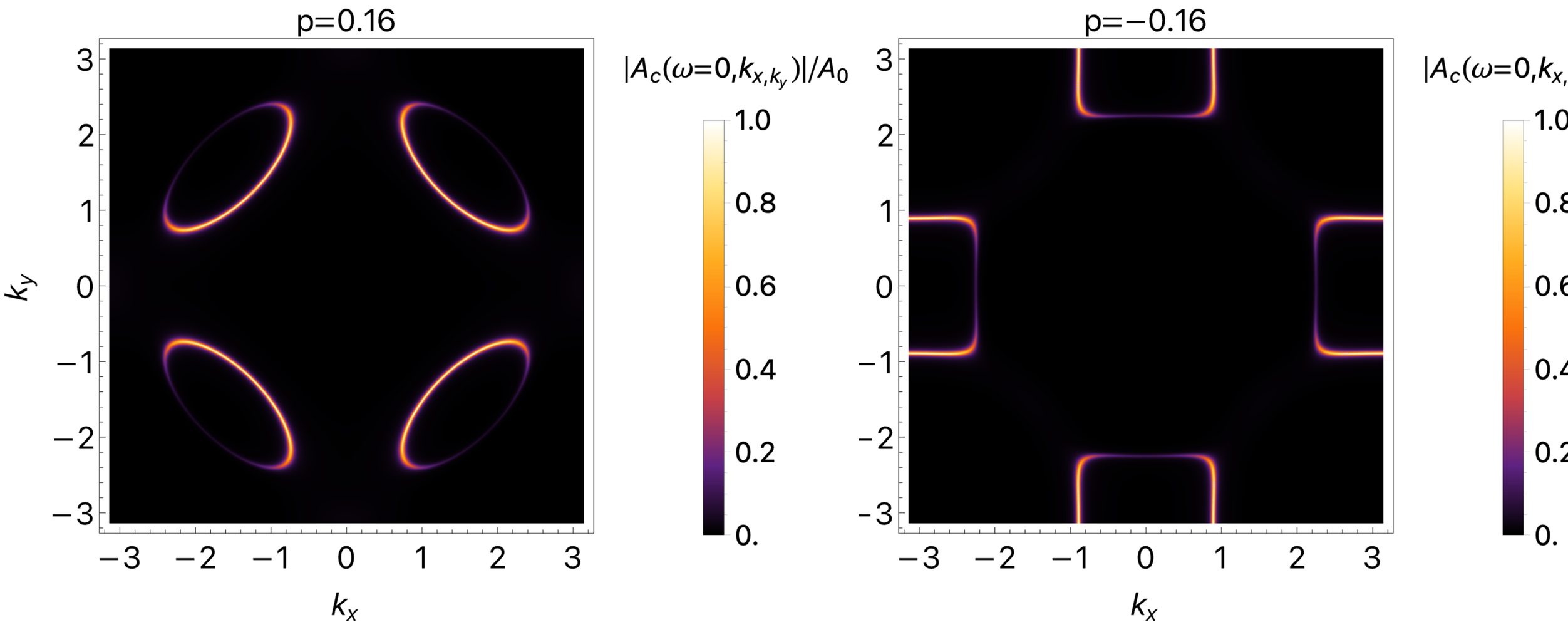

Figure 6: Spectral density of hole (left) and electron (right) pockets at $p = 0.16$ and $p = -0.16$ respectively for the SDW state. The fractional area of each hole pocket is $p/4$, and the fractional area of the electron pocket is $|p|/2$.

Fig 6 shows the electron spectral density (as measured by photoemission) at zero frequency for

both the electron and hole pockets.

1. Spin density wave order in the Hubbard model
2. Bosonic spinon theory of quantum spin liquids
3. Fermionic spinon theory of quantum spin liquids
4. Holon metal from a quantum spin liquid with bosonic spinons
5. d-wave superconductior from a quantum spin liquid with fermionic spinons
6. Fractionalized Fermi liquids (FL*)

Triangular lattice antiferromagnet

$KYbSe_2$

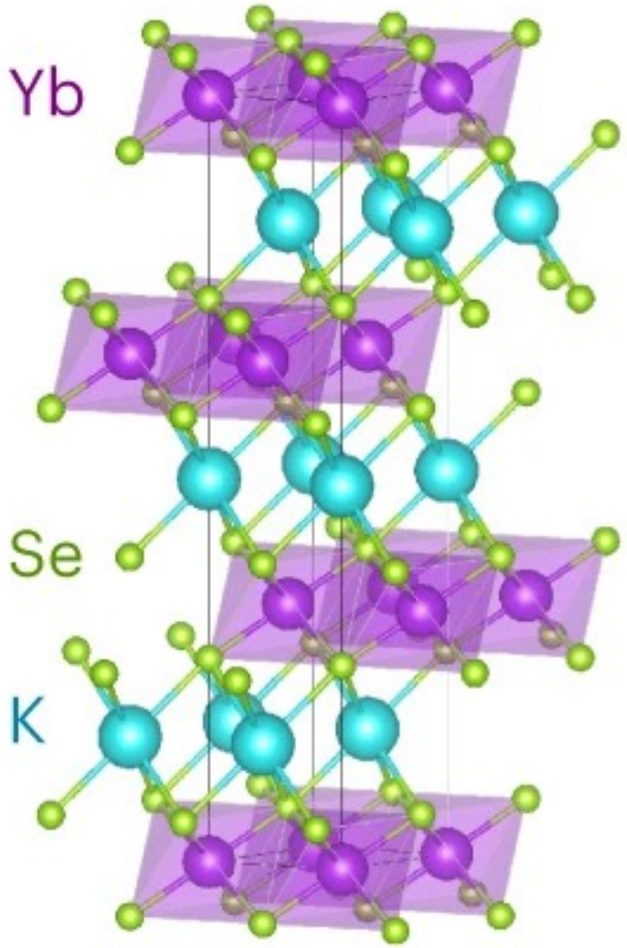

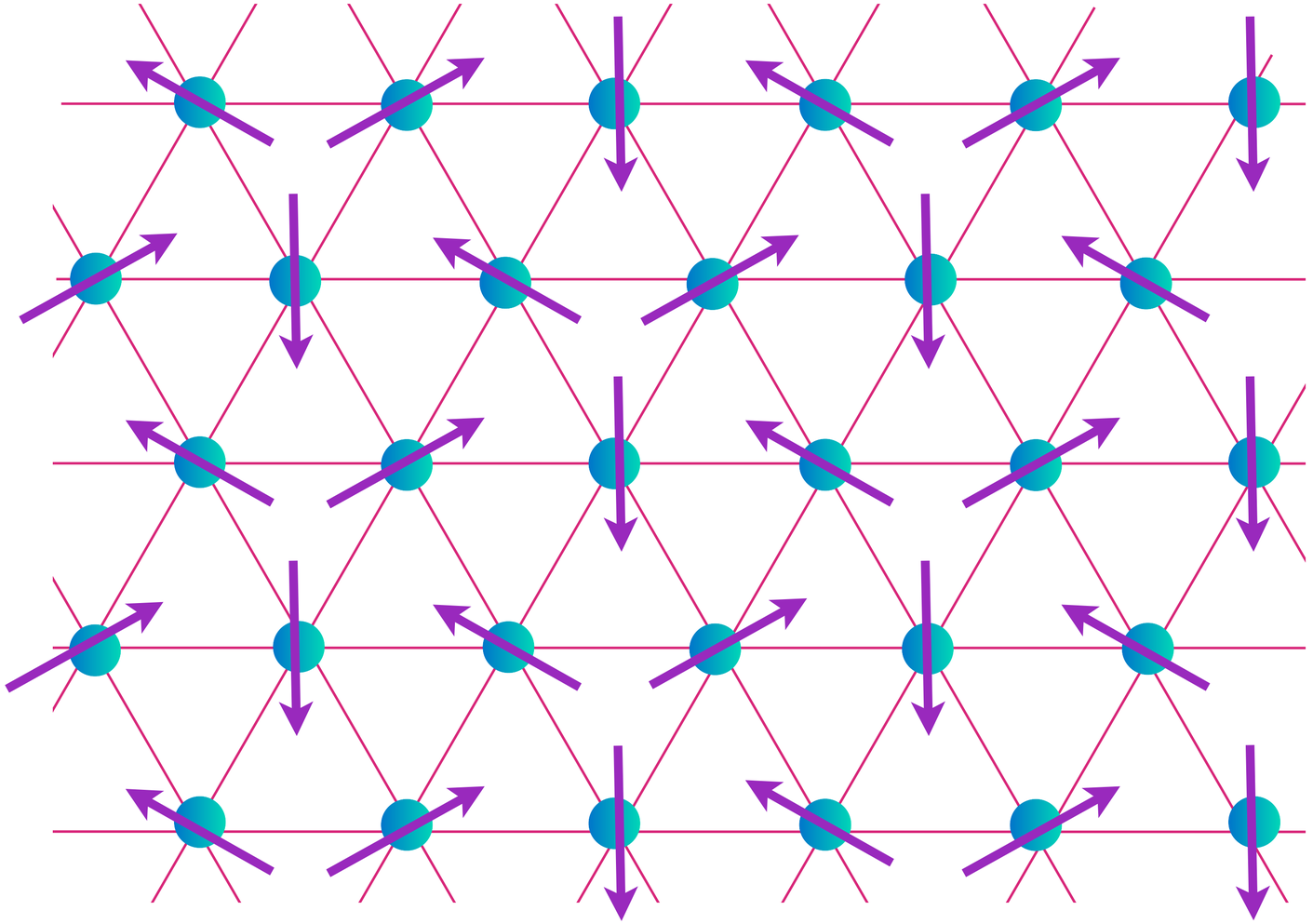

Nearest-neighbor model has ordered spins

Spin liquid: resonating valence bonds

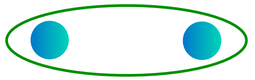

$$= \frac{1}{\sqrt{2}} \left(|\uparrow\downarrow\rangle - |\downarrow\uparrow\rangle \right)$$

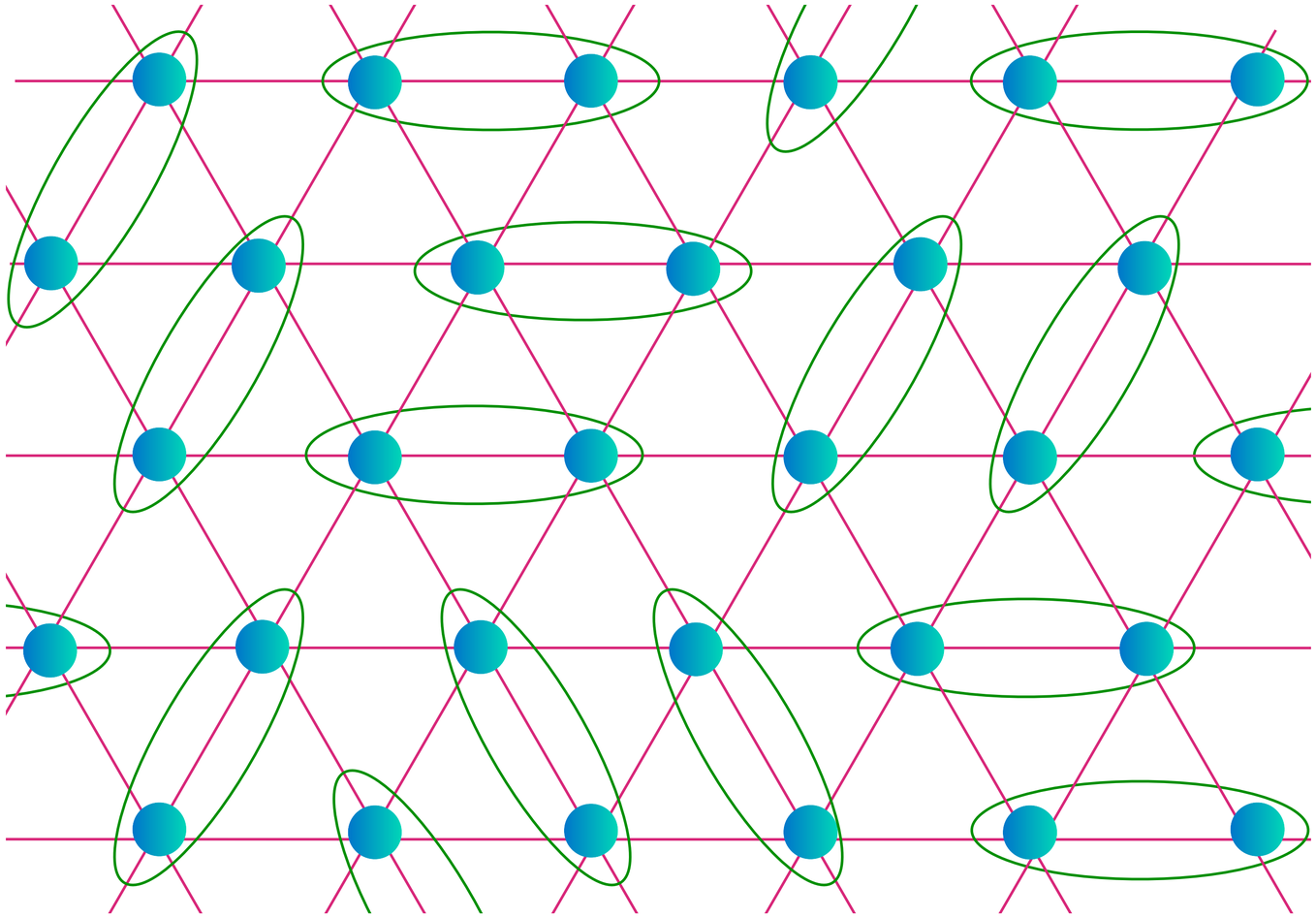

$$|G\rangle = \sum_{\mathcal{D}} c_{\mathcal{D}} \, |\mathcal{D}\rangle$$

$\mathcal{D} \rightarrow$ dimer covering of lattice

Patrik Fazekas and P. W. Anderson, *Philos. Mag.* **30**, 23 (1974).

Spin liquid: resonating valence bonds

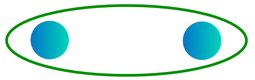

$$= \frac{1}{\sqrt{2}} \left(|\uparrow\downarrow\rangle - |\downarrow\uparrow\rangle \right)$$

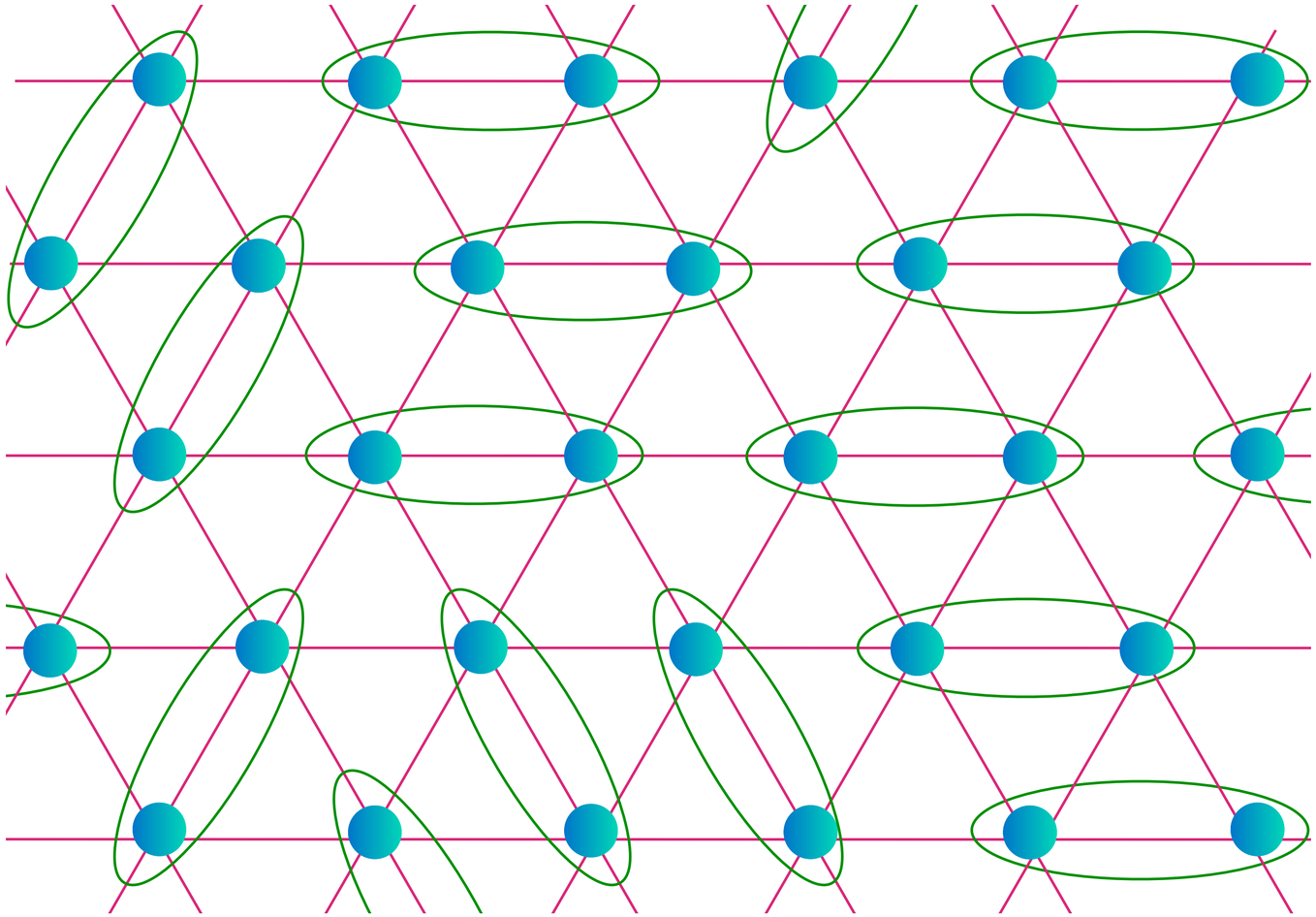

$$|G\rangle = \sum_{\mathcal{D}} c_{\mathcal{D}} \, |\mathcal{D}\rangle$$

$\mathcal{D} \rightarrow$ dimer covering of lattice

P. Fazekas and P. W. Anderson, *Philos. Mag.* **30**, 23 (1974).

Spin liquid: resonating valence bonds

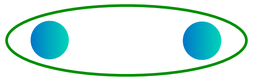

$$= \frac{1}{\sqrt{2}} \left(|\uparrow\downarrow\rangle - |\downarrow\uparrow\rangle \right)$$

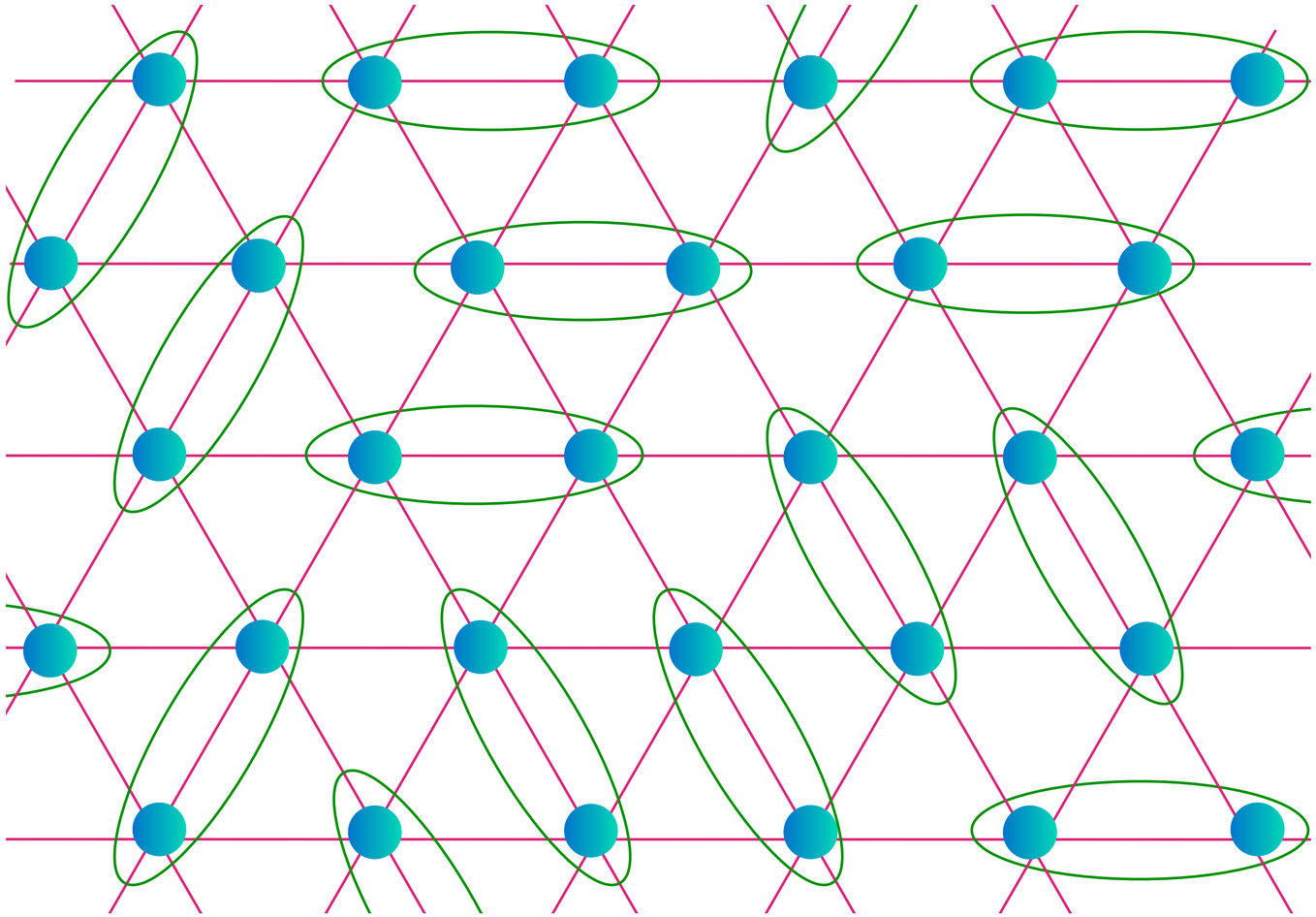

$$|G\rangle = \sum_{\mathcal{D}} c_{\mathcal{D}} \, |\mathcal{D}\rangle$$

$\mathcal{D} \rightarrow$ dimer covering of lattice

P. Fazekas and P. W. Anderson, *Philos. Mag.* **30**, 23 (1974).

Spin liquid: resonating valence bonds

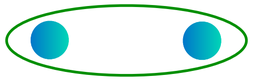

$$= \frac{1}{\sqrt{2}} \left(|\uparrow\downarrow\rangle - |\downarrow\uparrow\rangle \right)$$

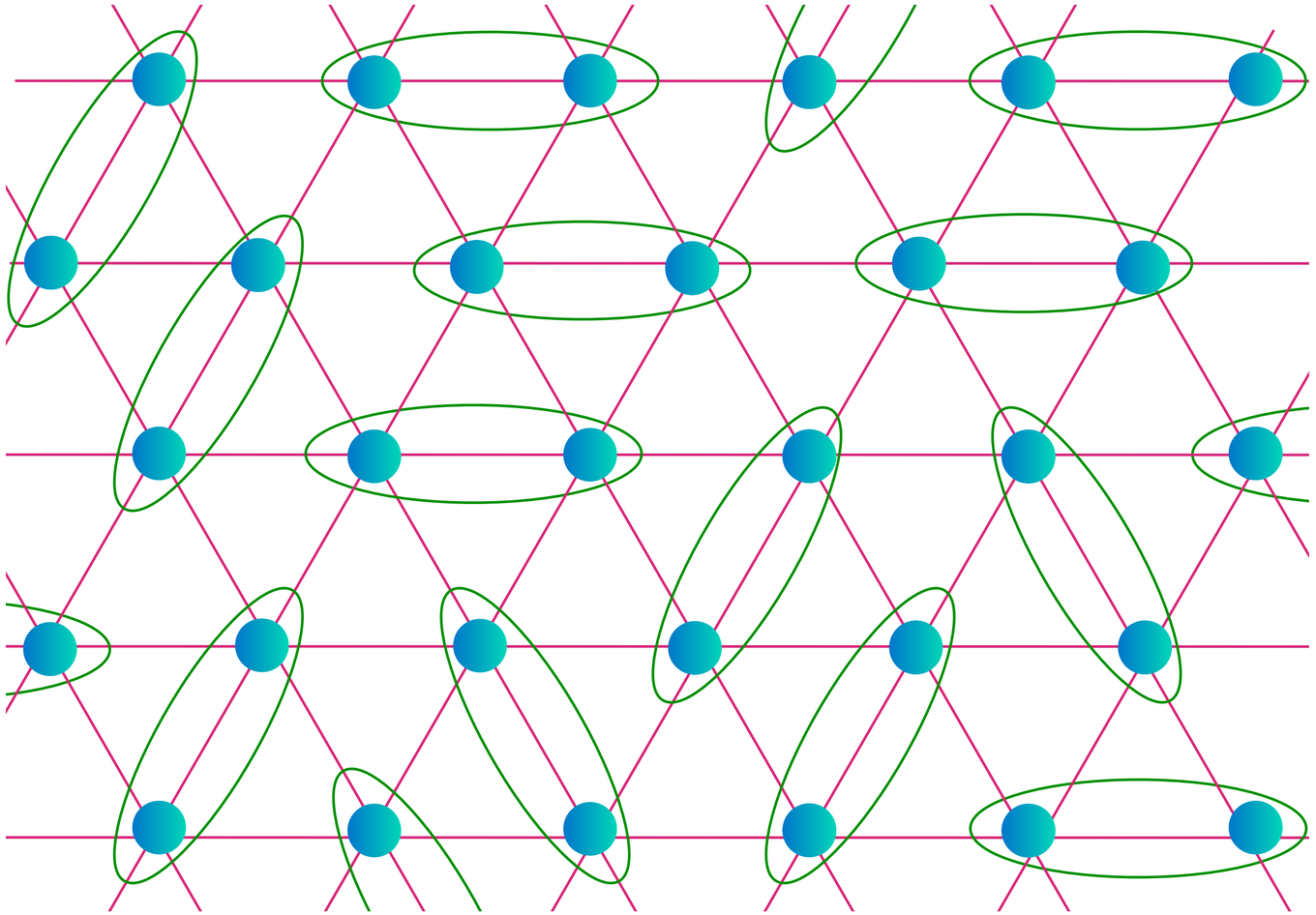

$$|G\rangle = \sum_{\mathcal{D}} c_{\mathcal{D}} \, |\mathcal{D}\rangle$$

$\mathcal{D} \rightarrow$ dimer covering of lattice

P. Fazekas and P. W. Anderson, *Philos. Mag.* **30**, 23 (1974).

Spin liquid: resonating valence bonds

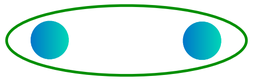

$$= \frac{1}{\sqrt{2}} \left(|\uparrow\downarrow\rangle - |\downarrow\uparrow\rangle \right)$$

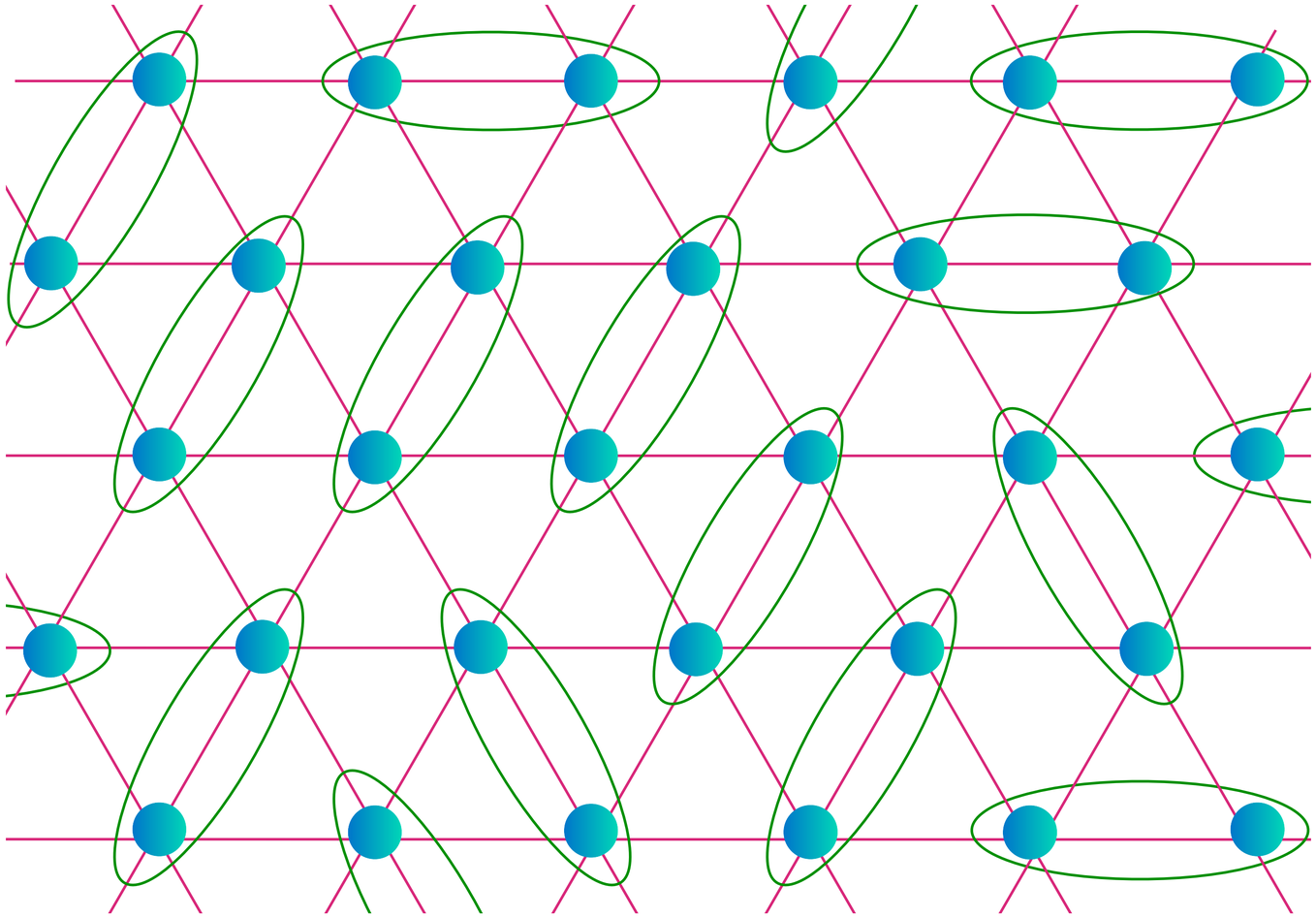

$$|G\rangle = \sum_{\mathcal{D}} c_{\mathcal{D}} \, |\mathcal{D}\rangle$$

$\mathcal{D} \rightarrow$ dimer covering of lattice

P. Fazekas and P. W. Anderson, *Philos. Mag.* **30**, 23 (1974).

Spin liquid: resonating valence bonds

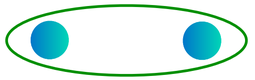

$$= \frac{1}{\sqrt{2}} \left(|\uparrow\downarrow\rangle - |\downarrow\uparrow\rangle \right)$$

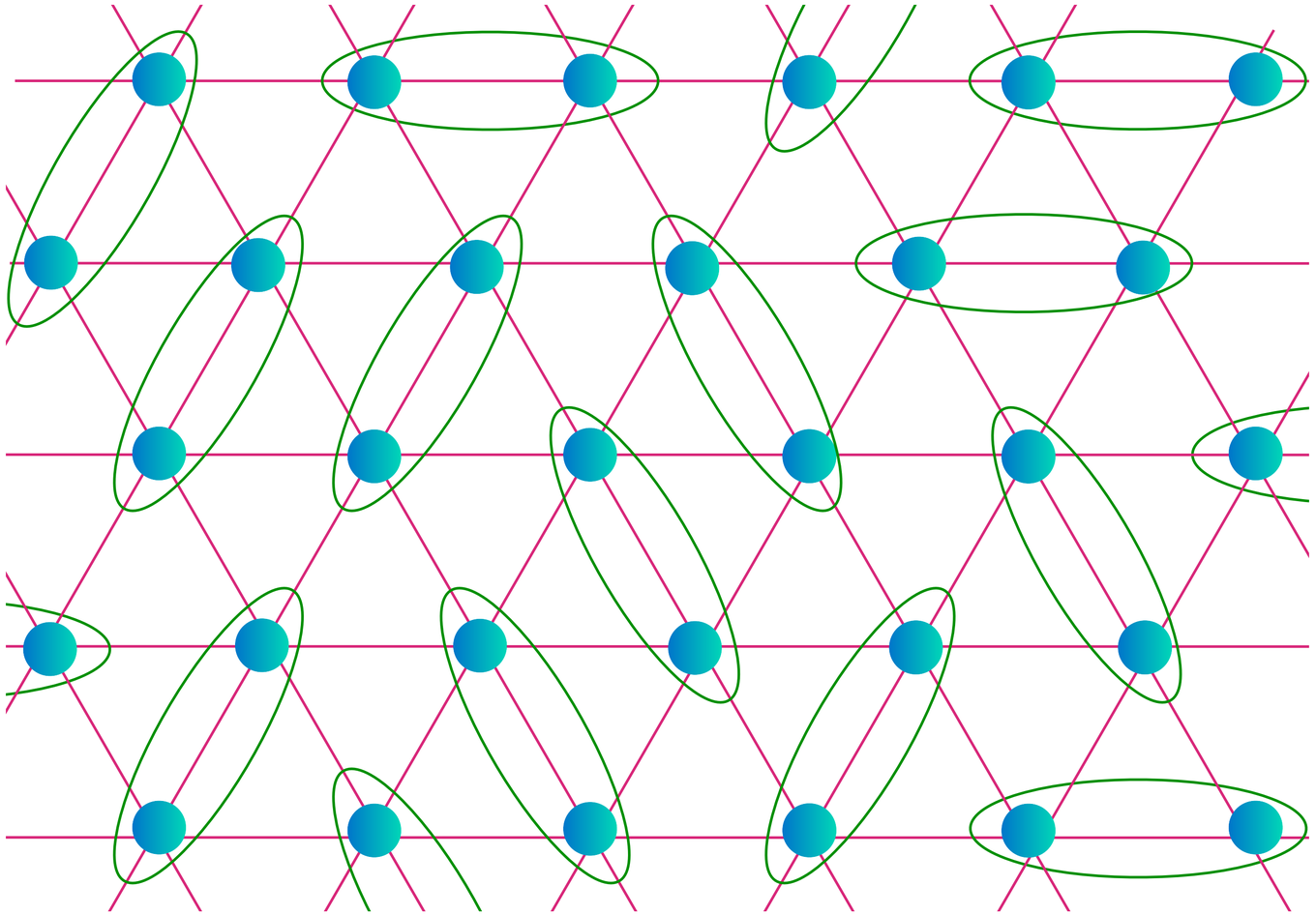

$$|G\rangle = \sum_{\mathcal{D}} c_{\mathcal{D}} \, |\mathcal{D}\rangle$$

$\mathcal{D} \rightarrow$ dimer covering of lattice

P. Fazekas and P. W. Anderson, *Philos. Mag.* **30**, 23 (1974).

Spin liquid: resonating valence bonds

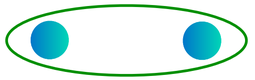

$$= \frac{1}{\sqrt{2}} \left(|\uparrow\downarrow\rangle - |\downarrow\uparrow\rangle \right)$$

$$|\Psi\rangle = C_1 \left| \right\rangle + C_2 \left| \right\rangle$$

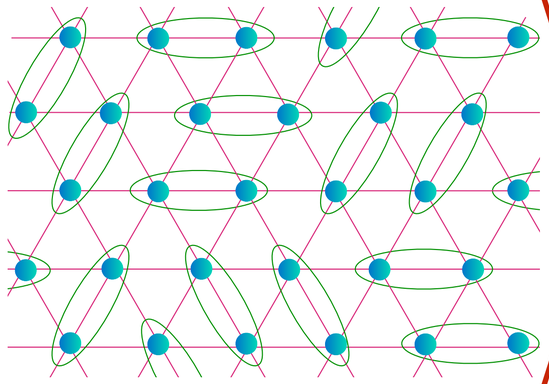

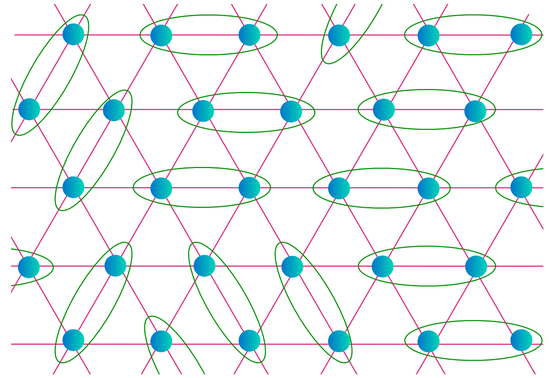

$$+ C_3 \left| \right\rangle + C_4 \left| \right\rangle + C_5 \left| \right\rangle + \ldots$$

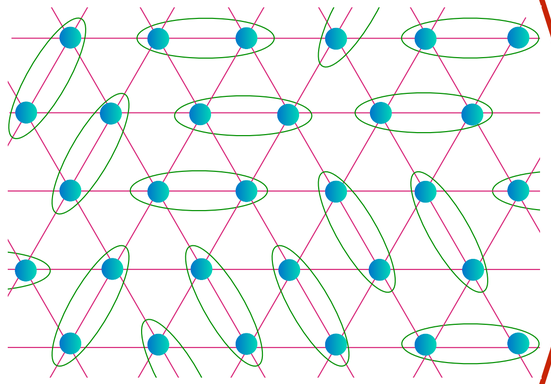

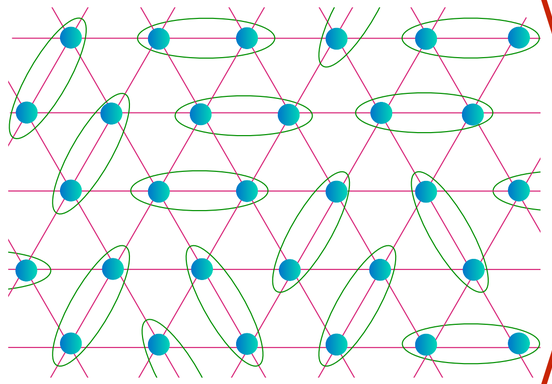

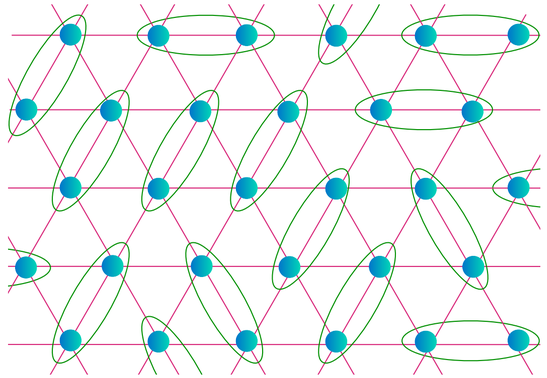

Spin liquid: resonating valence bonds

$$= \frac{1}{\sqrt{2}} \left(|\uparrow\downarrow\rangle - |\downarrow\uparrow\rangle \right)$$

$$|\Psi\rangle = C_1$$ 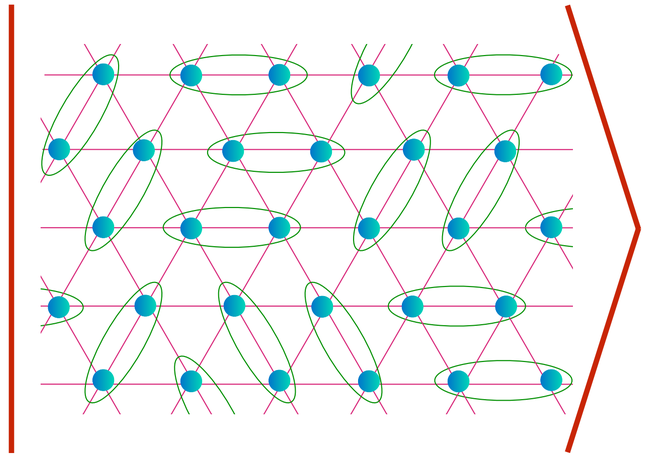

$$+$$ 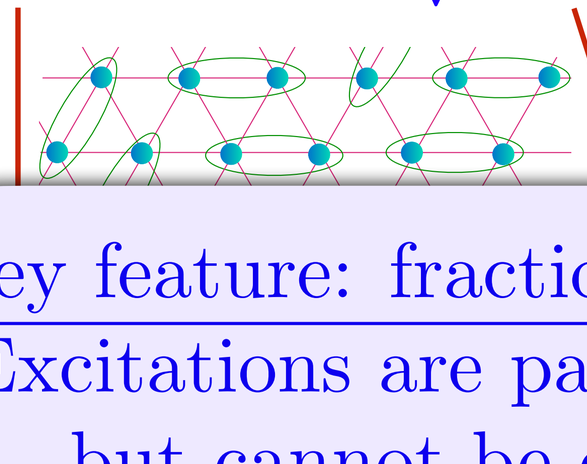

$$+ C_3$$ 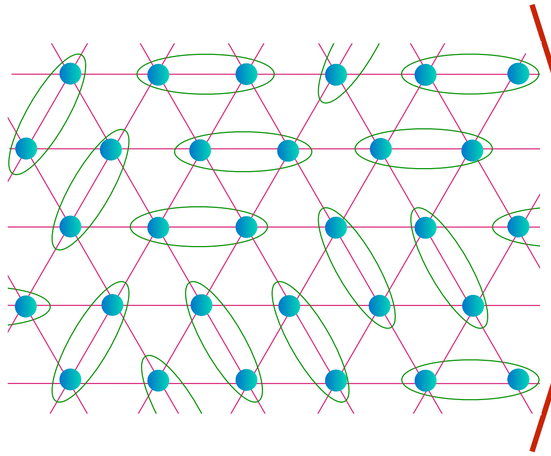

$$+ C_4$$ 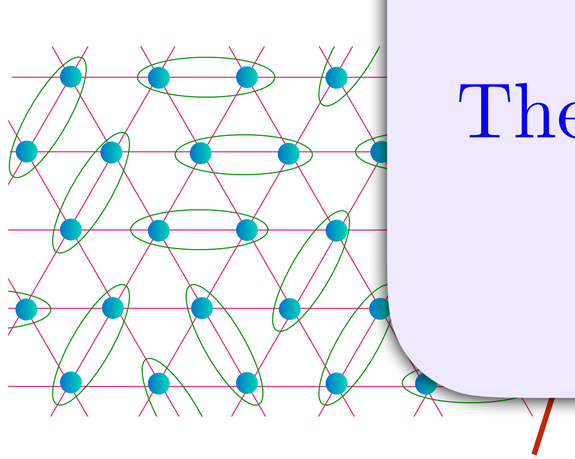

$$\ldots$$

Key feature: fractionalization.

Excitations are particle-like,
but cannot be created
by local operators.
The excitations are classified
under distinct
anyon sectors.

Spin liquid: resonating valence bonds

Anyon: a “spinon”

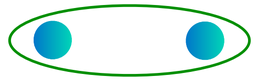

$$= \frac{1}{\sqrt{2}} \left(|\uparrow\downarrow\rangle - |\downarrow\uparrow\rangle \right)$$

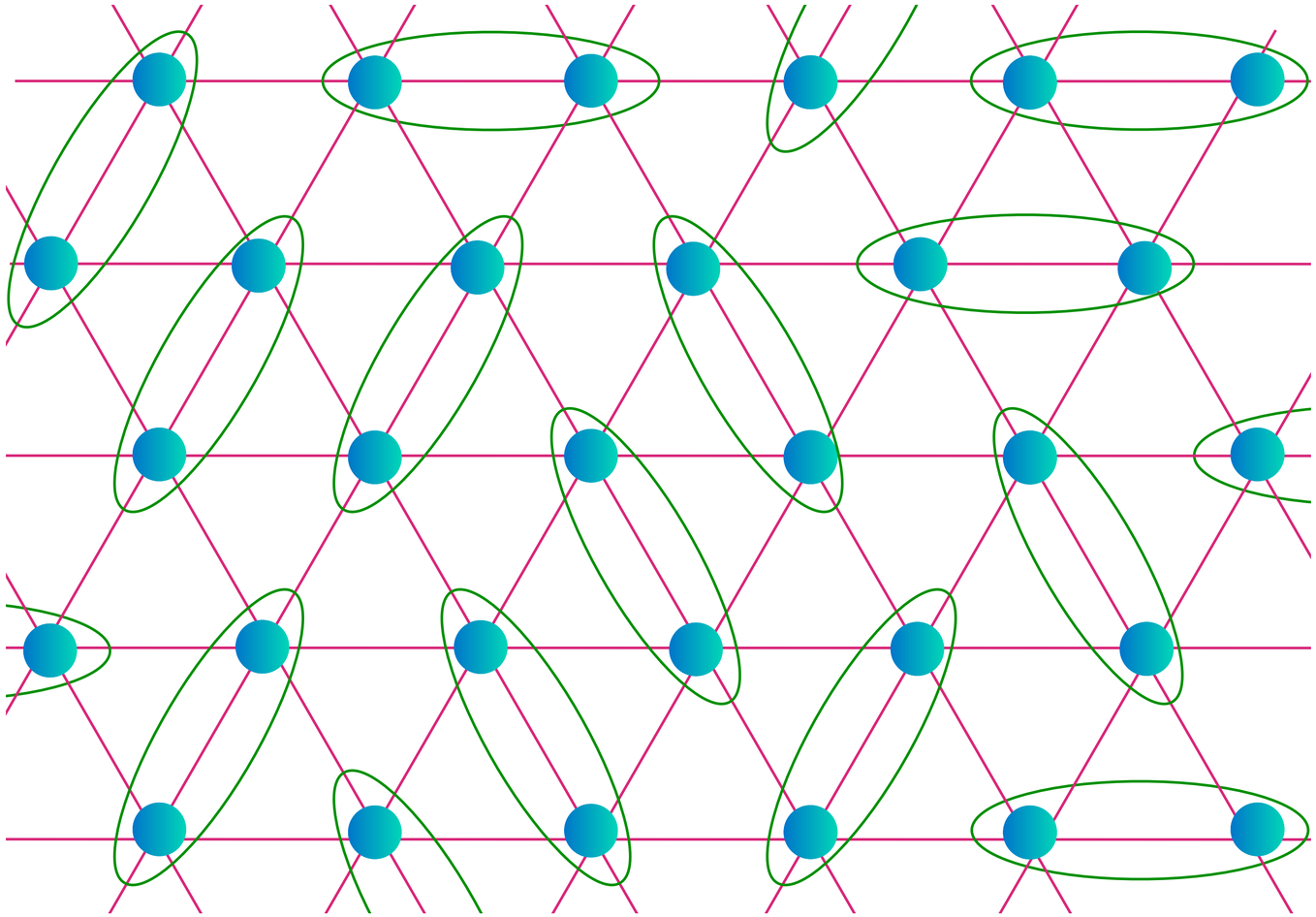

Spin liquid: resonating valence bonds

Anyon: a “spinon”

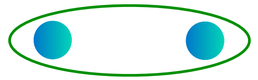

$$= \frac{1}{\sqrt{2}} \left(|\uparrow\downarrow\rangle - |\downarrow\uparrow\rangle \right)$$

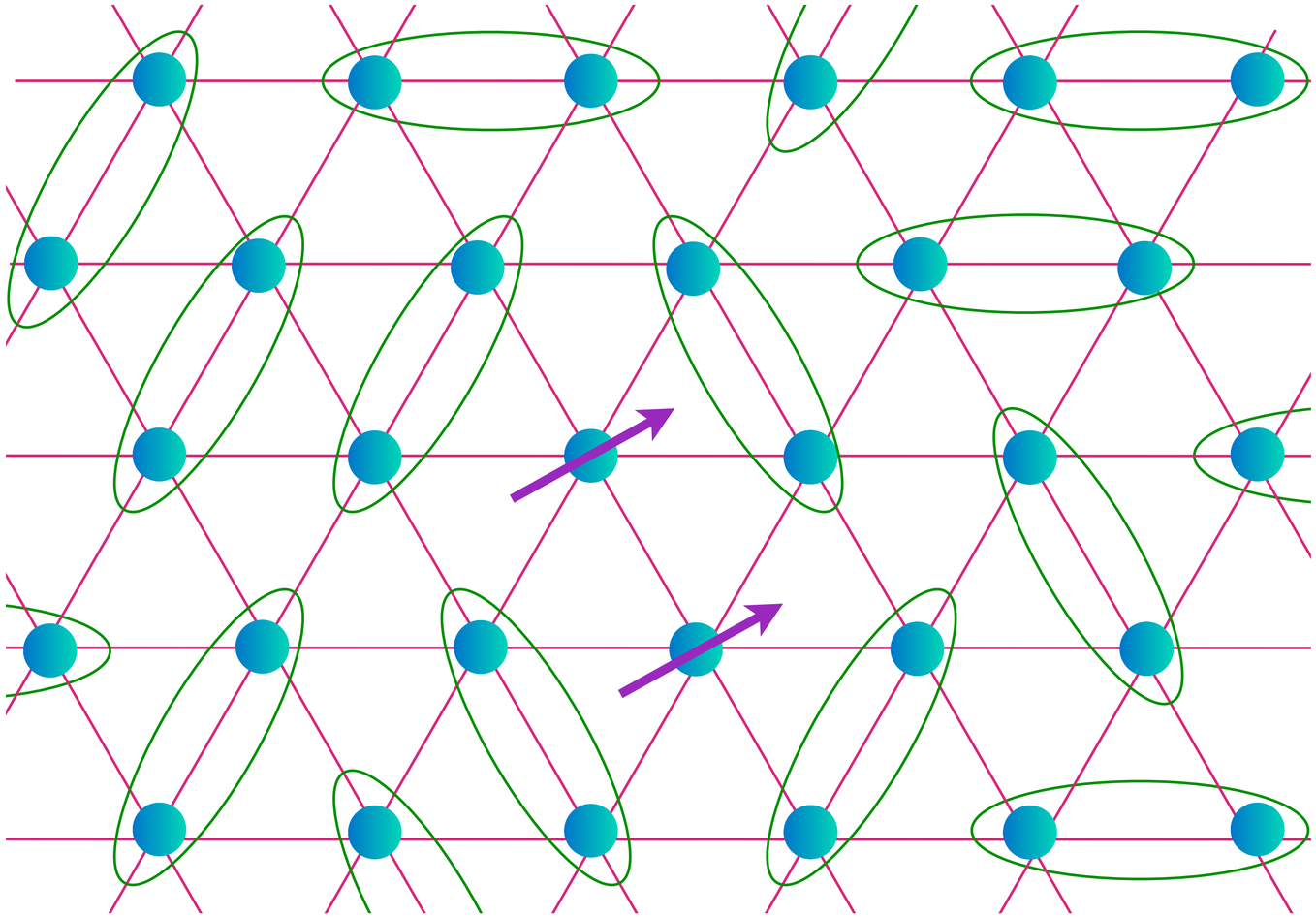

Spin liquid: resonating valence bonds

Anyon: a “spinon”

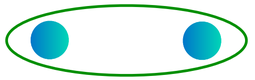

$$= \frac{1}{\sqrt{2}} \left(|\uparrow\downarrow\rangle - |\downarrow\uparrow\rangle \right)$$

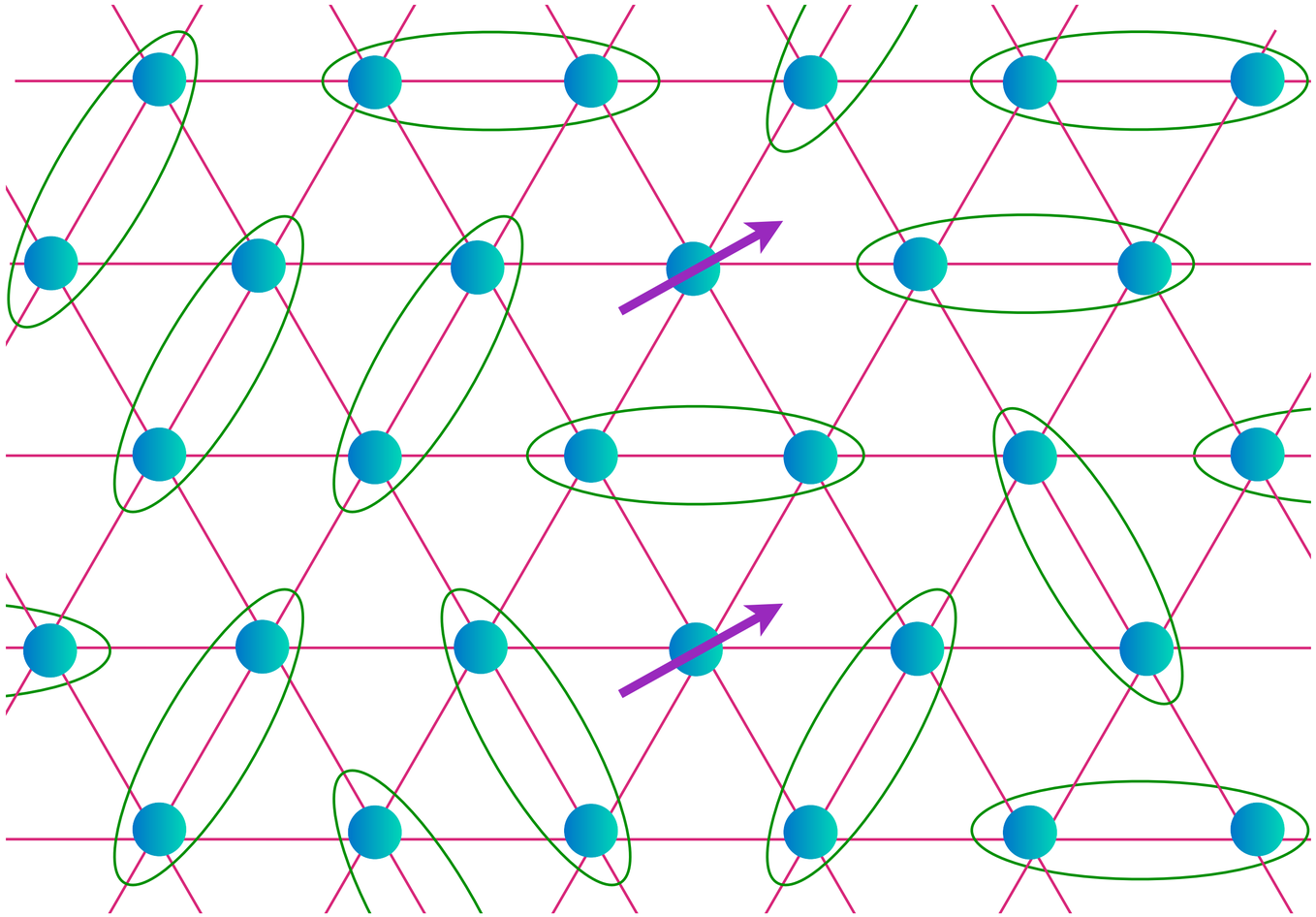

Spin liquid: resonating valence bonds

Anyon: a “spinon”

$$= \frac{1}{\sqrt{2}} \left(|\uparrow\downarrow\rangle - |\downarrow\uparrow\rangle \right)$$

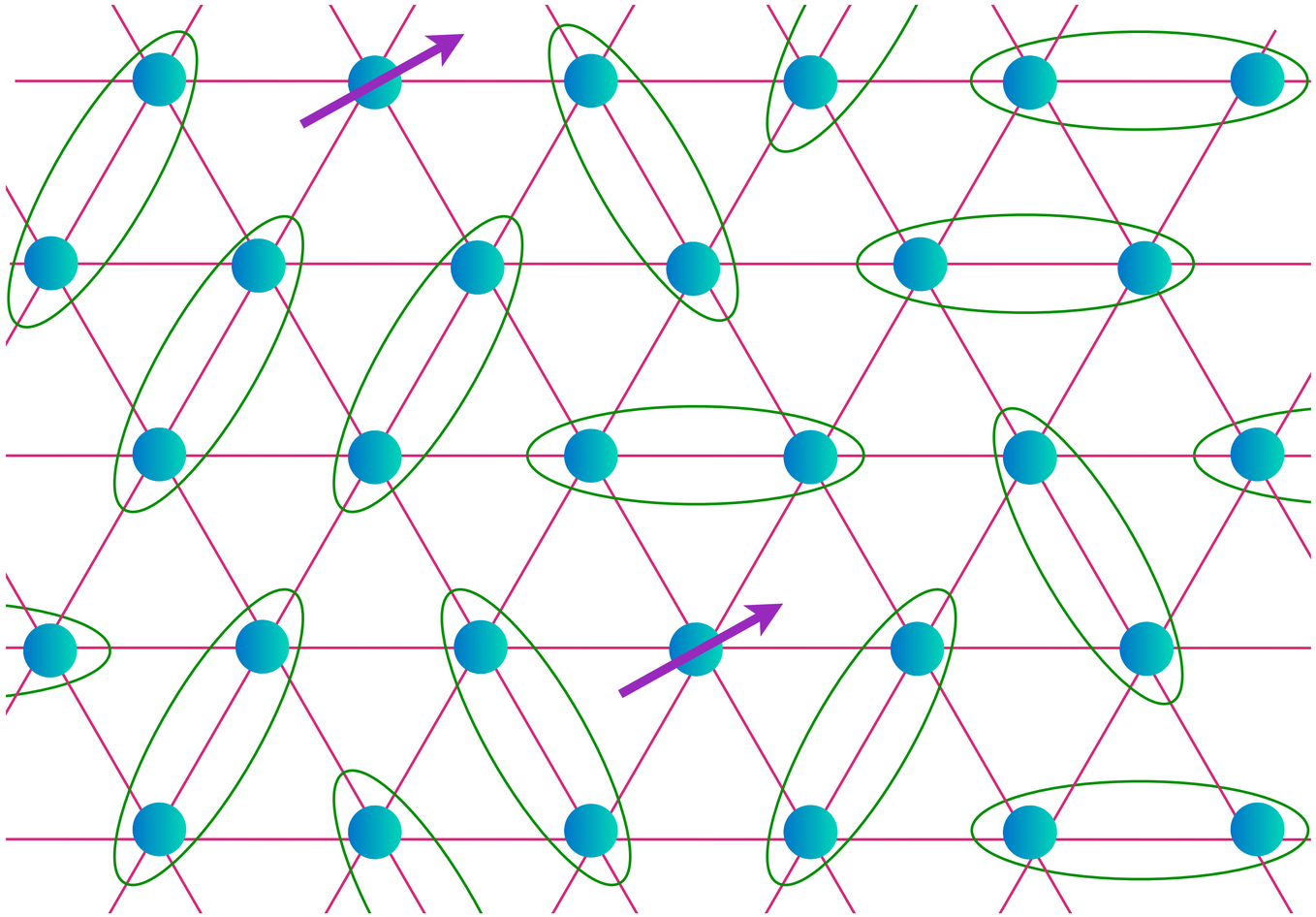

Spin liquid: resonating valence bonds

Anyon: a “spinon”

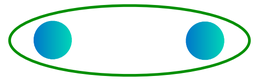

$$= \frac{1}{\sqrt{2}} \left(|\uparrow\downarrow\rangle - |\downarrow\uparrow\rangle \right)$$

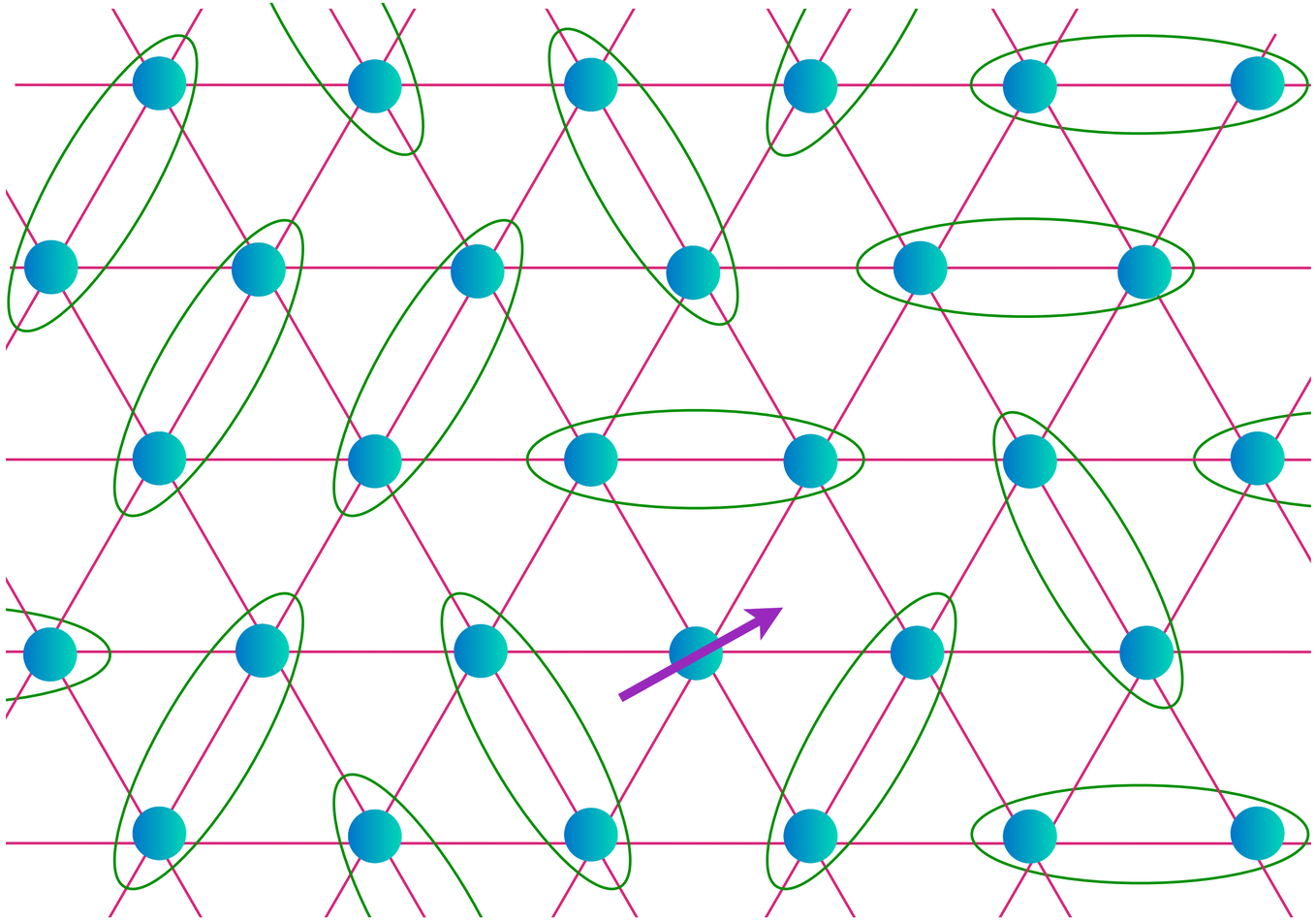

Spin liquid: resonating valence bonds

Anyon: a “spinon”

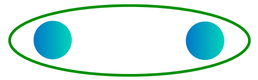

$$= \frac{1}{\sqrt{2}} \left(|\uparrow\downarrow\rangle - |\downarrow\uparrow\rangle \right)$$

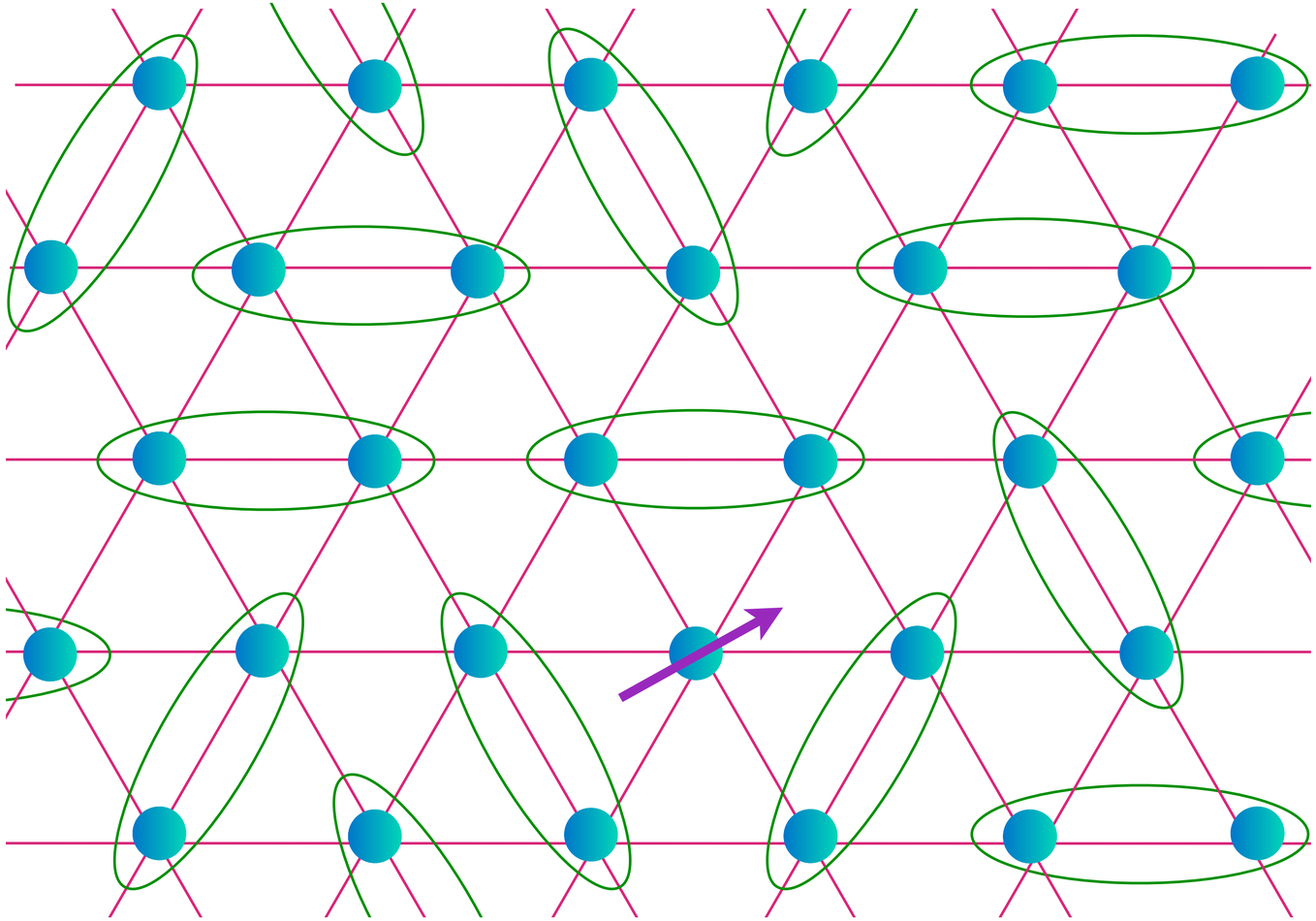

Spin liquid: resonating valence bonds

Anyon: a “spinon”

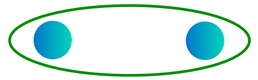

$$= \frac{1}{\sqrt{2}} \left(|\uparrow\downarrow\rangle - |\downarrow\uparrow\rangle \right)$$

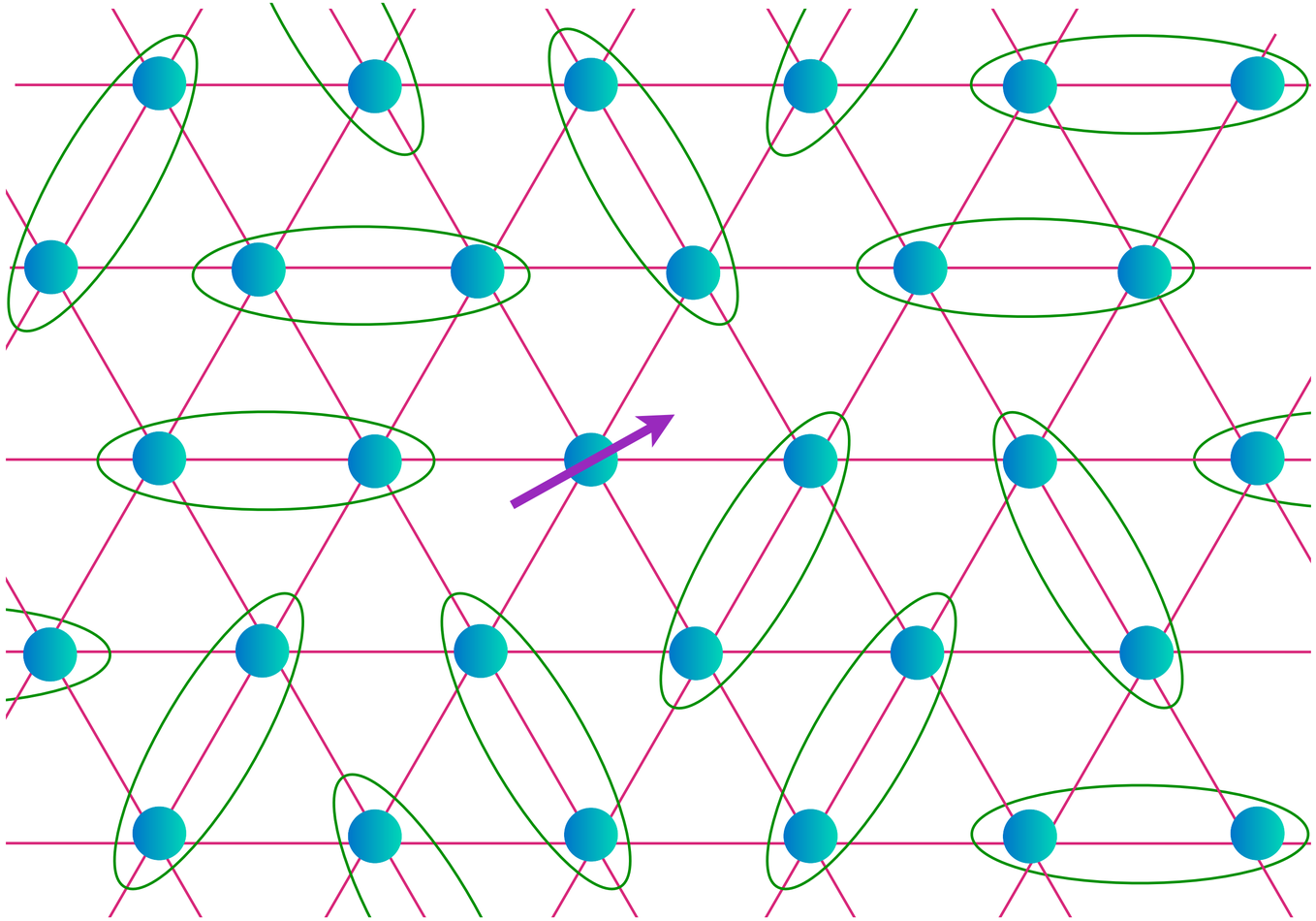

Spin liquid: resonating valence bonds

Anyon: a “spinon”

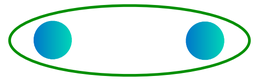

$$= \frac{1}{\sqrt{2}} \left(|\uparrow\downarrow\rangle - |\downarrow\uparrow\rangle \right)$$

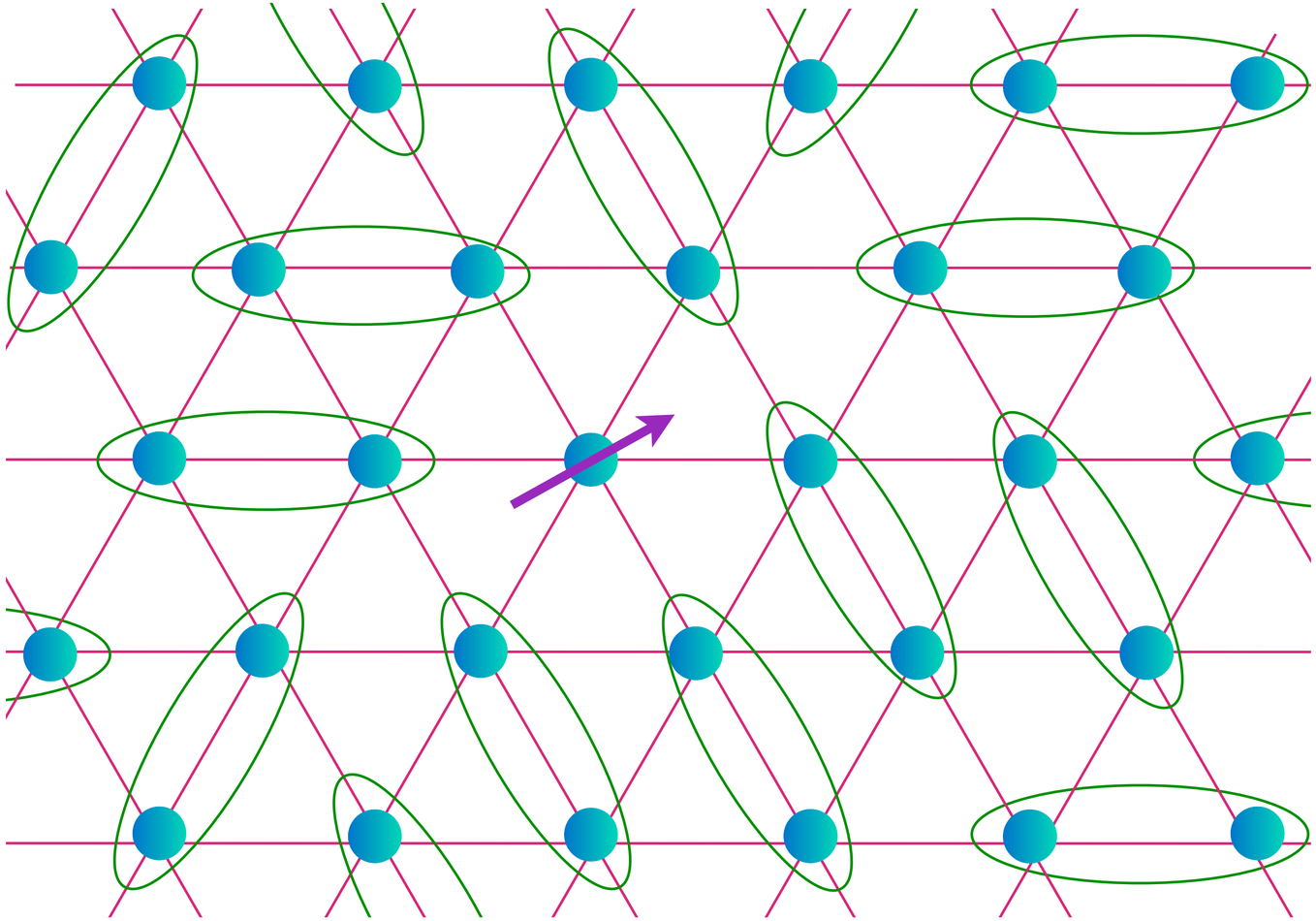

Spin liquid: resonating valence bonds

Anyon: a “spinon”

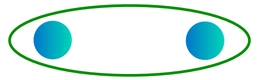

$$= \frac{1}{\sqrt{2}} \left(|\uparrow\downarrow\rangle - |\downarrow\uparrow\rangle \right)$$

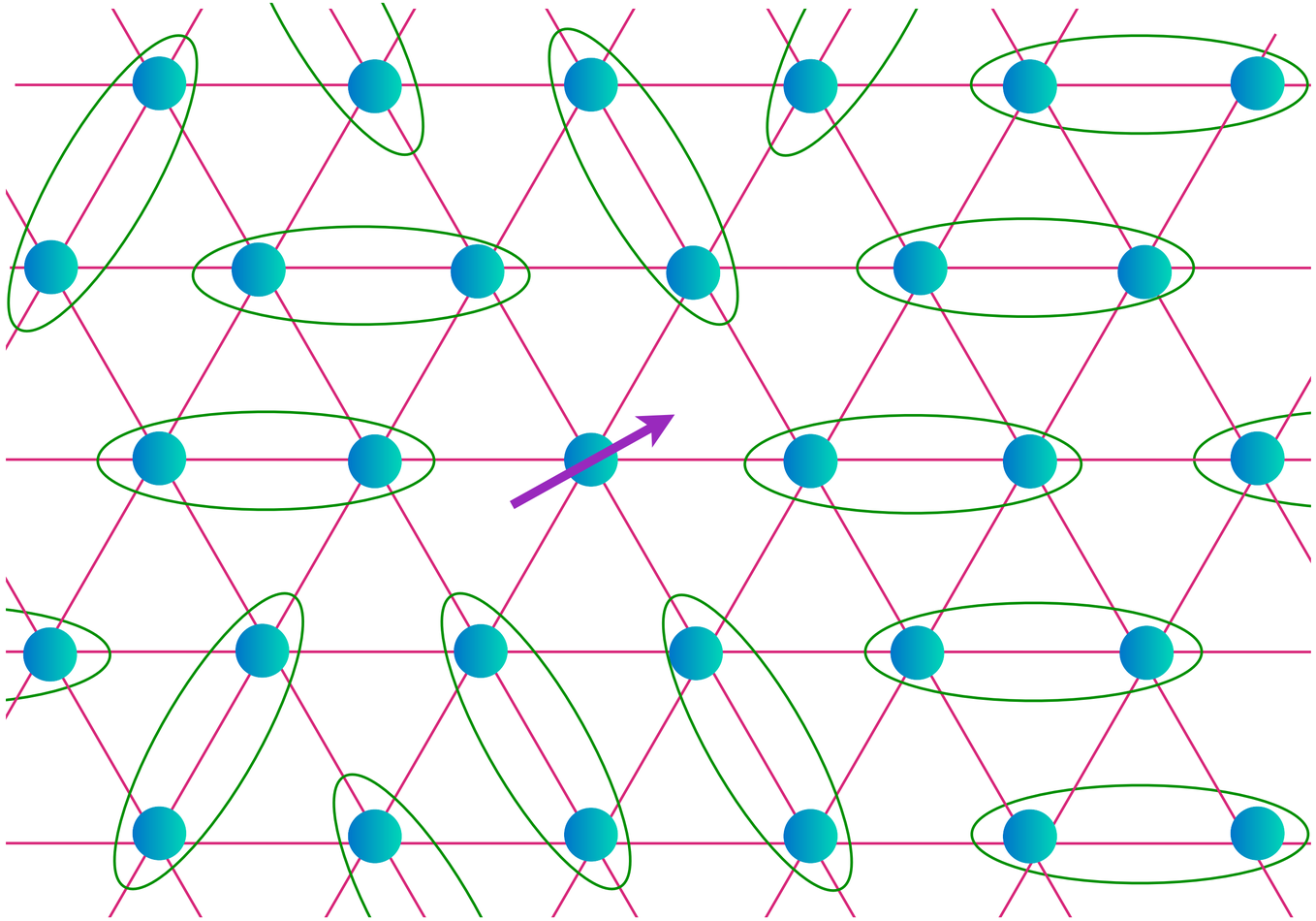

Spin liquid: resonating valence bonds

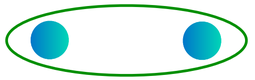

$$= \frac{1}{\sqrt{2}} \left(|\uparrow\downarrow\rangle - |\downarrow\uparrow\rangle \right)$$

$$|\Psi\rangle = C_1 \left| \right\rangle + C_2 \left| \right\rangle$$

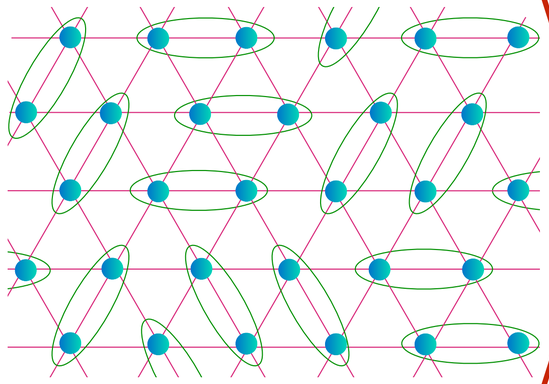

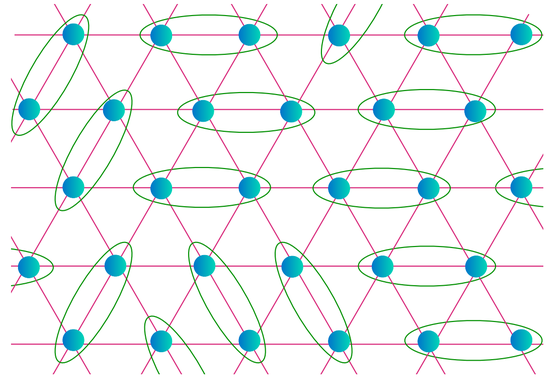

$$+ C_3 \left| \right\rangle + C_4 \left| \right\rangle + C_5 \left| \right\rangle + \ldots$$

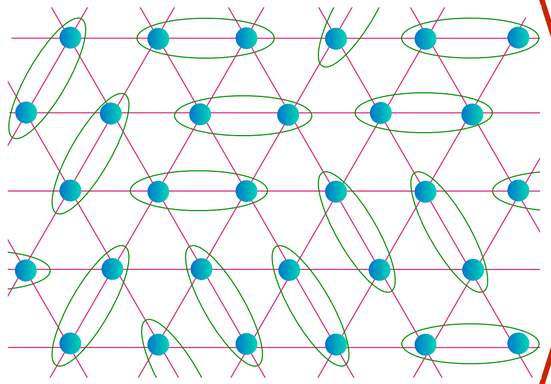

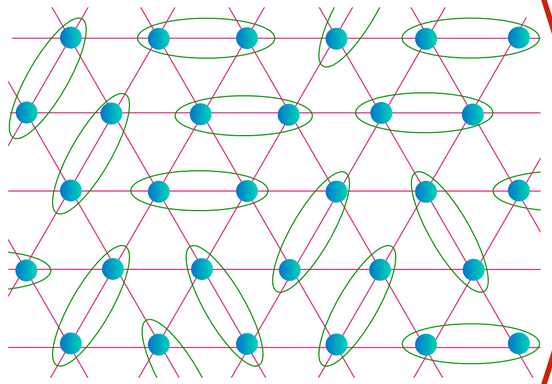

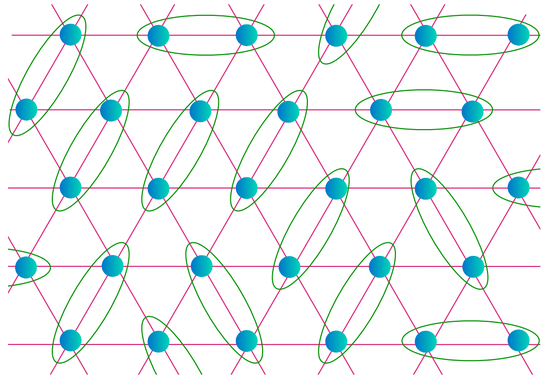

Another anyon—involves subtle changes in sign of superposition

Anyon: a "vison"

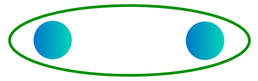

$$= \frac{1}{\sqrt{2}} \left(|\uparrow\downarrow\rangle - |\downarrow\uparrow\rangle \right)$$

$$|\Psi\rangle = C_1 \left| \right\rangle + C_2 \left| \right\rangle$$

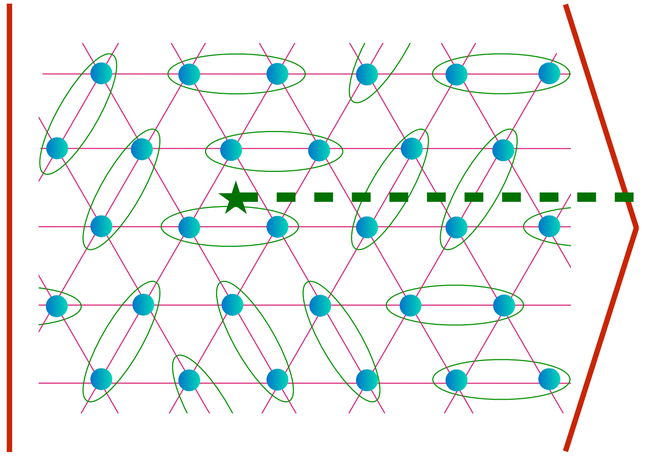

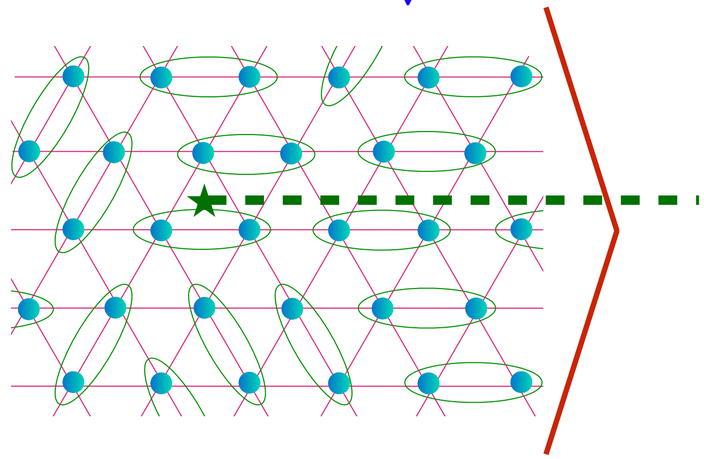

$$+ C_3 \left| \right\rangle + C_4 \left| \right\rangle + C_5 \left| \right\rangle + \ldots$$

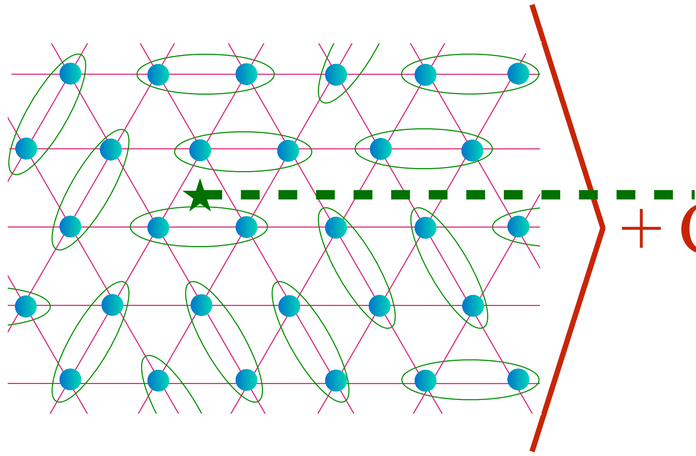

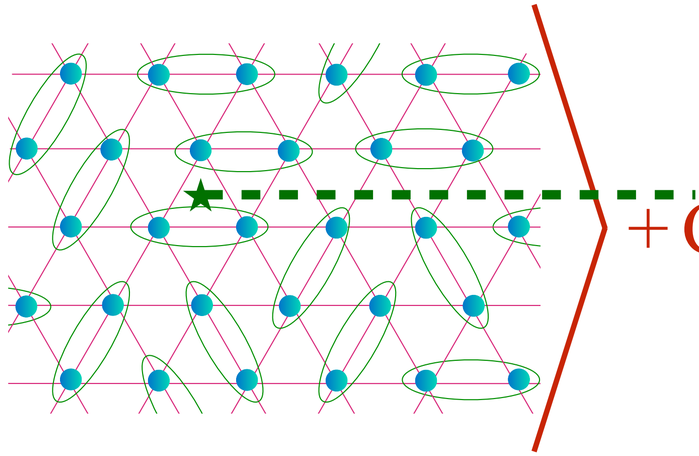

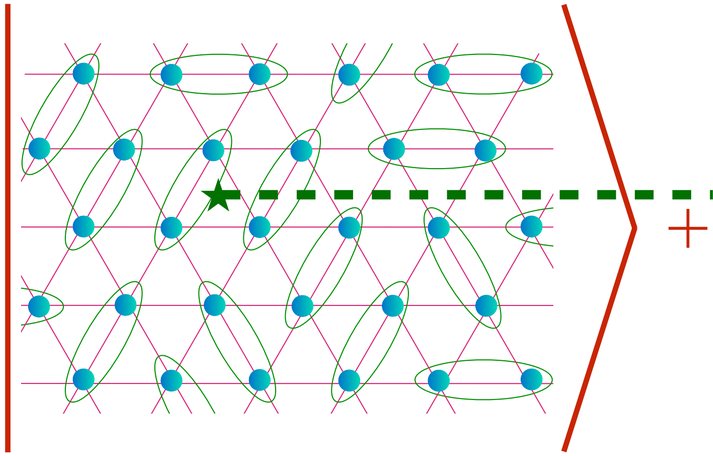

$$C_n \Rightarrow C_n \, (-1)^{\text{Number of dimers across green line}}$$

2. Bosonic spinon theory of quantum spin liquids

Section 1 has obtained an insulator at $p = 0$ with Néel order $\mathcal{N}$. Decreasing $\mathcal{N}$ eventually leads to a metallic state with $\mathcal{N} = 0$, even at $p = 0$. In this section we study the possibility of decreasing $\mathcal{N}$ to zero at $p = 0$ while the system remains an insulator *i.e.* without closing the gap to charged excitations.

As long as the charge gap is finite, we can perform a canonical transformation of the Hubbard model in Eq. (1) to spin-only Heisenberg antiferromagnet

$$\mathcal{H}_J = \sum_{\boldsymbol{i}<\boldsymbol{j}} J_{\boldsymbol{ij}}\, \boldsymbol{S_i} \cdot \boldsymbol{S_j}\,. \tag{17}$$

The $J_{\boldsymbol{ij}}$ are short-ranged antiferromagnetic exchange interactions between $S = 1/2$ spins $\boldsymbol{S_i}$ on sites $\boldsymbol{i}$. We will consider here the square and triangular lattices with nearest neighbor interactions, but the methods generalize to a wide class of lattices and interaction ranges.

In this section, we employ a method which fractionalizes the spin operator into bosonic partons. On the square lattice, this leads to the low energy U(1) gauge theory with complex scalars in Eq. (72), and to the phase diagram in Fig. 16. This phase diagram is in good agreement with numerical studies
[Ferrari and Becca, 2020, Nomura and Imada, 2021, Liu et al., 2024] of the square lattice antiferromagnet with first and second neighbor exchange (the J_1-J_2 model), and also of Sandvik's J-Q model [Takahashi et al., 2024].

Section 3 fractionalizes the spin operator into fermionic partons. This leads ultimately to a seemingly different low energy theory on the square lattice: a SU(2) gauge theory with massless Dirac fermions in Eq. (87), which initially did not agree with numerical studies of square lattice antiferromagnets. Wang *et al.* [Wang et al., 2017] argued that the bosonic and fermionic theories are equivalent, and that the confining phases of the SU(2) gauge theory lead to the same phase diagram as the bosonic partons. This equivalence is powerful, as it yields a toolbox of different approaches to study the square lattice spin liquid. In particular, upon including charge fluctuations, it is the fermionic parton theory that allows study of the confining instability of the square lattice spin liquid to d-wave superconductivity that we study in Sections 5 and 6.

In the bosonic parton approach, we introduce the Schwinger boson description [Arovas and Auerbach, 1988], in terms of elementary $S = 1/2$ bosons. For the group SU(2) the complete set of $(2S + 1)$ states on site $\boldsymbol{i}$ are represented as follows

$$|S, m\rangle \equiv \frac{1}{\sqrt{(S+m)!(S-m)!}} (b^\dagger_{\boldsymbol{i}\uparrow})^{S+m} (b^\dagger_{\boldsymbol{i}\downarrow})^{S-m} |0\rangle, \tag{18}$$

where $m = -S, \ldots S$ is the z component of the spin ($2m$ is an integer). We have introduced two flavors of Schwinger bosons on each site, created by the canonical operator $b^\dagger_{\boldsymbol{i}\alpha}$, with

$\alpha = \uparrow, \downarrow$, and $|0\rangle$ is the vacuum with no Schwinger bosons. The total number of Schwinger bosons, n_b, is the same for all the states; therefore

$$b^{\dagger}_{\boldsymbol{i}\alpha} b_{\boldsymbol{i}\alpha} = n_b \tag{19}$$

with

$$n_b = 2S\,. \tag{20}$$

The above representation of the states is completely equivalent to the operator identity between the spin and Schwinger boson operators

$$\boldsymbol{S_i} = \frac{1}{2} b^{\dagger}_{\boldsymbol{i}\alpha}\, \boldsymbol{\sigma}_{\alpha\beta}\, b_{\boldsymbol{i}\beta} \tag{21}$$

where $\ell = x, y, z$ and the $\boldsymbol{\sigma}$ are the usual 2×2 Pauli matrices.
The spin-states on two sites $\boldsymbol{i}, \boldsymbol{j}$ can combine to form a singlet in a unique manner - the wavefunction of the (unnormalized) singlet state is particularly simple in the boson formulation:

$$\left(\varepsilon_{\alpha\beta} b^{\dagger}_{\boldsymbol{i}\alpha} b^{\dagger}_{\boldsymbol{j}\beta}\right)^{2S} |0\rangle \tag{22}$$

Also, using the constraint in Eq. (19), the following Fierz-type identity can be established

$$\left(\varepsilon_{\alpha\beta} b^{\dagger}_{\boldsymbol{i}\alpha} b^{\dagger}_{\boldsymbol{j}\beta}\right)\left(\varepsilon_{\gamma\delta} b_{\boldsymbol{i}\gamma} b_{\boldsymbol{j}\delta}\right) = -2\boldsymbol{S_i}\cdot\boldsymbol{S_j} + n_b^2/2 + \delta_{\boldsymbol{ij}} n_b \tag{23}$$

where ε is the totally antisymmetric 2×2 tensor

$$\varepsilon = \begin{pmatrix} 0 & 1 \\ -1 & 0 \end{pmatrix}. \tag{24}$$

This implies that $\mathcal{H}_J$ can be rewritten in the form (apart from an additive constant)

$$\mathcal{H}_J = -\frac{1}{2}\sum_{\boldsymbol{i}<\boldsymbol{j}} J_{\boldsymbol{ij}}\left(\varepsilon_{\alpha\beta} b^{\dagger}_{\boldsymbol{i}\alpha} b^{\dagger}_{\boldsymbol{j}\beta}\right)\left(\varepsilon_{\gamma\delta} b_{\boldsymbol{i}\gamma} b_{\boldsymbol{j}\delta}\right) \tag{25}$$

This form makes it clear that $\mathcal{H}_J$ counts the number of singlet bonds.

2.1. Mean-field theory

We begin by the coherent state path integral of $\mathcal{H}_J$ in imaginary time τ at a temperature $\beta = 1/T$

$$\mathcal{Z}_J = \int \mathcal{D}\mathcal{Q}\mathcal{D}b\mathcal{D}\lambda \exp\left(-\int_0^\beta \mathcal{L}_J \, d\tau\right), \tag{26}$$

where

$$\mathcal{L}_J = \sum_{\boldsymbol{i}} \left[b^\dagger_{\boldsymbol{i}\alpha} \left(\frac{d}{d\tau} + i\lambda_{\boldsymbol{i}} \right) b_{\boldsymbol{i}\alpha} - i\lambda_{\boldsymbol{i}} n_b \right]$$

$$+ \sum_{<\boldsymbol{i},\boldsymbol{j}>} \left[\frac{J_{\boldsymbol{ij}} |\mathcal{Q}_{\boldsymbol{i},\boldsymbol{j}}|^2}{2} - \frac{J_{\boldsymbol{ij}} \mathcal{Q}^*_{\boldsymbol{i},\boldsymbol{j}}}{2} \varepsilon_{\alpha\beta} b_{\boldsymbol{i}\alpha} b_{\boldsymbol{j}\beta} + H.c. \right]. \tag{27}$$

Here the $\lambda_{\boldsymbol{i}}$ fix the boson number of n_b at each site; τ-dependence of all fields is implicit; $\mathcal{Q}$ was introduced by a Hubbard-Stratonovich decoupling of $\mathcal{H}_J$.
This procedure is similar to that employed in deriving the Landau-Ginzburg theory of superconductivity from electron pairing, with the crucial difference that now the Lagrangian

$\mathcal{L}_J$ has a $U(1)$ gauge invariance associated with the local constraint in Eq. (19):

$$\begin{aligned} b^\dagger_{i\alpha} &\rightarrow b^\dagger_{i\alpha} \exp\left(i\rho_i(\tau)\right) \\ \mathcal{Q}_{i,j} &\rightarrow \mathcal{Q}_{i,j} \exp\left(-i\rho_i(\tau) - i\rho_j(\tau)\right) \\ \lambda_i &\rightarrow \lambda_i + \frac{\partial \rho_i}{\partial \tau}(\tau)\,. \end{aligned} \tag{28}$$

The functional integral over $\mathcal{L}_J$ faithfully represents the partition function, but does require gauge fixing. This gauge invariance leads to emergent gauge field degrees of freedom, as we will see below.

We begin with mean-field saddle point of $\mathcal{Z}_J$ over the path integrals of $\mathcal{Q}$ and λ. The saddle-point approximation is valid in the limit of a large number of spin flavors, but we do not explore this here. With the saddle point values $\mathcal{Q}_{ij} = \bar{\mathcal{Q}}_{ij}$, $i\lambda_i = \bar{\lambda}_i$ we obtain a mean-field Hamiltonian for the $b_{i\alpha}$

$$\begin{aligned} \mathcal{H}_{J,MF} = \sum_{<i,j>} \left(\frac{J_{ij}|\bar{\mathcal{Q}}_{ij}|^2}{2} - \frac{J_{ij}\bar{\mathcal{Q}}^*_{ij}}{2} \varepsilon_{\alpha\beta} b^\alpha_i b^\beta_j + H.c. \right) \\ + \sum_i \bar{\lambda}_i (b^\dagger_{i\alpha} b_{i\alpha} - n_b)\,. \end{aligned} \tag{29}$$

This Hamiltonian is quadratic in the boson operators and all its eigenvalues can be determined by a Bogoluibov transformation. This leads in general to an expression of the form

$$\mathcal{H}_{J,MF} = E_{J,MF}[\bar{\mathcal{Q}}, \bar{\lambda}] + \sum_{\mu} \omega_{\mu}[\bar{\mathcal{Q}}, \bar{\lambda}]\gamma^{\dagger}_{\mu\alpha}\gamma_{\mu\alpha} \tag{30}$$

The index μ extends over $1 \ldots$.number of sites in the system, $E_{J,MF}$ is the ground state energy and is a functional of $\bar{\mathcal{Q}}$, $\bar{\lambda}$, ω_{μ} is the eigenspectrum of excitation energies which is also a function of $\bar{\mathcal{Q}}$, $\bar{\lambda}$, and the γ^{α}_{μ} represent the bosonic eigenoperators. The excitation spectrum thus consists of non-interacting spinor bosons. The ground state is determined by minimizing $E_{J,MF}$ with respect to the $\bar{\mathcal{Q}}_{\boldsymbol{ij}}$ subject to the constraints

$$\frac{\partial E_{MF}}{\partial \bar{\lambda}_{\boldsymbol{i}}} = 0 \tag{31}$$

The saddle-point value of the $\bar{\mathcal{Q}}$ satisfies

$$\bar{\mathcal{Q}}_{\boldsymbol{ij}} = \langle \varepsilon_{\alpha\beta} b_{\boldsymbol{i}\alpha} b_{\boldsymbol{j}\beta} \rangle \tag{32}$$

Note that $\bar{\mathcal{Q}}_{\boldsymbol{ij}} = -\bar{\mathcal{Q}}_{ji}$ indicating that $\bar{\mathcal{Q}}_{\boldsymbol{ij}}$ is a directed field - an orientation has to be chosen on every link.

These saddle-point equations have been solved for the square and triangular lattices with nearest neighbor exchange J, and they lead to stable and translationally invariant solutions for $\bar{\lambda}_{\boldsymbol{i}}$ and $\bar{\mathcal{Q}}_{\boldsymbol{ij}}$. The only saddle-point quantity which does not have the full symmetry of the lattice is the orientation of the $\bar{\mathcal{Q}}_{\boldsymbol{ij}}$. Note that although it appears that such a choice of orientation appears to break inversion or reflection symmetries, such symmetries are actually preserved: the $\bar{\mathcal{Q}}_{\boldsymbol{ij}}$ are not gauge-invariant, and all gauge-invariant observables do preserve all symmetries of the underlying Hamiltonian. For the square lattice, we have $\bar{\lambda}_{\boldsymbol{i}} = \bar{\lambda}$, $\bar{\mathcal{Q}}_{\boldsymbol{i},\boldsymbol{i}+\hat{x}} = \bar{\mathcal{Q}}_{\boldsymbol{i},\boldsymbol{i}+\hat{y}} = \bar{\mathcal{Q}}$. Similarly, on the triangular lattice we have $\bar{\mathcal{Q}}_{\boldsymbol{i},\boldsymbol{i}+\hat{e}_p} = \bar{\mathcal{Q}}$ for $p = 1, 2, 3$, where the unit vectors

$$\begin{aligned} \hat{e}_1 &= (1/2, \sqrt{3}/2) \\ \hat{e}_2 &= (1/2, -\sqrt{3}/2) \\ \hat{e}_3 &= (-1, 0) \end{aligned} \tag{33}$$

point between nearest neighbor sites of the triangular lattice. We sketch the orientation of the $\bar{\mathcal{Q}}_{\boldsymbol{ij}}$ on the triangular lattice in Fig. 7.

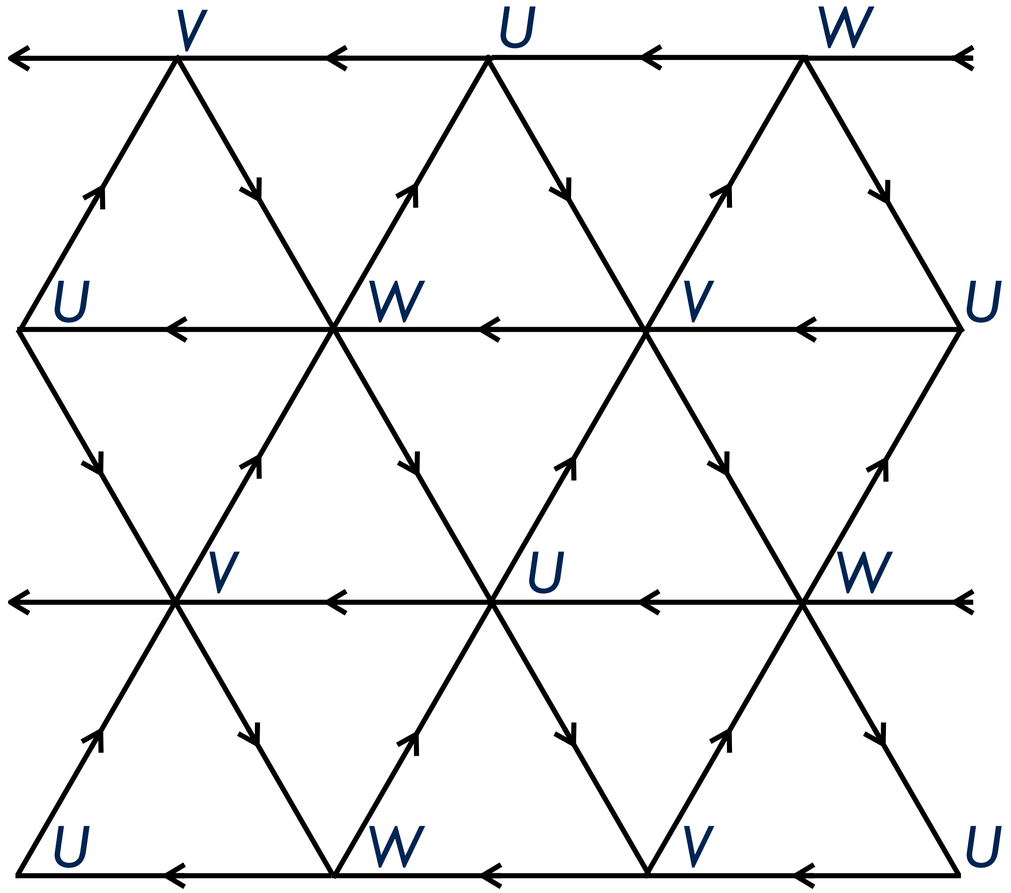

Figure 7: Orientation of the nearest neighbor $\bar{\mathcal{Q}}_{ij}$ on the triangular lattice. Also shown are the labels of the 3 sublattices.

We can also compute the dispersion $\omega_{\boldsymbol{k}}$ of the $\gamma_{\boldsymbol{k}}$ excitations. These are fractionalized bosonic particles which carry spin $S = 1/2$ ('spinons'). The dispersion on the square lattice is

$$\omega_{\boldsymbol{k}} = \left(\bar{\lambda}^2 - J^2\bar{\mathcal{Q}}^2(\sin k_x + \sin k_y)^2\right)^{1/2} \tag{34}$$

while that on the triangular lattice is [Sachdev, 1992]

$$\omega_{\boldsymbol{k}} = \left(\bar{\lambda}^2 - J^2\bar{\mathcal{Q}}^2(\sin k_1 + \sin k_2 + \sin k_3)^2\right)^{1/2} \tag{35}$$

with $k_p = \boldsymbol{k}\cdot\hat{e}_p$. These are the spinons and the spinon dispersion on the triangular lattice is plotted in Fig. 8, and that on the square lattice in Fig. 9.

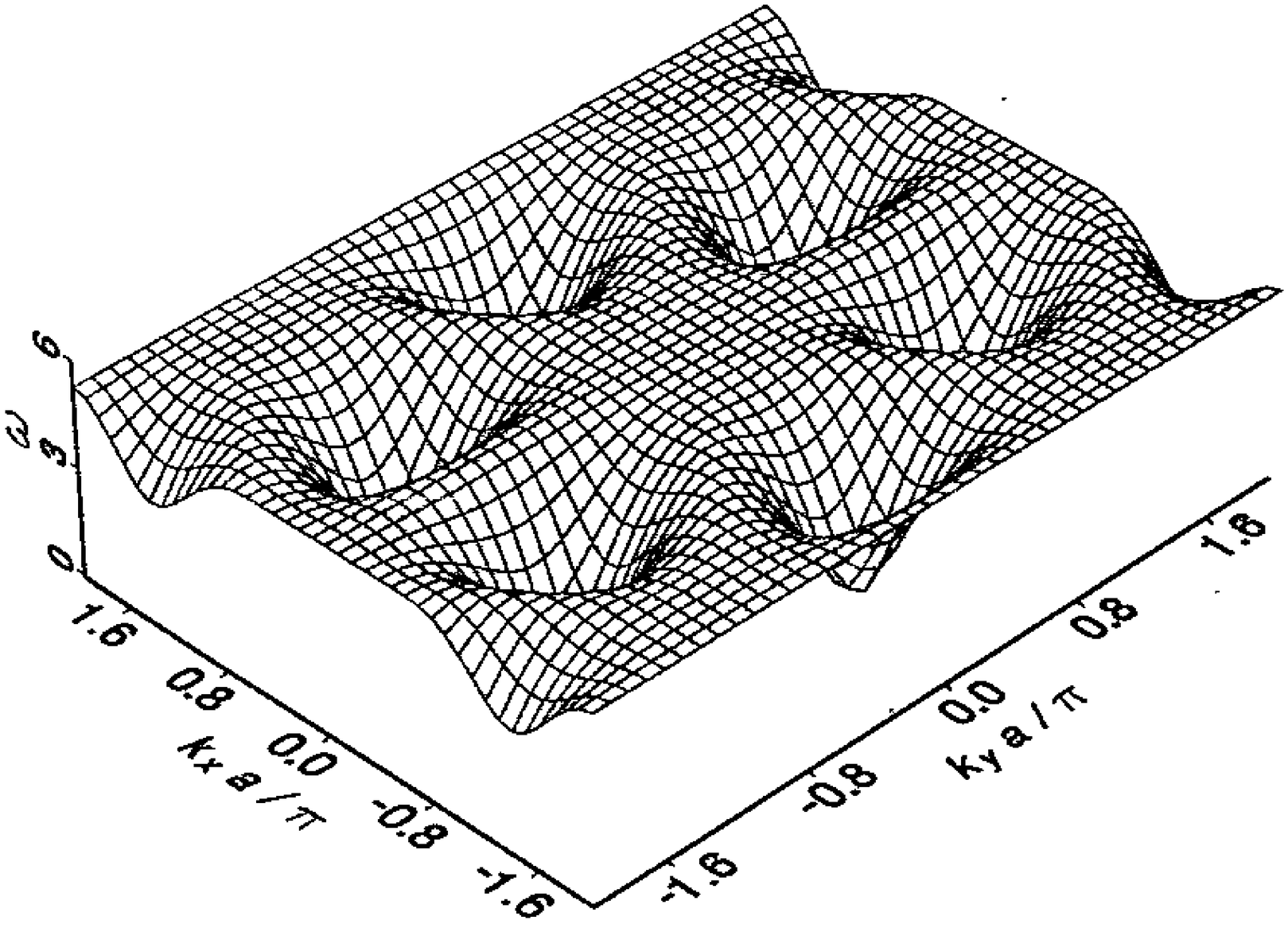

Figure 8: Spinon dispersion on the triangular lattice [Sachdev, 1992]. Reprinted with permission from

APS.

Notice that the spinons have minima at two degenerate points in the Brillouin zone for both lattices. For the square lattice, the minima are at $\boldsymbol{k} = \pm(\pi/2, \pi/2)$ with an energy gap of $\left(\bar{\lambda}^2 - 4J^2\bar{\mathcal{Q}}^2\right)^{1/2}$. For the triangular lattice they are at $\boldsymbol{k} = \pm(4\pi/3, 0)$ (and at wavevectors separated from these by reciprocal lattice vectors). So there are a total of 4 spinon excitations in both cases: 2 associated with the spin degeneracy of $S_z = \pm 1/2$, and 2 associated with the degeneracy in the Brillouin zone spectrum.

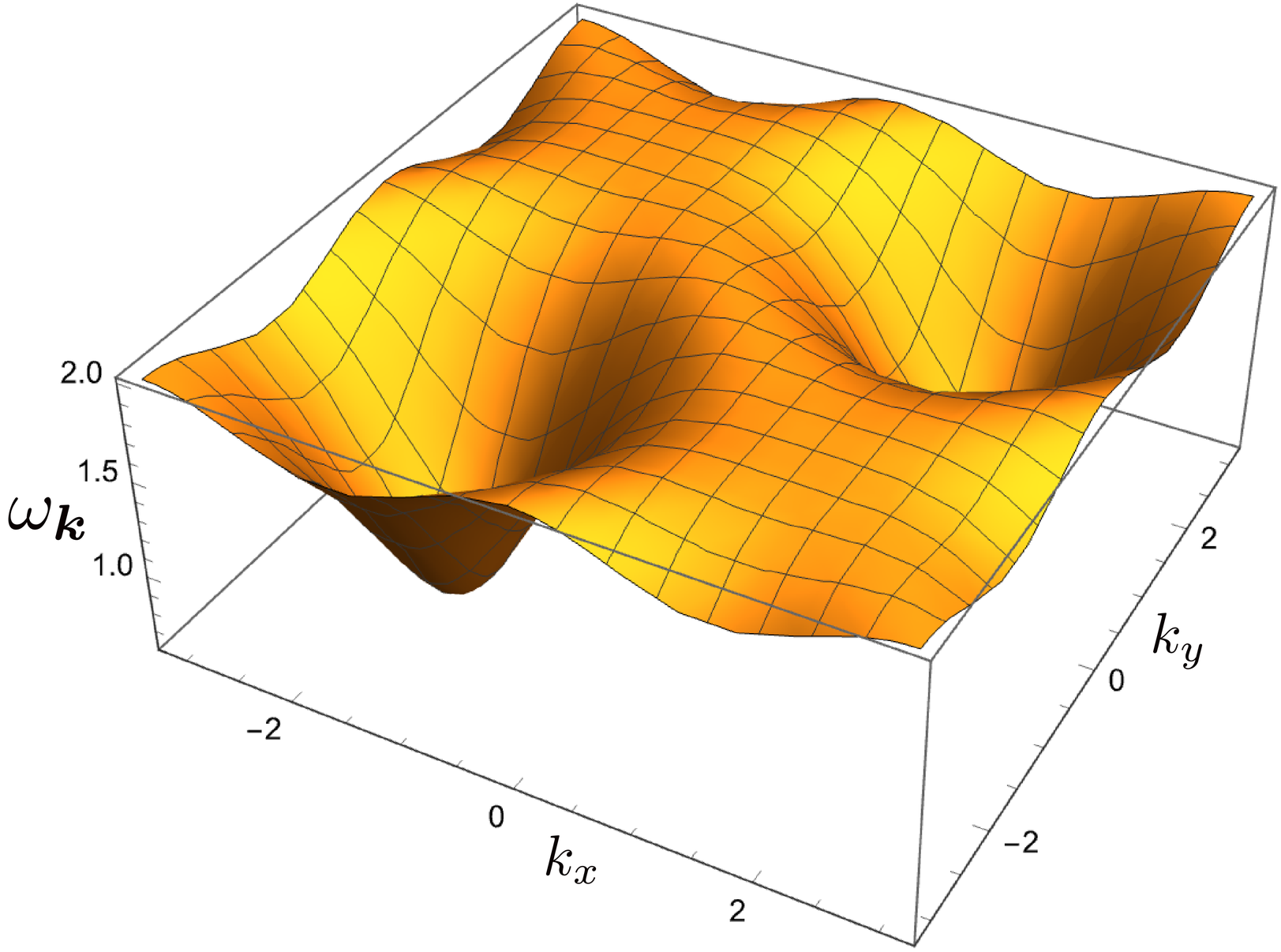

Figure 9: Dispersion of bosonic spinons in a square lattice spin liquid, from Eq. (34).

Next, we turn to spin-singlet excitations, *i.e.* understanding the nature of the spectrum of the $\mathcal{Q}_{ij}$ and λ_i fluctuations about the saddle point described above. At the outset, it appears that we can view such fluctuations as composites of 2-spinon excitations, as both $\mathcal{Q}_{ij}$ and λ_i couple to spinon pair operators, and so conclude that such excitations should not be viewed as the 'elementary' excitations of the quantum state found so far. Furthermore, the saddle-point has not broken any global symmetries of the Hamiltonian, and so it would appear that no such composite excitations has any reason to be low energy without fine-tuning.

However, it does turn out that there are separate elementary excitations in the singlet sector, and these arise from two distinct causes: (*i*) the gauge invariance in (28) leads to a gapless "photon" excitation; (*ii*) there are topologically non-trivial configurations of $\mathcal{Q}_{ij}$ which lead to excitations which appear as new saddle points. Excitations in the class (*i*) arise in the square lattice case, while those in class (*ii*) appear on the triangular lattice, and these will be considered separately in the following subsections.

2.2. Gauge excitations

The gauge transformations in (28) act on the phases of the $\mathcal{Q}_{\boldsymbol{ij}}$, and so it is appropriate to just focus on the fluctuations of the phases of the $\mathcal{Q}_{\boldsymbol{ij}}$ whose amplitudes are non-zero at the saddle-point.
We define

$$\begin{aligned} \mathcal{Q}_{\boldsymbol{i},\boldsymbol{i}+\hat{x}} &= \bar{\mathcal{Q}} \exp\left(i\Theta_{\boldsymbol{i}x}\right) \\ \mathcal{Q}_{\boldsymbol{i},\boldsymbol{i}+\hat{y}} &= \bar{\mathcal{Q}} \exp\left(i\Theta_{\boldsymbol{i}y}\right) \end{aligned} \tag{36}$$

Then, the gauge transformations in (28) can be written as

$$\begin{aligned} \Theta_{\boldsymbol{i}x}(\tau) &\rightarrow \Theta_{\boldsymbol{i}x}(\tau) - \rho_{\boldsymbol{i}}(\tau) - \rho_{\boldsymbol{i}+x}(\tau) \\ \Theta_{\boldsymbol{i}y}(\tau) &\rightarrow \Theta_{\boldsymbol{i}y}(\tau) - \rho_{\boldsymbol{i}}(\tau) - \rho_{\boldsymbol{i}+y}(\tau) \\ \lambda_{\boldsymbol{i}} &\rightarrow \lambda_{\boldsymbol{i}} + \frac{\partial \rho_{\boldsymbol{i}}}{\partial \tau}(\tau). \end{aligned} \tag{37}$$

The question before us is whether (28) imposes on us the presence of a gapless photon in the low energy and long-wavelength limit. The answer is affirmative, and the needed result is

obtained by parameterizing such fluctuations as follows

$$\begin{aligned} \Theta_{\boldsymbol{i}x}(\tau) &= \eta_{\boldsymbol{i}} a_x(\boldsymbol{r},\tau) \\ \Theta_{\boldsymbol{i}y}(\tau) &= \eta_{\boldsymbol{i}} a_y(\boldsymbol{r},\tau) \\ \lambda_{\boldsymbol{i}} &= -i\bar{\lambda} - \eta_{\boldsymbol{i}} a_\tau(\boldsymbol{r},\tau) \end{aligned} \tag{38}$$

where the a_μ are assumed to be smooth functions of spacetime parameterized by the continuum spatial co-ordinate r, and imaginary time τ; the factor $\eta_{\boldsymbol{i}}$, defined in Eq. (11), has opposite signs on any pair of nearest-neighbor sites. Then, taking the continuum limit of (37) with $\rho_{\boldsymbol{i}}(\tau) = \eta_{\boldsymbol{i}}\rho(r,\tau)$, we deduce from (38) that

$$\begin{aligned} a_x &\rightarrow a_x - \partial_x \rho \\ a_y &\rightarrow a_y - \partial_y \rho \\ a_\tau &\rightarrow a_\tau - \partial_\tau \rho \end{aligned} \tag{39}$$

So we reach the very important conclusion that a_μ transforms just like a continuum U(1) gauge field! Note that the factor $\eta_{\boldsymbol{i}}$ in this U(1) gauge transformation implies from (28) that the spinons $b_{\boldsymbol{i}}$ carry opposite gauge charges on the two sublattices.

As in traditional field-theoretic analyses, (39) imposes the requirement that the long-wavelength action of the a_μ fluctuations must have the form

$$\mathcal{S}_b = \int d^3x \frac{1}{2K'} (\epsilon_{\mu\nu\lambda} \partial_\nu a_\lambda)^2, \tag{40}$$

and this describes a gapless a_μ photon excitation, with a suitable velocity of 'light'. So, on the square lattice, the spectrum of spin-singlet states includes a linearly-dispersing photon mode. Such a state is a U(1) spin liquid. Actually, the gapless photon of this U(1) spin liquid is ultimately not stable because of monopole tunneling events; this involves a long and interesting story [Read and Sachdev, 1989, Read and Sachdev, 1990, Senthil et al., 2004b, Senthil et al., 2004a] which we will discuss briefly in Section 5. In the following subsection, we will consider the case of the triangular lattice, where, the U(1) photon is gapped by the Higgs mechanism to yield a $\mathbb{Z}_2$ spin liquid.

Now we have to consider 3 separate values of $\mathcal{Q}_{\boldsymbol{ij}}$ per site, and so we replace (36) by

$$\mathcal{Q}_{\boldsymbol{i},i+\hat{e}_p} = \bar{\mathcal{Q}} \exp\left(i\Theta_{p,\boldsymbol{i}}\right) \tag{41}$$

where $p = 1, 2, 3$, the vectors $\hat{e}_p$ were defined (33), $\bar{\mathcal{Q}}$ is the mean-field value, and Θ_p is a real phase. The effective action for the $\Theta_{p,\boldsymbol{i}}$ must be invariant under

$$\Theta_{p,\boldsymbol{i}} \to \Theta_{p,\boldsymbol{i}} - \rho_{\boldsymbol{i}} - \rho_{\boldsymbol{i}+\hat{e}_p}. \tag{42}$$

Upon performing a Fourier transform, with the link variables Θ_p placed on the center of the links, the gauge invariance takes the form

$$\Theta_p(\boldsymbol{k}) \to \Theta_p(\boldsymbol{k}) - 2\rho(\boldsymbol{k})\cos(k_p/2) \tag{43}$$

The momentum $\boldsymbol{k}$ takes values in the first Brillouin zone of the triangular lattice. This invariance implies that the effective action for the Θ_p can only be a function of the following gauge-invariant combinations:

$$I_{pq}(\boldsymbol{k}) = 2\cos(k_q/2)\Theta_p(\boldsymbol{k}) - 2\cos(k_p/2)\Theta_q(\boldsymbol{k}) \tag{44}$$

We now wish to take the continuum limit at points in the Brillouin zone where the action involves only gradients of the Θ_p fields and thus has the possibility of gapless excitations. The same analysis could have been applied to the square lattice, in which case there is only one invariant I_{xy}. In this case, we choose $\boldsymbol{k} = \boldsymbol{g} + \boldsymbol{q}$, with $\boldsymbol{g} = (\pi, \pi)$ (this corresponds to the choice of $\eta_{\boldsymbol{i}}$ above) and $\boldsymbol{q}$ small; then $I_{xy} = q_x\Theta_y - q_y\Theta_x$ which is clearly the U(1) flux invariant under (39).

The situation is more complex for the case of the triangular lattice [Sachdev, 1992]. Now there are 3 independent I_{pq} invariants, and it is not difficult to see that only two of the three values

of $\cos(k_p/2)$ can vanish at any point of the Brillouin zone. One such point is the wavevector

$$\boldsymbol{g} = \frac{2\pi}{\sqrt{3}a}(0,1) \tag{45}$$

where

$$\begin{aligned} \boldsymbol{g}\cdot\hat{e}_1 &= \pi \\ \boldsymbol{g}\cdot\hat{e}_2 &= -\pi \\ \boldsymbol{g}\cdot\hat{e}_3 &= 0. \end{aligned} \tag{46}$$

Taking the continuum limit with the fields varying with momenta with close to $\boldsymbol{g}$ we find that the I_{pq} depend only upon gradients of Θ_1 and Θ_2. It is also helpful to parametrize the Θ_p in the following suggestive manner (analogous to (38))

$$\begin{aligned} \Theta_1(\boldsymbol{r}) &= ia_1(\boldsymbol{r})e^{i\boldsymbol{g}\cdot\boldsymbol{r}} \\ \Theta_2(\boldsymbol{r}) &= -ia_2(\boldsymbol{r})e^{i\boldsymbol{g}\cdot\boldsymbol{r}} \\ \Theta_3(\boldsymbol{r}) &= H(\boldsymbol{r})e^{i\boldsymbol{g}\cdot\boldsymbol{r}} \end{aligned} \tag{47}$$

It can be verified that the condition for the reality of Θ_p is equivalent to demanding that a_1, a_2, H be real. We will now take the continuum limit with a_1, a_2, H varying slowly on the

scale of the lattice spacing. It is then not difficult to show that the invariants I_{pq} then reduce to (after a Fourier transformation):

$$\begin{aligned} I_{12} &= \partial_2 a_1 - \partial_1 a_2 \\ I_{31} &= \partial_1 H - 2a_1 \\ I_{32} &= \partial_2 H - 2a_2, \end{aligned} \tag{48}$$

where $\partial_{\boldsymbol{i}}$ is the spatial gradient along the direction $\hat{e}_{\boldsymbol{i}}$. Thus the a_1, a_2 are the components of a U(1) gauge field, with the components are taken along an 'oblique' co-ordinate system defined by the axes $\hat{e}_1, \hat{e}_2$; this is just as in the square lattice. However, in addition to I_{12}, we also have the invariants I_{31} and I_{32} in the triangular lattice; we observe that this involves the field H which transforms like the phase of charge ± 2 Higgs field under the U(1) gauge invariance. So the fluctuations of an isotropic triangular lattice will be characterized by an action of the form

$$\mathcal{S}_b = \int d^3x \frac{1}{2K'} \left[I_{12}^2 + I_{31}^2 + I_{32}^2 \right], \tag{49}$$

which replaces (40). This is the action expected in the *Higgs phase* of a U(1) gauge theory. The Higgs condensate gaps out the U(1) photon, and so there are no gapless singlet excitations

on the triangular lattice. This is a necessary condition for mapping the present state onto a $\mathbb{Z}_2$ spin liquid (the reason for this nomenclature will become clearer in the following subsection). The presentation so far of the gauge fluctuations described by a charge ± 2 Higgs field coupled to a U(1) gauge field would be appropriate for an anisotropic triangular lattice in which the couplings along the $\hat{e}_3$ direction are different from those along $\hat{e}_1$ and $\hat{e}_2$. For an isotropic triangular lattice, all three directions must be treated equivalently, and then there is no simple way to take the continuum limit in the gauge sector: we have to work with the action in (49), but with the invariants specified as in (44). Such an action does not have a gapless photon anywhere in the Brillouin zone, and all gauge excitations remain gapped. There are other choices for the wavevector $\boldsymbol{g}$ in (45) at which the other pairs of values of $\cos(k_p/2)$ vanish; these are the points

$$\frac{2\pi}{\sqrt{3}}\left(\frac{\sqrt{3}}{2},-\frac{1}{2}\right) \quad , \quad \frac{2\pi}{\sqrt{3}}\left(\frac{-\sqrt{3}}{2},-\frac{1}{2}\right) , \tag{50}$$

which are related to the analysis above by the rotational symmetry of the triangular lattice.

2.3. Topological excitations on the triangular lattice

The analysis in Section 2 described small fluctuations in the phases of the $\mathcal{Q}_{ij}$ about their saddle-point values $\bar{\mathcal{Q}}$. On the triangular lattice, we found that such fluctuations led only to gapped excitations, which at higher energies become part of the two-spinon continuum. Now we consider excitations which involve large deviations from the spatially uniform saddle point values, and which turn out to be topologically protected. These excitations are closely connected to the vortices in charged superfluids. Consider a scalar field Ψ with charge q coupled to the electromagnetic U(1) gauge field $\boldsymbol{A}$. This has stable vortex-like saddle points with flux $n\Phi_0$, with $\Phi_0 = hc/q$, for all integer n. We have seen above that the on the triangular lattice, the Schwinger boson state has fluctuations described by a charge 2 Higgs field H coupled to a U(1) gauge field a_μ. In this case, we are normalizing the gauge field so that $\hbar c \Rightarrow 1$, and so we can expect vortex solutions with a_μ flux $n(2\pi)/2$, for all integer n. However, this is not quite correct. A crucial difference between the present theory and the electromagnetic gauge field is that the a_μ gauge field is 'compact': this mean that a gauge field $a_{x,y}$ is identical to $a_{x,y} + 2\pi$, and tunneling events which change the total flux by 2π are allowed (these are 'monopoles', which will be considered further in Section 5). This means that all vortex solutions with even n are identical to each other, as are those with odd n. The $n = 0$ case corresponds to no vortex at all, and so there is only a single non-trivial vortex with $n = 1$ and flux π. This is the sought-after *vison*. Note that because fluxes π and $-\pi$ are

identical, the vison saddle point preserves time-reversal symmetry. Similar excitations appear in a $\mathbb{Z}_2$ gauge theory, and hence the $\mathbb{Z}_2$ spin liquid nomenclature.

In this section, we will obtain the vison saddle point solution by working with a lattice effective action: this is essential to account for the influence of the monopoles. So we look for spatially non-uniform solutions of the saddle-point equations (31) and (32). In general, solving such equations is a demanding numerical task, and so we will be satisfied with a simplified analysis which is valid when the spin gap is large. In the large spin gap limit, we can integrate out the Schwinger bosons, and write the energy as a local functional of the $\mathcal{Q}_{ij}$. This functional is strongly constrained by the gauge transformations in (28): for time-independent $\mathcal{Q}_{ij}$, this functional takes the form

$$E[\{\mathcal{Q}_{ij}\}] = -\sum_{i<j}\left(\alpha|\mathcal{Q}_{ij}|^2 + \frac{\beta}{2}|\mathcal{Q}_{ij}|^4\right) - K\sum_{\text{even loops}} \mathcal{Q}_{ij}\mathcal{Q}^*_{jk}\ldots\mathcal{Q}^*_{\ell i} \tag{51}$$

Here α, β, and K are coupling constants determined by the parameters in the Hamiltonian of the antiferromagnet. We have shown them to be site-independent, because we have only displayed terms in which all links/loops are equivalent; they can depend upon links/loops for longer range couplings provided the full lattice symmetry is preserved.

We can now search for saddle points of the energy functional in (51). Far from the center of

the vison, we have $|\mathcal{Q}^v_{ij}| = \bar{\mathcal{Q}}$, so that the energy differs from the ground state energy only by a finite amount. Closer to the center there are differences in the magnitudes. However, the key difference is in the signs of the link variables, as illustrated in Fig. 10: there is a 'branch-cut' emerging from the vison core along which $\text{sgn}(\mathcal{Q}^v_{ij}) = -\text{sgn}(\bar{\mathcal{Q}}_{ij})$. The results of a numerical minimization [Huh et al., 2011] of $E[\{\mathcal{Q}_{ij}\}]$ on the the triangular lattice are shown in Fig. 10.

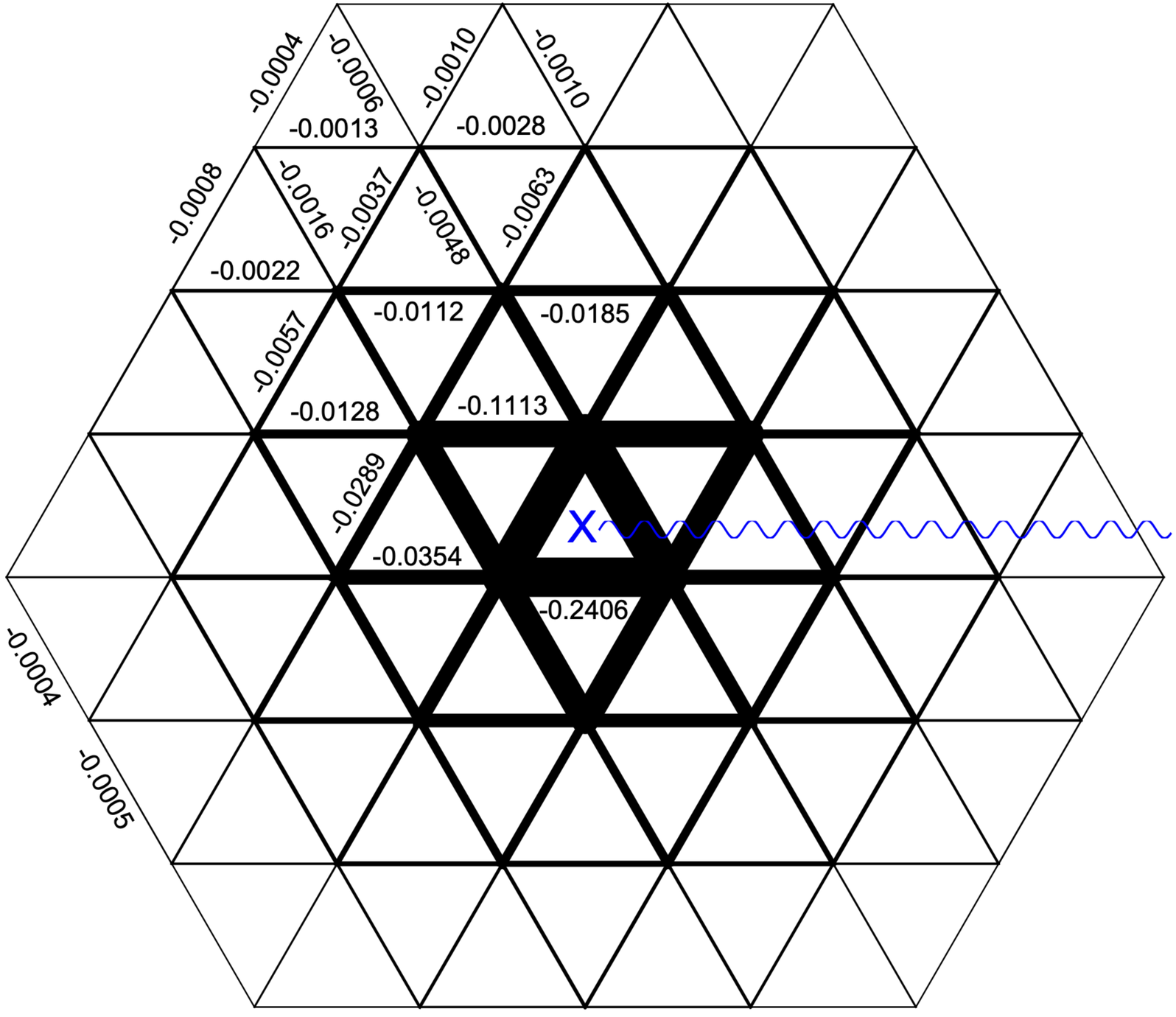
-0.0004
-0.0006
-0.0010
-0.0010
-0.0013
-0.0028
-0.0008
-0.0016
-0.0037
-0.0048
-0.0063
-0.0022
-0.0112
-0.0185
-0.0057
-0.0128
-0.1113
-0.0289
X
-0.0354
-0.2406
-0.0004
-0.0005

Figure 10: A vison on the triangular lattice [Huh et al., 2011]. The center of the vison is marked by the X. The wavy line is the 'branch-cut' where we have $\mathrm{sgn}(\mathcal{Q}^{v}_{ij}) = -\mathrm{sgn}(\bar{\mathcal{Q}}_{ij})$ only on the links crossed by the line. Plotted is the minimization result of $E[\{\bar{\mathcal{Q}}_{ij}\}]$ with $\alpha = 1, \beta = -2, K = 0.5$. Minimization is done with the cluster embedded in a vison-free lattice with all nearest neighbor links equal to $\bar{\mathcal{Q}}_{ij}$. The numbers are $(\bar{\mathcal{Q}}_{ij} - \mathcal{Q}^{v}_{ij})$ and the thickness of the links are proportional to $(\mathcal{Q}^{v}_{ij} - \bar{\mathcal{Q}}_{ij})^{1/2}$. Reprinted with permission from APS.

The magnitudes of $\mathcal{Q}^{v}_{ij}$ are suppressed close to the vison, and converge to $\bar{\mathcal{Q}}_{ij}$ as we move away from the vison (modulo the sign change associated with the branch cut), analogous to those in Abrikosov vortices. Despite the branch-cut breaking the 3-fold rotation symmetry, the gauge-invariant fluxes of $\mathcal{Q}^{v}_{ij}$ preserve the rotation symmetry.
So we have found a stable real-vortex solution which preserves time-reversal, and has a finite excitation energy. We have also anticipated that this vortex will be identified with the vison particle of the $\mathbb{Z}_2$ spin liquid: more evidence for this identification will appear in Sections 2 and 3.

2.4. Dynamics of excitations on the triangular lattice

For the case of the triangular lattice, Sections 1 and 3 have identified two types of elementary excitations: bosonic spinons with a 2-fold spin and a 2-fold lattice degeneracy, and a topological excitation which we have anticipated will become with vison particle of a $\mathbb{Z}_2$ spin liquid. We will now describe the dynamics of the interactions between these excitations, and indeed verify that they reproduce the general structure associated with the $\mathbb{Z}_2$ spin liquid.
A similar analysis can also be carried for the U(1) spin liquid on the square lattice. However, defer consideration of this case to Section 5.
The general structure of the theory controlling the low energy spectrum becomes clearer upon taking a suitable continuum limit of the Lagrangian in (27), while replacing $\mathcal{Q}_{ij} = \bar{\mathcal{Q}}_{ij}$ and $i\lambda_i = \bar{\lambda}$. We take the continuum limit after separating 3 sites, u, v, w, in each unit cell (see Fig. 7). We write the boson operators on these sites as $b_u^\alpha = u_\alpha$, $b_v^\alpha = v_\alpha$ etc. Then to the needed order in spatial gradients, the Lagrangian density becomes [Huh et al., 2010]

$$\begin{aligned}\mathcal{L} &= u_\alpha^* \frac{\partial u_\alpha}{\partial \tau} + v_\alpha^* \frac{\partial v_\alpha}{\partial \tau} + w_\alpha^* \frac{\partial w_\alpha}{\partial \tau} + \bar{\lambda}\left(|u_\alpha|^2 + |v_\alpha|^2 + |w_\alpha|^2\right) \\ &\quad - \frac{3J\bar{\mathcal{Q}}}{2}\mathcal{J}_{\alpha\beta}\left(u_\alpha v_\beta + v_\alpha w_\beta + w_\alpha u_\beta\right) + \text{c.c.} \\ &+ \frac{3J\bar{\mathcal{Q}}}{8}\mathcal{J}_{\alpha\beta}\left(\boldsymbol{\nabla} u_\alpha \cdot \boldsymbol{\nabla} v_\beta + \boldsymbol{\nabla} v_\alpha \cdot \boldsymbol{\nabla} w_\beta + \boldsymbol{\nabla} w_\alpha \cdot \boldsymbol{\nabla} u_\beta\right] + \text{c.c.} \end{aligned} \tag{52}$$

We now perform a unitary transformation to new variables x_α, y_α, z_α. These are chosen to diagonalize only the non-gradient terms in $\mathcal{L}$.

$$\begin{pmatrix} u_\alpha \\ v_\alpha \\ w_\alpha \end{pmatrix} = \frac{z_\alpha}{\sqrt{6}} \begin{pmatrix} 1 \\ \zeta \\ \zeta^2 \end{pmatrix} + \mathcal{J}_{\alpha\beta} \frac{z_\beta^*}{\sqrt{6}} \begin{pmatrix} -i \\ -i\zeta^2 \\ -i\zeta \end{pmatrix} + \frac{y_\alpha}{\sqrt{6}} \begin{pmatrix} 1 \\ \zeta \\ \zeta^2 \end{pmatrix} + \mathcal{J}_{\alpha\beta} \frac{y_\beta^*}{\sqrt{6}} \begin{pmatrix} i \\ i\zeta^2 \\ i\zeta \end{pmatrix} + \frac{x_\alpha}{\sqrt{3}} \begin{pmatrix} 1 \\ 1 \\ 1 \end{pmatrix}. \tag{53}$$

where $\zeta \equiv e^{2\pi i/3}$. The tensor structure above makes it clear that this transformation is rotationally invariant, and that x_α, y_α, z_α transform as spinors under SU(2) spin rotations. Inserting Eq. (53) into $\mathcal{L}$ we find

$$\begin{aligned} \mathcal{L} &= x_\alpha^* \frac{\partial x_\alpha}{\partial \tau} + y_\alpha^* \frac{\partial z_\alpha}{\partial \tau} + z_\alpha^* \frac{\partial y_\alpha}{\partial \tau} + (\bar{\lambda} - 3\sqrt{3} J \bar{\mathcal{Q}}/2)|z_\alpha|^2 \\ &+ (\bar{\lambda} + 3\sqrt{3} J \bar{\mathcal{Q}}/2)|y_\alpha|^2 + \bar{\lambda}|x_\alpha|^2 + \frac{3J\bar{\mathcal{Q}}\sqrt{3}}{8} \left(|\partial_x z_\alpha|^2 + |\partial_y z_\alpha|^2 \right) + \ldots \end{aligned} \tag{54}$$

The ellipses indicate omitted terms involving spatial gradients in the x_α and y_α which we will not keep track of. This is because the fields y_α and x_α are massive relative to z_α, and so can

be integrated out. This yields the effective Lagrangian

$$\begin{aligned}\mathcal{L}_z &= \frac{1}{(\bar{\lambda}+3\sqrt{3}J\bar{\mathcal{Q}}/2)}|\partial_\tau z_\alpha|^2+\frac{3J\bar{\mathcal{Q}}\sqrt{3}}{8}\left(|\partial_x z_\alpha|^2+|\partial_y z_\alpha|^2\right)\\ &\quad +(\bar{\lambda}-3\sqrt{3}J\bar{\mathcal{Q}}/2)|z_\alpha|^2+\ldots \end{aligned} \tag{55}$$

Note that the omitted spatial gradient terms in x_α, y_α do contribute a correction to the spatial gradient term in (55), and we have not accounted for this.
So we reach the important conclusion that the spinons are described by a relativistic complex scalar field z_α. Counting the two values of α, and the particle and anti-pariticle excitations, we have a total of 4 spinons, as expected.
Next, we consider the higher order terms in (55), which will arise from including the fluctuations of the gapped fields $\mathcal{Q}$ and λ. Rather than computing these from the microscopic Lagrangian, it is more efficient to deduce their structure from symmetry considerations. The representation in (53), and the connection of the u_α, v_α, w_α to the lattice degrees of freedom, allow us to deduce the following symmetry transformations of the x_α, y_α, z_α:

Under a global spin rotation by the SU(2) matrix $g_{\alpha\beta}$, we have $z_\alpha \to g_{\alpha\beta}z_\beta$, and similarly for x_α, and y_α.

Under a 120° lattice rotation, we have $u_\alpha \to v_\alpha$, $v_\alpha \to w_\alpha$, $w_\alpha \to u_\alpha$. From (53), we see that this symmetry is realized by

$$z_\alpha \to \zeta z_\alpha \ , \ y_\alpha \to \zeta y_\alpha \ , \ x_\alpha \to x_\alpha. \tag{56}$$

Note that this is distinct from the SU(2) rotation because $\det(\zeta) \neq 1$.

Finally, there is a crucial $\mathbb{Z}_2$ gauge symmetry, which is the remnant of the U(1) gauge symmetry in Eq. (28). This is the transformation

$$z_{\boldsymbol{i}\alpha} \to \mu_{\boldsymbol{i}} z_{\boldsymbol{i}\alpha} \tag{57}$$

where $\mu_{\boldsymbol{i}} = \pm 1$ has an arbitrary site-dependence.

It is easy to verify that Eq. (54) is invariant under all the symmetry operations above. These symmetry operators make it clear that the only allowed quartic term for the Heisenberg Hamiltonian is $\left(\sum_\alpha |z_\alpha|^2\right)^2$: this quartic term added to $\mathcal{L}_z$ yields a theory with O(4) symmetry, corresponding to rotations between the 4 real fields that can be extracted from the 2 complex field z_α.

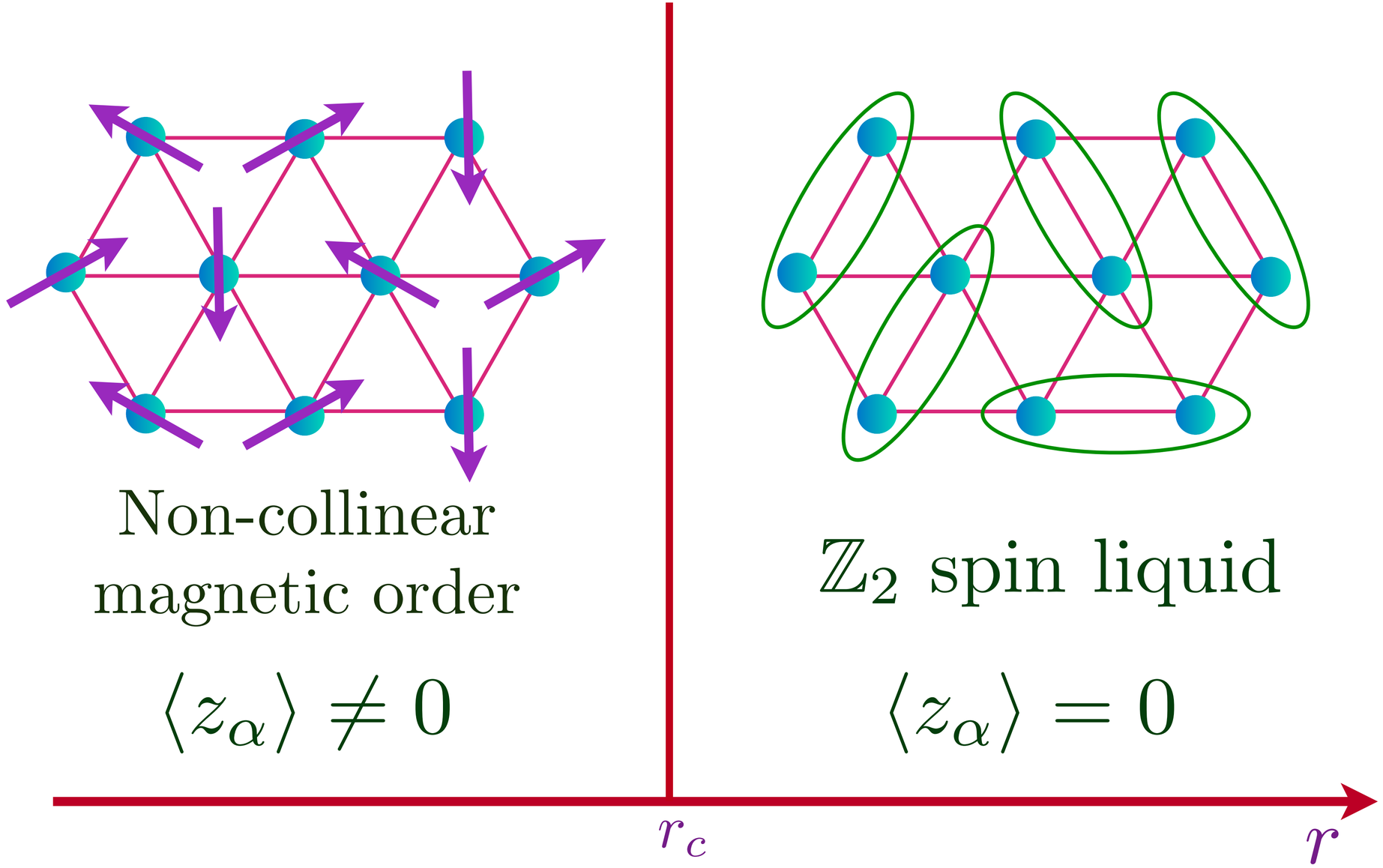

Figure 11: Magnetic ordering transition driven by tuning r in (58). Fractionalized anyonic excitations are present only for $r > r_c$, and so there is a 'confinement' transition at $r = r_c$. The critical theory is expressed in terms of bosonic spinons z_α, and is an example of deconfined critical theory. There is

evidence for such a transition in $KYbSe_2$ [Scheie et al., 2024].

We also observe from (55) that the z_α field will condense when

$$r = (\bar{\lambda} - 3\sqrt{3}J\bar{\mathcal{Q}}/2) \tag{58}$$

becomes negative as κ is varied across κ_c. This condensation breaks the spin rotation symmetry, and leads to a quantum phase transition to a phase with coplanar antiferromgnetic long-range order, as illustrated in Fig. 11. This order parameter of this coplanar antiferromagnet is related to $\mathbb{Z}_2$ gauge-invariant bilinears of z_α by

$$\boldsymbol{S_i} \propto \mathrm{Im}\left[\exp\left(i\boldsymbol{Q}\cdot\boldsymbol{r}\right)\varepsilon_{\alpha\gamma}z_\gamma\boldsymbol{\sigma}_{\alpha\beta}z_\beta\right] , \tag{59}$$

where the wavevector $\boldsymbol{Q} = (4\pi/a)(1/3, 1/\sqrt{3})$.
Let us now consider the motion of the vison elementary excitation, which we illustrated earlier in Fig. 12. The vison is located at the center of a triangle, and so can tunnel between neighboring triangular cells. We are interested here in any possible Berry phases the vison could pick up upon tunneling around a closed path.
In Section 3, we characterized the vison by the saddle-point configuration $\mathcal{Q}^v_{\boldsymbol{ij}}$ of the bond variables in the Hamiltonian (29). By diagonalizing this Hamiltonian

[Sachdev, 1992, Huh et al., 2011], we can show that the wavefunction of the vison can be written as

$$|\Psi^{v}\rangle = \mathcal{P} \exp\left(\sum_{\boldsymbol{i}<j} f^{v}_{\boldsymbol{ij}}\, \mathcal{J}_{\alpha\beta} b^{\dagger}_{\boldsymbol{i}\alpha} b^{\dagger}_{j\beta}\right) |0\rangle, \tag{60}$$

where $|0\rangle$ is the boson vaccum, $\mathcal{P}$ is a projection operator which selects only states which obey (19), and the boson pair wavefunction $f^{v}_{\boldsymbol{ij}} = -f^{v}_{\boldsymbol{ji}}$ is determined from (29) by a Bogoliubov transformation.

Let us now consider the motion of a single vison [Huh et al., 2011]. The gauge-invariant Berry phases are those associated with a periodic motion, and so let us consider the motion of a vison along a general closed loop $\mathcal{C}$. We illustrated the simple case where $\mathcal{C}$ encloses a single site of the triangular lattice in Fig. 12.

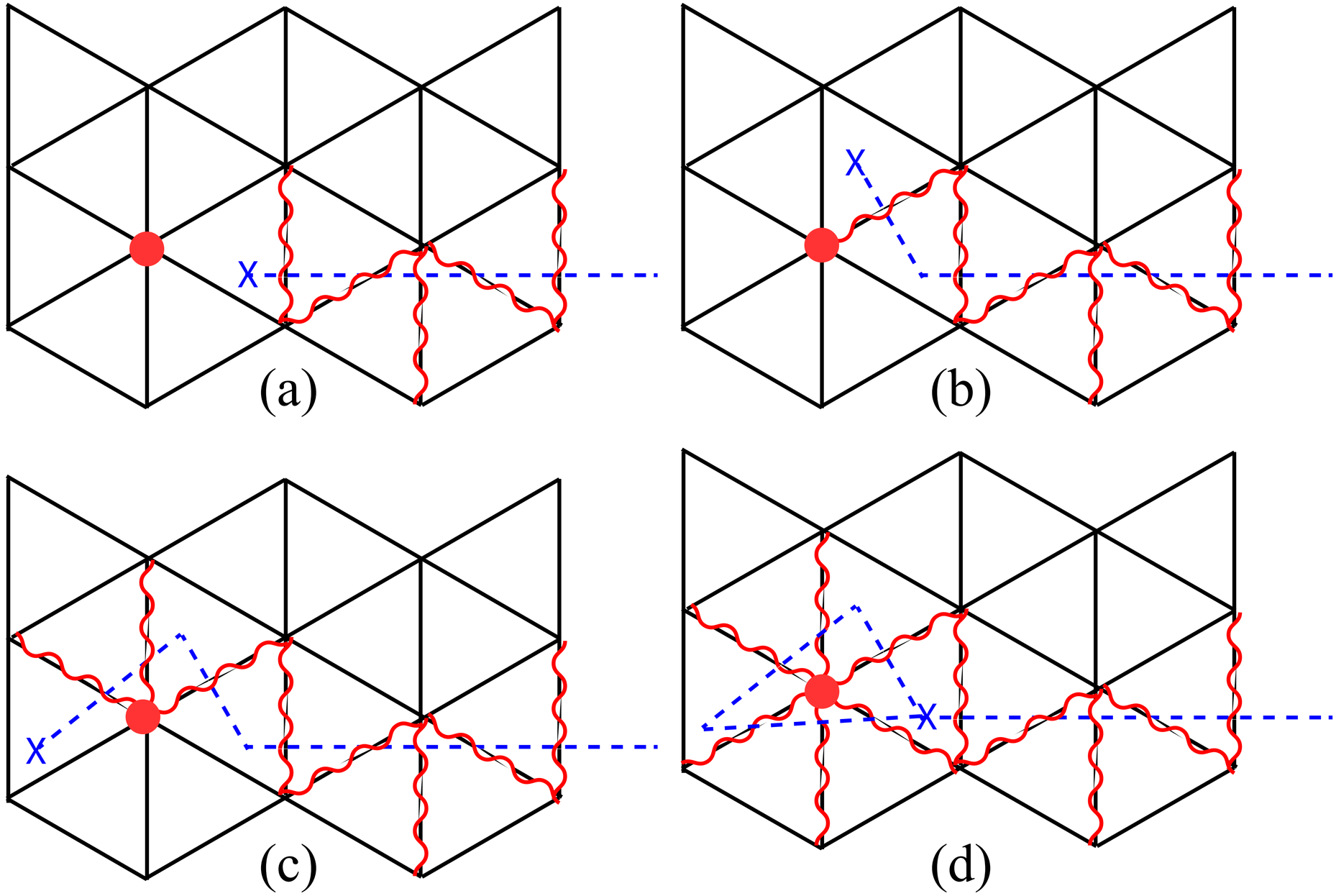

Figure 12: Adiabatic motion of a vison (denoted by the X) around a single site of the triangular lattice

(denoted by the filled circle). The initial state is in (a), and the final state is in (d), and these differ by a gauge transformation under which $b_{i\alpha} \to -b_{i\alpha}$ only on the filled circle site.

The wavy lines indicate $\mathrm{sgn}(\mathcal{Q}^{\nu}_{ij}) = -\mathrm{sgn}(\bar{\mathcal{Q}}_{ij})$, as in Fig. 10. The last state is gauge-equivalent to the first state, after the gauge transformation $b^{\alpha}_{i} \to -b^{\alpha}_{i}$ only for the site i marked by the filled circle. As long as the vison wavefunction can be chosen to be purely real, it is clear that no Berry phase is accumulated from the time-evolution of the wavefunction as the vison tunnels around the path $\mathcal{C}$. However, there can still be a non-zero Berry phase because a gauge-transformation is required to map the final state to the initial state. The analysis in Fig. 12 shows that the required gauge transformation is

$$\begin{aligned} b^{\alpha}_{i} &\to -b^{\alpha}_{i}, && \text{for } i \text{ inside } \mathcal{C} \\ b^{\alpha}_{i} &\to b^{\alpha}_{i}, && \text{for } i \text{ outside } \mathcal{C}. \end{aligned} \tag{61}$$

By Eq. (19), each site has $n_b = 2S$ bosons, and so the total Berry phase accumulated by $|\Psi^{\nu}\rangle$ is

$$\pi n_b \times (\text{number of sites enclosed by } \mathcal{C})\,. \tag{62}$$

For the important case of $S = 1/2$, the vison experiences a flux of π for every site of the triangular lattice. This phase factor of π is related to an 'anomaly' associated with the global

U(1) boson number symmetry, and translational symmetry [Bonderson et al., 2016, Else and Senthil, 2021], and was first noted in Refs. [Jalabert and Sachdev, 1991, Sachdev and Vojta, 1999] as a feature of $\mathbb{Z}_2$ spin liquids with half-integer spin. In particular, this result implies the RVB state is an *odd* $\mathbb{Z}_2$ spin liquid. A notable features of (62) is that the quantized integer value of $n_b = 2S$ is important. Memory of this quantization was lost in the mean field theory of Section 1, which was sensible also for non-integer values of n_b. So inclusion of the vison fluctuations restores the quantization of spin. A more complete theory for the vison fluctuations appears below in Section 4. Proceeding the identification of the present Schwinger boson spin liquid with the $\mathbb{Z}_2$ spin liquid, we need to establish that the spinons and visons are mutual semions. This is immediately apparent from a glance at Figs. 10 and 13.

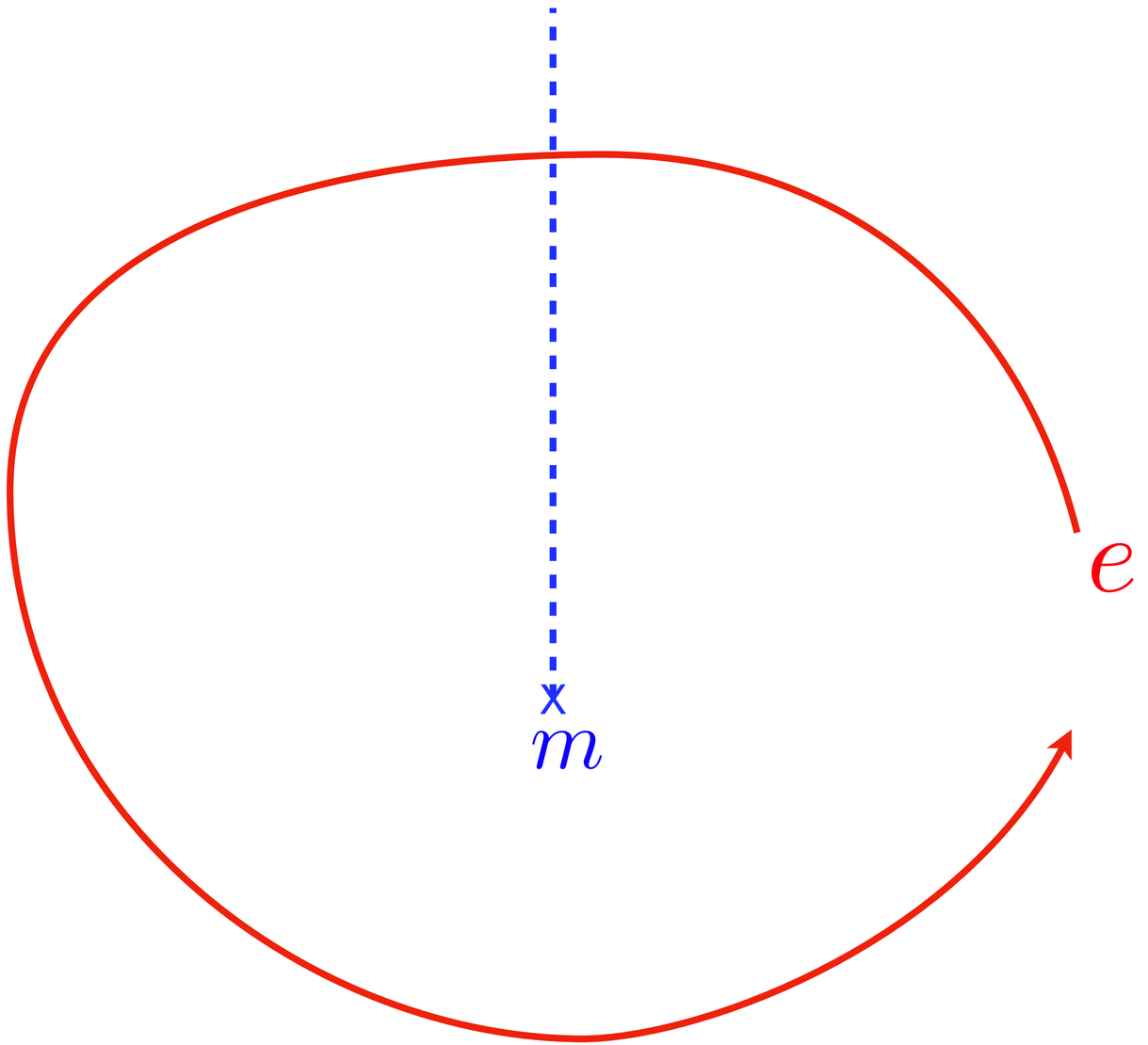

Figure 13: Mutual statistics of e and m particles. This process leads to a Berry phase of -1, when the e particle crosses the branch cut of the m particle.

The $\mathcal{Q}^{v}_{ij}$ transport the spinons from site to site, and for spinon encircling a vison in a large circuit, the only difference between the cases with and without the vison is the branch cut. This branch cut yields an additional phase of π in the vison amplitude, and provides the needed phase for mutual semion statistics [Read and Sachdev, 1991, Wen, 1991].

We can now identify the e, ϵ, and m anyons, in the abstract topological characterization of the $\mathbb{Z}_2$ spin liquid obtained from the toric code. The e anyon is the the Schwinger boson itself, b_α. This is mutual semion with respect to the vison, and so we identify the vison with the m particle. Finally, the ϵ anyon is obtained by the fusion $\epsilon = e \times m$, and so the ϵ anyon is a bound state of e and m. The ϵ anyon is a *fermion* as can be deduced by computing the Berry phase associated with exchanging one bound state of e and m with another bound state, as shown in Fig. 14.

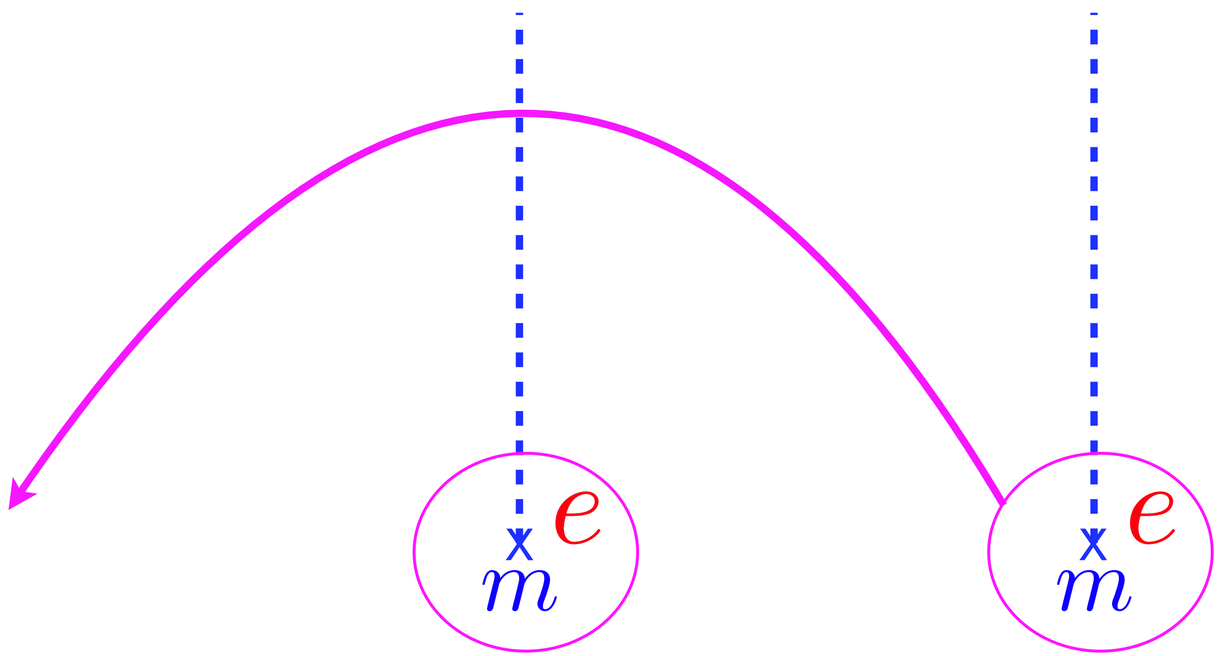

Figure 14: Two ϵ particles undergoing an exchange: after traversing the path shown, a translation returns the ϵ particles to the original state. Each ϵ particle is a bound state of a vison (the m particle) and the s_α bosonic spinon (the e particle). This process leads to a Berry phase of -1, when the moving e particle crosses the branch cut of the stationary m particle.

(Note that this 'long-distance' Berry phase is multiplied by the 'short-distance' vison motion phases discussed in Section 2.) It is quite remarkable that a microscopic theory of bosonic spins $\boldsymbol{S}$, expressed in terms of fractionalized bosons s_α, yields an excitation which is a fermion: this is one indication of the presence of long-range entanglement and topological order.
An alternative formulation of the $\mathbb{Z}_2$ spin liquid on the triangular lattice proceeds by expressing

the spins $\boldsymbol{S}$ in terms of Schwinger fermions f_α. For the $\mathbb{Z}_2$ spin liquid, the f_α spinons would become the ϵ particles, and the bosonic e would be the bound state of the f_α and the m vison. So ultimately, independent of whether we choose to fractionalize the $\boldsymbol{S}$ spins in terms of bosonic or fermionic partons, we obtain the same characterization of the observable excitations in the resulting $\mathbb{Z}_2$ spin liquid. This identity also extends to the symmetry transformations of the anyons, as has been shown in some detail on the kagome lattice [Lu et al., 2017].
We now combine the above results for the dynamics of spinons and visons to write down a $\mathbb{Z}_2$ gauge theory which couples the $z_{\boldsymbol{i}\alpha}$ to a dynamic $\mathbb{Z}_2$ gauge field $Z_{\boldsymbol{ij}}$ on the links of a 3-dimensional hexagonal lattice (*i.e.* stacked triangular lattices):

$$\mathcal{Z}_{\mathbb{Z}_2} = \sum_{Z_{\boldsymbol{ij}}=\pm 1} \prod_i \int dz_{\boldsymbol{i}\alpha} \delta\left(\sum_\alpha |z_{\boldsymbol{i}\alpha}|^2 - 1\right) \left\{\prod_i Z_{\boldsymbol{i},\boldsymbol{i}+\tau}\right\}^{2S} \exp\left(-H_{\mathbb{Z}_2}[z_\alpha, Z]\right)$$

$$H_{\mathbb{Z}_2}[z_\alpha, Z] = -J_2 \sum_{\langle ij\rangle} Z_{\boldsymbol{ij}} \left(z^*_{\boldsymbol{i}\alpha} z_{\boldsymbol{j}\alpha} + \text{c.c.}\right) - K \sum_{\triangle,\square} \prod_{\boldsymbol{ij}\in\triangle,\square} Z_{\boldsymbol{ij}} \,. \tag{63}$$

Here the $z_{\boldsymbol{i}\alpha}$ reside on the sites $\boldsymbol{i}$ of the hexagonal lattice, and the K term acts on the triangular plaquettes of the spatial plane, and the rectangular plaquettes along the temporal direction. The $Z_{\boldsymbol{ij}}$ descend from the $\mathcal{Q}_{\boldsymbol{ij}}$ by fixing their magnitudes and allowing their signs to

be dynamical via

$$\mathcal{Q}_{ij} \Rightarrow \left|\mathcal{Q}_{ij}\right| Z_{ij} \tag{64}$$

Then from Eq. (28), the $\mathbb{Z}_2$ gauge transformation in Eq. (57) acts on the $\mathbb{Z}_2$ gauge field via

$$Z_{ij} \rightarrow \mu_i Z_{ij} \mu_j \, . \tag{65}$$

The novel term in Eq. (63), beyond those found in the lattice gauge theory literature, is the prefactor of the exponential in the curly brackets: this is the Berry phase term for half-integer spin S. It is a direct consequence of the presence of a background $\mathbb{Z}_2$ gauge charge on each site, as implied by Eqs. (19) and (61) [Shackleton and Sachdev, 2025], and so accounts of the motion of visons in a background π flux.
The partition function in Eq. (63) has been studied by quantum Monte Carlo, and yields the phase diagram in Fig. 15.

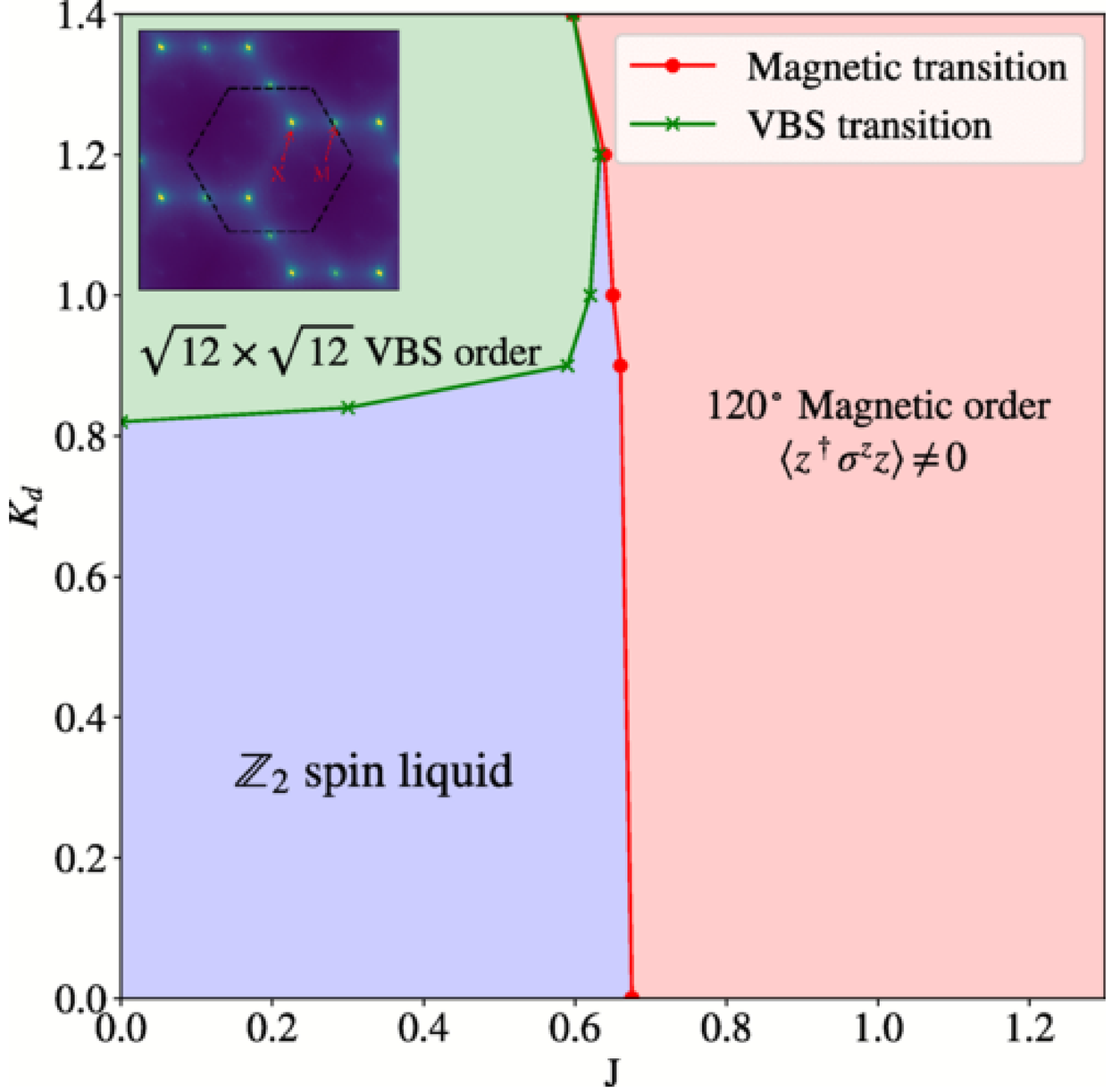

Figure 15: Phase diagram of $\mathcal{Z}_{\mathbb{Z}_2}$ in Eq. (63) obtained via sign-problem-free quantum Monte Carlo in

Ref. [Shackleton and Sachdev, 2025].

Apart from the ordered antiferromagnet and the $\mathbb{Z}_2$ spin liquid in Fig. 11, here we obtain a valence bond solid (VBS) state as a consequence of the Berry phase term [Jalabert and Sachdev, 1991, Sachdev and Vojta, 1999]. This is gapped state which preserves spin rotation invariance, but breaks lattice translational symmetry.
The transition from the ordered antiferromagnet to the $\mathbb{Z}_2$ spin liquid is not influenced by the Berry phase term (because the visons remains gapped at this transition), and is described by the O(4) Wilson-Fisher critical theory [Chubukov et al., 1994b, Chubukov et al., 1994a]. However, there is an important difference in the structure of the observable order parameter. Note that z_α was obtained from the continuum limit of the spinon s_α, and so it is fractionalized degree of freedom, carrying a unit $\mathbb{Z}_2$ charge. Correlators of z_α are therefore not observable, only those of gauge-invariant bilinear combinations. This is denoted by stating the universality class of the transition is actually O(4)*. This critical theory has the same exponents as the O(4) theory, but some observables in a finite geometry are different [Whitsitt and Sachdev, 2016]. As the critical fields of the theory are fractionalized spinons, this is an example of a 'deconfined critical point'.
Near the multicritical region where the 3 phases meet in Fig. 15, there could be additional

deconfined criticality [Shackleton and Sachdev, 2025] associated with a U(1) gauge theory of fermionic spinons [Song et al., 2020a, Song et al., 2019, Wietek et al., 2024] which we do not explore here.

2.5. Dynamics of excitations on the square lattice

We now examine the low energy theory on the square lattice in the regime where the energy gap of the spinon excitations is small. Here, we can take a continuum limit for the spinons, and also account for the fluctuations of $\mathcal{Q}$ and λ. For the spinons, we introduce the wavevector at the minimum spinon gap $\boldsymbol{k}_0 = (\pi/2, \pi/2)$ and parameterize on the checkerboard A and B sublattices (with $\boldsymbol{i}_x + \boldsymbol{i}_y$ even and odd)

$$\begin{aligned} b_{A\boldsymbol{i}\alpha} &= \psi_{1\alpha}(\boldsymbol{r_i}) e^{i\boldsymbol{k}_0 \cdot \boldsymbol{r_i}} \\ b_{B\boldsymbol{i}\alpha} &= -i\varepsilon_{\alpha\beta}\psi_{2\beta}(\boldsymbol{r_i}) e^{i\boldsymbol{k}_0 \cdot \boldsymbol{r_i}} \, . \end{aligned} \tag{66}$$

For $\mathcal{Q}$ and λ, we use the parameterization already discussed in Section 1.
We insert these parameterizations into the spinon action, perform a gradient expansion, and transform the Lagrangian $\mathcal{L}_J$ into (a is the lattice spacing)

$$\begin{aligned} \mathcal{L}_z = \int \frac{d^2 r}{2a^2} \Bigg[& \psi_{1\alpha}^* \left(\frac{d}{d\tau} + i a_\tau \right) \psi_{1\alpha} + \psi_{2\alpha}^* \left(\frac{d}{d\tau} - i a_\tau \right) \psi_{2\alpha} \\ & + \bar{\lambda} \left(|\psi_{1\alpha}|^2 + |\psi_{2\alpha}|^2 \right) - 2J\bar{\mathcal{Q}} \left(\psi_{1\alpha}\psi_{2\alpha} + \psi_{1\alpha}^* \psi_{2\alpha}^* \right) \\ & + (J/2)\bar{\mathcal{Q}} a^2 \left[(\boldsymbol{\nabla} + i\boldsymbol{a}) \psi_{1\alpha} (\boldsymbol{\nabla} - i\boldsymbol{a}) \psi_{2\alpha} \right. \\ & \left. + (\boldsymbol{\nabla} - i\boldsymbol{a}) \psi_{1\alpha}^* (\boldsymbol{\nabla} + i\boldsymbol{a}) \psi_{2\alpha}^* \right] \Bigg| \, . \end{aligned} \tag{67}$$

We now introduce the fields

$$\begin{aligned} z_\alpha &= (\psi_{1\alpha} + \psi^*_{2\alpha})/\sqrt{2} \\ \pi_\alpha &= (\psi_{1\alpha} - \psi^*_{2\alpha})/\sqrt{2}\,, \end{aligned}$$

to map Eq. (67) to

$$\begin{aligned} \mathcal{L}_z = \int \frac{d^2 r}{2a^2} \Bigg[& \pi^*_\alpha \left(\frac{d}{d\tau} + i a_\tau \right) z_\alpha - \pi_\alpha \left(\frac{d}{d\tau} - i a_\tau \right) z^*_\alpha \\ & + \bar{\lambda} \left(|z_\alpha|^2 + |\pi_\alpha|^2 \right) - 2J\bar{\mathcal{Q}} \left(|z_\alpha|^2 - |\pi_\alpha|^2 \right) \\ & + (J/2)\bar{\mathcal{Q}} a^2 \left[|(\boldsymbol{\nabla} + i\boldsymbol{a})\, z_\alpha|^2 - |(\boldsymbol{\nabla} + i\boldsymbol{a})\, \pi_\alpha|^2 \right] \Bigg]\,. \end{aligned} \tag{68}$$

From Eq. (68), it is clear that the the π fields have 'mass' $\bar{\lambda} + 2J\bar{\mathcal{Q}}$, while the z fields have a mass $\bar{\lambda} - 2J\bar{\mathcal{Q}}$ which vanishes at a quantum phase transition where the z_α condense, leading to Néel order. The π fields can therefore be safely integrated out, and $\mathcal{L}_z$ yields the following effective action, valid at distances much larger than the lattice

spacing [Read and Sachdev, 1989, Read and Sachdev, 1990]:

$$S_{\rm eff} = \int \frac{d^2r}{4\sqrt{2}a} \int d\tau \left\{ |(\partial_\mu - ia_\mu) z_\alpha|^2 + \frac{\Delta^2}{c^2} |z^\alpha|^2 \right\} . \tag{69}$$

Here μ extends over x, y, τ, $c = \sqrt{2} J \bar{\mathcal{Q}} a$ is the spin-wave velocity, we have rescaled $\tau \to \tau/c$, and $\Delta = (\bar{\lambda}^2 - 4J^2 \bar{\mathcal{Q}}_1^2)^{1/2}$ is the gap towards spinon excitations. Thus the long-wavelength theory describes a spin liquid with of a massive, spin-1/2, relativistic, boson z_α (spinon) excitation coupled to a U(1) gauge field a_μ.

The continuum theory also makes it easy to determine the fate of the antiferromagnet when the spin energy gap vanishes. We expect that z_α will bose condense, and this will break the spin rotation symmetry; a term quartic in z_α will be needed to stabilize the condensate. But z_α carries a U(1) gauge charge, and so is not directly observable. Following the definitions of the underlying spin operators, it is not difficult to show that the gauge-invariant composite

$$\boldsymbol{\mathcal{N}} = z_\alpha^* \boldsymbol{\sigma}_{\alpha\beta} z_\beta \sim \eta_{\boldsymbol{i}} \boldsymbol{S_i} \tag{70}$$

is just the Néel order parameter of Fig. 2.

However, there is an important ingredient that our low energy theory has not yet considered. These are non-perturbative fluctuations of a_μ which are Dirac monopoles in 2+1 dimensional

spacetime. We will not carry out a full analysis here, and merely summarize some important consequences. An important result is that the spin liquid noted above is ultimately not a spin liquid. It is unstable to proliferation of monopoles, and ultimately confines a valence bond solid. But monopoles do not have a significant effect on the Néel state.

On general symmetry grounds, we extend Eq. (69) to a theory for the vicinity of the quantum critical point at which the spinon gap vanishes [Sachdev and Jalabert, 1990]:

$$\begin{aligned}
\mathcal{S}_{U(1)} &= \int d^3x \, (\mathcal{L}_z + \mathcal{L}_{\rm monopole}) + \mathcal{S}_B \\
\mathcal{L}_z &= |(\partial_\mu - i a_\mu) z_\alpha|^2 + g|z_\alpha|^2 + u \left(|z_\alpha|^2\right)^2 + K(\epsilon_{\mu\nu\lambda}\partial_\nu a_\lambda)^2 \\
\mathcal{L}_{\rm monopole} &= -y \left(\mathcal{M}_a + \mathcal{M}_a^\dagger\right) \\
\mathcal{S}_B &= i2S \sum_{\boldsymbol{i}} \eta_{\boldsymbol{i}} \int d\tau \, a_{\boldsymbol{i}\tau} \, .
\end{aligned} \tag{71}$$

The theory $\mathcal{L}_z$ is also known as the $\mathbb{CP}^1$ model. We have included monopoles $\mathcal{M}_a$ in the gauge field a_μ, and also the Berry phase of the spinons in the ground state.

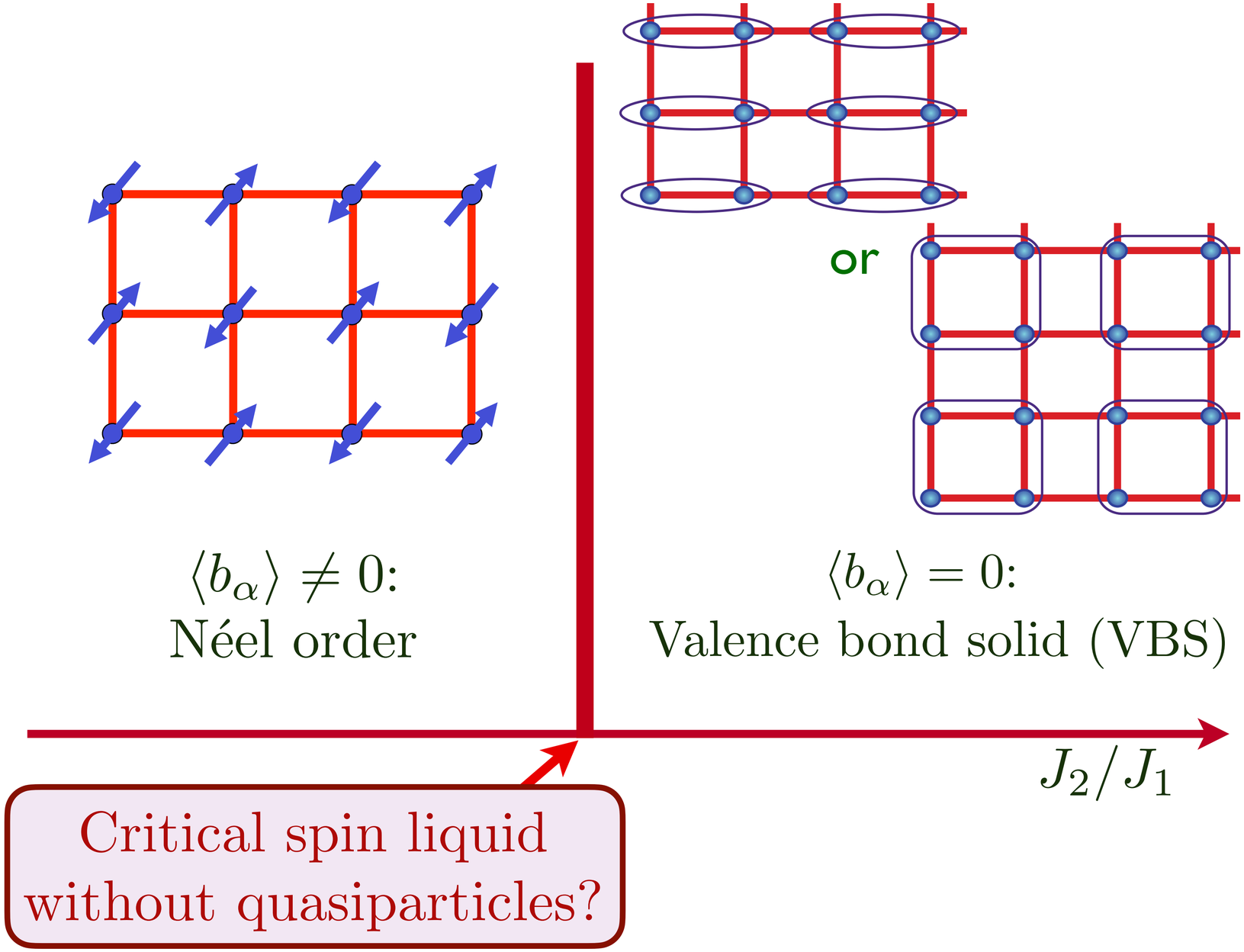

Figure 16: Phase diagram of the U(1) gauge theory with bosonic spinons, Eq. (72). The Néel order

appears in a Higgs phase where the bosonic spinons are condensed. The VBS order appears in the confining phase, and is induced by the Berry phases of the confining monopoles. The same phase diagram applies to the fermionic spinon theory in Eq. (94), and the SO(5) σ-model with the WZW term in Eq. (101).

As we tune the coupling g in Eq. (71), we can expect the 2 phases shown in Fig. 16:
(*i*) Néel phase, $g < g_c$: the spinon z_α condenses in a Higgs phase with $\langle z_\alpha \rangle \neq 0$. The a_μ gauge field is Higgsed, and spin rotation symmetry is broken by opposite polarization of the spins on the two sublattices.
(*ii*) Valence bond solid (VBS), $g > g_c$: the spinons are gapped. For half-integer spin S, there is broken translational symmetry by the crystallization of valence bonds in the pattern shown in Fig. 16.
We now obtain a potential gapless spin liquid if there is a continuous quantum phase transition at $g = g_c$. For half-integer spin S, the single monopole terms in Eq. (71) average to zero at long wavelengths from the Berry phases, and only quadrupoled monopole terms survive. So we can simplify the continuum theory for the vicinity of the quantum critical point to [Senthil et al., 2004b, Senthil et al., 2004a]

$$\mathcal{L}_z = |(\partial_\mu - i a_\mu) z_\alpha|^2 + g|z_\alpha|^2 + u\left(|z_\alpha|^2\right)^2 + K(\epsilon_{\mu\nu\lambda}\partial_\nu a_\lambda)^2 - y_4\left(\mathcal{M}_a^4 + \mathcal{M}_a^{\dagger 4}\right), \qquad (72)$$

where y_4 is the quadrupoled monopole fugacity. There is ample numerical evidence that y_4 is irrelevant near a possible critical point, and so the question reduces to whether the theory $\mathcal{L}_z$ at $y_4 = 0$ exhibits a critical point which realizes a conformal field theory in 2+1 dimensions. This is a question that has been studied extensively in numerics, and it is clear that a 'deconfined critical' description is suitable over a substantial length scale: with fractionalized spinons interacting with a U(1) gauge field in the absence of monopoles [Nahum et al., 2015, Chen et al., 2024, Liu et al., 2024, Chester and Su, 2024, Takahashi et al., 2024, Zhou et al., 2024b].

1. Spin density wave order in the Hubbard model

2. Bosonic spinon theory of quantum spin liquids

3. Fermionic spinon theory of quantum spin liquids

4. Holon metal from a quantum spin liquid
   with bosonic spinons

5. d-wave superconductior from a quantum spin liquid
   with fermionic spinons

6. Fractionalized Fermi liquids (FL*)

3. Fermionic spinon theory of quantum spin liquids

We now present an alternative analysis of the square lattice antiferromagnet in Eq. (17), replacing the bosonic partons in Eq. (21) by fermionic partons. This will ultimately lead to the same phase diagram as in Fig. 16, but with a dual description of the phases and the criticality. This dual fermionic description turns out to be the most efficient way to describe the connection between the critical spin liquid and *d*-wave superconductivity in the doped antiferromagnet, as we will see in Section 5.

The following Schwinger *fermion* representation applies only for $S = 1/2$

$$\boldsymbol{S_i} = \frac{1}{2} f^\dagger_{\boldsymbol{i}\alpha}\, \boldsymbol{\sigma}_{\alpha\beta}\, f_{\boldsymbol{i}\beta} \tag{73}$$

where $f_{\boldsymbol{i}\alpha}$ are canonical fermions obeying the constraint

$$\sum_\alpha f^\dagger_{\boldsymbol{i}\alpha} f_{\boldsymbol{i}\alpha} = 1 \quad , \quad \text{for all } \boldsymbol{i}. \tag{74}$$

While the bosonic parton representation led to the U(1) gauge symmetry in Eq. (28), it turns out the Eqs. (73) and (74) have a larger SU(2) gauge invariance, and this will be crucial to our results. The analysis is clearest upon introducing a matrix notation for the fermions

$$\mathcal{F}_{\boldsymbol{i}} \equiv \begin{pmatrix} f_{\boldsymbol{i}\uparrow} & -f_{\boldsymbol{i}\downarrow} \\ f^\dagger_{\boldsymbol{i}\downarrow} & f^\dagger_{\boldsymbol{i}\uparrow} \end{pmatrix} \tag{75}$$

This matrix obeys the 'reality' condition

$$\mathcal{F}_{\boldsymbol{i}}^{\dagger} = \sigma^{y} \mathcal{F}_{\boldsymbol{i}}^{T} \sigma^{y} . \tag{76}$$

Now we can write Eq. (73) as

$$\boldsymbol{S_i} = -\frac{1}{4} \mathrm{Tr}(\mathcal{F}_{\boldsymbol{i}} \sigma^{z} \boldsymbol{\sigma}^{T} \sigma^{z} \mathcal{F}_{\boldsymbol{i}}^{\dagger}) . \tag{77}$$

The SU(2) gauge symmetry is now associated with a SU(2) matrix $V_{\boldsymbol{i}}$ under which [Affleck et al., 1988, Dagotto et al., 1988, Coleman and Andrei, 1989]

$$\mathcal{F}_{\boldsymbol{i}} \rightarrow V_{\boldsymbol{i}} \mathcal{F}_{\boldsymbol{i}} , \tag{78}$$

which is easily seen to leave the spin operator in Eq. (77) invariant. The global spin rotation symmetry is however

$$\mathcal{F}_{\boldsymbol{i}} \rightarrow \mathcal{F}_{\boldsymbol{i}} \sigma^{z} \Omega^{T} \sigma^{z} . \tag{79}$$

where Ω is the $S = 1/2$ spin rotation matrix defined by

$$\begin{pmatrix} f_{\boldsymbol{i}\uparrow} \\ f_{\boldsymbol{i}\downarrow} \end{pmatrix} \rightarrow \Omega \begin{pmatrix} f_{\boldsymbol{i}\uparrow} \\ f_{\boldsymbol{i}\downarrow} \end{pmatrix} . \tag{80}$$

Next we insert Eq. (77) into Eq. (17), and perform Hubbard-Stratonovich transformation to obtain an effective Hamiltonian for the spinons, following the same procedure as for bosonic spinons. We skip the intermediate steps, and focus directly on the fermion bilinear Hamiltonian on symmetry grounds; we obtain the mean-field nearest-neighbor spin liquid Hamiltonian for the spinons of the π-flux phase [Affleck and Marston, 1988]:

$$\begin{aligned}\mathcal{H}_{SLf} &= \frac{iJ}{2}\sum_{\langle ij\rangle} e_{ij}\left[\mathrm{Tr}\left(\mathcal{F}_i^\dagger \mathcal{F}_j\right) - \mathrm{Tr}\left(\mathcal{F}_j^\dagger \mathcal{F}_i\right)\right] \\ &= iJ\sum_{\langle ij\rangle} e_{ij}\left(\Psi_i^\dagger \Psi_j - \Psi_j^\dagger \Psi_i\right); \quad \Psi_i \equiv \begin{pmatrix} f_{i\uparrow} \\ f_{i\downarrow}^\dagger \end{pmatrix}, \end{aligned} \tag{81}$$

where $e_{ij} = \pm 1$ represents π-flux on the fermions as shown in Fig. 17. We choose $e_{ij} = -e_{ji}$ and

$$e_{i,i+\hat{x}} = 1\,, \quad e_{i,i+\hat{y}} = (-1)^x\,, \tag{82}$$

where $i = (x, y)$, $\hat{x} = (1, 0)$, $\hat{y} = (0, 1)$.

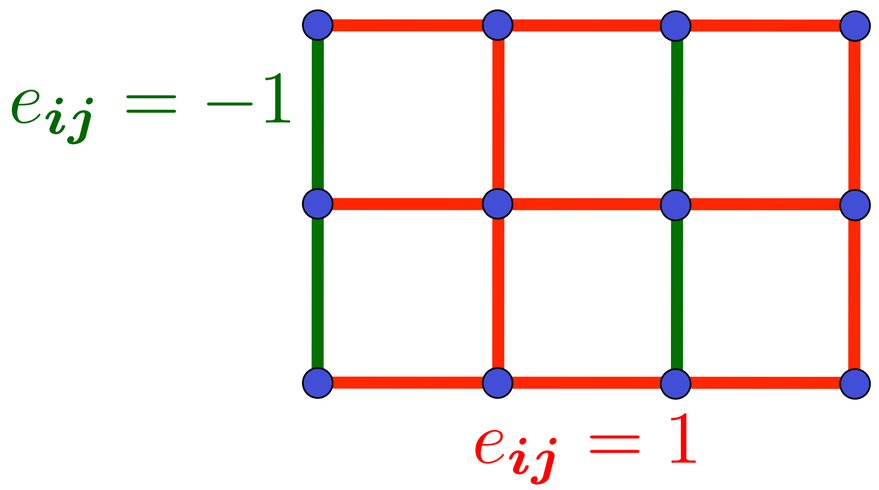

$$T_x T_y = -T_y T_x$$

Figure 17: Background π flux acting on the spinons f, and also on the chargons B.

In the chosen form, it is evident that $\mathcal{H}_{Slf}$ is invariant under the global spin rotation in Eq. (79), and also at least the gobal gauge transformation associate with Eq. (78). We have chosen the hopping to be pure imaginary because of the identity

$$\mathrm{Tr}\left(\mathcal{F}_{\boldsymbol{i}}^{\dagger}\mathcal{F}_{\boldsymbol{j}}\right) = -\mathrm{Tr}\left(\mathcal{F}_{\boldsymbol{j}}^{\dagger}\mathcal{F}_{\boldsymbol{i}}\right) . \tag{83}$$

We can now easily diagonalize the Hamiltonion in Eq. (81), and obtain the fermionic dispersion spectrum analogous to Eq. (34)

$$\omega_{\boldsymbol{k}} = \pm 2J\left(\sin^2 k_x + \sin^2 k_y\right)^{1/2} . \tag{84}$$

We show a plot of this analogous to Fig. 9 in Fig. 18.

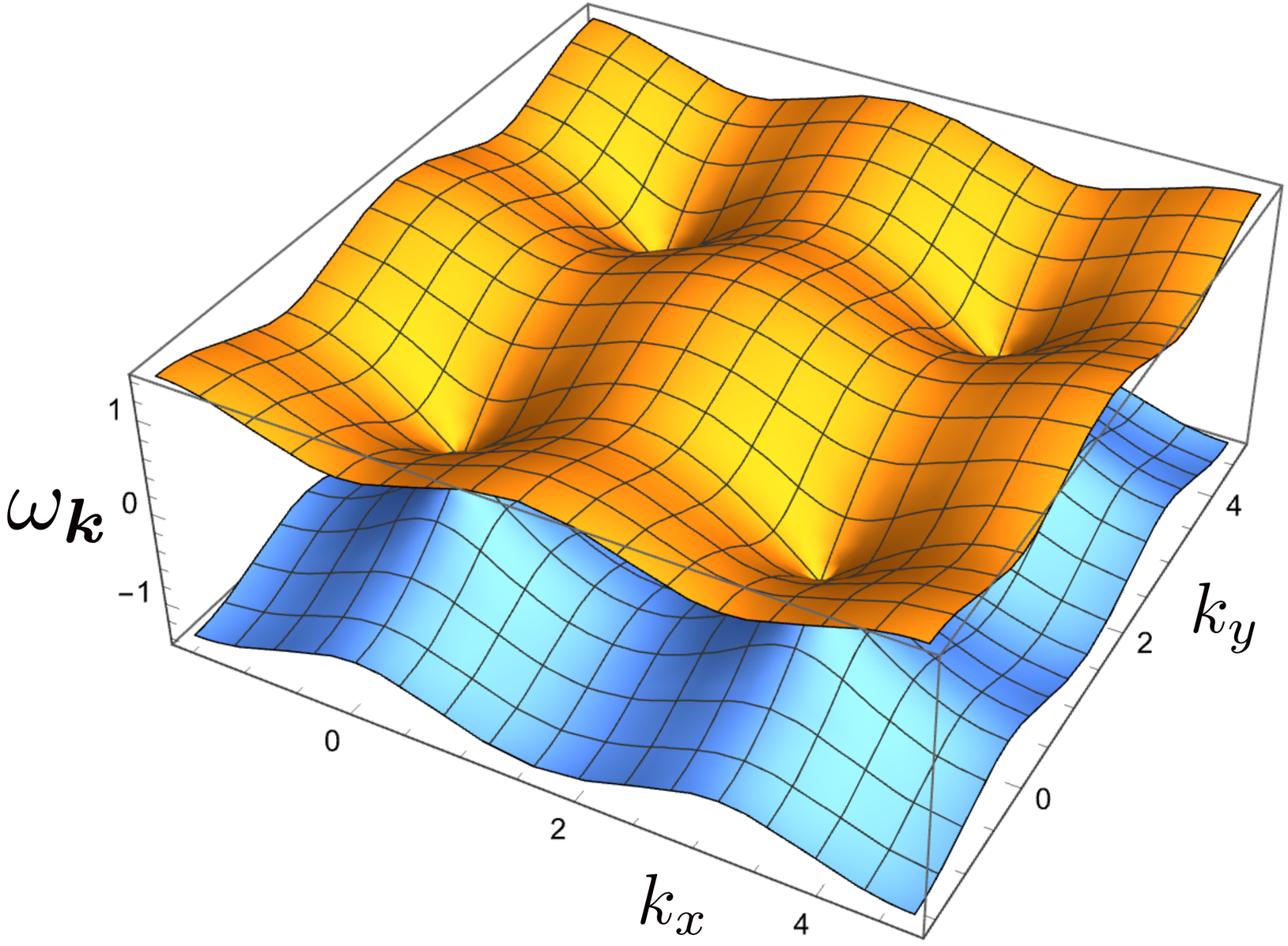

Figure 18: Dispersion of fermionic spinons in Eq. (84).

Unlike the bosonic spinons, the energy of the fermionic spinons is allowed to be negative, and the negative energy fermion states are occupied in the ground state. The constraint in Eq. (74) is then automatically satisfied. Notice the two independent nodal Dirac points at $\boldsymbol{k}_v$, $v = 1, 2$ with

$$\boldsymbol{k}_1 = (0, 0) \quad , \quad \boldsymbol{k}_2 = (0, \pi) \, . \tag{85}$$

The index v is the 'valley'.

3.1. Low energy SU(2) gauge theory.

Going beyond mean field theory, while still remaining on the lattice, we extend the mean field Hamiltonian in Eq. (81) to be invariant under space-dependent SU(2) gauge symmetries. To achieve this, we need to introduce a SU(2) gauge field $U_{ij} = U_{ji}^\dagger$ on each lattice link upon which the SU(2) gauge transformation acts as

$$U_{ij} \to V_i \, U_{ij} \, V_j^\dagger \, . \tag{86}$$

Then, by gauge invariance, we extend Eq. (81) to

$$\begin{aligned} \mathcal{H}_{SLf} &= \frac{iJ}{2} \sum_{\langle ij \rangle} e_{ij} \left[\mathrm{Tr} \left(\mathcal{F}_i^\dagger U_{ij} \mathcal{F}_j \right) - \mathrm{Tr} \left(\mathcal{F}_j^\dagger U_{ji} \mathcal{F}_i \right) \right] \\ &= iJ \sum_{\langle ij \rangle} e_{ij} \left(\Psi_i^\dagger U_{ij} \Psi_j - \Psi_j^\dagger U_{ji} \Psi_i \right) ; \quad \Psi_i \equiv \begin{pmatrix} f_{i\uparrow} \\ f_{i\downarrow}^\dagger \end{pmatrix} , \end{aligned} \tag{87}$$

The first form in terms of $\mathcal{F}$ makes both the SU(2) gauge invariance and the SU(2) spin rotation invariance explicit, while in the second form in terms of Ψ only the gauge invariance is explicit.

If we had not used the pure imaginary hopping in Eq. (81), then the mean-field Hamiltonian would break ('Higgs') the SU(2) gauge symmetry to a smaller symmetry. A 'staggered flux'

ansatz which breaks the SU(2) down to U(1) has commonly been used in the literature [Lee et al., 2006]. However, it is now known that this U(1) spin liquid allows single monopole perturbations [Alicea, 2008, Song et al., 2020b] (unlike the quadrupole monopole perturbations in Eq. (72)), and such single monopole terms are expected to drive a strong instability to confinement. So we don't consider the staggered-flux U(1) spin liquid.

The continuum formulation of this theory can be obtained by following the same procedure as in Section 5, but we have to carefully account for the SU(2) gauge symmetry. First, neglecting gauge fluctuations of U_{ij} for now, let us write Eq. (81) in momentum space, in terms of the fermions $\mathcal{F}_s(\boldsymbol{k})$, where $s = A, B$ is a sublattice index. Now the sublattices refer to sites with $\boldsymbol{i}_x$ even and odd, which are the two sites in the unit cell. We obtain

$$\mathcal{H}_{SLf} = -J \sum_{\boldsymbol{k}} \mathrm{Tr} \left(\mathcal{F}^\dagger(\boldsymbol{k}) \left[\rho^x \sin(k_x) + \rho^z \sin(k_y) \right] \mathcal{F}^\dagger(\boldsymbol{k}) \right) , \tag{88}$$

where ρ^ℓ, with $\ell = x, y, z$, are Pauli matrices in sublattice space. Next, analogous to Eq. (66),

we take the continuum limit near the valley momenta in terms of $\mathcal{X}_{sv}(\boldsymbol{r},\tau)$

$$\begin{aligned}\mathcal{F}_{A\boldsymbol{i}} &= \sum_v \mathcal{X}_{Av}(\boldsymbol{r},\tau)e^{i\boldsymbol{k}_v\cdot\boldsymbol{r}_i} \\ \mathcal{F}_{B\boldsymbol{i}} &= \sum_v \mathcal{X}_{Bv}(\boldsymbol{r},\tau)e^{i\boldsymbol{k}_v\cdot\boldsymbol{r}_i}\end{aligned} \tag{89}$$

for $\boldsymbol{i}$ on the A and B sublattices respectively. This yields the imaginary time Lagrangian density

$$\mathcal{L}_{\mathcal{X}} = \frac{1}{2}\mathrm{Tr}\left(\mathcal{X}^\dagger\left[\partial_\tau + 2Ji\rho^x\partial_x + 2Ji\rho^z\mu^z\partial_y\right]\mathcal{X}\right)\,, \tag{90}$$

where μ^ℓ are the Pauli matrices in valley space. We recall that the fermion $\mathcal{X}_{sv}$ has four-components, and each component is a 2×2 matrix which obeys the reality condition in Eq. (76). We can write this in a relativistic Dirac form

$$\mathcal{L}_{\mathcal{X}} = \frac{i}{2}\mathrm{Tr}\left(\bar{\mathcal{X}}\gamma^\mu\partial_\mu\mathcal{X}\right)\,, \tag{91}$$

with the definitions

$$\bar{\mathcal{X}} = -i\mathcal{X}^\dagger\gamma^0 \quad , \quad \gamma^0 = \rho^y\mu^z \quad , \quad \gamma^x = \rho^z\mu^z \quad , \quad \gamma^y = -\rho^x\,, \tag{92}$$

where we have absorbed factor of $c = 2J$ for the velocity of light. Finally, it is a simple matter to include the SU(2) gauge field by taking the continuum limit by writing

$$U_{\boldsymbol{ij}} = \exp\left(-iA^{\ell}_{\boldsymbol{ij}}\sigma^{\ell}\right) \tag{93}$$

(where σ^{ℓ} are the Pauli matrices in SU(2) gauge space) and expanding the exponential. We then obtain

$$\mathcal{L}_{\mathcal{X}} = \frac{i}{2}\mathrm{Tr}\left(\bar{\mathcal{X}}\gamma^{\mu}\left[\partial_{\mu} - iA^{\ell}_{\mu}\sigma^{\ell}\right]\mathcal{X}\right) . \tag{94}$$

The theory in Eq. (94) is the analog of the $\mathcal{L}_z$ in Eq. (71) for bosonic spinons. The latter theory was a U(1) gauge theory with two relativistic complex scalars z_{α}. In the present case, we have a SU(2) gauge theory with $N_f = 2$ massless Dirac fermions, associated with valley index v. The global symmetry of z_{α} was just spin rotations $z \to Rz$. In contrast, here we have emergent global symmetry which combines spin and valley rotations. A first guess is a SU(4) symmetry generalizing Eq. (79)

$$\mathcal{X} \to \mathcal{X}L\,, \tag{95}$$

where L acts on spin and valley space with $L^{\dagger}L = 1$. However, imposition of the reality condition Eq. (76) shows that we also need

$$L^{T} = \sigma^{y}L^{\dagger}\sigma^{y}\,, \tag{96}$$

and so the symmetry is only Sp(4)=SO(5)/$\mathbb{Z}_2$ [Ran and Wen, 2006, Wang et al., 2017]. In terms of the Hermitian Lie algebra elements M, with $L = e^{iM}$, the reality condition is

$$M^T = -\sigma^y M \sigma^y \,. \tag{97}$$

Requiring that M commute with the γ^μ, we can now write down the 10 elements of the Lie algebra of Sp(4)=SO(5)/$\mathbb{Z}_2$

$$M = \{\sigma^x, \sigma^y, \sigma^z, \mu^z\sigma^x, \mu^z\sigma^y, \mu^z\sigma^z, \rho^x\mu^y, \rho^x\mu^x\sigma^x, \rho^x\mu^x\sigma^y, \rho^x\mu^x\sigma^z\} \,. \tag{98}$$

The remaining 5 SU(4) generators which commute with the γ^μ are ($t = 1 \ldots 5$)

$$\Gamma^t = \{\mu^z, \rho^x\mu^x, \rho^x\mu^y\sigma^x, \rho^x\mu^y\sigma^y, \rho^x\mu^y\sigma^z\} \,. \tag{99}$$

The Γ^t all anti-commute with each other, and transform as a SO(5) vector under the generators in Eq. (98). It is now straightforward to check by working back to the lattice operators from the information above that the vector $i\mathrm{Tr}\left(\bar{\mathcal{X}}\Gamma^t\mathcal{X}\right)$ corresponds precisely to the 5 components of the orders parameters shown in Fig. 16: the first two components are the VBS order, and the last 3 components are the Néel order $\boldsymbol{\mathcal{N}}$ in Eq. (70) [Ran and Wen, 2006, Wang et al., 2017].

Wang *et al.* [Wang et al., 2017] have argued that the likely fate of the SU(2) gauge theory upon confinement is a state which the SO(5) symmetry is spontaneously broken with $\langle i\mathrm{Tr}\left(\bar{\mathcal{X}}\Gamma^t\mathcal{X}\right)\rangle \neq 0$. The lattice model does not have exact SO(5) symmetry, and the choice between the Néel and VBS components of Γ^t is made by additional 4-fermi terms that can be added to Eq. (94). So the ultimate fate of the theory is essentially identical to the fate of the bosonic spinon theory in Section 1, as illustrated in Fig. 16. This is essentially the reason for the duality between the theories in Section 1 and 1, and Wang *et al.* have provided additional topological arguments.

3.2. SO(5) non-linear σ-model

There is a third formulation of the theories in Section 1 and 1 which is useful for some purposes, as we illustrate in Fig. 19.

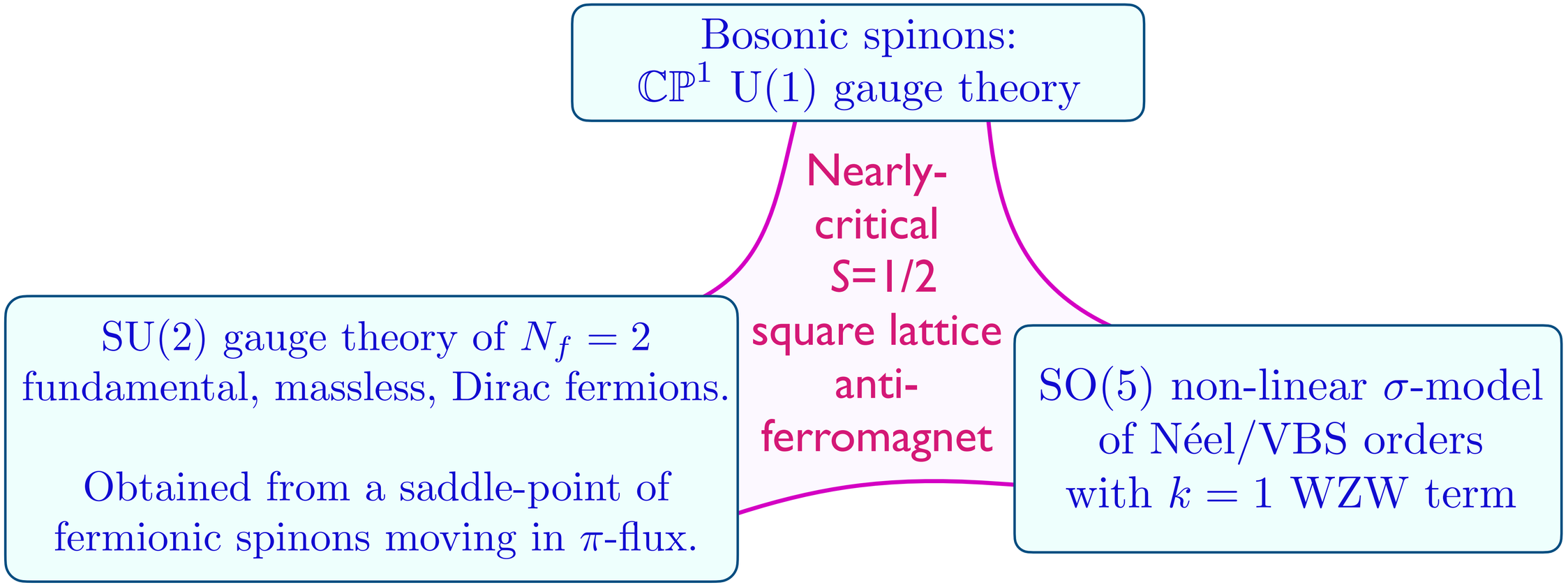

Figure 19: Three field-theoretical formulations of the $S = 1/2$ square lattice antiferromagnet near the Néel-VBS transition in Fig. 16. All three are valid descriptions [Wang et al., 2017], but the SU(2) gauge theory of Dirac fermions is the most convenient starting point to describe the connection to *d*-wave superconductivity.

This is obtained most simply by coupling Eq. (94) to the SO(5) vector order parameter, and integrating out the fermions. Introducing the SO(5) fundamental unit length field n_t, $n_t n_t = 1$ to Eq. (94)

$$\mathcal{L}_{\mathcal{X}n} = \frac{i}{2}\mathrm{Tr}\left(\bar{\mathcal{X}}\gamma^\mu\left[\partial_\mu - iA_\mu^\ell\sigma^\ell\right]\mathcal{X}\right) - in_t\mathrm{Tr}\left(\bar{\mathcal{X}}\Gamma^t\mathcal{X}\right), \tag{100}$$

we integrate out the Dirac fermions following the analysis of Ref. [Abanov and Wiegmann, 2000] and obtain

$$\mathcal{L}_n = \frac{1}{2g}\left(\partial_\mu n_t\right)^2 + 2\pi i\Gamma[n_t] \tag{101}$$

The last term is the Wess-Zumino-Witten (WZW) term at level 1: it is a Berry phase associated with spacetime textures of n_t, a higher dimensional analog of the Berry phase of a single spin which is proportional to area enclosed by a spherical path [Lee and Sachdev, 2015, Wang et al., 2017]: an explicit expression of $\Gamma[n_t]$ requires 4+1 dimensions with an emergent spatial direction. Upon reduction to a O(3) non-linear sigma model for the Néel order parameter $\boldsymbol{\mathcal{N}}$ in Eq. (70), the WZW term reduces [Tanaka and Hu, 2005] to the Berry phases of the monopoles noted near Eq. (72). Also, note that while the SO(5) symmetry is explicit in the fermionic spinon theory in

Eq. (94), it is not explicit in the bosonic spinon theory in Eq. (72), but expected to be emergent [Senthil and Fisher, 2006].

The form in Eq. (101) has been exploited in recent numerical work on the fuzzy sphere [Zhou et al., 2024b]. Their results, and those of a number of other numerical works [Hering et al., 2019, Nahum et al., 2015, Ferrari and Becca, 2020, Nomura and Imada, 2021, Chen et al., 2024, Liu et al., 2024, Chester and Su, 2024, Takahashi et al., 2024] show that the critical spin liquid defined by Eq. (72), Eq. (94), or (101) is stable over a substantial intermediate energy and length scales, before ultimately confining into a Néel or VBS state. This intermediate range stability is not a bug, but a feature ideal for our purpose in Section 6 of defining a FL* state at intermediate temperatures, which ultimately confines to variety of other states at low temperatures.

1. Spin density wave order in the Hubbard model

2. Bosonic spinon theory of quantum spin liquids

3. Fermionic spinon theory of quantum spin liquids

4. Holon metal from a quantum spin liquid with bosonic spinons

5. d-wave superconductior from a quantum spin liquid with fermionic spinons

6. Fractionalized Fermi liquids (FL*)

Ordinary metal

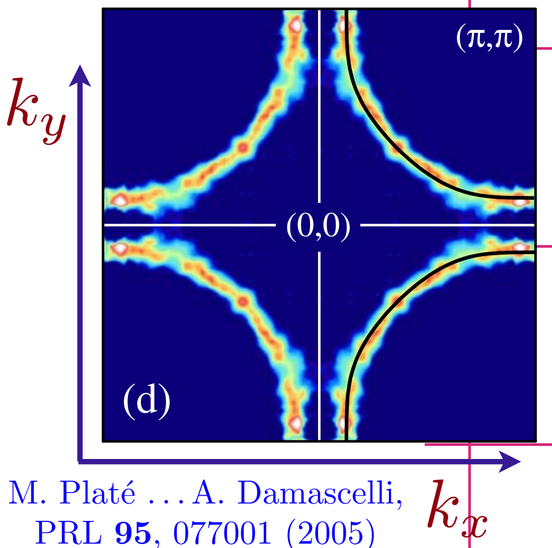

M. Platé ... A. Damascelli,
PRL **95**, 077001 (2005)

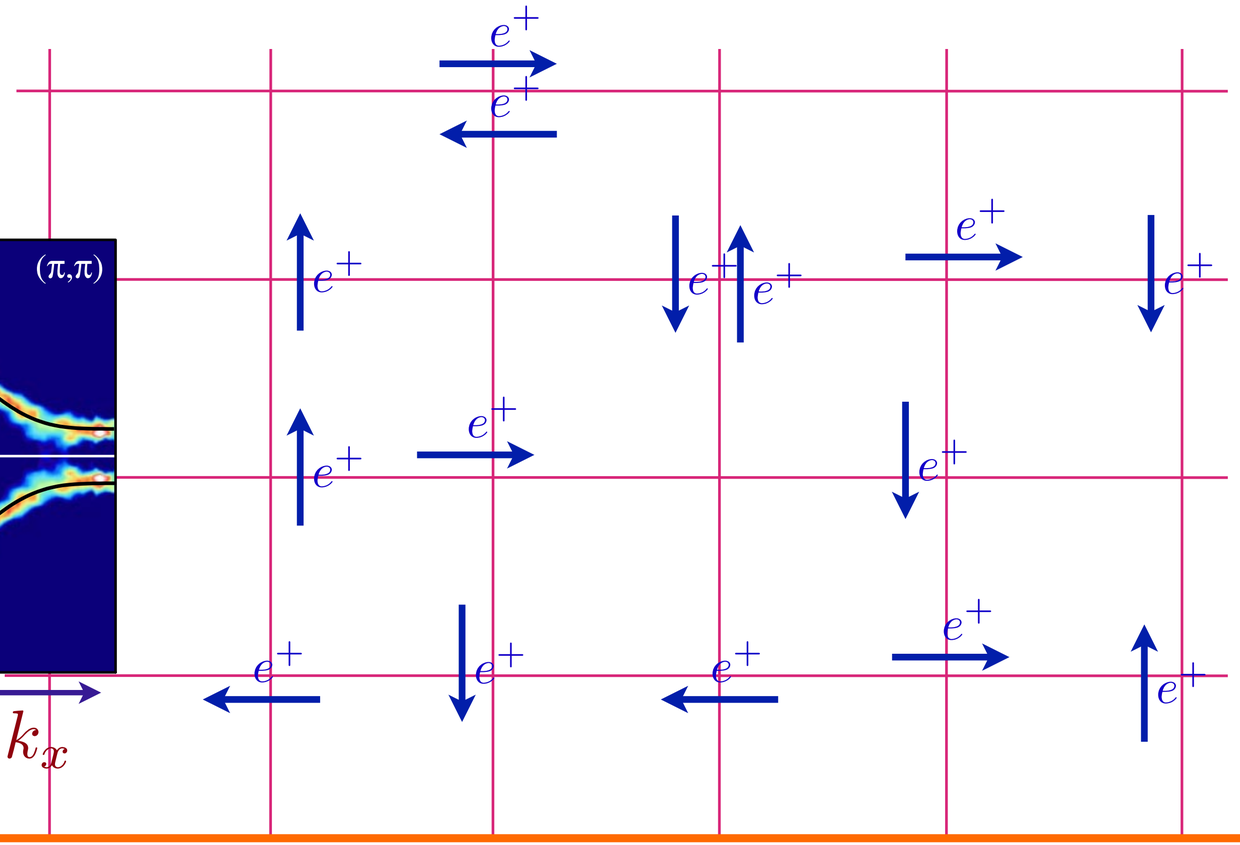

Luttinger area.
No broken symmetry

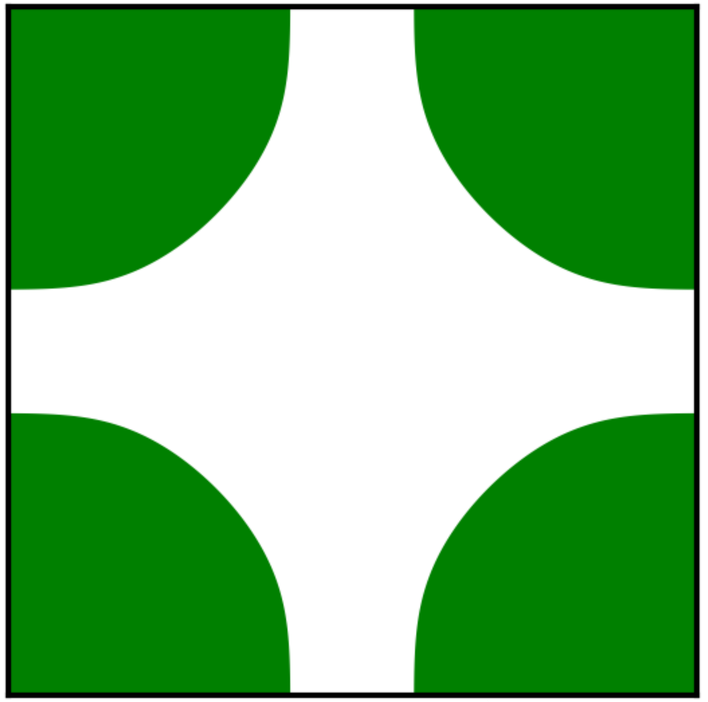

Area $(1+p)/2$

At large p, we obtain a gas of nearly free fermionic holes of density $1+p$ (relative to the filled band with 2 electrons per site)

Insulating antiferromagnet

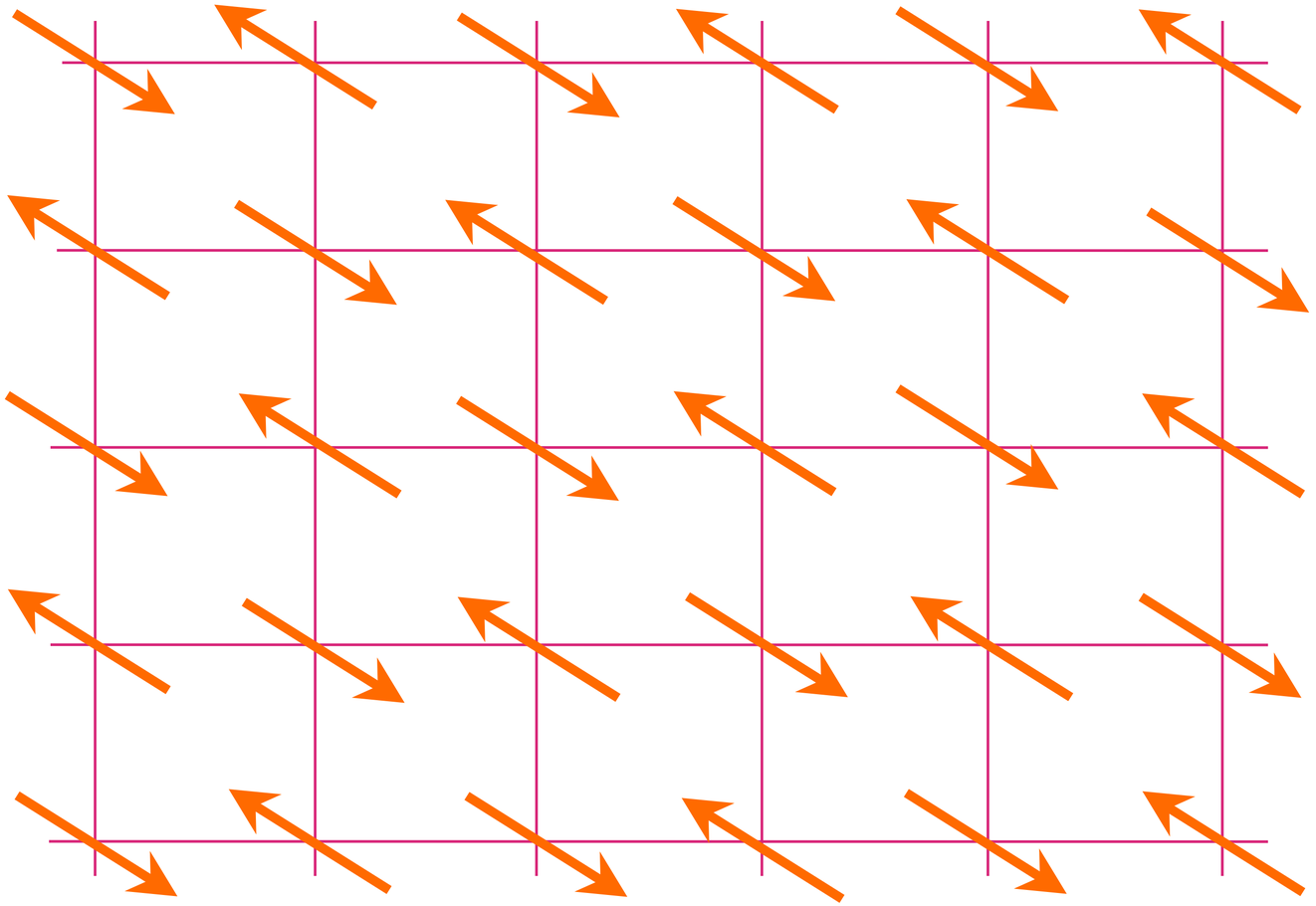

Doping an insulating antiferromagnet with holes of density p

AF metal

Fermi liquid with density p of spin 1/2, charge $+e$ holes. Yamaji effect requires inter-layer spin correlations (not present in Hg-1201).

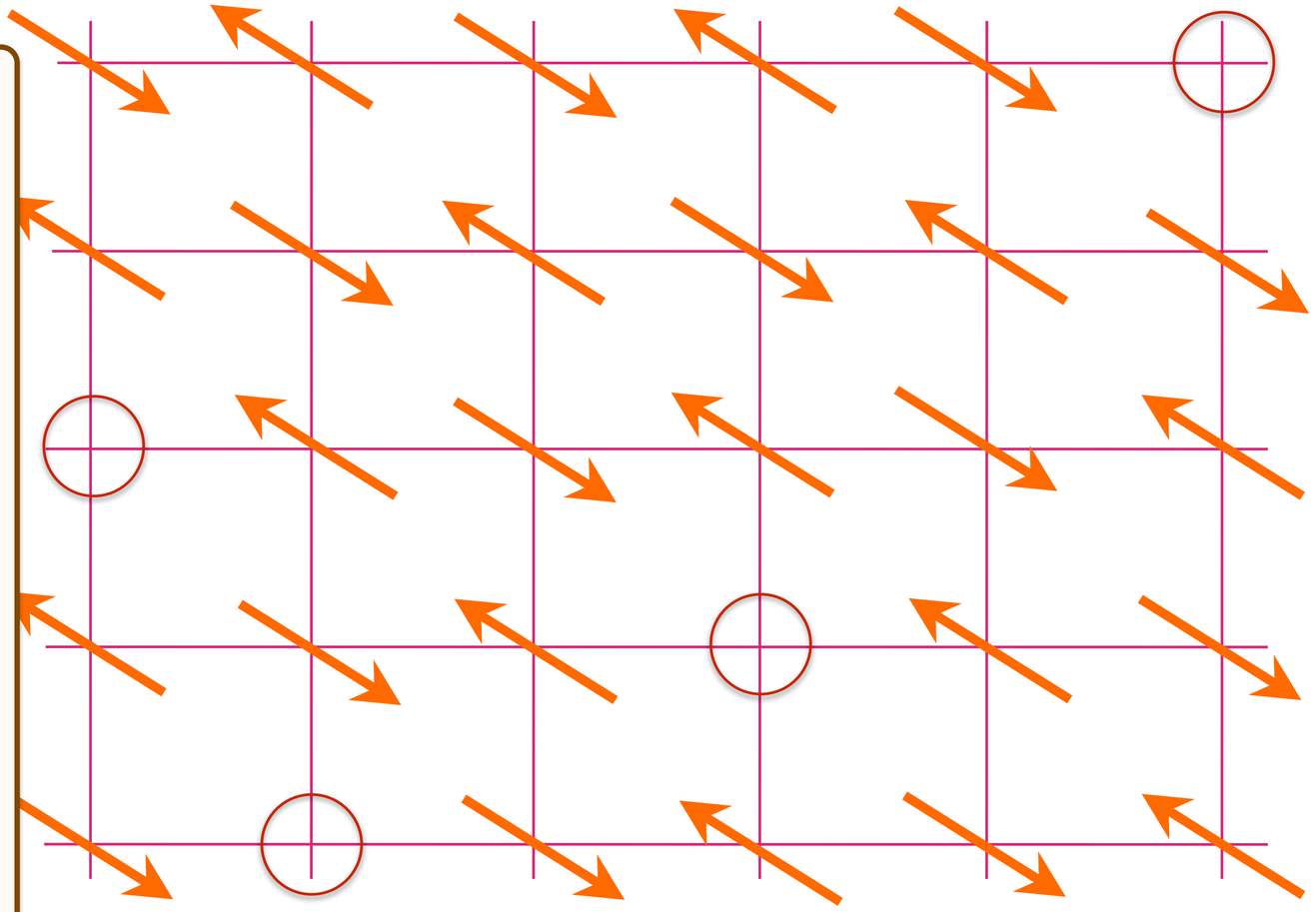

Luttinger area.
Broken symmetry

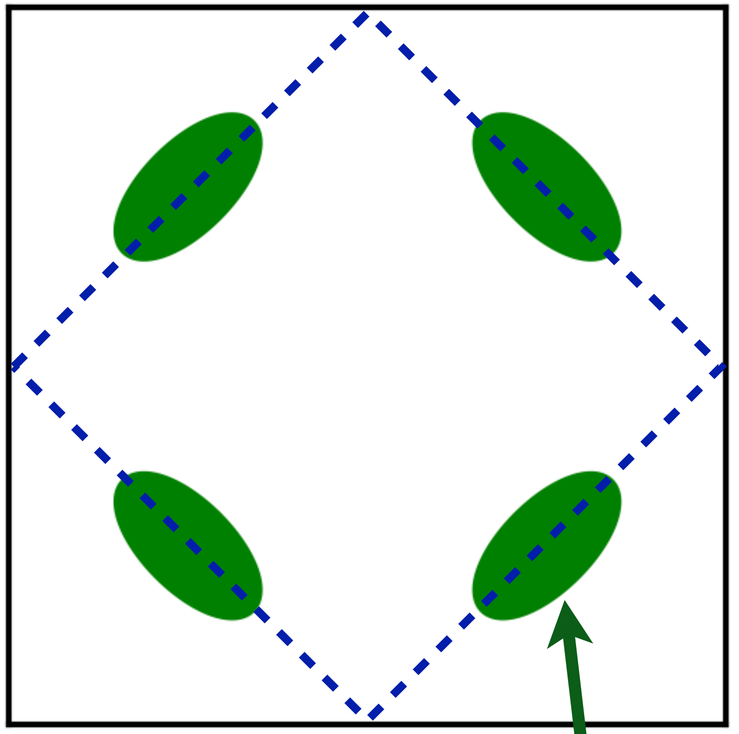

Talk by Xingjiang Zhou at 09:00

Doping an insulating antiferromagnet with holes of density p

Holon metal

Spin liquid with density p of spinless, charge $+e$ holons. No coherent inter-layer transport, so no Yamaji effect.

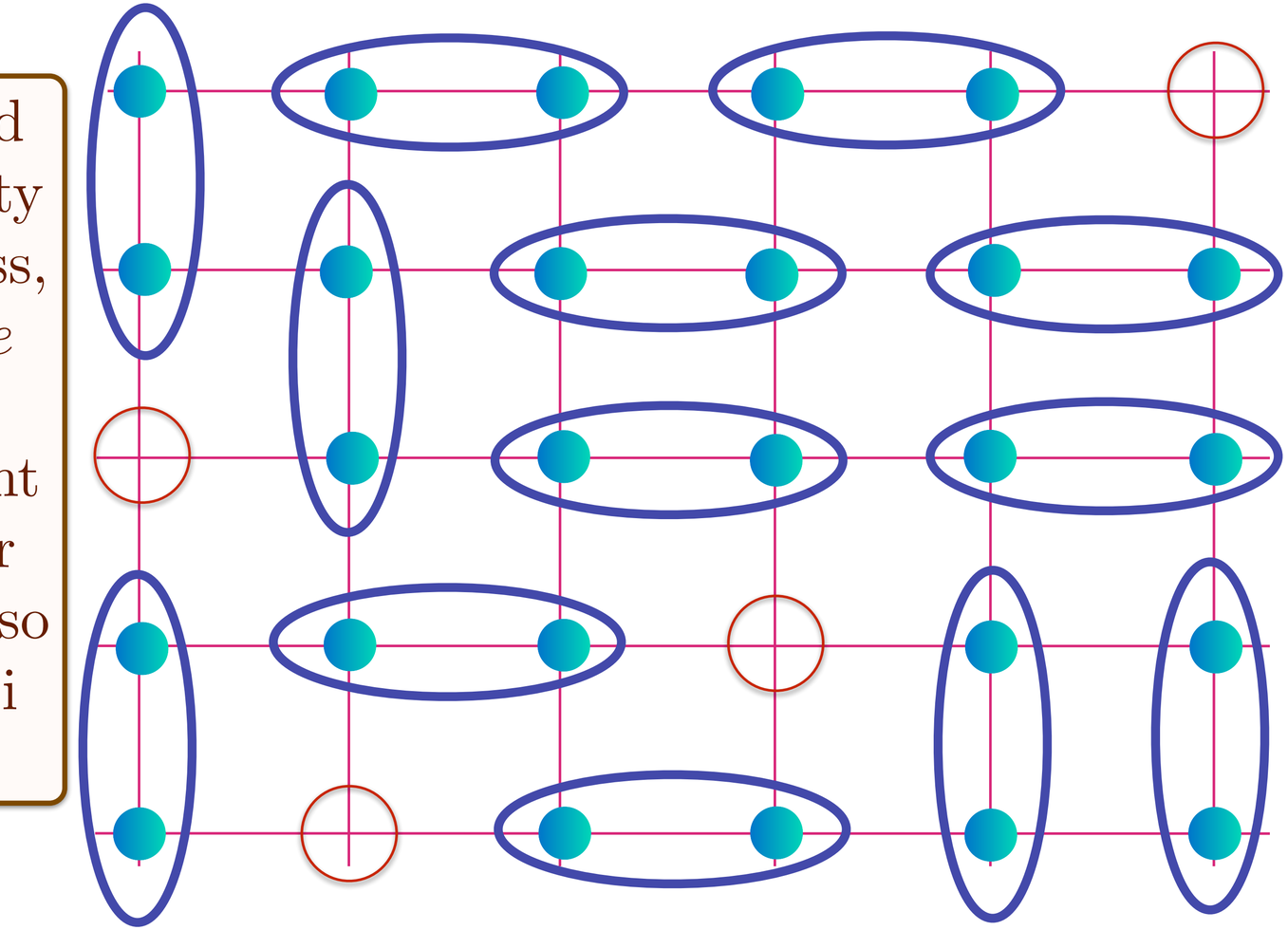

$= (|\uparrow\downarrow\rangle - |\downarrow\uparrow\rangle)/\sqrt{2}$

Oshikawa anomaly is satisfied by sum of spin liquid (1) and Fermi surface anomalies (p)

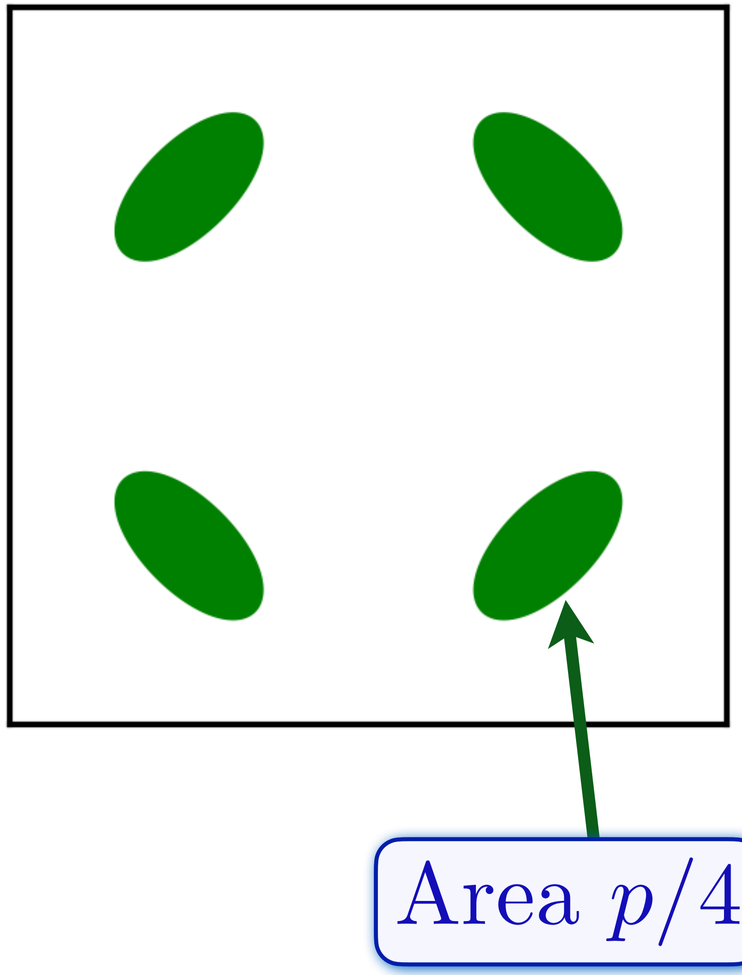

R. K. Kaul, Y. B. Kim, S. S., T. Senthil, Nature Physics **4**, 28 (2008)

Doping an insulating antiferromagnet with holes of density p

Holon metal

Spin liquid with density p of spinless, charge $+e$ holons. No coherent inter-layer transport, so no Yamaji effect.

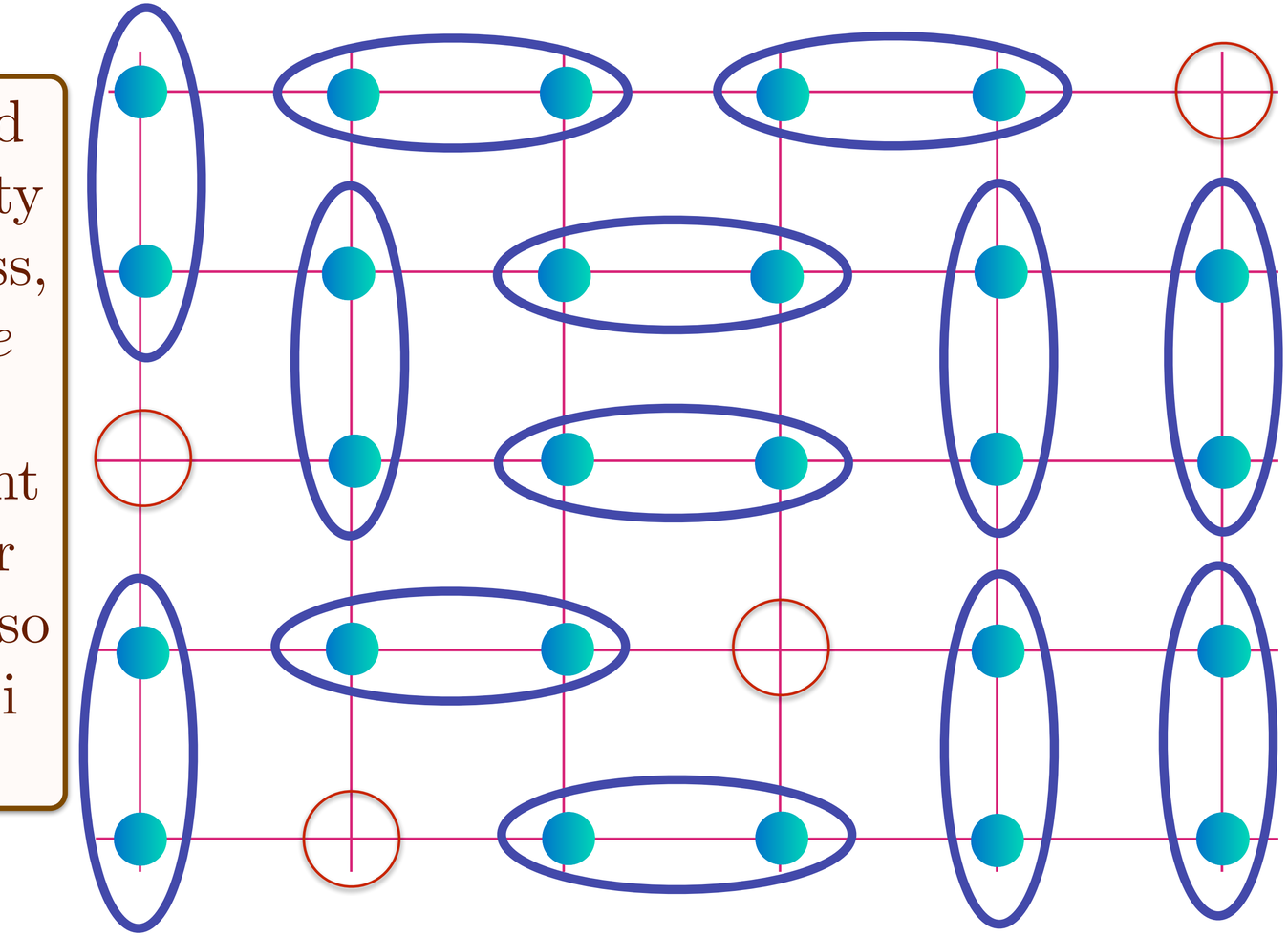

$= (|\uparrow\downarrow\rangle - |\downarrow\uparrow\rangle)/\sqrt{2}$

Oshikawa anomaly is satisfied by sum of spin liquid (1) and Fermi surface anomalies (p)

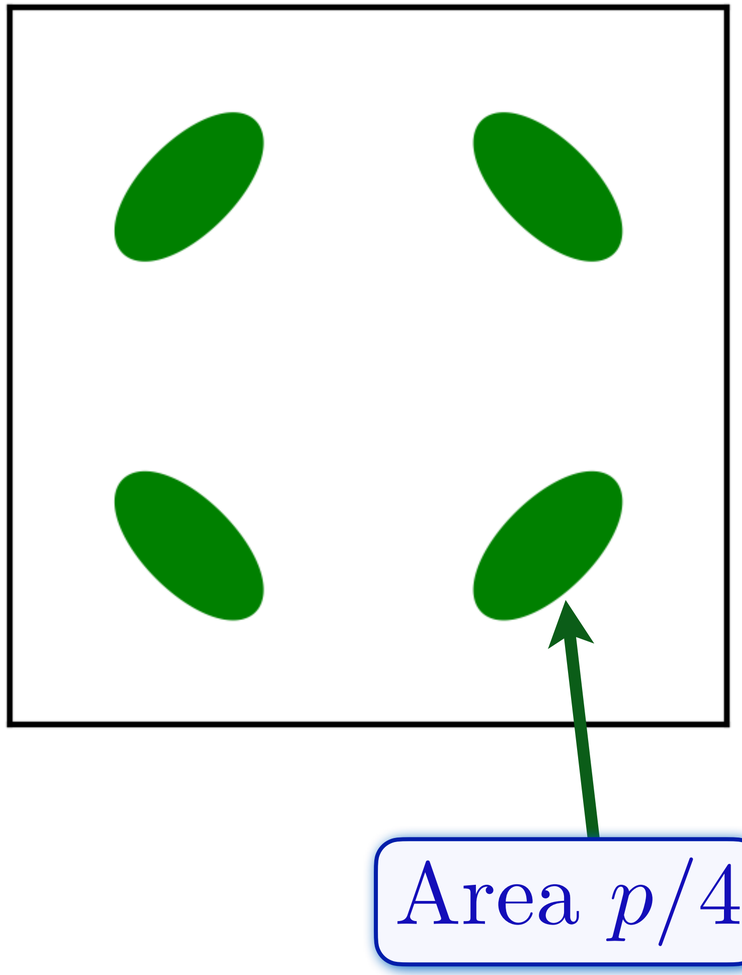

R. K. Kaul, Y. B. Kim, S. S., T. Senthil, Nature Physics **4**, 28 (2008)

Doping an insulating antiferromagnet with holes of density p

Holon metal

Spin liquid with density p of spinless, charge $+e$ holons. No coherent inter-layer transport, so no Yamaji effect.

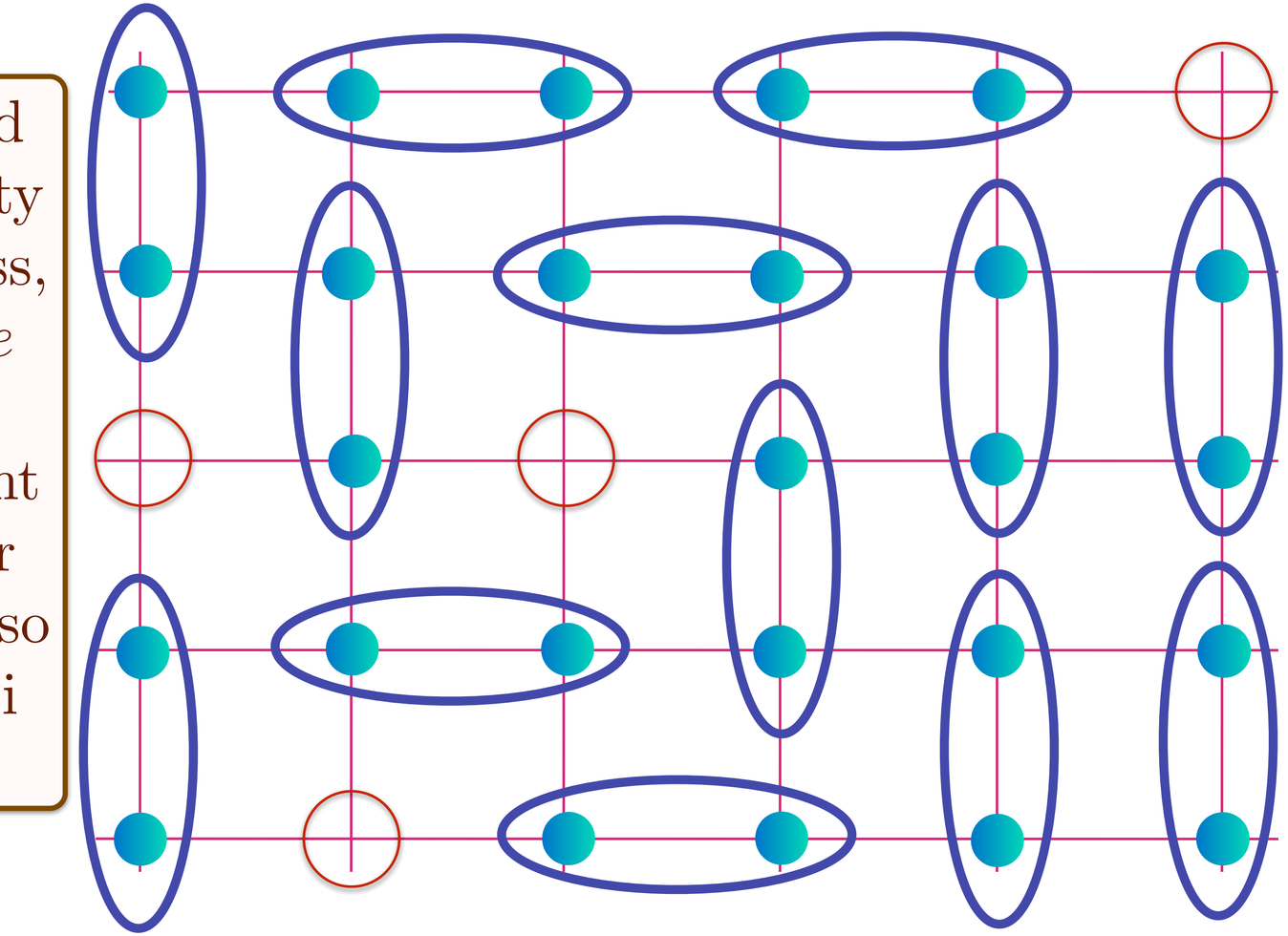

$= (|\uparrow\downarrow\rangle - |\downarrow\uparrow\rangle)/\sqrt{2}$

Oshikawa anomaly is satisfied by sum of spin liquid (1) and Fermi surface anomalies (p)

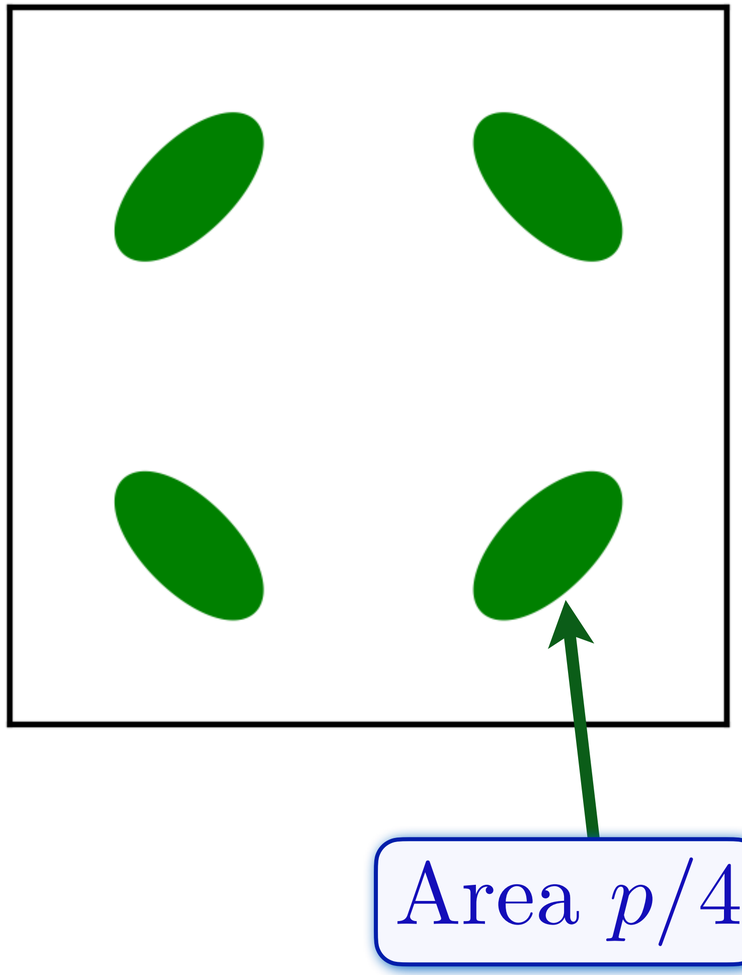

R. K. Kaul, Y. B. Kim, S. S., T. Senthil, Nature Physics **4**, 28 (2008)

Doping an insulating antiferromagnet with holes of density p

Holon metal

Spin liquid with density p of spinless, charge $+e$ holons. No coherent inter-layer transport, so no Yamaji effect.

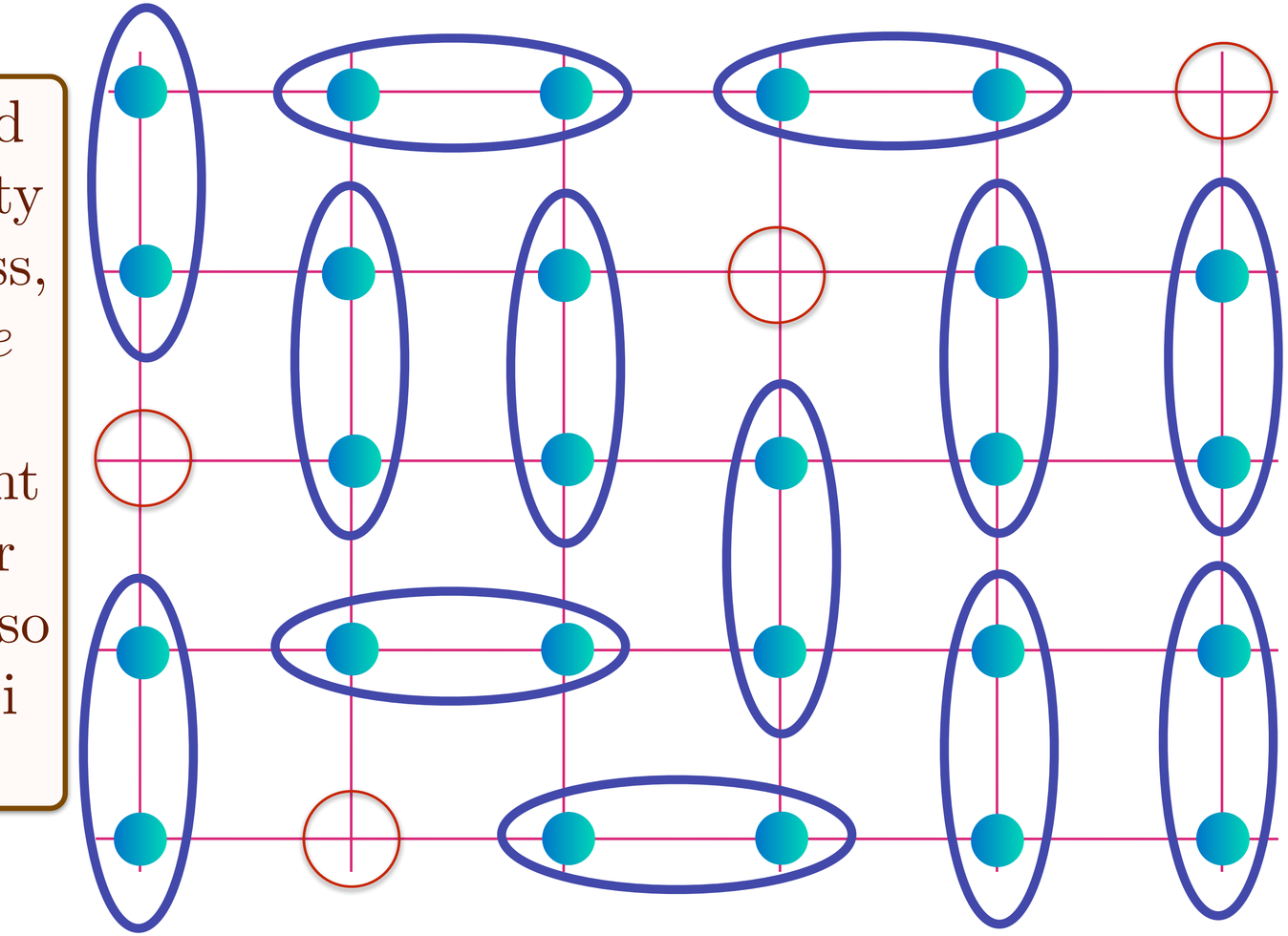

$= (|\uparrow\downarrow\rangle - |\downarrow\uparrow\rangle)/\sqrt{2}$

Oshikawa anomaly is satisfied by sum of spin liquid (1) and Fermi surface anomalies (p)

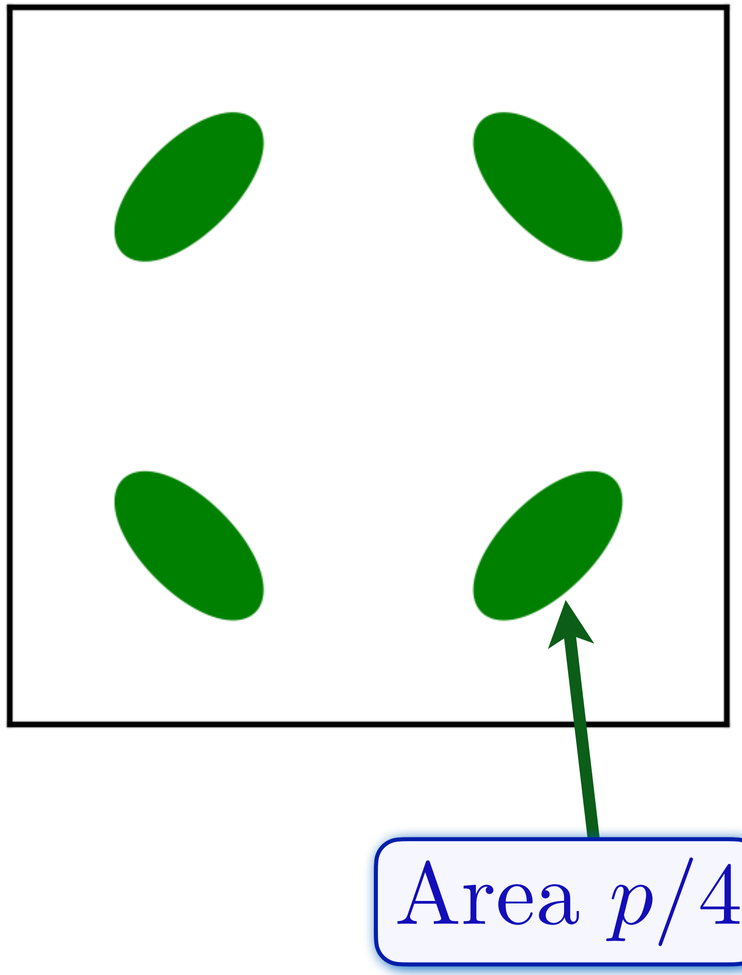

R. K. Kaul, Y. B. Kim, S. S., T. Senthil, Nature Physics **4**, 28 (2008)

Doping an insulating antiferromagnet with holes of density p

Holon metal

Spin liquid with density p of spinless, charge $+e$ holons. No coherent inter-layer transport, so no Yamaji effect.

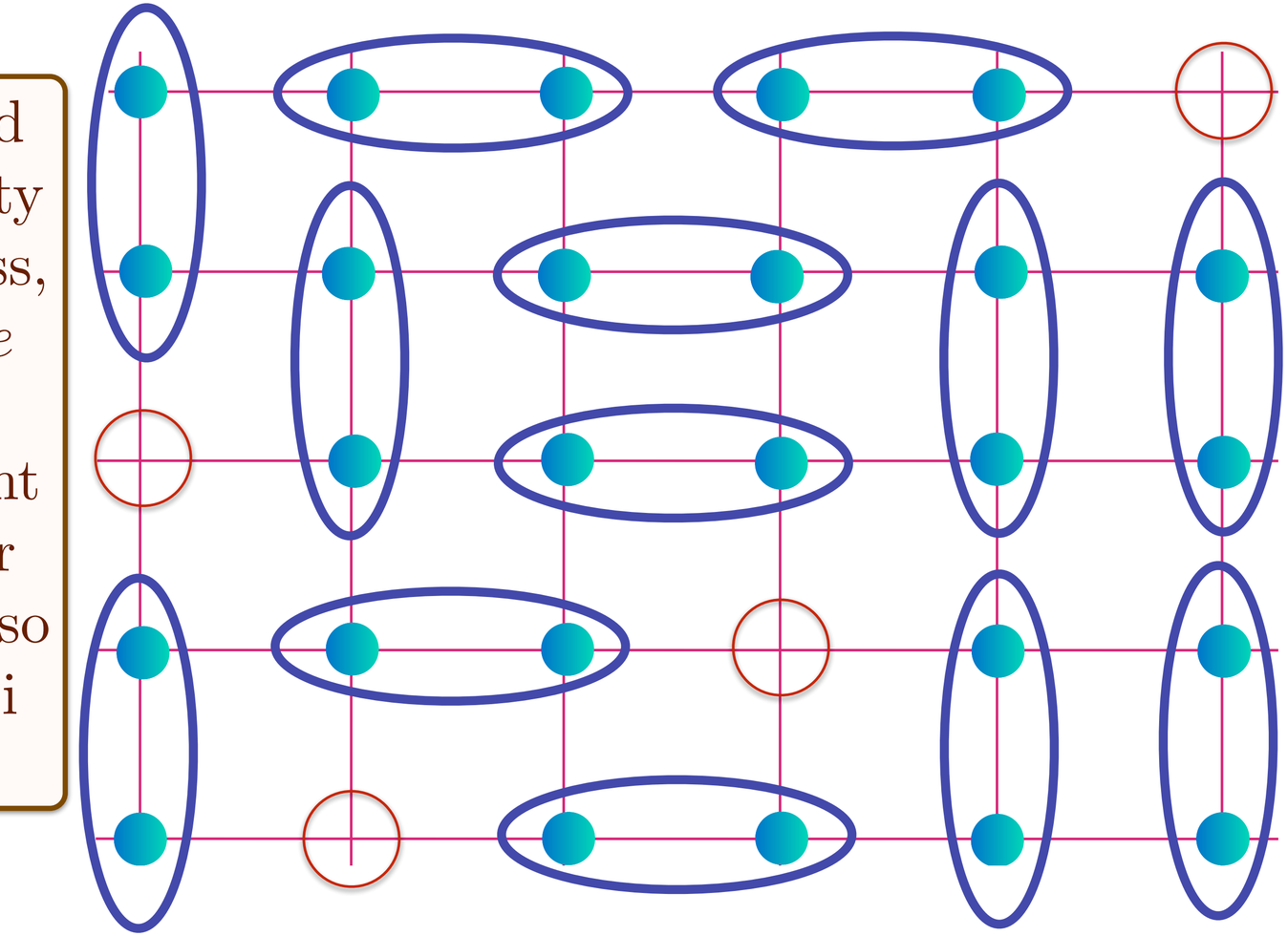

$$= \left(|\uparrow\downarrow\rangle - |\downarrow\uparrow\rangle\right)/\sqrt{2}$$

Oshikawa anomaly is satisfied by sum of spin liquid (1) and Fermi surface anomalies (p)

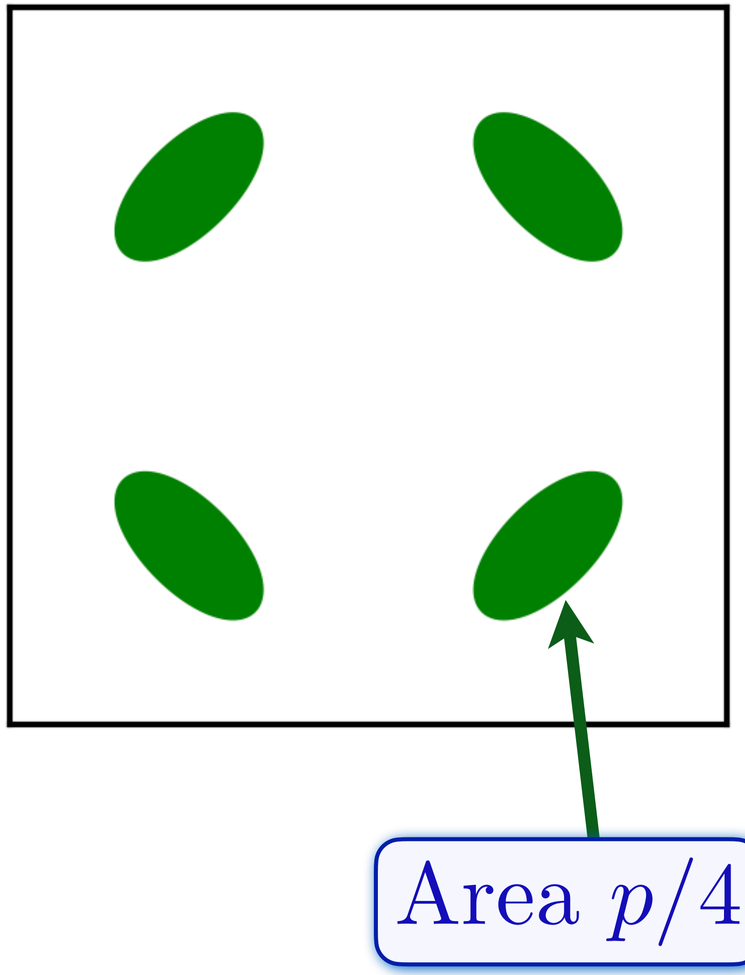

R. K. Kaul, Y. B. Kim, S. S., T. Senthil, Nature Physics **4**, 28 (2008)

4. Holon metal from a quantum spin liquid with bosonic spinons

This section dopes the spin liquid state of Section 1 with holes of density p. We already discussed the fate of the ordered antiferromagnet upon doping in Section 1, and here we will discuss the fate of the spin liquid.

For the Néel state in Section 1 we obtained a Fermi liquid metal with hole pockets of spin-1/2, charge e quasiparticles. After accounting for the doubling of the unit cell, there are 2 independent pockets in Fig. 5, and so the fractional area of each pocket is $p/4$.

In the present section, doping the spin liquid will yield a *holon metal*, where has Fermi pockets of *spinless*, charge e quasiparticles, *i.e.* holons. There is no doubling of the unit cell here, and we will see that there are 4 independent pockets. So the area of each holon pocket is again $p/4$. But such pockets are not directly observable in photoemission, as the electron operator is a composite of a holon and a spinon. However the holon pockets will contribute to magnetotransport observables restricted to motion within each square lattice plane.

We will argue in Section 6 that the holon metal does not provide a satisfactory description of the cuprate pseudogap. However, recent work [Lebrat et al., 2024, Nikolaenko et al., 2025] has argued that the holon metal is indeed appropriate for the Hubbard model on the Lieb lattice.

A popular way to dope a spin liquid is to introduce a fermionic holon h, so that the electron operator can be written as

$$c_{\boldsymbol{i}\alpha} = h^{\dagger}_{\boldsymbol{i}} b_{\boldsymbol{i}\alpha} \, . \tag{102}$$

However, this approach runs into complications associated with the sublattice assignment of opposite U(1) gauge charges in Eq. (66). We shall instead follow a simpler approach which is ultimately equivalent to Eq. (102), but is applicable more broadly. The central idea here is to transform the electron operator into a rotating reference frame in spin space [Shraiman and Siggia, 1988, Schulz, 1990, Dupuis, 2002, Borejsza and Dupuis, 2004, Sachdev et al., 2009, Chowdhury and Sachdev, 2015a, Chowdhury and Sachdev, 2015b, Chatterjee et al., 2017, Sachdev et al., 2019, Bonetti and Metzner, 2022, Scholle et al., 2023, Nikolaenko et al., 2025]

$$\begin{pmatrix} c_{\boldsymbol{i},\uparrow} \\ c_{\boldsymbol{i},\downarrow} \end{pmatrix} = R_{\boldsymbol{i}} \begin{pmatrix} \psi_{\boldsymbol{i},+} \\ \psi_{\boldsymbol{i},-} \end{pmatrix}, \qquad R_{\boldsymbol{i}}^{\dagger} R_{\boldsymbol{i}} = R_{\boldsymbol{i}} R_{\boldsymbol{i}}^{\dagger} = \mathbb{1}. \tag{103}$$

The fermions in the rotating reference frame are spinless 'chargons' ψ_s, with $s = \pm$, carrying the electromagnetic charge. The SU(2) rotation matrix $R_{\boldsymbol{i}}$ is represented by two complex numbers

$$R_{\boldsymbol{i}} = \begin{pmatrix} z_{\boldsymbol{i},\uparrow} & -z_{\boldsymbol{i},\downarrow}^{*} \\ z_{\boldsymbol{i},\downarrow} & z_{\boldsymbol{i},\uparrow}^{*} \end{pmatrix}, \qquad |z_{\boldsymbol{i},\uparrow}|^2 + |z_{\boldsymbol{i},\downarrow}|^2 = 1. \tag{104}$$

Indeed, we eventually identify z_α with the spinons of the spin liquid described by the complex scalars of the $\mathbb{CP}^1$ field theory in Eq. (71).

A key property of the decomposition in Eq. (103) is that it introduces a SU(2) gauge invariance [Sachdev et al., 2009].

$$R_{\boldsymbol{i}} \rightarrow R_{\boldsymbol{i}}\, W_{\boldsymbol{i}}^{\dagger}$$
$$\begin{pmatrix} \psi_{\boldsymbol{i},+} \\ \psi_{\boldsymbol{i},-} \end{pmatrix} \rightarrow W_{\boldsymbol{i}} \begin{pmatrix} \psi_{\boldsymbol{i},+} \\ \psi_{\boldsymbol{i},-} \end{pmatrix}, \tag{105}$$

where $W_{\boldsymbol{i}}$ is the SU(2) matrix generating the gauge transformation. This gauge invariance is distinct from the SU(2) gauge invariance of the fermionic spinons in Section 3, which is instead associated with a transformation in pseudospin space.
We now apply this tranformation to the paramagnon theory in Eq. (4). Then, we write the Yukawa coupling between the paramagnon $\boldsymbol{\mathcal{P}_i}$ and the electrons as

$$\boldsymbol{\mathcal{P}_i} \cdot c_{\boldsymbol{i}\alpha}^{\dagger} \frac{\boldsymbol{\sigma}_{\alpha\beta}}{2} c_{\boldsymbol{i}\beta} \Rightarrow \boldsymbol{H_i} \cdot \psi_{\boldsymbol{i},s}^{\dagger} \frac{\boldsymbol{\sigma}_{ss'}}{2} \psi_{\boldsymbol{i},s'}\,. \tag{106}$$

We have now introduced a 'Higgs' field $\boldsymbol{H_i}$ [Sachdev et al., 2009] given by

$$\boldsymbol{\sigma} \cdot \boldsymbol{H_i} = R_{\boldsymbol{i}}^{\dagger}\, \boldsymbol{\sigma} \cdot \boldsymbol{\mathcal{P}_i}\, R_{\boldsymbol{i}}. \tag{107}$$

It is easy to deduce from Eq. (107) that $\boldsymbol{H}$ transforms as an adjoint under the SU(2) gauge transformation

$$\boldsymbol{\sigma} \cdot \boldsymbol{H_i} \rightarrow W_{\boldsymbol{i}}\, \boldsymbol{\sigma} \cdot \boldsymbol{H_i}\, W_{\boldsymbol{i}}^{\dagger} \tag{108}$$

The action of the SU(2) gauge transformation W_i, should be distinguished from the action of global SU(2) spin rotations Ω under which

$$\begin{aligned} R_{\boldsymbol{i}} &\rightarrow \Omega\, R_{\boldsymbol{i}} \\ \begin{pmatrix} c_{\boldsymbol{i}\uparrow} \\ c_{\boldsymbol{i}\downarrow} \end{pmatrix} &\rightarrow \Omega \begin{pmatrix} c_{\boldsymbol{i}\uparrow} \\ c_{\boldsymbol{i}\downarrow} \end{pmatrix} \\ \psi_{i,s} &\rightarrow \psi_{i,s} \\ \boldsymbol{H}_i &\rightarrow \boldsymbol{H}_i\,. \end{aligned} \tag{109}$$

Note that R carries global spin, and so describes spinons. On the other hand $\boldsymbol{H}$ and ψ are spinless.

We can now use the SU(2) gauge theory of ψ, R, and $\boldsymbol{H}$ to describe the phases of the Hubbard model. The many possibilities are discussed at some length in Refs. [Sachdev et al., 2009, Chatterjee et al., 2017, Scheurer and Sachdev, 2018, Sachdev et al., 2019, Bonetti and Metzner, 2022, Scholle et al., 2023, Nikolaenko et al., 2025].

We limit ourselves here to the simplest case of the state obtained by rotationally averaging the Néel state of Section 1. The doped spin liquid so obtained corresponds to condensing the Higgs field as

$$\langle \boldsymbol{H_i} \rangle = \eta_{\boldsymbol{i}} \, (0, 0, H_0) \tag{110}$$

where $\eta_{\boldsymbol{i}}$ is the sublattice staggering of Eq. (11). Such a condensate preserves spin rotation invariance, but breaks the SU(2) gauge invariance down to U(1). So the low energy theory is a U(1) gauge theory, with a gauge field a_μ which is the same as that introduced in Eq. (38), and which also appears in the $\mathbb{CP}^1$ theory of R in Eq. (71). The effective theory for the chargons ψ can be obtained from Eq. (4) after (*i*) replacing the electrons $c_{\boldsymbol{i}\alpha}$ by the chargon $\psi_{\boldsymbol{i},s}$, (*ii*) replacing the paramagnon $\boldsymbol{\mathcal{P}_i}$ by the Higgs condensate in Eq. (110), and (*iii*) minimally coupling the ψ to the U(1) gauge field a_μ. So we obtain the effective chargon action

$$\mathcal{S}_\psi = \int_0^\beta d\tau \Bigg[\sum_{\boldsymbol{i},s} \psi^\dagger_{\boldsymbol{i},s} (\partial_\tau - \mu - i a_\tau) \psi_{\boldsymbol{i},s} - \sum_{\boldsymbol{i},\boldsymbol{j},s,s'} t_{\boldsymbol{ij}} e^{i a_{\boldsymbol{ij}}} \psi^\dagger_{\boldsymbol{i},s} \psi_{\boldsymbol{j},s} + \sum_{\boldsymbol{i},s,s'} H_0 \cdot \psi^\dagger_{\boldsymbol{i},s} \frac{\sigma^z_{ss'}}{2} \psi_{\boldsymbol{i},s'} \Bigg], \tag{111}$$

where t_{ij} are the hoppings corresponding to the dispersion $\varepsilon_{\boldsymbol{k}}$ in Eq. (4). At leading order, this yields chargon pockets of spinless fermions which are the same as the pockets of electrons in the ordered Néel state. At higher order, the gauge will renormalized the dispersion so that the pockets lose the reflection symmetry about the magnetic Brillouin zone boundary present in the Néel state.

1. Spin density wave order in the Hubbard model

2. Bosonic spinon theory of quantum spin liquids

3. Fermionic spinon theory of quantum spin liquids

4. Holon metal from a quantum spin liquid
   with bosonic spinons

5. d-wave superconductior from a quantum spin liquid
   with fermionic spinons

6. Fractionalized Fermi liquids (FL*)

5. *d*-wave superconductor and charge orders from a quantum spin liquid with fermionic spinons

We now turn to the fermionic spinon theory of an insulating square lattice spin liquid in Section 3. We wish to consider a more general situation in which the gap to charged excitations can vanish [Christos et al., 2024]. In the cuprates, gapless charged excitations appear when we dope the antiferromagnet. But we can also consider the case where the charge gap vanishes while the electronic density remains the same as in an insulator. In the latter case, there can be an emergent particle-hole symmetry, which simplifies considerations of quantum criticality. We can decrease the charge gap by describing the insulator by an underlying Hubbard model with on-site repulsion U, and reducing the value of U, or by adding additional off-site interactions. Such models have been considered in numerical studies [Assaad et al., 1996, Götz et al., 2022, Götz et al., 2024b, Götz et al., 2024a, Xu and Grover, 2021, Xing et al., 2021, Feng et al., 2022, Cai et al., 2021, Cai et al., 2022, Wang et al., 2025, Han and Kivelson, 2023, Cai et al., 2024]. We will now show that the SU(2) gauge theory of Eq. (87) has fates other than those in Fig. 16 once charged excitations are included, the most interesting of which is a d-wave superconductor with gapless nodal quasiparticles.

In terms of adiabatic continuity, this d-wave superconductor is precisely the BCS superconductor observed in the cuprates. However, the d-wave superconductor obtained in this section has one significant quantitative difference from the observations: it has a

Lorentz-invariant form of its dispersion, with the two velocities only the square lattice diagonals, v_F and v_Δ, being equal to each other (see Fig. 31B). The cuprates instead have $v_F \gg v_\Delta$. We will resolve this problem in an interesting manner in Section 6 when we consider the transition from FL* to a d-wave superconductor in the doped case.

The only matter field in Section 3 is the fermion $\mathcal{F}$, which has electrical charge 0, spin 1/2, and is a gauge SU(2) fundamental. As we are allowing for charged fluctuations, we need to define an electron operator, which has charge $-e$, spin 1/2, and is a gauge SU(2) singlet. This directly leads us to introducing a boson B which has charge $+e$, spin 0, and is a gauge SU(2) fundamental, so that a composite of $\mathcal{F}$ and B will have the same quantum numbers as the electron. We now show that this information is sufficient to deduce an effective action for B, and to reach our main conclusions. We will give a more microscopic definition of the field B in the doped case later near Eq. (131).

First, similar to Eq. (75), we introduce a matrix notation for the electron $\mathcal{C}$ and the boson B:

$$\mathcal{C}_{\boldsymbol{i}} \equiv \begin{pmatrix} c_{\boldsymbol{i}\uparrow} & -c_{\boldsymbol{i}\downarrow} \\ c^\dagger_{\boldsymbol{i}\downarrow} & c^\dagger_{\boldsymbol{i}\uparrow} \end{pmatrix}, \quad B_{\boldsymbol{i}} \equiv \begin{pmatrix} B_{1\boldsymbol{i}} \\ B_{2\boldsymbol{i}} \end{pmatrix}, \quad \mathcal{B}_{\boldsymbol{i}} \equiv \begin{pmatrix} B_{1\boldsymbol{i}} & -B^*_{2\boldsymbol{i}} \\ B_{2\boldsymbol{i}} & B^*_{1\boldsymbol{i}} \end{pmatrix}, \tag{112}$$

all of which obey the reality condition analagous to Eq. (76). Then we write the fact that the

electron operator is a composite of the boson B (the 'chargon') and the spinon $\mathcal{F}$ by

$$\mathcal{C}_{\boldsymbol{i}} \sim \mathcal{B}_{\boldsymbol{i}}^{\dagger}\, \mathcal{F}_{\boldsymbol{i}}\,. \tag{113}$$

In terms of the matrix components, we can write Eq. (113) as

$$c_{\boldsymbol{i}\alpha}^{\dagger} \sim B_{1\boldsymbol{i}} f_{\boldsymbol{i}\alpha}^{\dagger} + B_{2\boldsymbol{i}} \varepsilon_{\alpha\beta} f_{\boldsymbol{i}\beta}\,, \tag{114}$$

where $\varepsilon_{\alpha\beta}$ is the unit antisymmetric tensor for spin SU(2) in Eq. (24).
Now we can use Eq. (113) to determine the symmetry transformations of $\mathcal{B}$ from those of $\mathcal{F}$, using the fact the $\mathcal{C}$ is gauge invariant and transforms trivially under all symmetries. A boson with the same quantum numbers as our B has been considered in earlier work [Dagotto et al., 1988, Coleman and Andrei, 1989, Wen and Lee, 1996], but with an important difference. In the earlier work, the expectation value of $B^{\dagger}B$ was set to be equal to the doping density. That is not the case in our work, as the doping density also includes the density of fermionic holes (see Section 6).
The generalization of the SU(2) gauge transformation in Eq. (78) is

$$\begin{aligned} \mathcal{C}_{\boldsymbol{i}} \to \mathcal{C}_{\boldsymbol{i}} \qquad &, \quad \mathcal{F}_{\boldsymbol{i}} \to V_{\boldsymbol{i}}\, \mathcal{F}_{\boldsymbol{i}} \\ \mathcal{B}_{\boldsymbol{i}} \to V_{\boldsymbol{i}}\, \mathcal{B}_{\boldsymbol{i}} \qquad &, \quad U_{\boldsymbol{ij}} \to V_{\boldsymbol{i}}\, U_{\boldsymbol{ij}}\, V_{\boldsymbol{i}}^{\dagger}\,, \end{aligned} \tag{115}$$

while the generalization of the global SU(2) spin rotation in Eq. (79) is

$$\begin{aligned} \mathcal{C}_{\boldsymbol{i}} \to \mathcal{C}_{\boldsymbol{i}}\, \sigma^z R^T \sigma^z \quad &, \quad \mathcal{F}_{\boldsymbol{i}} \to \mathcal{F}_{\boldsymbol{i}}\, \sigma^z R^T \sigma^z \\ \mathcal{B}_{\boldsymbol{i}} \to \mathcal{B}_{\boldsymbol{i}} \quad &, \quad U_{\boldsymbol{ij}} \to U_{\boldsymbol{ij}}\,. \end{aligned} \tag{116}$$

Finally, the U(1) charge conservation symmetry acts as

$$\begin{aligned} \mathcal{C}_{\boldsymbol{i}} \to \Theta\, \mathcal{C}_{\boldsymbol{i}} \quad &, \quad \mathcal{F}_{\boldsymbol{i}} \to \mathcal{F}_{\boldsymbol{i}} \\ \mathcal{B}_{\boldsymbol{i}} \to \mathcal{B}_{\boldsymbol{i}}\, \Theta^\dagger \quad &, \quad U_{\boldsymbol{ij}} \to U_{\boldsymbol{ij}}\,, \end{aligned} \tag{117}$$

where

$$\Theta = \begin{pmatrix} e^{i\theta} & 0 \\ 0 & e^{-i\theta} \end{pmatrix}. \tag{118}$$

See also Table 2 later for a summary of these gauge and symmetry transformations.
We now obtain an energy functional for B in a Landau-type expansion [Christos et al., 2023]. Such a functional must also involve the gauge field $U_{\boldsymbol{ij}}$ of Section 3 to maintain gauge invariance. The fermion f experiences a π flux with pure imaginary hopping, while the electron c has purely real hopping with zero flux (in the absence of an applied physical magnetic field).

From these facts and Eq. (113) we reach the important conclusion that the boson B must also have purely imaginary hopping with π-flux (the iw term in Eq. (120) below). So the relation

$$T_x T_y = -T_y T_x \,, \tag{119}$$

realizing the π-flux applies both to the spinons and to B. We can also reach these conclusions, and obtain other constraints, by examining the action of all symmetry operators of f, and use Eq. (113) to deduce the action of symmetry operations on B: the results are summarized in Table 1.

Symmetry	f_α	B_a
T_x	$(-1)^y f_\alpha$	$(-1)^y B_a$
T_y	f_α	B_a
P_x	$(-1)^x f_\alpha$	$(-1)^x B_a$
P_y	$(-1)^y f_\alpha$	$(-1)^y B_a$
P_{xy}	$(-1)^{xy} f_\alpha$	$(-1)^{xy} B_a$
$\mathcal{T}$	$(-1)^{x+y} \varepsilon_{\alpha\beta} f_\beta$	$(-1)^{x+y} B_a$

Table 1: Projective transformations of the f spinons and B chargons on lattice sites $\boldsymbol{i} = (x, y)$ under the symmetries $T_x : (x, y) \to (x+1, y)$; $T_y : (x, y) \to (x, y+1)$; $P_x : (x, y) \to (-x, y)$;

$P_y : (x, y) \to (x, -y)$; $P_{xy} : (x, y) \to (y, x)$; and time-reversal $\mathcal{T}$. The indices α, β refer to global SU(2) spin, while the index $a = 1, 2$ refers to gauge SU(2).

These considerations lead to the energy functional $\mathcal{E}_2[B, U] + \mathcal{E}_4[B, U]$ with terms quadratic and quartic in B respenctively:

$$\begin{aligned}
\mathcal{E}_2[B,U] &= (r + 2\sqrt{2}w) \sum_{\boldsymbol{i}} B^\dagger_{\boldsymbol{i}} B_{\boldsymbol{i}} + iw \sum_{\langle \boldsymbol{ij} \rangle} e_{\boldsymbol{ij}} \left(B^\dagger_{\boldsymbol{i}} U_{\boldsymbol{ij}} B_{\boldsymbol{j}} - B^\dagger_{\boldsymbol{j}} U_{\boldsymbol{ji}} B_{\boldsymbol{i}} \right) \\
&\quad + \kappa \sum_{\square} \left\{ 1 - \frac{1}{2} \mathrm{ReTr} \prod_{\boldsymbol{ij} \in \square} U_{\boldsymbol{ij}} \right\} \\
\mathcal{E}_4[B,U] &= \frac{u}{2} \sum_{\boldsymbol{i}} \rho^2_{\boldsymbol{i}} + V_1 \sum_{\boldsymbol{i}} \rho_{\boldsymbol{i}} \left(\rho_{\boldsymbol{i}+\hat{\boldsymbol{x}}} + \rho_{\boldsymbol{i}+\hat{\boldsymbol{y}}} \right) + g \sum_{\langle \boldsymbol{ij} \rangle} \left| \Delta_{\boldsymbol{ij}} \right|^2 + J_1 \sum_{\langle \boldsymbol{ij} \rangle} Q^2_{\boldsymbol{ij}} \\
&\quad + K_1 \sum_{\langle \boldsymbol{ij} \rangle} J^2_{\boldsymbol{ij}} + V_{11} \sum_{\boldsymbol{i}} \rho_{\boldsymbol{i}} \left(\rho_{\boldsymbol{i}+\hat{\boldsymbol{x}}+\hat{\boldsymbol{y}}} + \rho_{\boldsymbol{i}+\hat{\boldsymbol{x}}-\hat{\boldsymbol{y}}} \right) \\
&\quad + V_{22} \sum_{\boldsymbol{i}} \rho_{\boldsymbol{i}} \left(\rho_{\boldsymbol{i}+2\hat{\boldsymbol{x}}+2\hat{\boldsymbol{y}}} + \rho_{\boldsymbol{i}+2\hat{\boldsymbol{x}}-2\hat{\boldsymbol{y}}} \right) \ . \qquad (120)
\end{aligned}$$

The quartic terms are expressed as products of bilinears of B which are associated with various gauge-invariant observables as identified below

$$
\begin{aligned}
&\text{site charge density: } \left\langle c^\dagger_{i\alpha} c_{i\alpha} \right\rangle \sim \rho_i = B^\dagger_i B_i \\
&\text{bond density: } \left\langle c^\dagger_{i\alpha} c_{j\alpha} + c^\dagger_{j\alpha} c_{i\alpha} \right\rangle \sim Q_{ij} = Q_{ji} = \mathrm{Im}\left(B^\dagger_i e_{ij} U_{ij} B_j \right) \\
&\text{bond current: } i\left\langle c^\dagger_{i\alpha} c_{j\alpha} - c^\dagger_{j\alpha} c_{i\alpha} \right\rangle \sim J_{ij} = -J_{ji} = \mathrm{Re}\left(B^\dagger_i e_{ij} U_{ij} B_j \right) \\
&\text{Pairing: } \left\langle \varepsilon_{\alpha\beta} c_{i\alpha} c_{j\beta} \right\rangle \sim \Delta_{ij} = \Delta_{ji} = \varepsilon_{ab} B_{ai} e_{ij} U_{ij} B_{bj} \, .
\end{aligned}
\tag{121}
$$

We have retained terms involving nearest neighbor sites, and a few terms with longer-range density-density interactions.

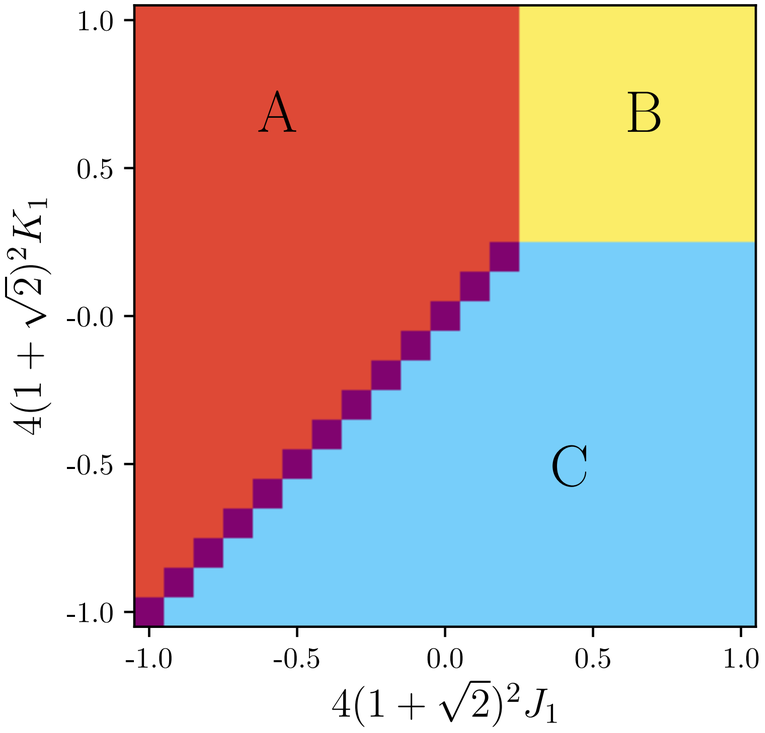

$\langle B \rangle \neq 0$

Including only nearest-neighbor couplings in B

$\langle B \rangle = 0$

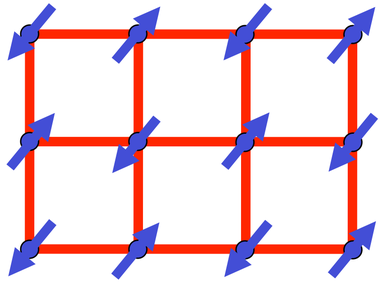

Confining phase: Néel order

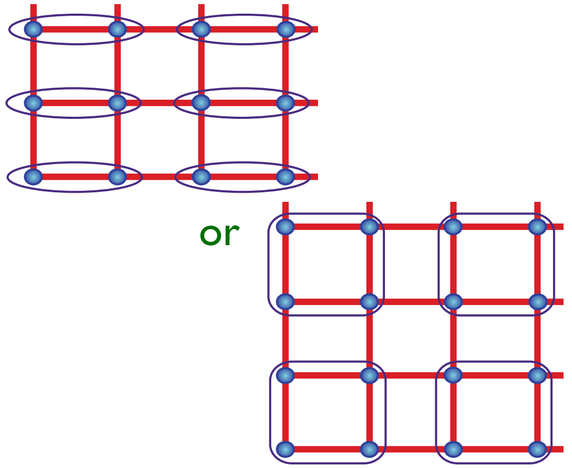

Confining phase: VBS order

s

r

Phase B
d-wave SC

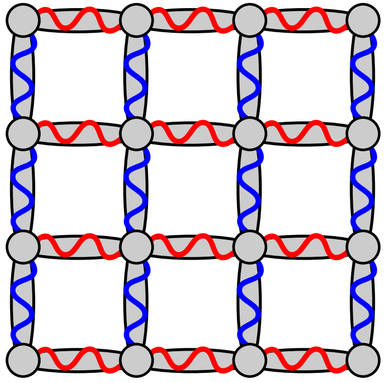

Phase C
d-density

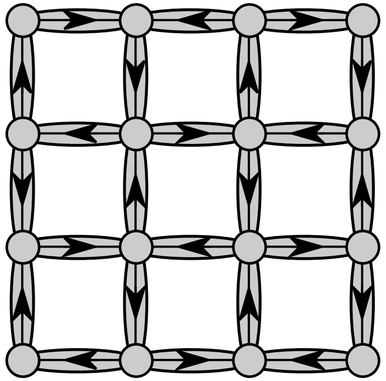

Phase A
(π,0) stripe

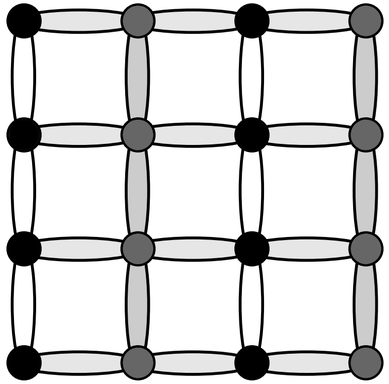

Phase A
(0,π) stripe

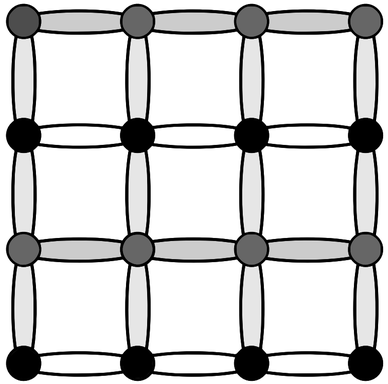

Figure 20: Mean field phase diagram obtained by minimization of the Higgs potential of B, $\mathcal{E}_2 + \mathcal{E}_4$ (from Ref. [Christos et al., 2023]). For $r > 0$, there is no Higgs condensate $\langle B \rangle = 0$, and we obtain the same phases as in the insulator from the confinement of the fermionic spinons described by Eq. (87). For $r < 0$, $\langle B \rangle \neq 0$, and we minimized the Higgs potential with only nearest neighbor interactions by setting $V_{11} = V_{22} = 0$.

A schematic global phase diagram is shown in Fig. 20, as a function of the tuning parameter r, which is the 'mass' of B.

When r is large and positive, then we can ignore the B sector, and revert to the spinon only theory of Section 3. The low energy theory is Eq. (94), and we expect a confining insulator with either Néel or VBS order as the ground state.

When r is negative, B condenses, and this has the salutary effect of making the gauge field A massive, as in the Higgs phenomenon. In this case, a mean-field treatment of interactions in the bosonic sector by minimizing $\mathcal{E}_2[B, U] + \mathcal{E}_4[B, U]$ is qualitatively valid.

For negative r, Fig. 20 shows the phases obtained by minimizing the energy functional with nearest-neighbor interactions only, $V_{11} = V_{22} = 0$. Three phases are found:

A. This state has charge stripe order with period 2, centered on the sites.

B. A d-wave superconductor, with $\Delta_{\boldsymbol{i},\boldsymbol{i}+\hat{\boldsymbol{x}}} = -\Delta_{\boldsymbol{i},\boldsymbol{i}+\hat{\boldsymbol{y}}}$.

C. A "d-density wave" state which has a staggered pattern of spontaneous current.

Including further neighbor interactions can induce other phases, including period-4 charge order and pair density waves [Christos et al., 2023, Bonetti et al., 2024, Pandey et al., 2025]), as shown in Fig. 21.

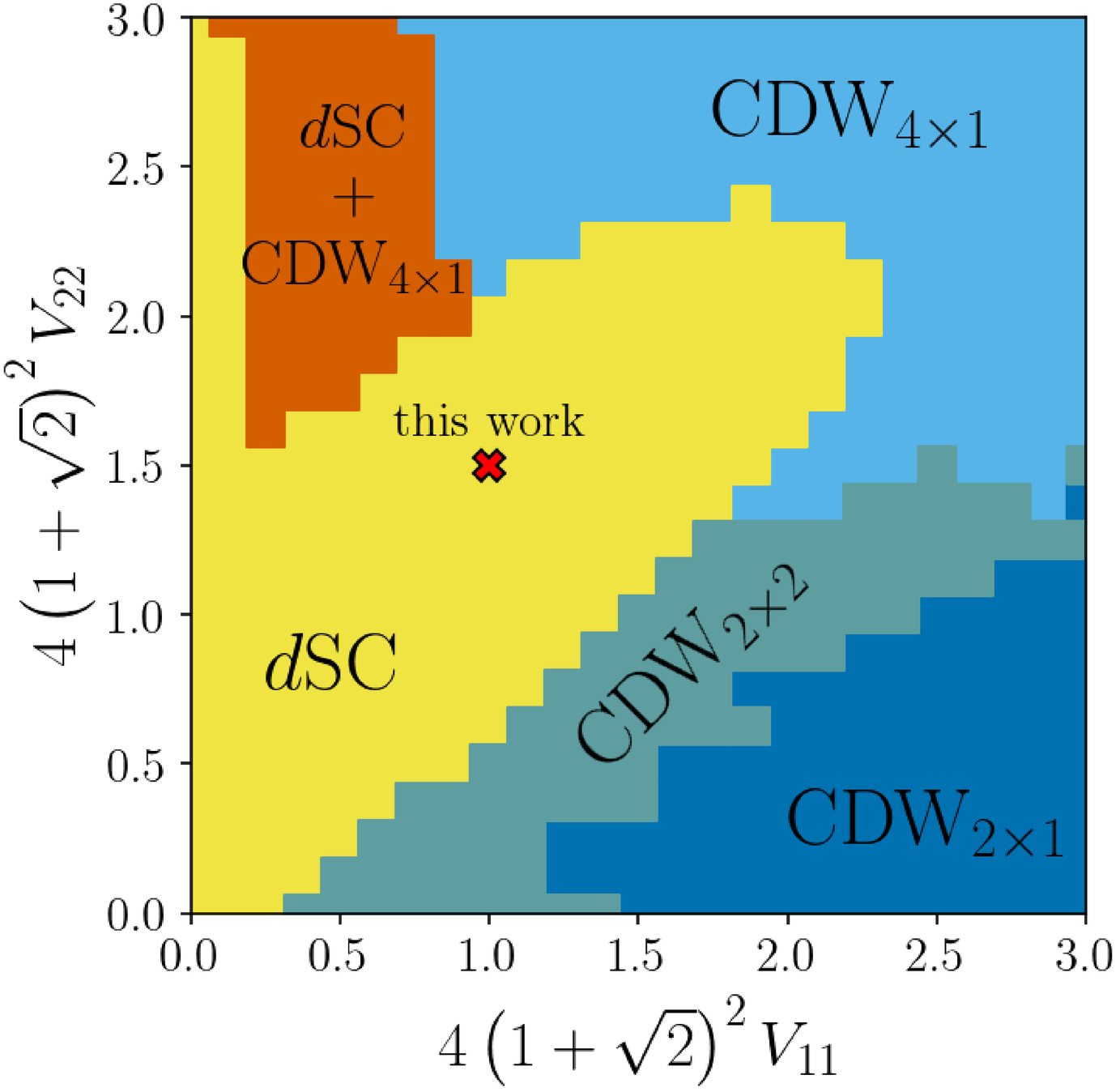
dSC
+
CDW$_{4\times1}$
CDW$_{4\times1}$
this work
dSC
CDW$_{2\times2}$
CDW$_{2\times1}$
3.0
2.5
2.0
1.5
1.0
0.5
0.0
0.0
0.5
1.0
1.5
2.0
2.5
3.0
$4\left(1+\sqrt{2}\right)^2 V_{22}$
$4\left(1+\sqrt{2}\right)^2 V_{11}$

Figure 21: From Ref. [Pandey et al., 2025]. Mean-Field phase diagram of Eq. (120) a function of the further neighbor interactions V_{11} and V_{22}, extending that in Fig. 20. The other parameters are $r = -0.732$, $w = 0.40$, $u = 0$, $V_1 = 0$, $g = 0.021446$, $J_1 = K_1 = 2/(4(1+\sqrt{2})^2)$. dSC is d-wave superconductivity, CDW$_{n\times m}$ is a charge density wave with a supercell with $n \times m$ lattice sites. The red cross marks the parameter values chosen for the Monte Carlo simulations in Ref. [Pandey et al., 2025].

An interesting feature is that these orders are degenerate in the quadratic energy functional $\mathcal{E}_2$, and the degeneracy is broken only at quartic order in $\mathcal{E}_4$. The fact that the leading term is degenerate provides a rationale for nearly-degenerate multiple competing or 'intertwined' orders [Christos et al., 2023]; more conventional Landau theory approaches [Jaefari et al., 2010, Hayward et al., 2014, Lee, 2014, Nie et al., 2015, Fradkin et al., 2015, Pépin and Freire, 2023, Fradkin, 2025] do not have any term in which the degeneracy is exact without fine-tuning.

Our primary interest for now is the d-wave supercondutor, phase B. Remarkably, the structure of the π-flux spin liquid, and consequently the π-flux on B leads to d-wave pairing, and not s-wave pairing. Also, once B is condensed, we can identify $c \sim f$ via Eq. (113), and so the electron spectral function will inherit nodal Bogoliubov quasiparticles from the massless Dirac spinons. The main phenomenological difficulty is that the Bogoliubov quasiparticles will have isotropic dispersion, as in Eq. (84) and Fig. 18; we will address this difficulty in Section 6.

However, other features of the d-wave state obtained from the energy functional in Eq. (120) do match observations, including vortices with flux $h/(2e)$ (despite the boson B having charge e), and competing charge order halos of vortex cores.
Going beyond a classical treatment of B and U, we need to consider a quantum lattice model to study the interplay of the full array of competing order parameters and deconfined criticality. This is obtained by extending the energy functionals in Eq. (120) and the lattice fermion theory in Eq. (87) to

$$\mathcal{L} = \sum_{\boldsymbol{i}} |D_\tau B_{\boldsymbol{i}}|^2 + \mathcal{E}_2[B, U] + \mathcal{E}_4[B, U] + \sum_{\boldsymbol{i}} \Psi^\dagger_{\boldsymbol{i}} D_\tau \Psi_{\boldsymbol{i}} + \mathcal{H}_{SLf} + \mathcal{L}_{YM}[U] \,. \tag{122}$$

Here D_τ represents a covariant time derivative with the SU(2) gauge field U, and $\mathcal{L}_{YM}$ is the lattice Yang-Mills Lagrangian for U. We have added only a relativistic time derivative term for $\hat{B}$, which is the allowed term at half-filling with particle-hole symmetry. Away from half-filling, we will also have to include the hole pockets to be discussed in Section 6, and that will likely lead to difficulties with the sign problem.

1. Spin density wave order in the Hubbard model

2. Bosonic spinon theory of quantum spin liquids

3. Fermionic spinon theory of quantum spin liquids

4. Holon metal from a quantum spin liquid
   with bosonic spinons

5. d-wave superconductior from a quantum spin liquid
   with fermionic spinons

6. Fractionalized Fermi liquids (FL*)

Fractionalized Fermi liquids (FL*)

Doping the $\mathbb{CP}^1$ spin liquid yields a holon metal state described in Section 4, which is a candidate for the pseudogap metal. However, as we will discuss below, the holon metal is incompatible with recent angle-dependent magnetoresistance (ADMR) experiments [Fang et al., 2022, Chan et al., 2025].

Doping the fermionic spin liquid can lead to a d-wave superconductor, as described in Section 5. However, the velocities of the nodal quasiparticles are nearly isotropic, with $v_F \sim v_\Delta$.

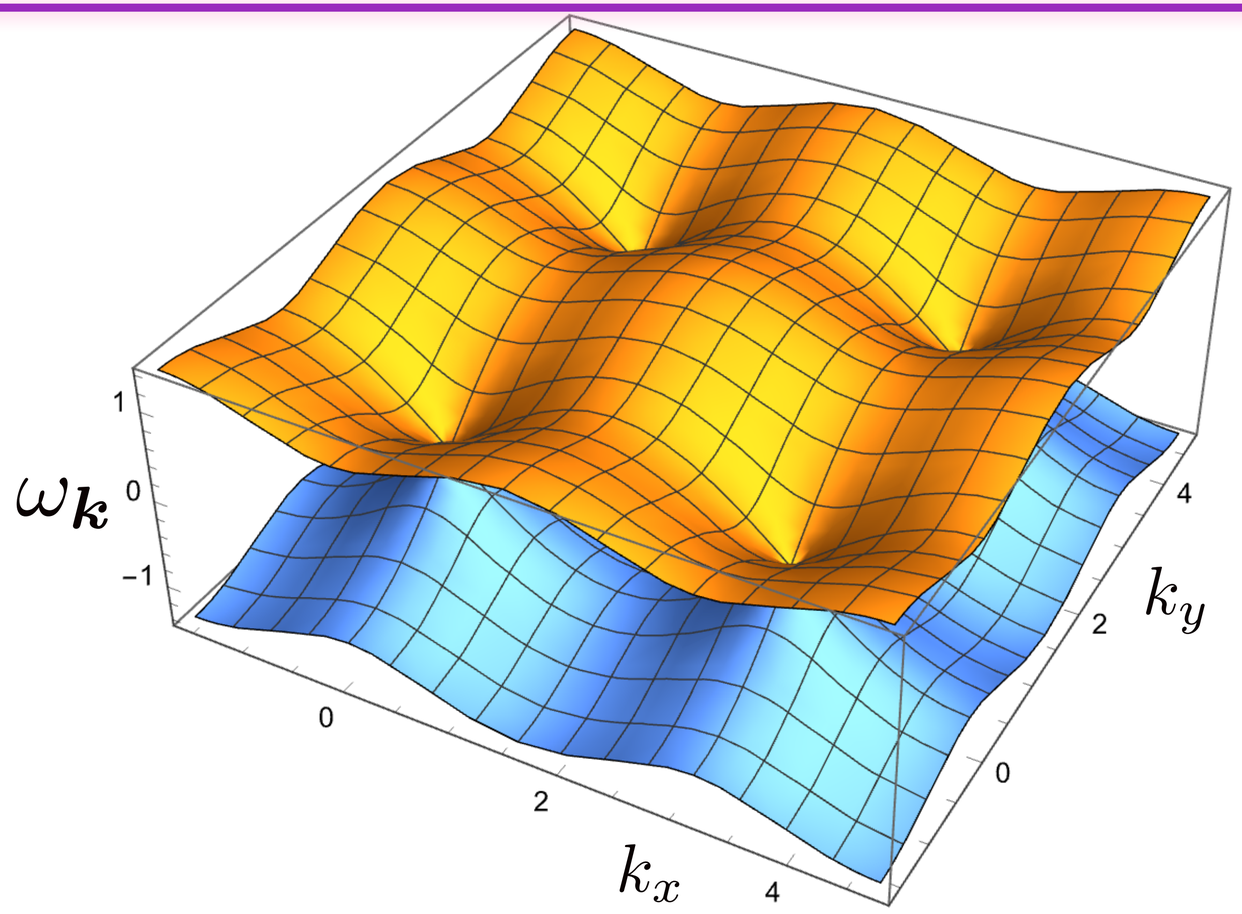

Figure 18: Dispersion of fermionic spinons in Eq. (85).

We now show that replacing the holon metal with another doped spin liquid phase, the fractionalized Fermi liquid (FL*), resolves both (and other) difficulties above. It agrees with the ADMR measurements in the pseudogap, and a confinement transition from FL* yields a d-wave superconductor with anisotropic nodal velocities.

Fermi liquid

Spin-1/2 holes of density
$\rho = 1 + p$

Positive Hall coefficient
of carrier density ρ

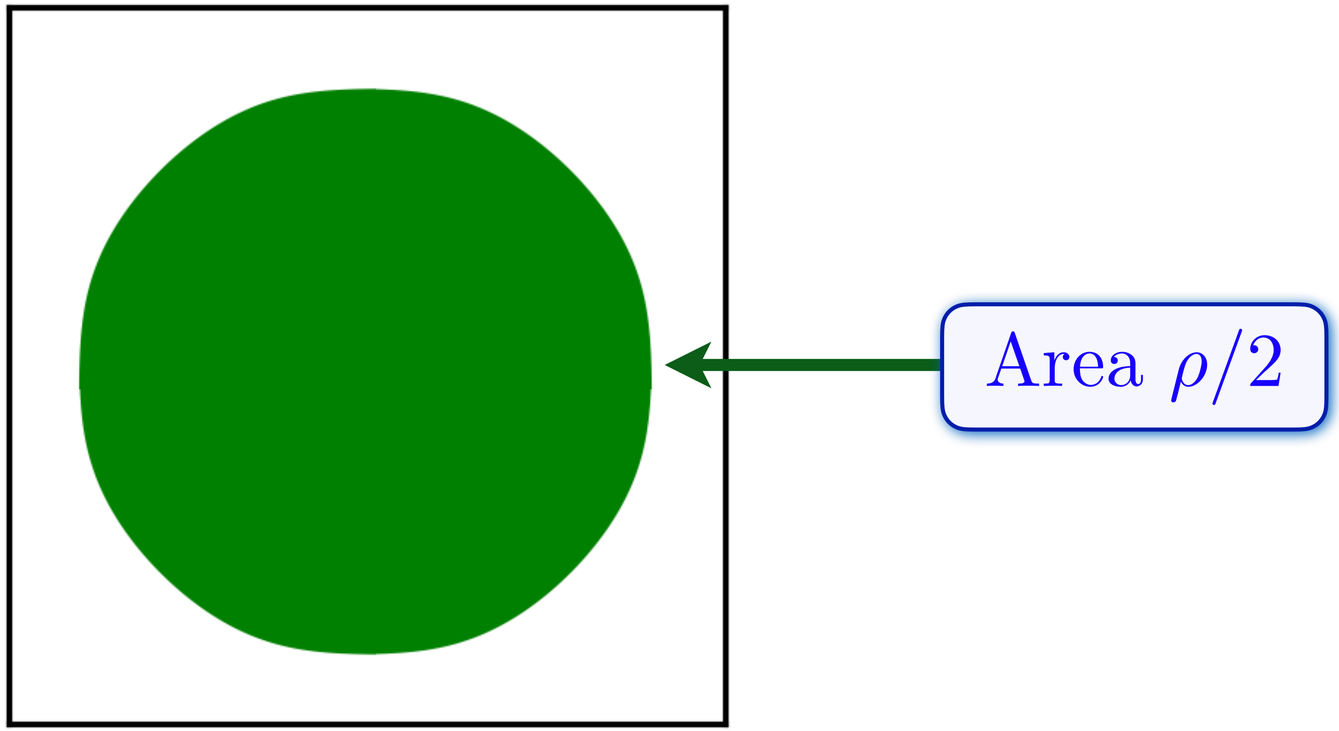

Luttinger, 1960: Area enclosed by the Fermi surface is the same as that for free fermions *with the same symmetry.*

Fermi liquid

Spin-1/2 holes of density
$\rho = 1 + p$

Positive Hall coefficient
of carrier density ρ

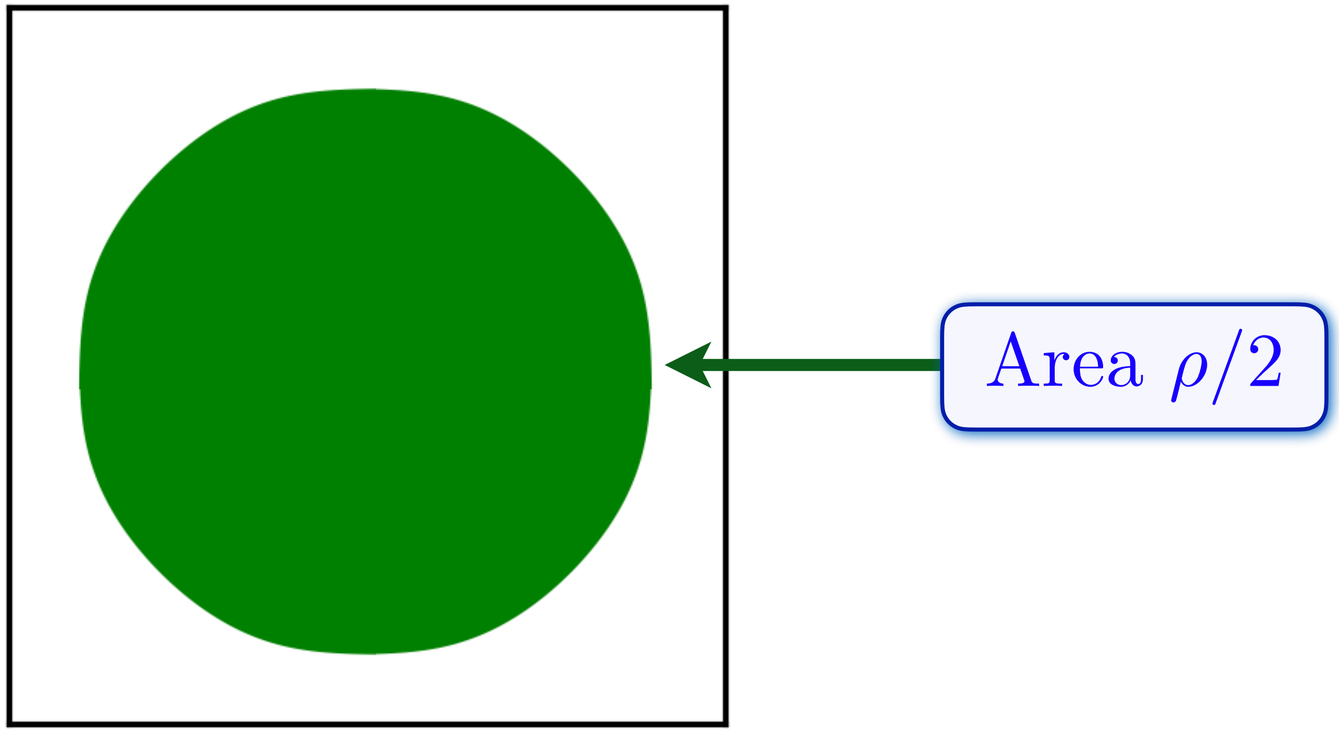

Luttinger, 1960: Area enclosed by the Fermi surface is the same as that for free fermions *with the same symmetry.*

Oshikawa, 2000: Area constrained by a 't Hooft anomaly of global U(1) and translations

Fractionalized Fermi liquid (FL*)

Spin-1/2 holes of density
$\rho = 1 + p$

Positive Hall coefficient
of carrier density $\rho - 1$

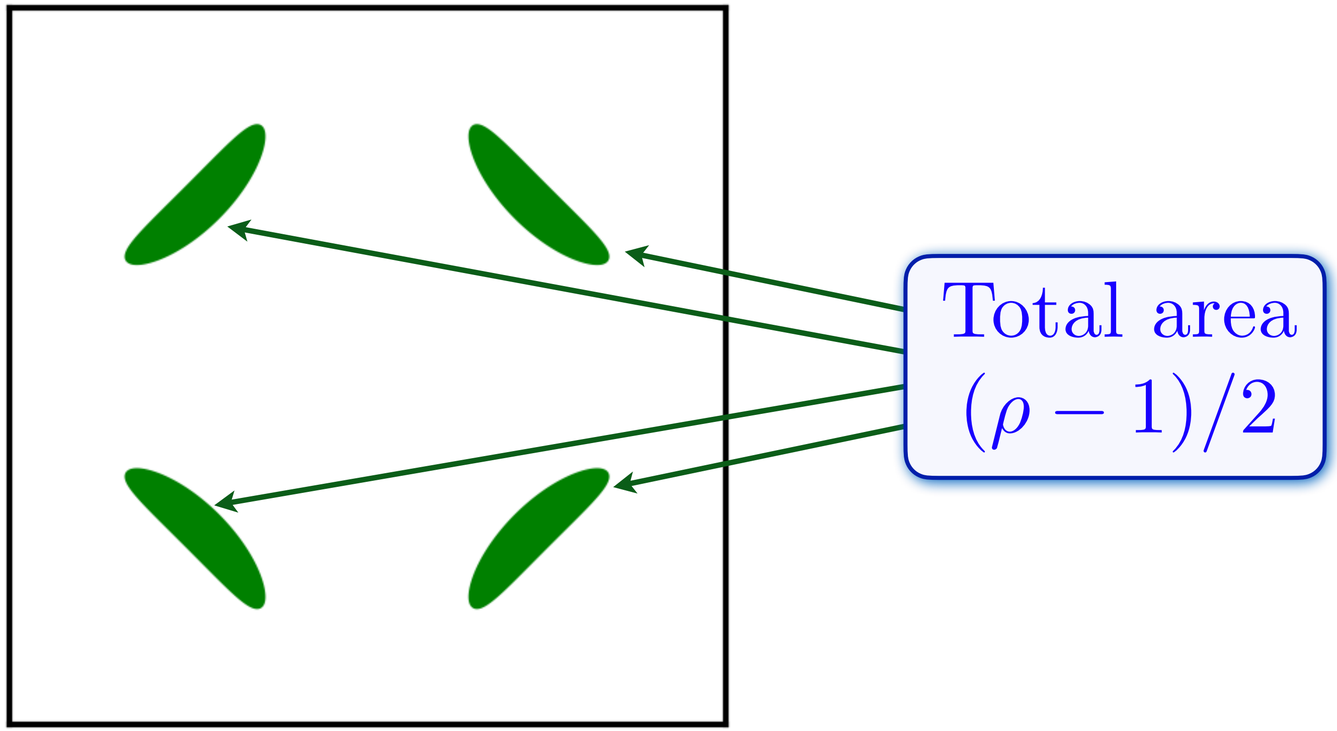

Oshikawa anomaly is satisfied by the sum of
spin liquid (1) and
Fermi surface anomalies $(\rho - 1)$

T. Senthil, S. S., M. Vojta, PRL **90**, 216403 (2003); T. Senthil, M. Vojta, and S. S., PRB **69**, 035111 (2004)

Doping an insulating antiferromagnet with holes of density p

Holon metal

Spin liquid with density p of spinless, charge $+e$ holons. No coherent inter-layer transport, so no Yamaji effect.

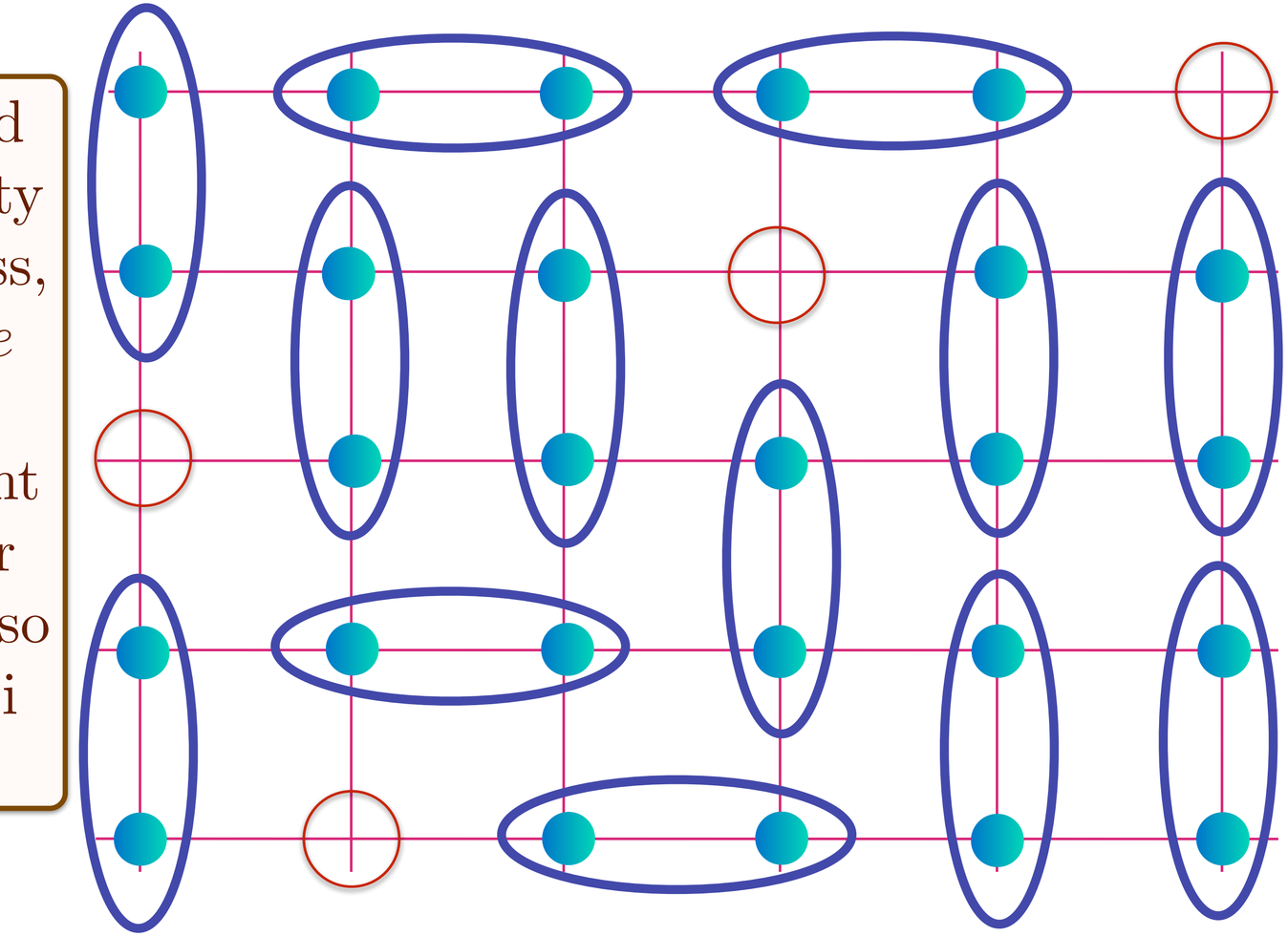

$= (|\uparrow\downarrow\rangle - |\downarrow\uparrow\rangle)/\sqrt{2}$

Oshikawa anomaly is satisfied by sum of spin liquid (1) and Fermi surface anomalies (p)

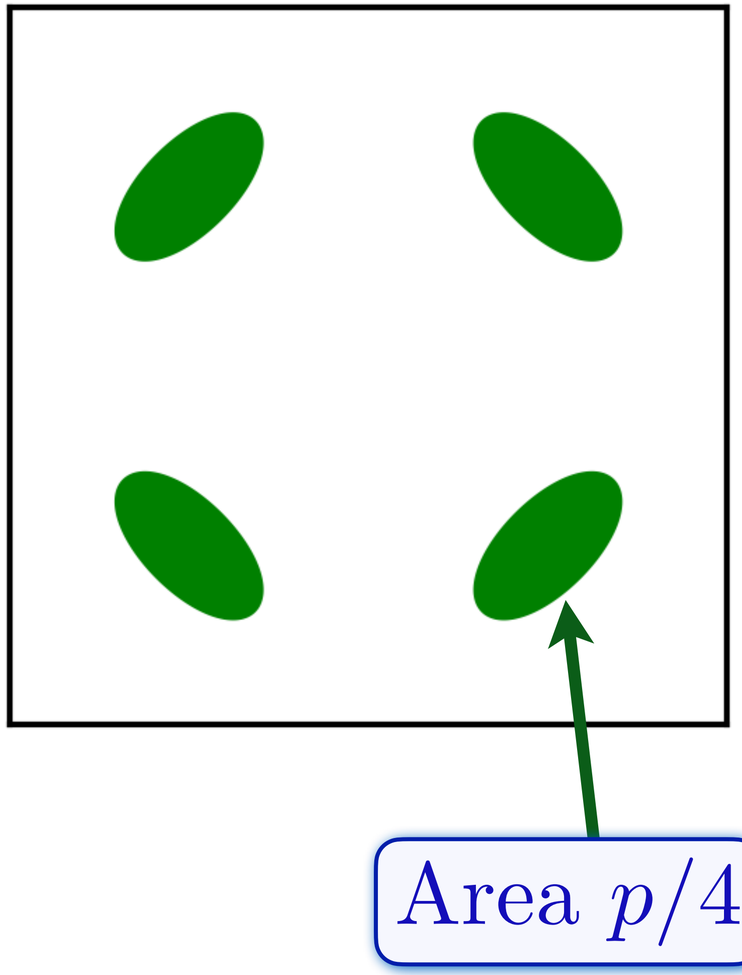

R. K. Kaul, Y. B. Kim, S. S., T. Senthil, Nature Physics **4**, 28 (2008)

Doping an insulating antiferromagnet with holes of density p

Holon metal

Spin liquid with density p of spinless, charge $+e$ holons. No coherent inter-layer transport, so no Yamaji effect.

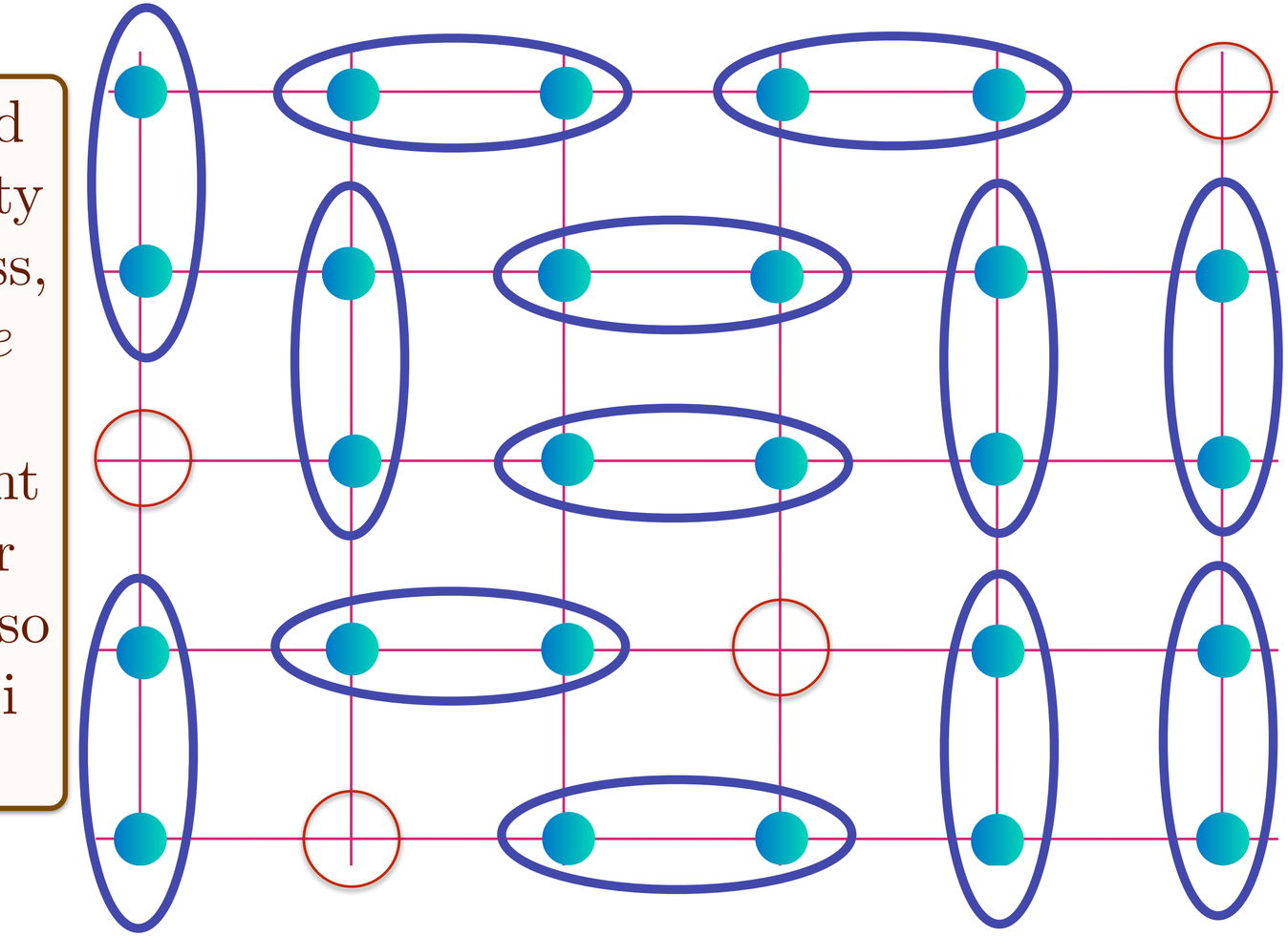

$$= \left(|\uparrow\downarrow\rangle - |\downarrow\uparrow\rangle\right)/\sqrt{2}$$

Oshikawa anomaly is satisfied by sum of spin liquid (1) and Fermi surface anomalies (p)

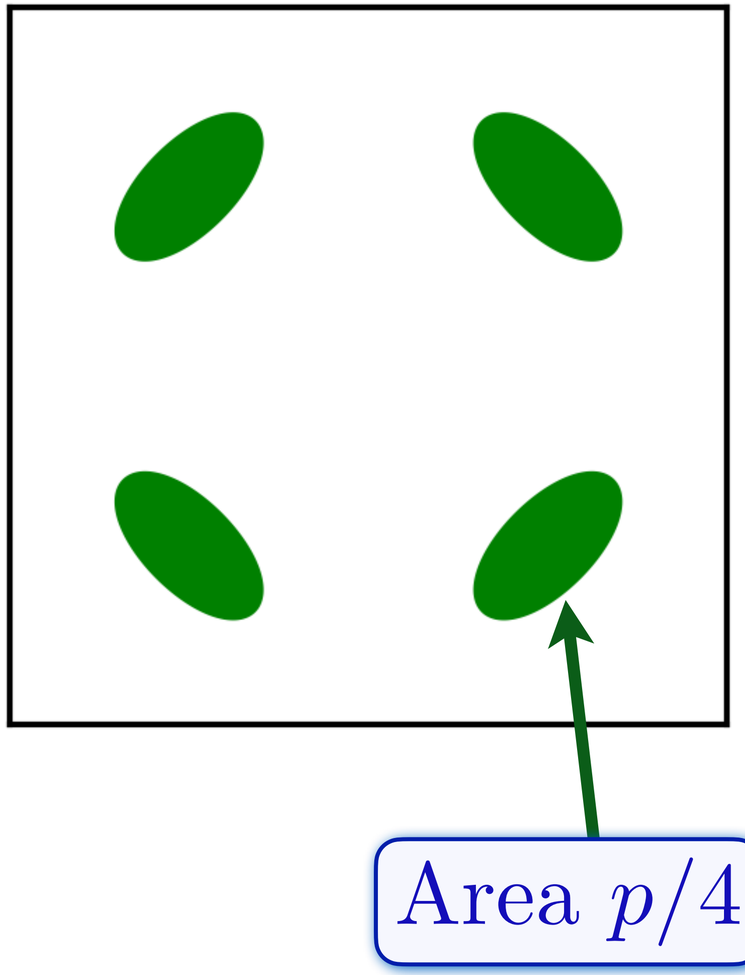

R. K. Kaul, Y. B. Kim, S. S., T. Senthil, Nature Physics **4**, 28 (2008)

Doping an insulating antiferromagnet with holes of density p

Holon metal excited states

Oshikawa anomaly is satisfied by sum of spin liquid (1) and Fermi surface anomalies (p)

Charge 0, spin-1/2 spinons

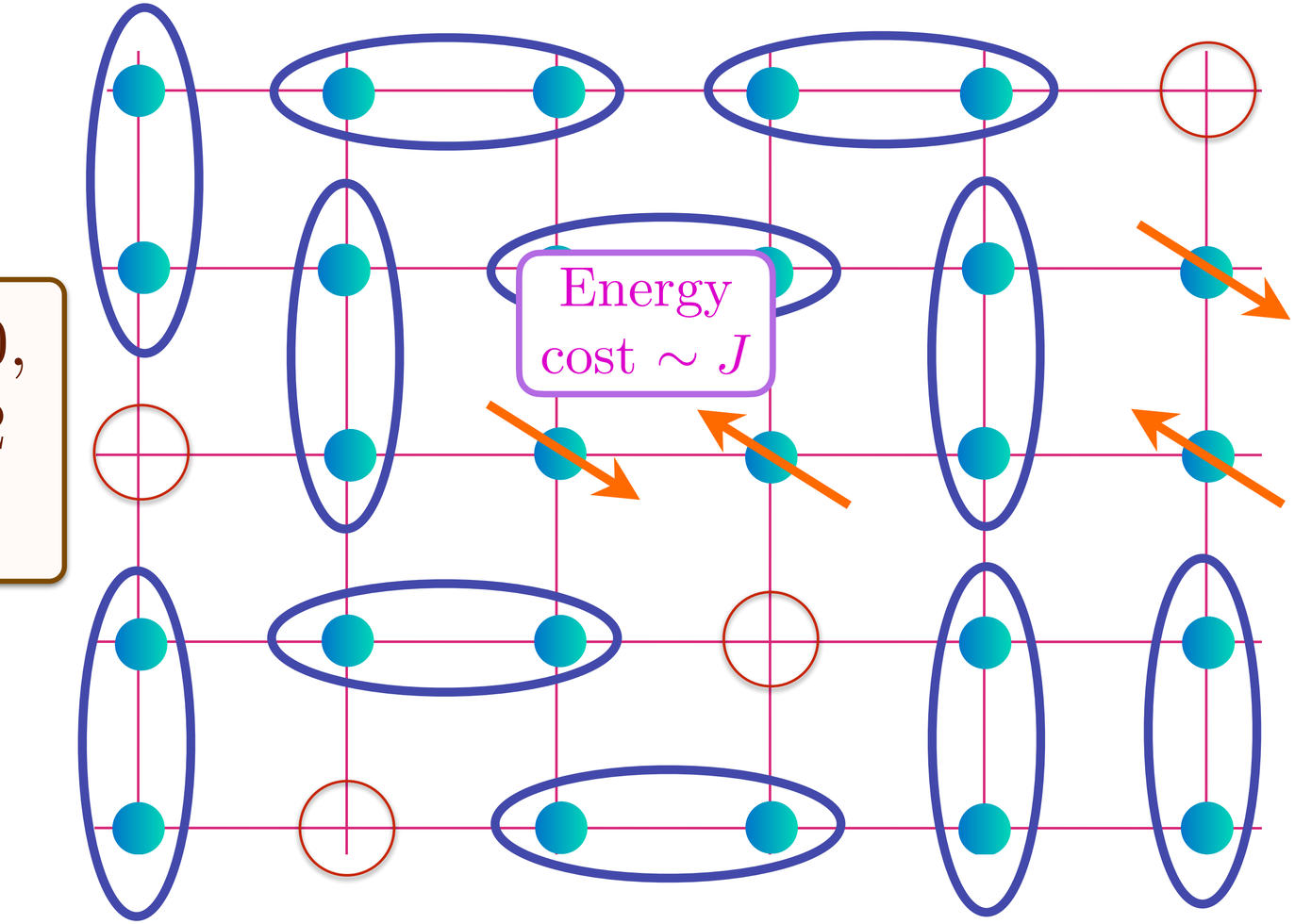

$= (|\uparrow\downarrow\rangle - |\downarrow\uparrow\rangle)/\sqrt{2}$

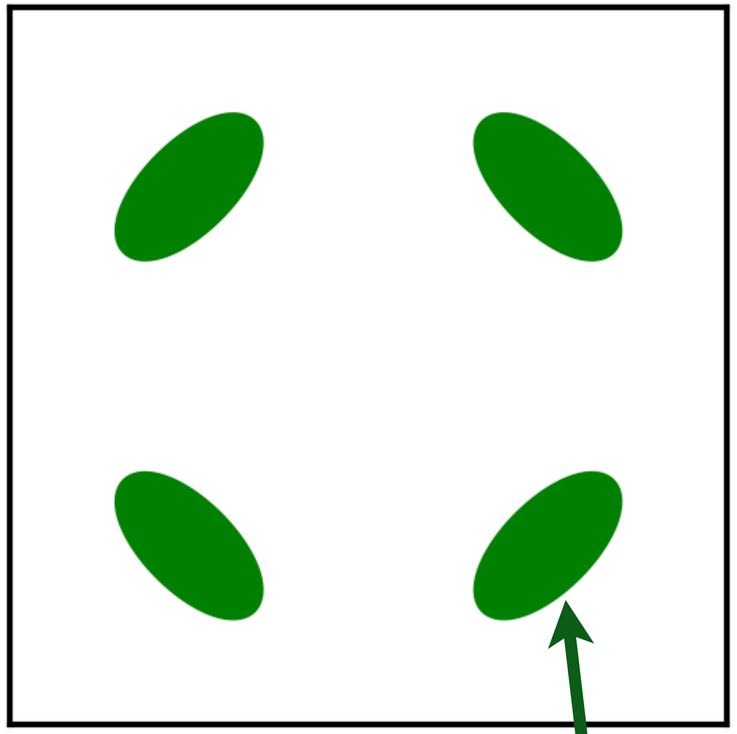

Area $p/4$

Doping an insulating antiferromagnet with holes of density p

Holon metal excited states

Oshikawa anomaly is satisfied by sum of spin liquid (1) and Fermi surface anomalies (p)

Charge 0, spin-1/2 spinons

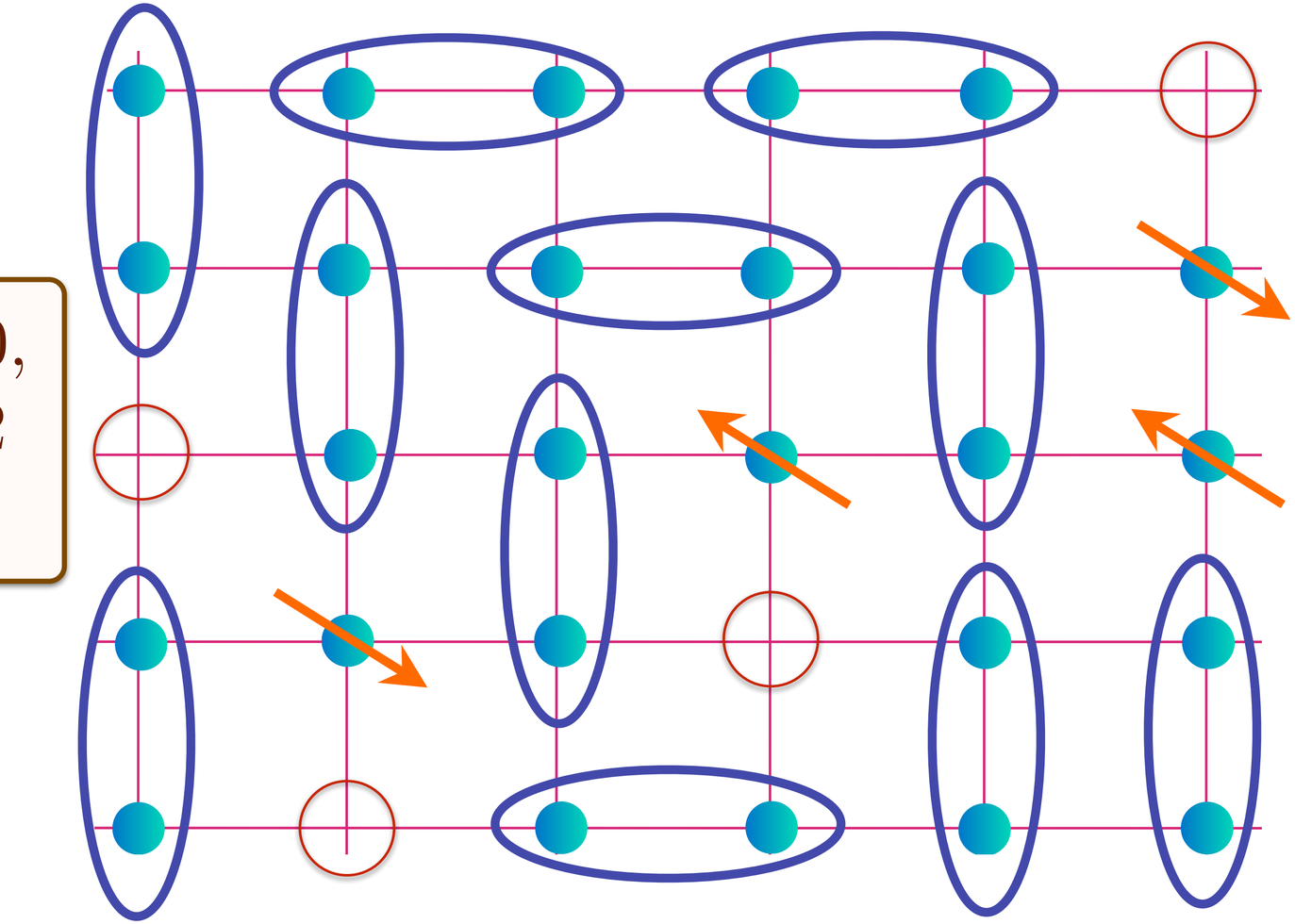

$= (|\uparrow\downarrow\rangle - |\downarrow\uparrow\rangle)/\sqrt{2}$

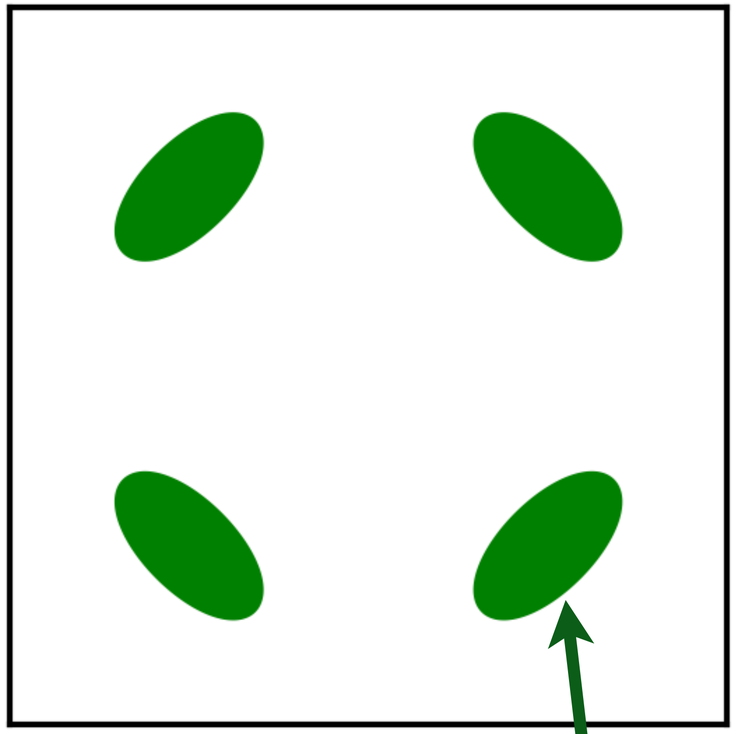

Area $p/4$

Doping an insulating antiferromagnet with holes of density p

Holon metal excited states

Oshikawa anomaly is satisfied by sum of spin liquid (1) and Fermi surface anomalies (p)

Charge 0, spin-1/2 spinons

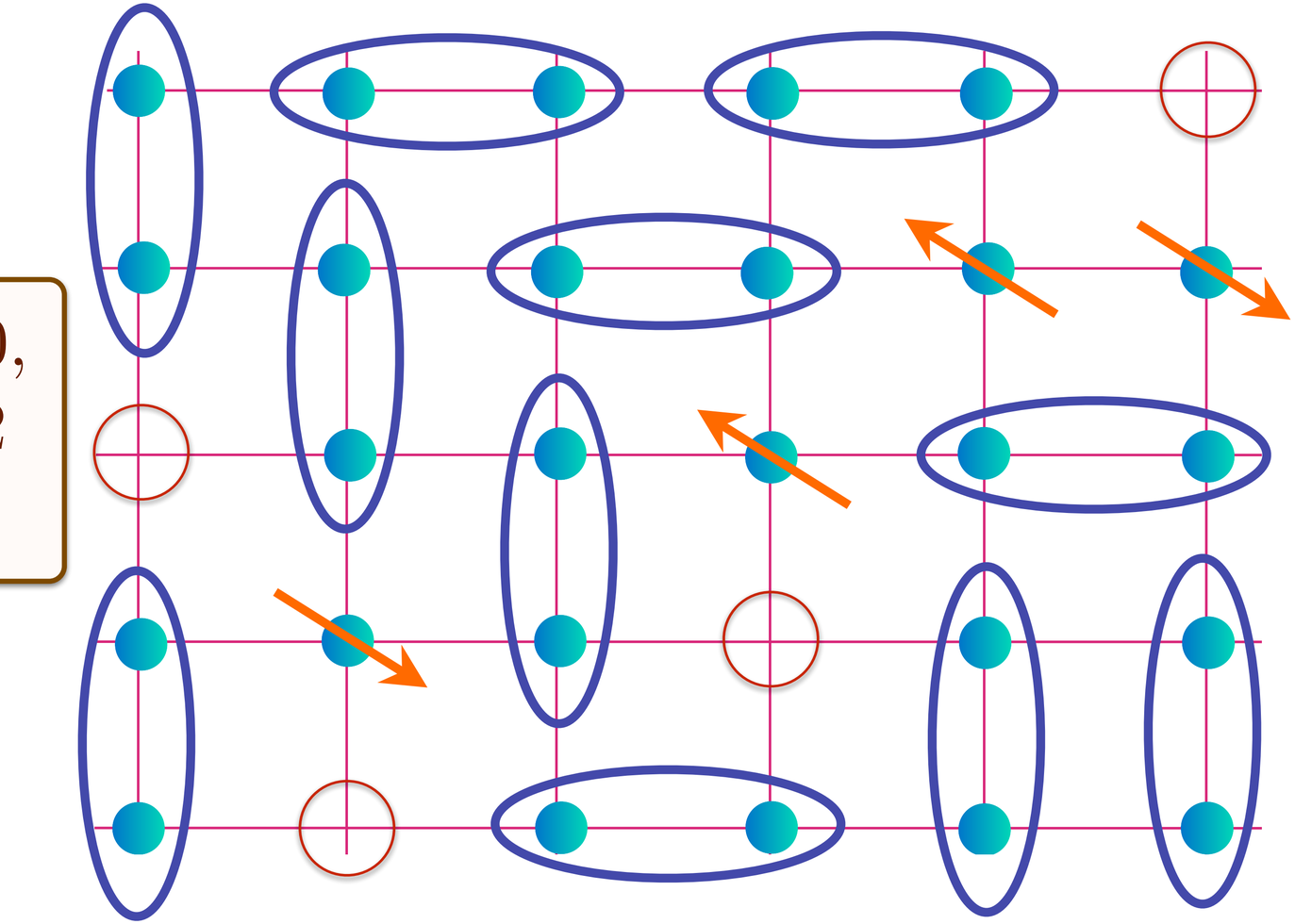

$= (|\uparrow\downarrow\rangle - |\downarrow\uparrow\rangle)/\sqrt{2}$

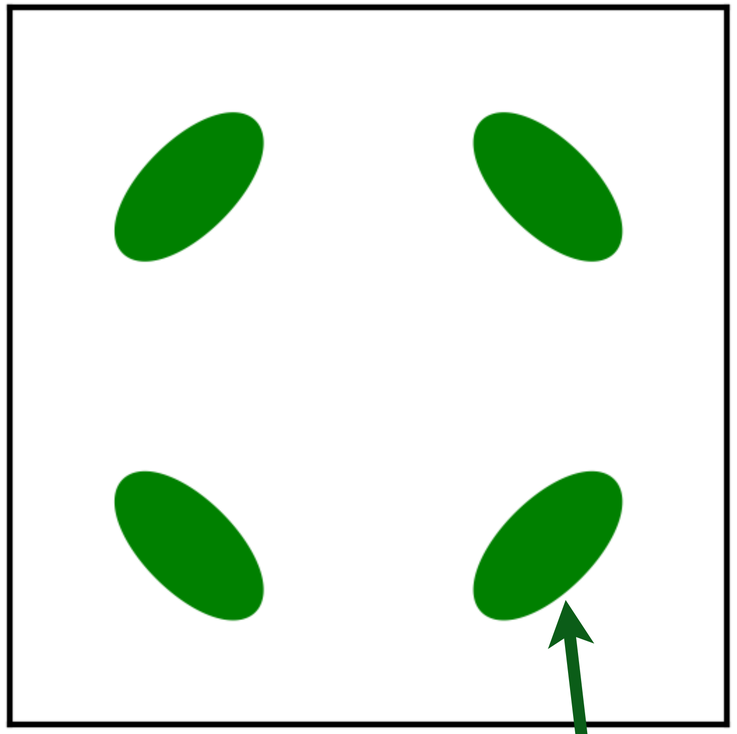

Area $p/4$

Doping an insulating antiferromagnet with holes of density p

Holon metal excited states

Oshikawa anomaly is satisfied by sum of spin liquid (1) and Fermi surface anomalies (p)

Charge 0, spin-1/2 spinons

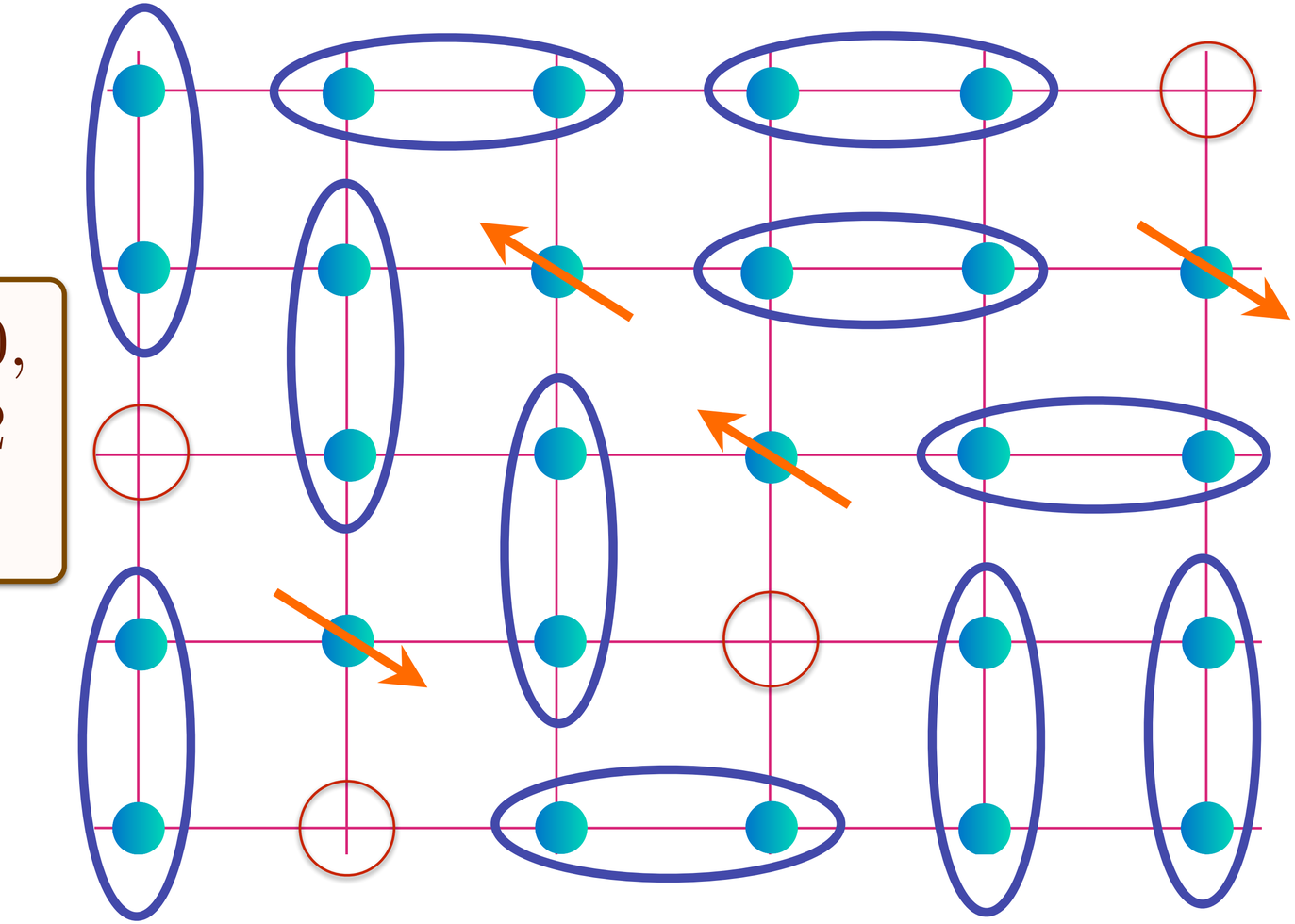

$= (|\uparrow\downarrow\rangle - |\downarrow\uparrow\rangle)/\sqrt{2}$

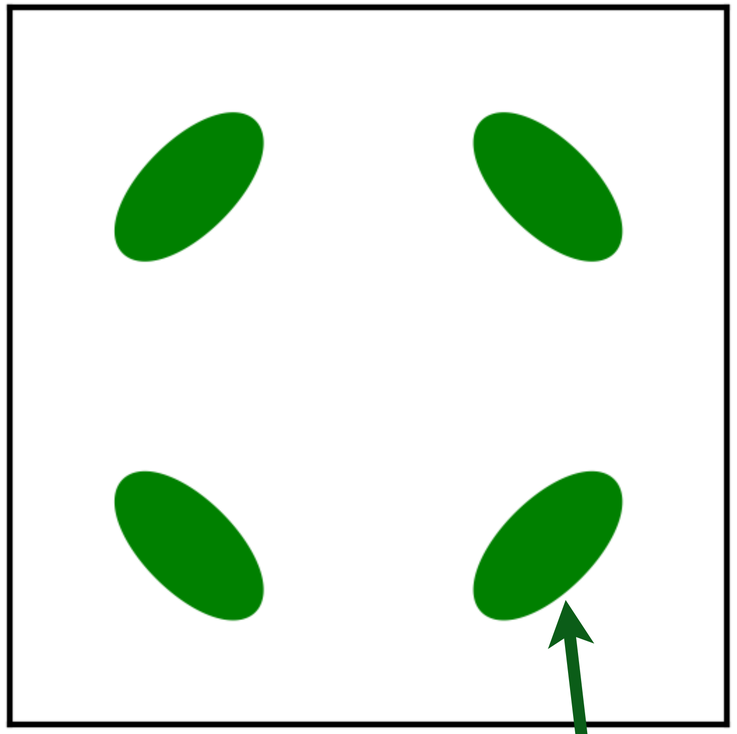

Area $p/4$

Doping an insulating antiferromagnet with holes of density p

Holon metal excited states

Oshikawa anomaly is satisfied by sum of spin liquid (1) and Fermi surface anomalies (p)

Charge 0, spin-1/2 spinons

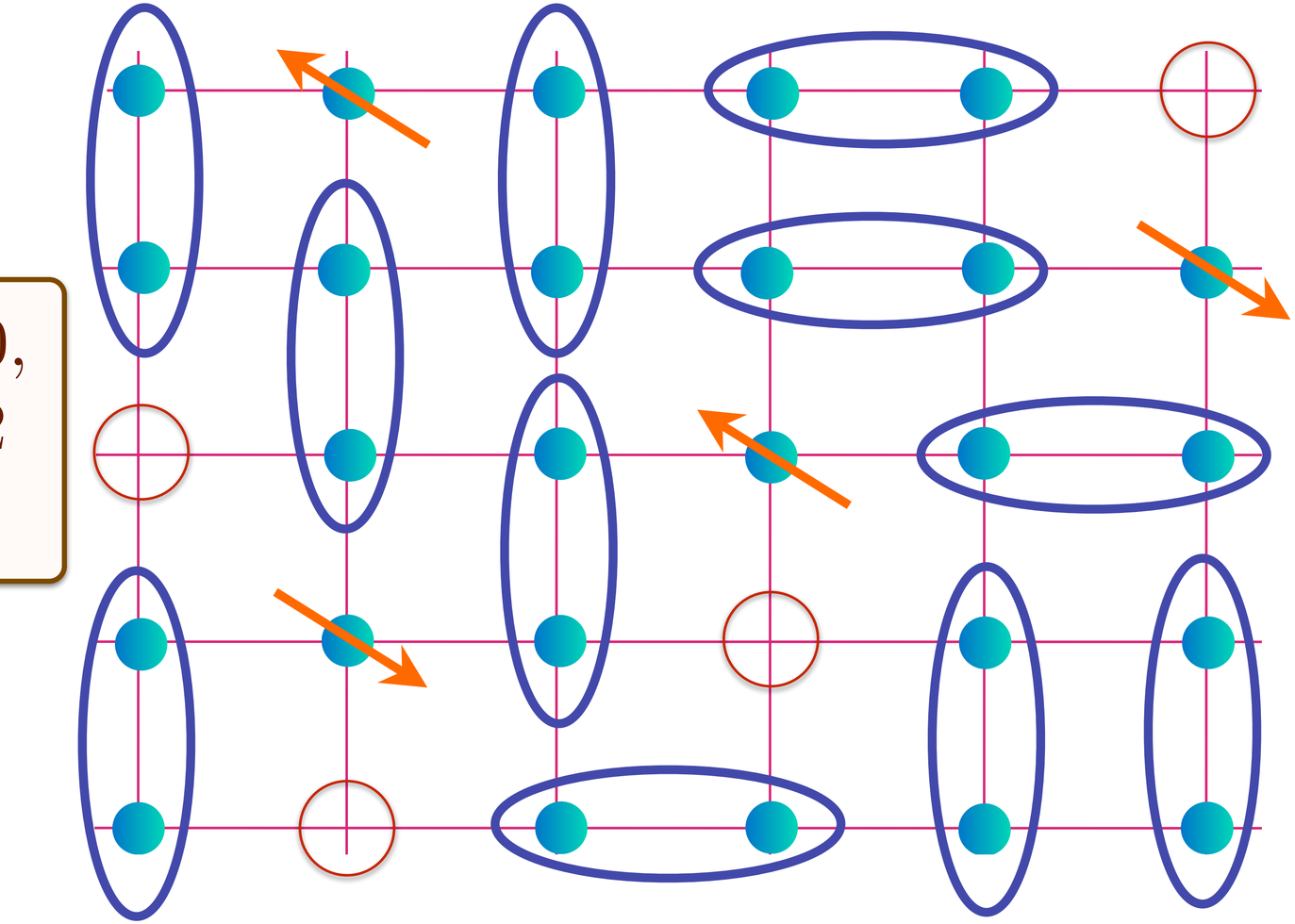

$= (|\uparrow\downarrow\rangle - |\downarrow\uparrow\rangle)/\sqrt{2}$

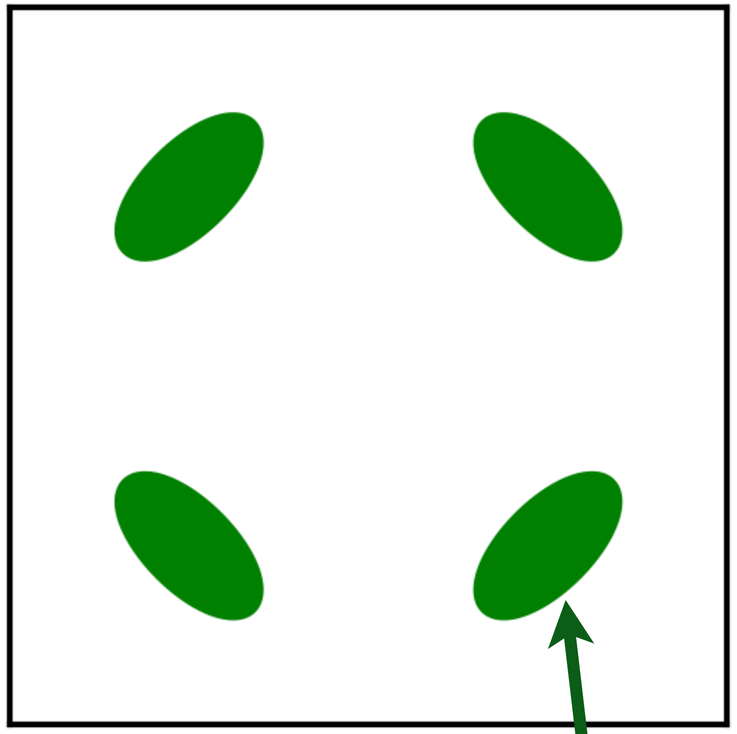

Area $p/4$

Doping an insulating antiferromagnet with holes of density p

Holon metal excited states

Oshikawa anomaly is satisfied by sum of spin liquid (1) and Fermi surface anomalies (p)

Charge 0, spin-1/2 spinons

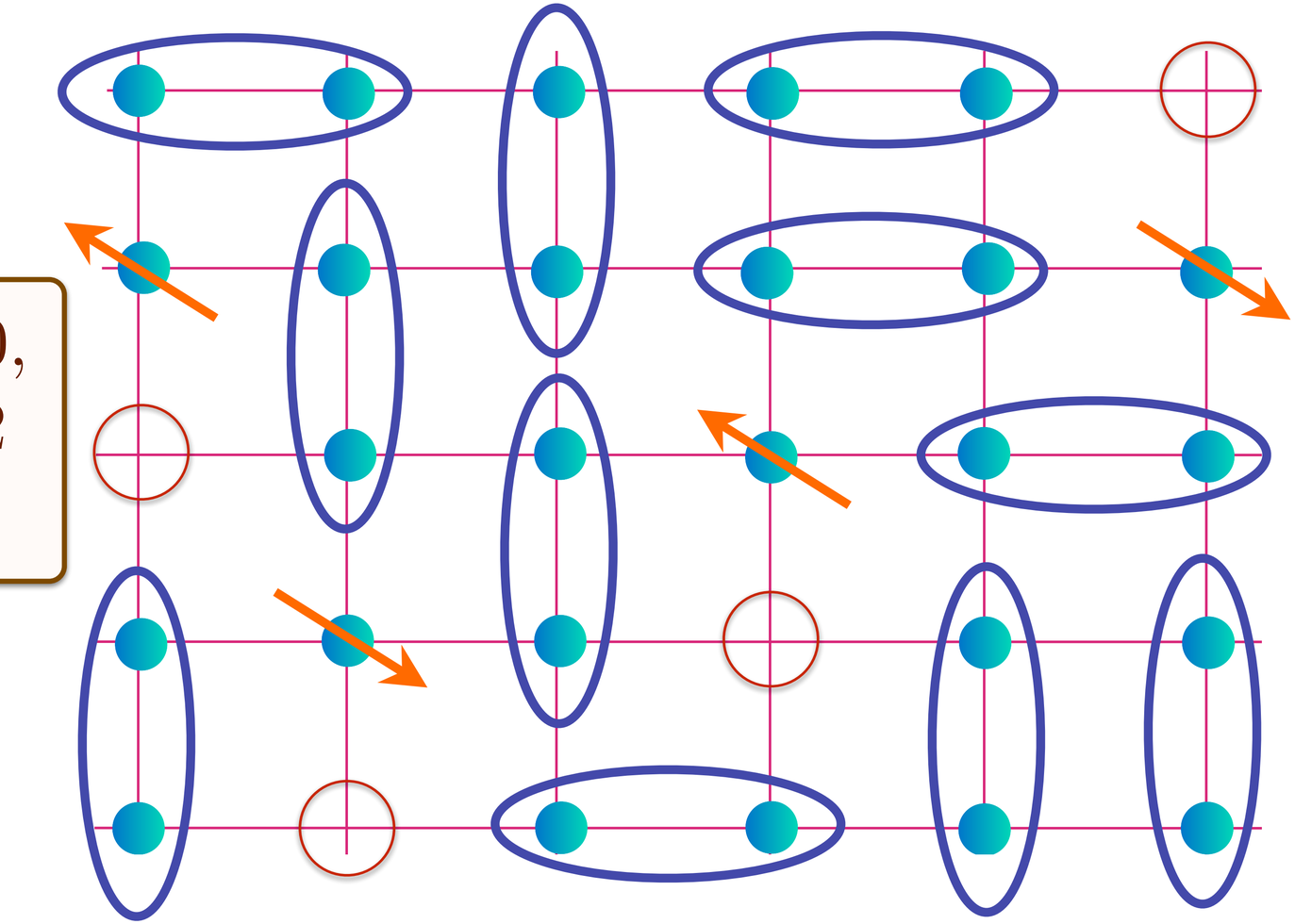

$= (|\uparrow\downarrow\rangle - |\downarrow\uparrow\rangle)/\sqrt{2}$

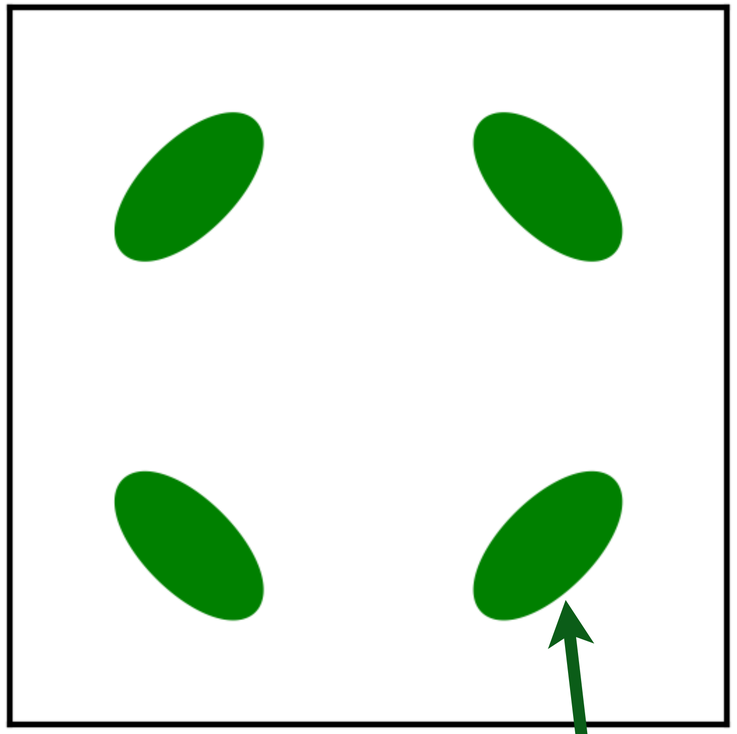

Area $p/4$

Doping an insulating antiferromagnet with holes of density p

Holon metal excited states

Oshikawa anomaly is satisfied by sum of spin liquid (1) and Fermi surface anomalies (p)

Charge 0, spin-1/2 spinons

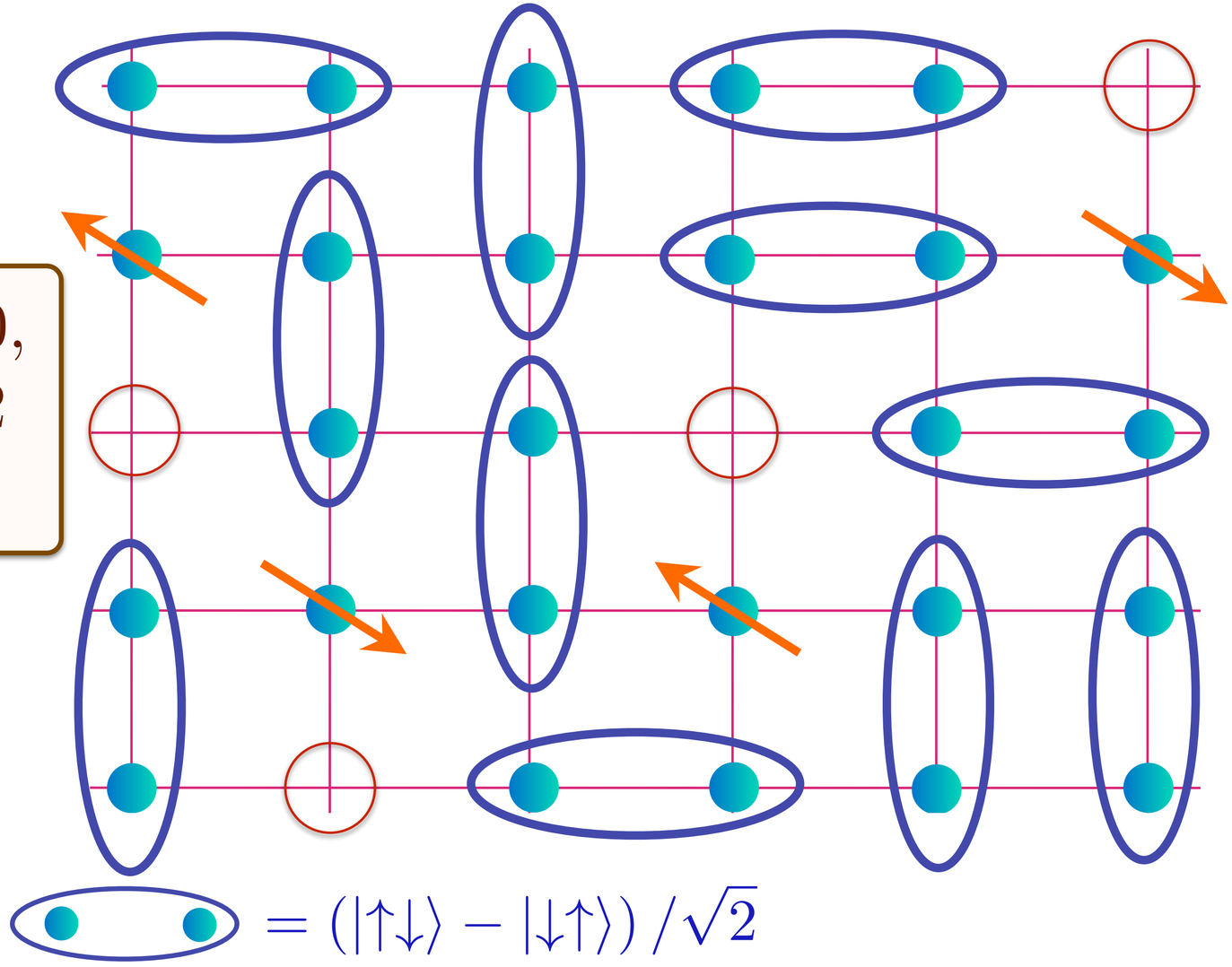

$= (|\uparrow\downarrow\rangle - |\downarrow\uparrow\rangle)/\sqrt{2}$

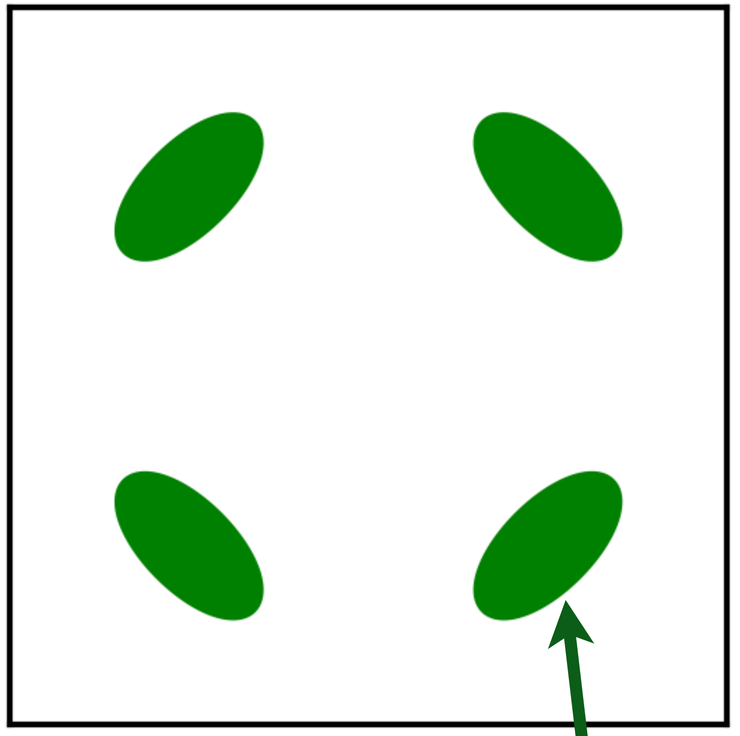

Area $p/4$

Doping an insulating antiferromagnet with holes of density p

Holon metal excited states

Oshikawa anomaly is satisfied by sum of spin liquid (1) and Fermi surface anomalies (p)

Charge 0, spin-1/2 spinons

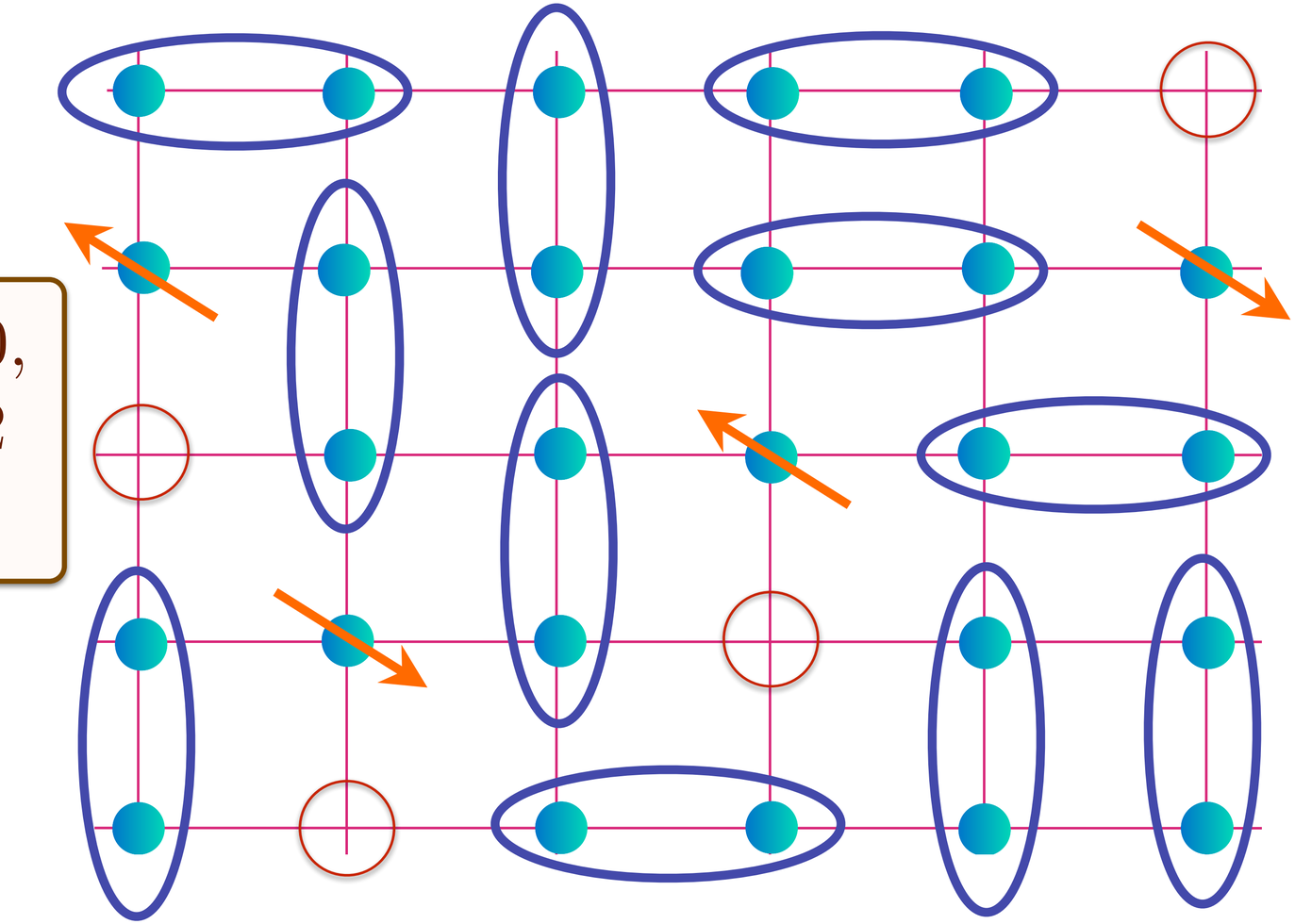

$= (|\uparrow\downarrow\rangle - |\downarrow\uparrow\rangle)/\sqrt{2}$

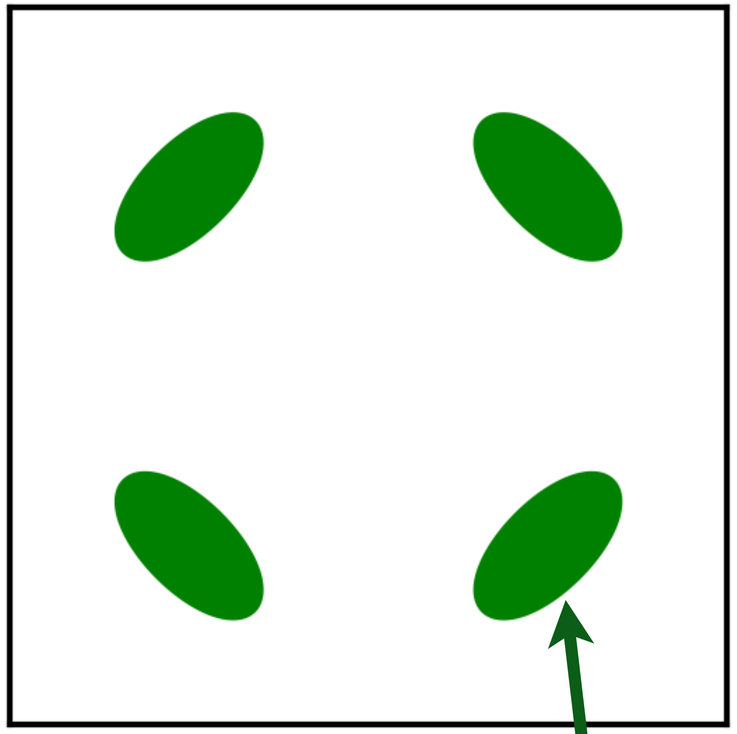

Area $p/4$

Doping an insulating antiferromagnet with holes of density p

FL*

Oshikawa anomaly is satisfied by sum of spin liquid (1) and Fermi surface anomalies (p)

Metal with density p of spin-1/2, charge $+e$ 'holes' (or 'magnetic polarons') with coherent inter-layer transport for Yamaji effect.

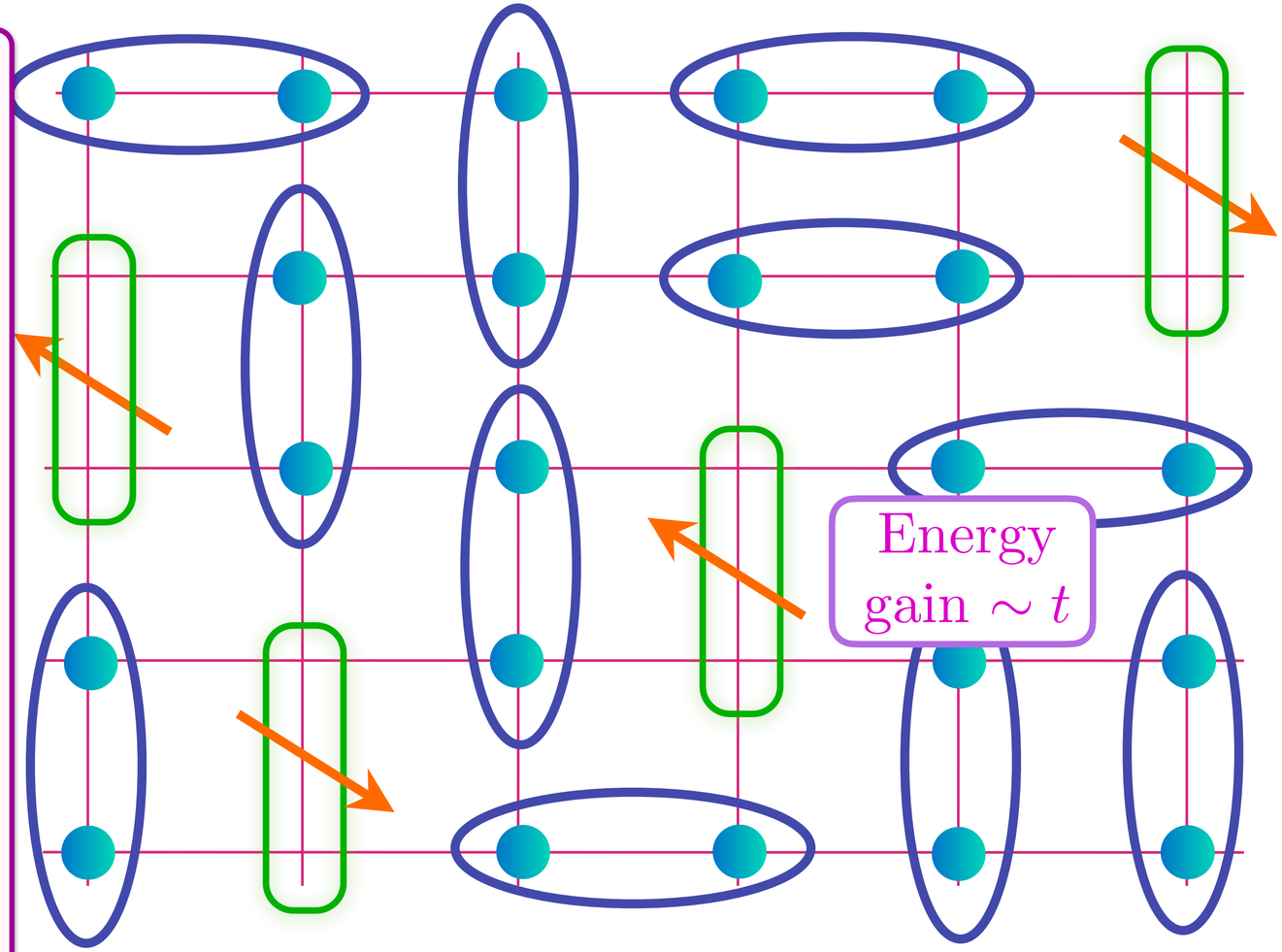

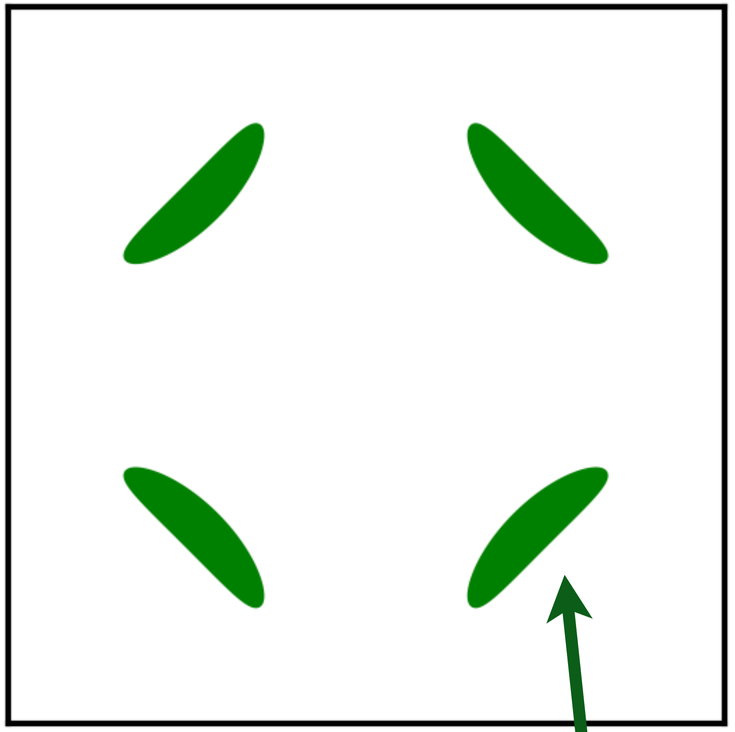

Area $p/8$

$= (|\uparrow\downarrow\rangle - |\downarrow\uparrow\rangle)/\sqrt{2}$ $= (|\uparrow \circ\rangle + |\circ \uparrow\rangle)/\sqrt{2}$

T. Senthil, S. S., M. Vojta, PRL **90**, 216403 (2003); R. K. Kaul, A. Kolezhuk, M. Levin, S.S., T. Senthil, PRB **75**, 235122 (2007)
M. Punk, A. Allais, and S. Sachdev, PNAS **112**, 9552 (2015)

Doping an insulating antiferromagnet with holes of density p

FL*

Oshikawa anomaly is satisfied by sum of spin liquid (1) and Fermi surface anomalies (p)

Metal with density p of spin-1/2, charge $+e$ 'holes' (or 'magnetic polarons') with coherent inter-layer transport for Yamaji effect.

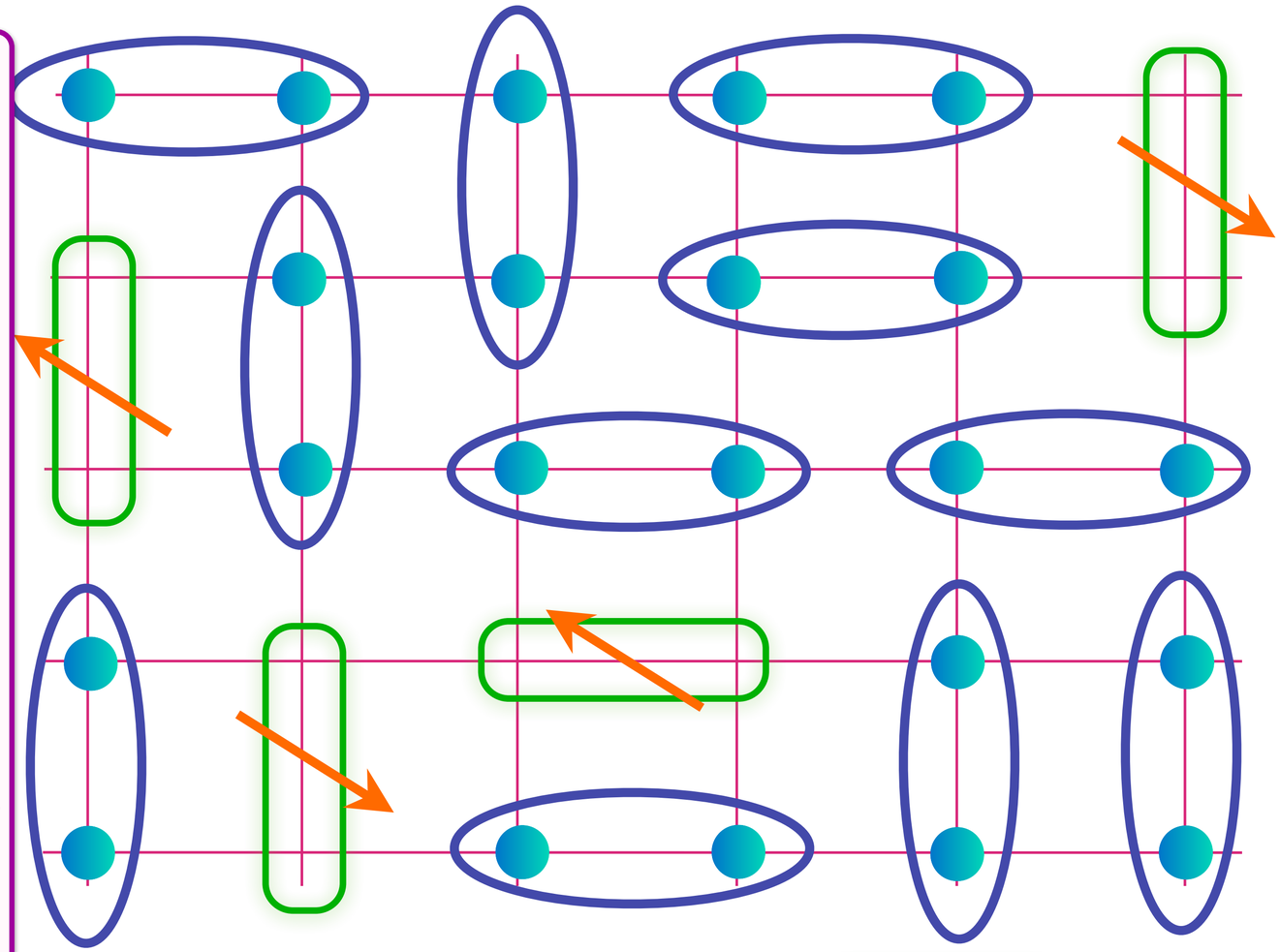

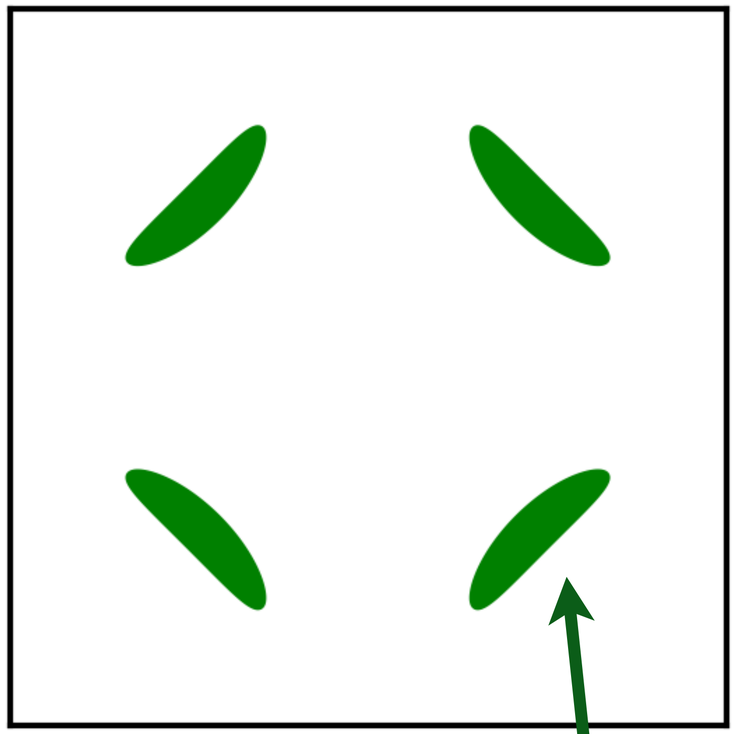

Area $p/8$

$= (|\uparrow\downarrow\rangle - |\downarrow\uparrow\rangle)/\sqrt{2}$ $= (|\uparrow \circ\rangle + |\circ \uparrow\rangle)/\sqrt{2}$

T. Senthil, S. S., M. Vojta, PRL **90**, 216403 (2003); R. K. Kaul, A. Kolezhuk, M. Levin, S.S., T. Senthil, PRB **75**, 235122 (2007)
M. Punk, A. Allais, and S. Sachdev, PNAS **112**, 9552 (2015)

Doping an insulating antiferromagnet with holes of density p

FL*

Oshikawa anomaly is satisfied by sum of spin liquid (1) and Fermi surface anomalies (p)

Metal with density p of spin-1/2, charge $+e$ 'holes' (or 'magnetic polarons') with coherent inter-layer transport for Yamaji effect.

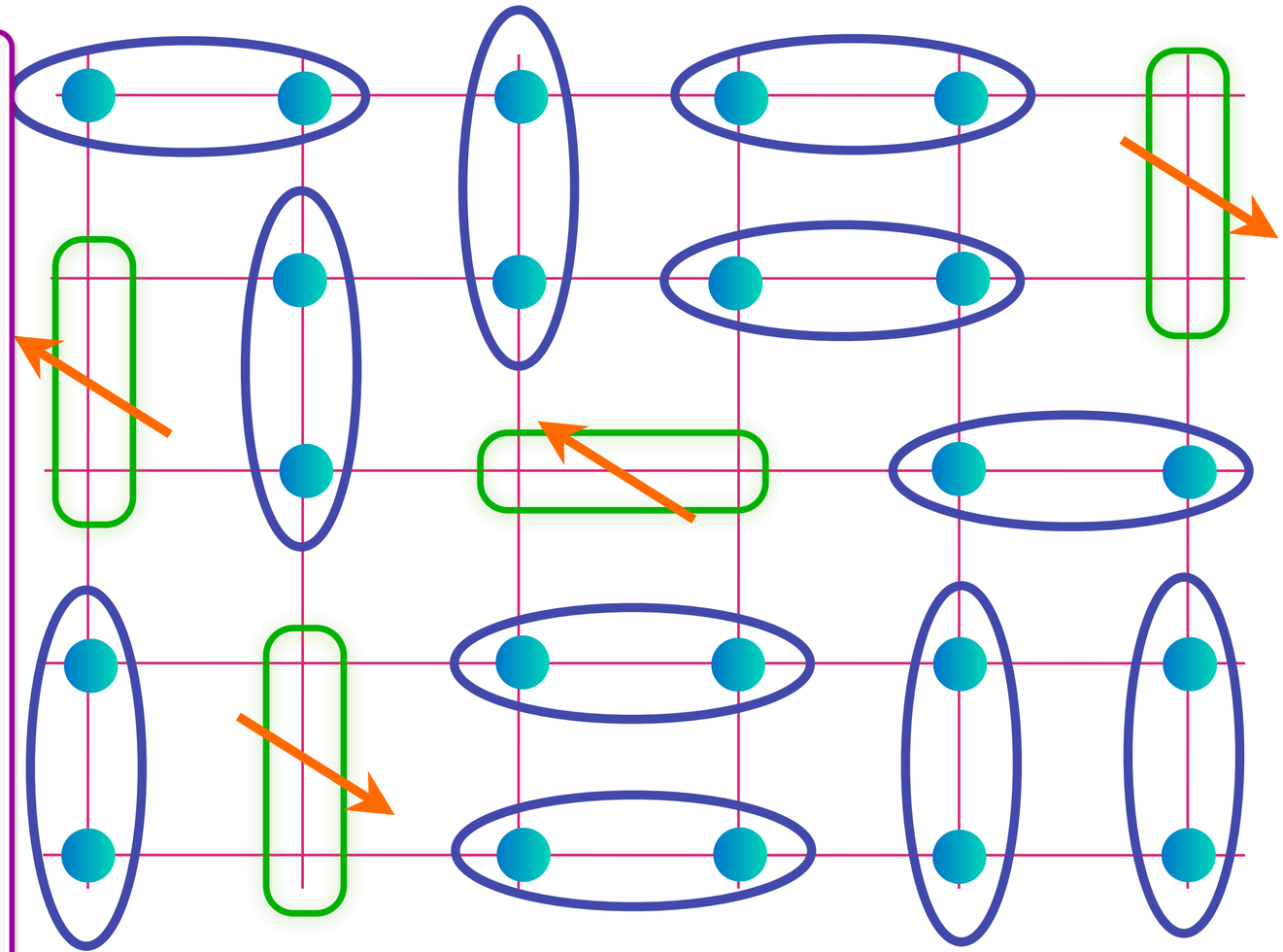

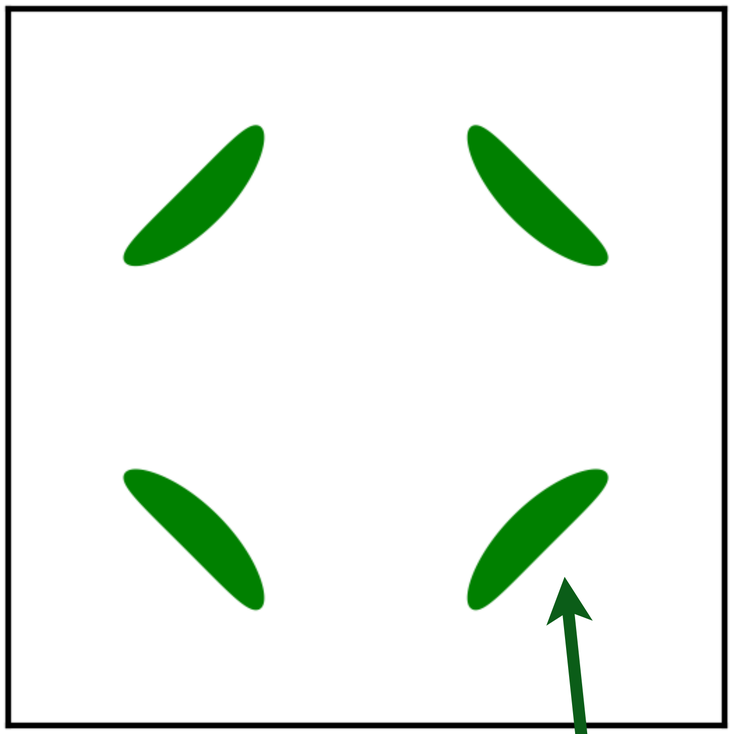

Area $p/8$

$= (|\uparrow\downarrow\rangle - |\downarrow\uparrow\rangle)/\sqrt{2}$ $= (|\uparrow \circ\rangle + |\circ \uparrow\rangle)/\sqrt{2}$

T. Senthil, S. S., M. Vojta, PRL **90**, 216403 (2003); R. K. Kaul, A. Kolezhuk, M. Levin, S.S., T. Senthil, PRB **75**, 235122 (2007)
M. Punk, A. Allais, and S. Sachdev, PNAS **112**, 9552 (2015)

Doping an insulating antiferromagnet with holes of density p

FL*

Metal with density p of spin-1/2, charge $+e$ 'holes' (or 'magnetic polarons') with coherent inter-layer transport for Yamaji effect.

Oshikawa anomaly is satisfied by sum of spin liquid (1) and Fermi surface anomalies (p)

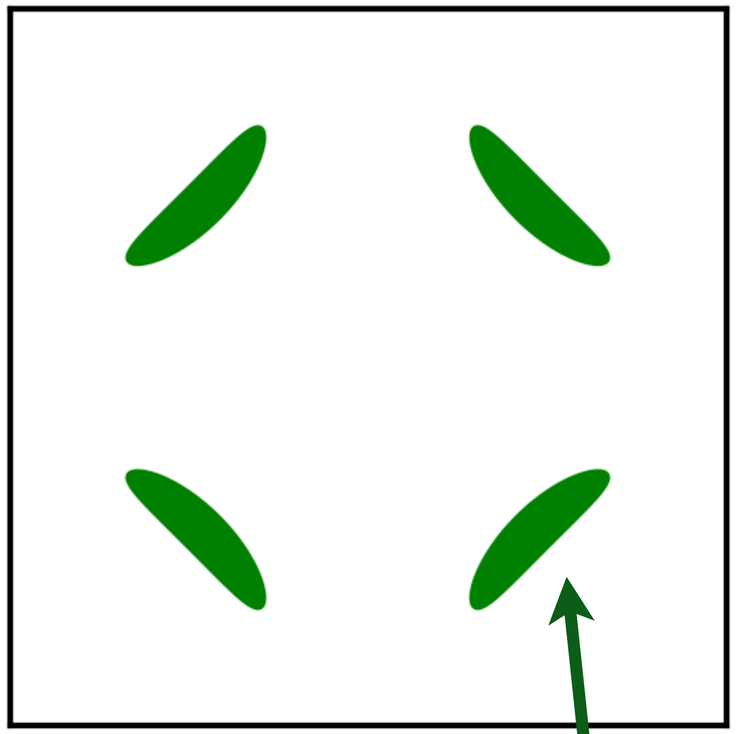

Area $p/8$

$= (|\uparrow\downarrow\rangle - |\downarrow\uparrow\rangle)/\sqrt{2}$ $= (|\uparrow \circ\rangle + |\circ \uparrow\rangle)/\sqrt{2}$

T. Senthil, S. S., M. Vojta, PRL **90**, 216403 (2003); R. K. Kaul, A. Kolezhuk, M. Levin, S.S., T. Senthil, PRB **75**, 235122 (2007)
M. Punk, A. Allais, and S. Sachdev, PNAS **112**, 9552 (2015)

Doping an insulating antiferromagnet with holes of density p

FL*

Metal with density p of spin-1/2, charge $+e$ 'holes' (or 'magnetic polarons') with coherent inter-layer transport for Yamaji effect.

Oshikawa anomaly is satisfied by sum of spin liquid (1) and Fermi surface anomalies (p)

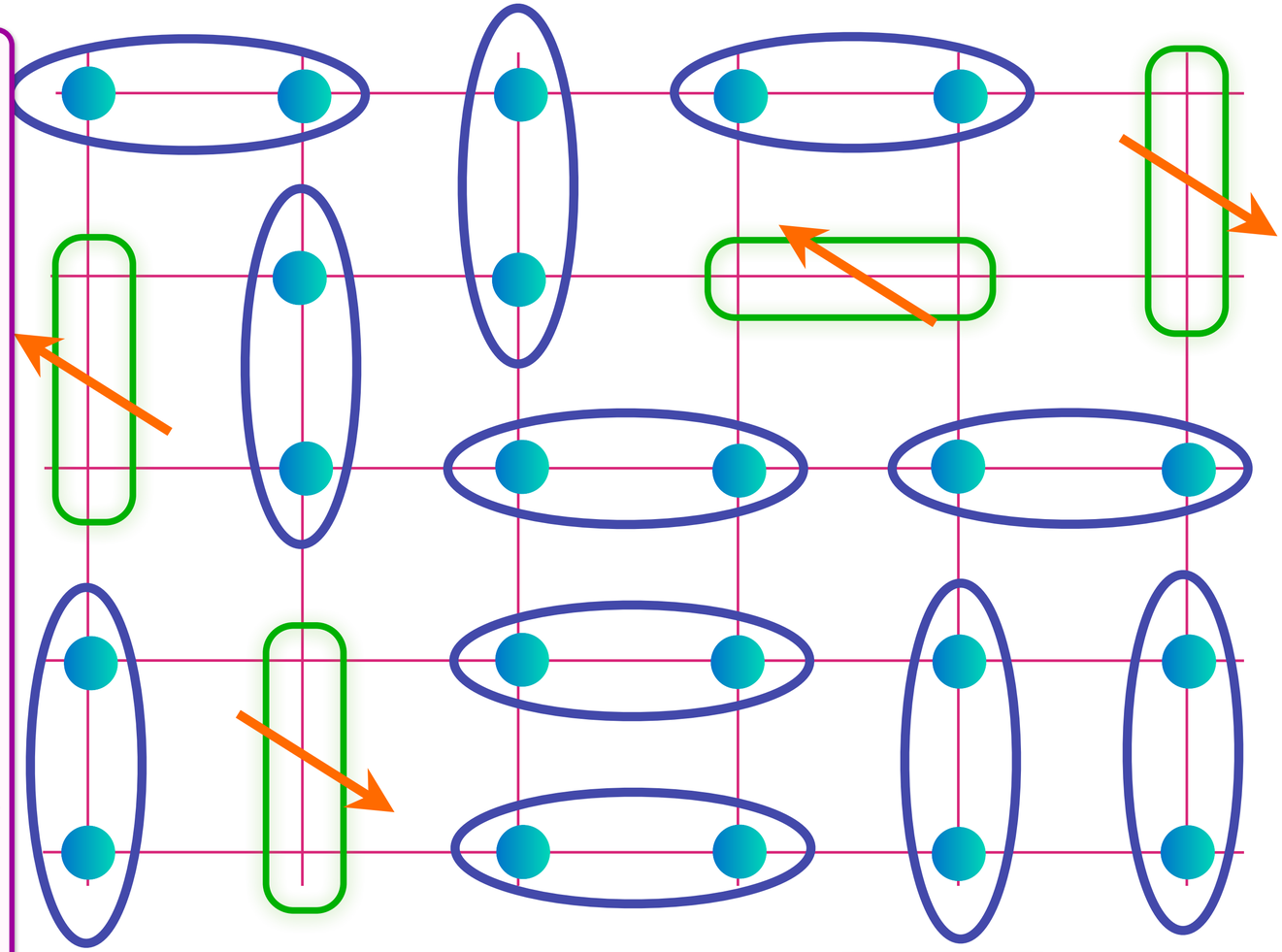

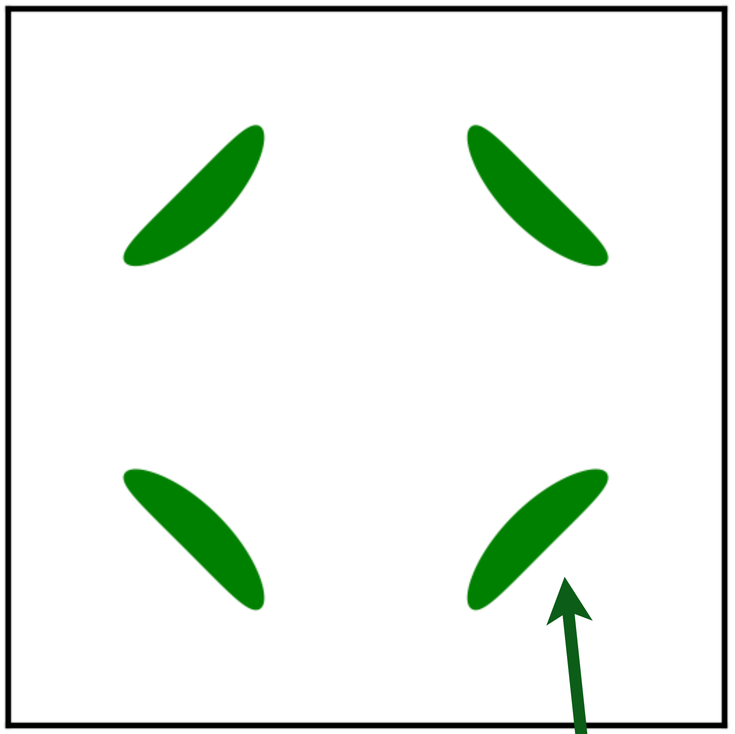

Area $p/8$

$= (|\uparrow\downarrow\rangle - |\downarrow\uparrow\rangle)/\sqrt{2}$ $= (|\uparrow \circ\rangle + |\circ \uparrow\rangle)/\sqrt{2}$

T. Senthil, S. S., M. Vojta, PRL **90**, 216403 (2003); R. K. Kaul, A. Kolezhuk, M. Levin, S.S., T. Senthil, PRB **75**, 235122 (2007)
M. Punk, A. Allais, and S. Sachdev, PNAS **112**, 9552 (2015)

Doping an insulating antiferromagnet with holes of density p

FL*

Metal with density p of spin-1/2, charge $+e$ 'holes' (or 'magnetic polarons') with coherent inter-layer transport for Yamaji effect.

Oshikawa anomaly is satisfied by sum of spin liquid (1) and Fermi surface anomalies (p)

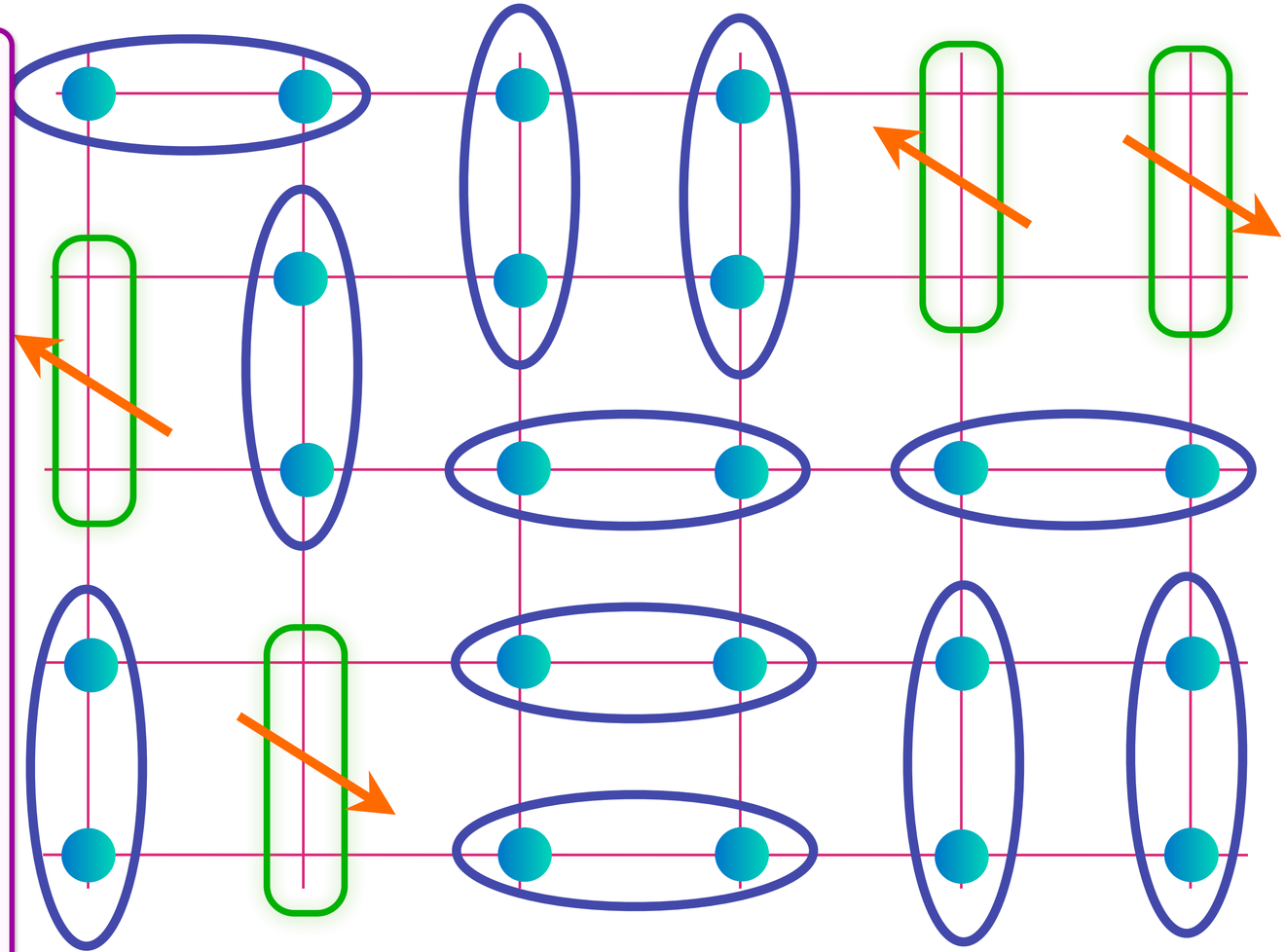

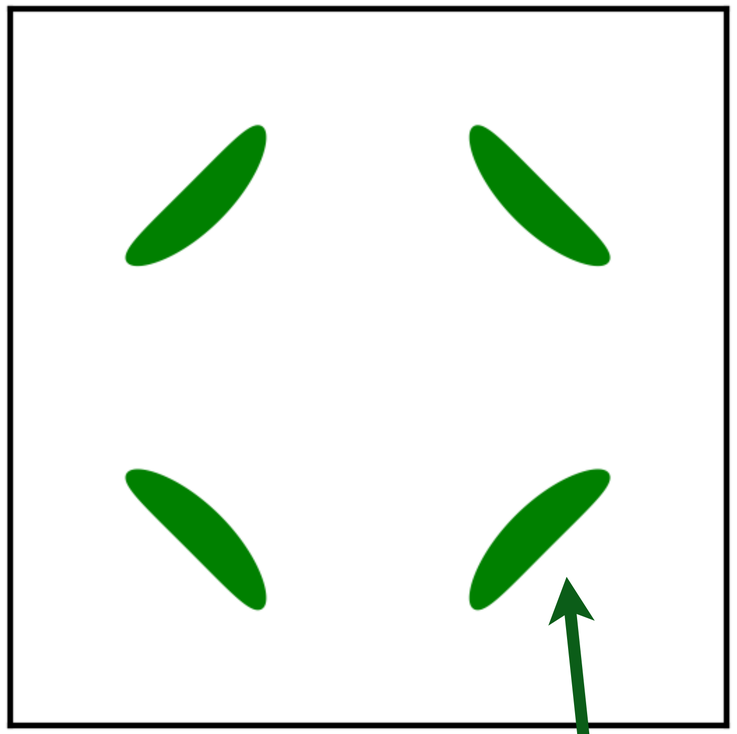

Area $p/8$

$= (|\uparrow\downarrow\rangle - |\downarrow\uparrow\rangle)/\sqrt{2}$

$= (|\uparrow \circ\rangle + |\circ \uparrow\rangle)/\sqrt{2}$

T. Senthil, S. S., M. Vojta, PRL **90**, 216403 (2003); R. K. Kaul, A. Kolezhuk, M. Levin, S.S., T. Senthil, PRB **75**, 235122 (2007)
M. Punk, A. Allais, and S. Sachdev, PNAS **112**, 9552 (2015)

Doping an insulating antiferromagnet with holes of density p

FL*

Oshikawa anomaly is satisfied by sum of spin liquid (1) and Fermi surface anomalies (p)

Metal with density p of spin-1/2, charge $+e$ 'holes' (or 'magnetic polarons') with coherent inter-layer transport for Yamaji effect.

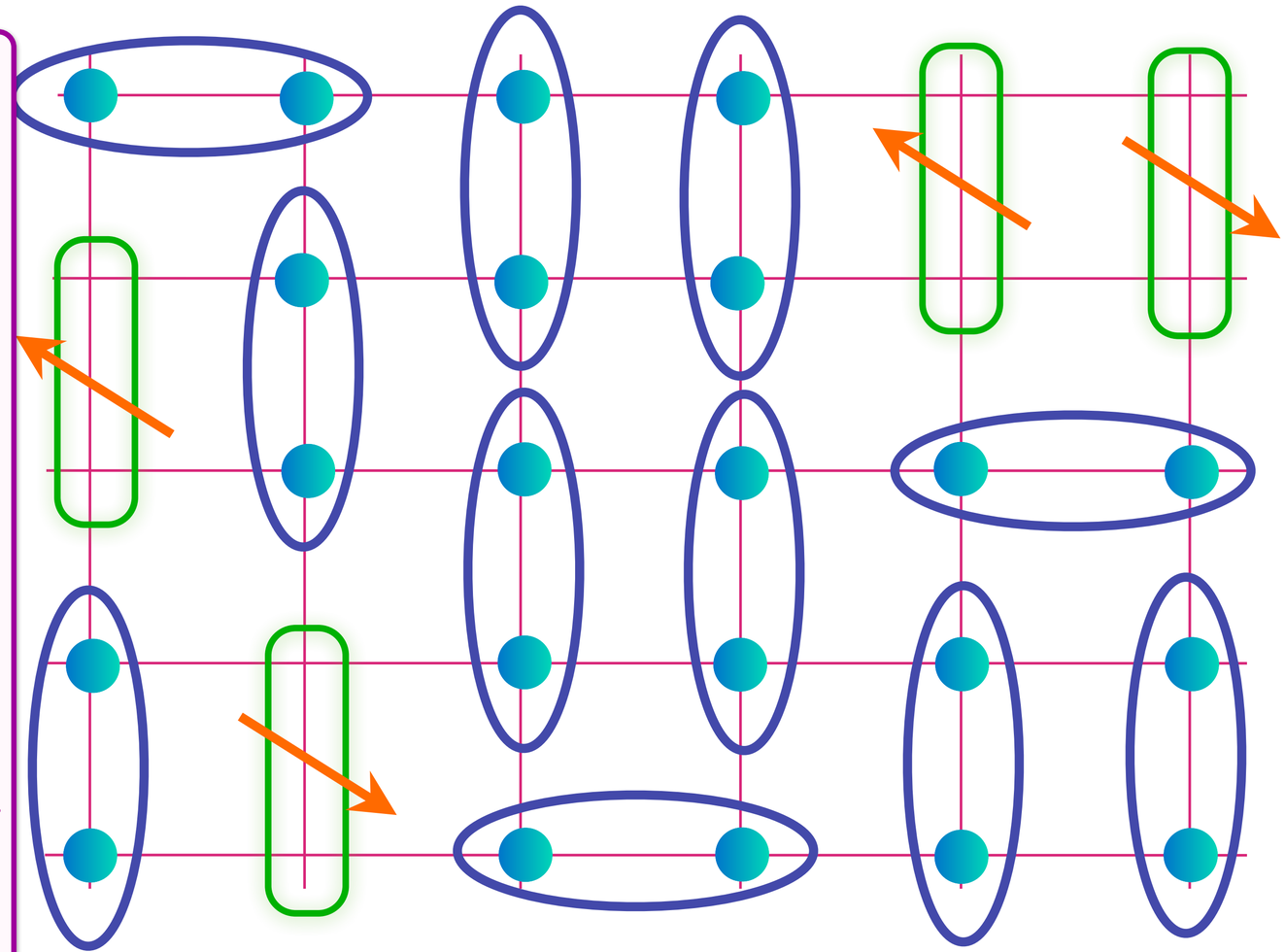

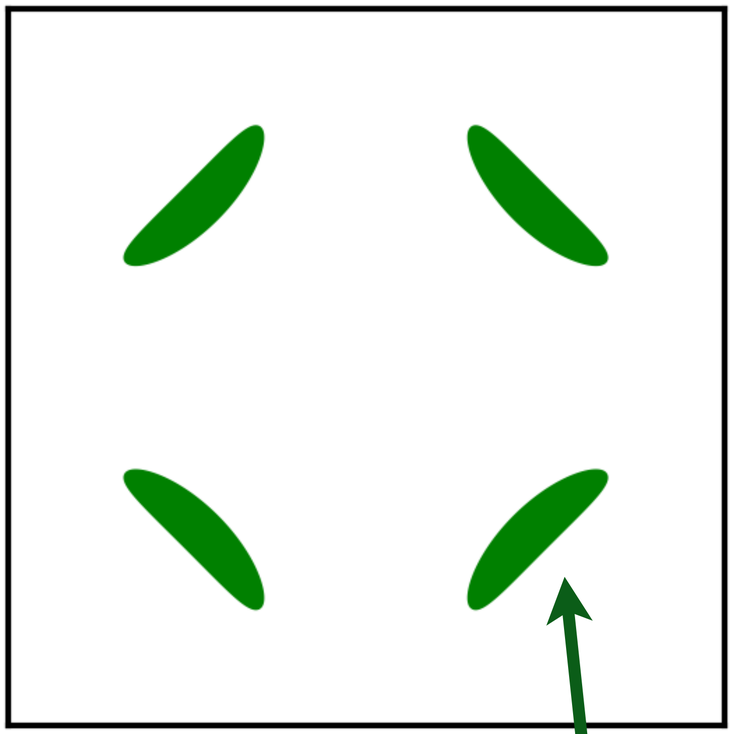

Area $p/8$

$= (|\uparrow\downarrow\rangle - |\downarrow\uparrow\rangle)/\sqrt{2}$ $= (|\uparrow \circ\rangle + |\circ \uparrow\rangle)/\sqrt{2}$

T. Senthil, S. S., M. Vojta, PRL **90**, 216403 (2003); R. K. Kaul, A. Kolezhuk, M. Levin, S.S., T. Senthil, PRB **75**, 235122 (2007)
M. Punk, A. Allais, and S. Sachdev, PNAS **112**, 9552 (2015)

Doping an insulating antiferromagnet with holes of density p

FL*

Metal with density p of spin-1/2, charge $+e$ 'holes' (or 'magnetic polarons') with coherent inter-layer transport for Yamaji effect.

Oshikawa anomaly is satisfied by sum of spin liquid (1) and Fermi surface anomalies (p)

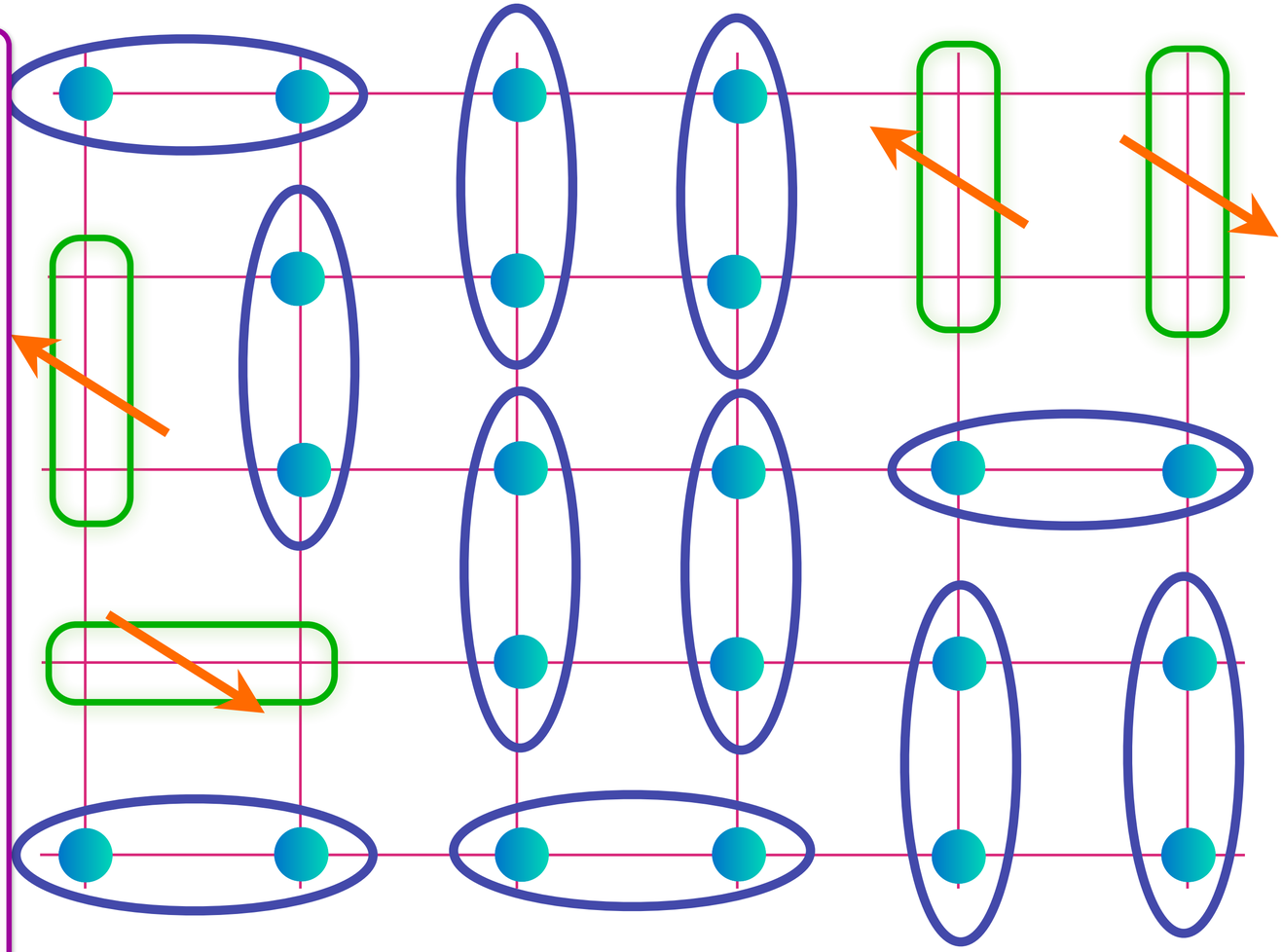

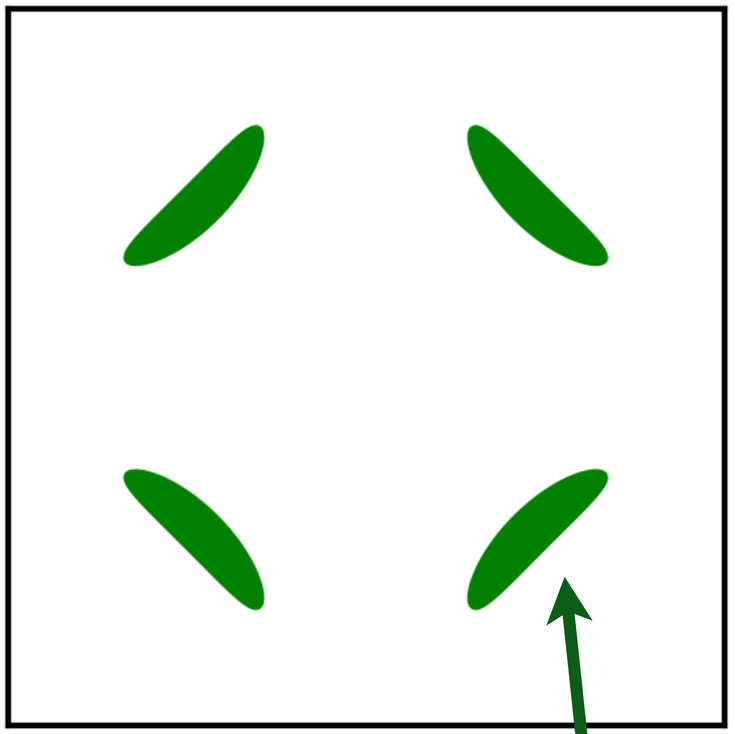

Area $p/8$

$= (|\uparrow\downarrow\rangle - |\downarrow\uparrow\rangle)/\sqrt{2}$

$= (|\uparrow \circ\rangle + |\circ \uparrow\rangle)/\sqrt{2}$

T. Senthil, S. S., M. Vojta, PRL **90**, 216403 (2003); R. K. Kaul, A. Kolezhuk, M. Levin, S.S., T. Senthil, PRB **75**, 235122 (2007)
M. Punk, A. Allais, and S. Sachdev, PNAS **112**, 9552 (2015)

Doping an insulating antiferromagnet with holes of density p

FL*

Oshikawa anomaly is satisfied by sum of spin liquid (1) and Fermi surface anomalies (p)

Metal with density p of spin-1/2, charge $+e$ 'holes' (or 'magnetic polarons') with coherent inter-layer transport for Yamaji effect.

Exact Solution of a Two-Species Quantum Dimer Model for Pseudogap Metals

Johannes Feldmeier, Sebastian Huber, and Matthias Punk
Physics Department, Arnold Sommerfeld Center for Theoretical Physics and Center for NanoScience, Ludwig-Maximilians-University Munich, 80333 Munich, Germany

(Received 12 December 2017; published 3 May 2018)

We present an exact ground state solution of a quantum dimer model introduced by Punk, Allais, and Sachdev [Quantum dimer model for the pseudogap metal, Proc. Natl. Acad. Sci. U.S.A. **112**, 9552 (2015).], which features ordinary bosonic spin-singlet dimers as well as fermionic dimers that can be viewed as bound states of spinons and holons in a hole-doped resonating valence bond liquid. Interestingly, this model captures several essential properties of the metallic pseudogap phase in high-T_c cuprate superconductors. We identify a line in parameter space where the exact ground state wave functions can be constructed at an arbitrary density of fermionic dimers. At this exactly solvable line the ground state has a huge degeneracy, which can be interpreted as a flat band of fermionic excitations. Perturbing around the exactly solvable line, this degeneracy is lifted and the ground state is a fractionalized Fermi liquid with a small pocket Fermi surface in the low doping limit.

PHYSICAL REVIEW LETTERS **120,** 187001 (2018)

Keimer, Kivelson, Norman, Uchida, and Zaanen, *Nature* **518**, 179 (2015)

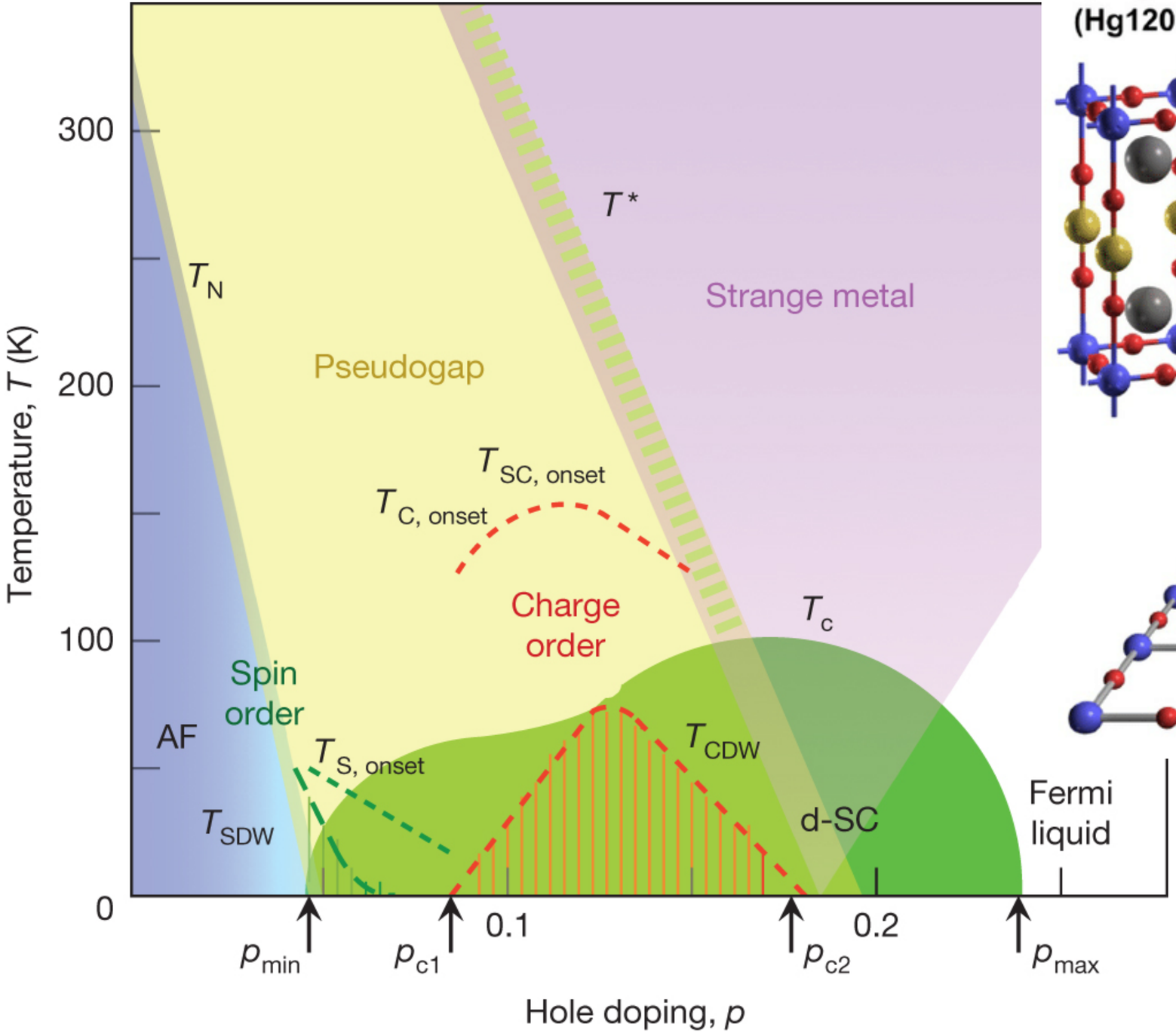

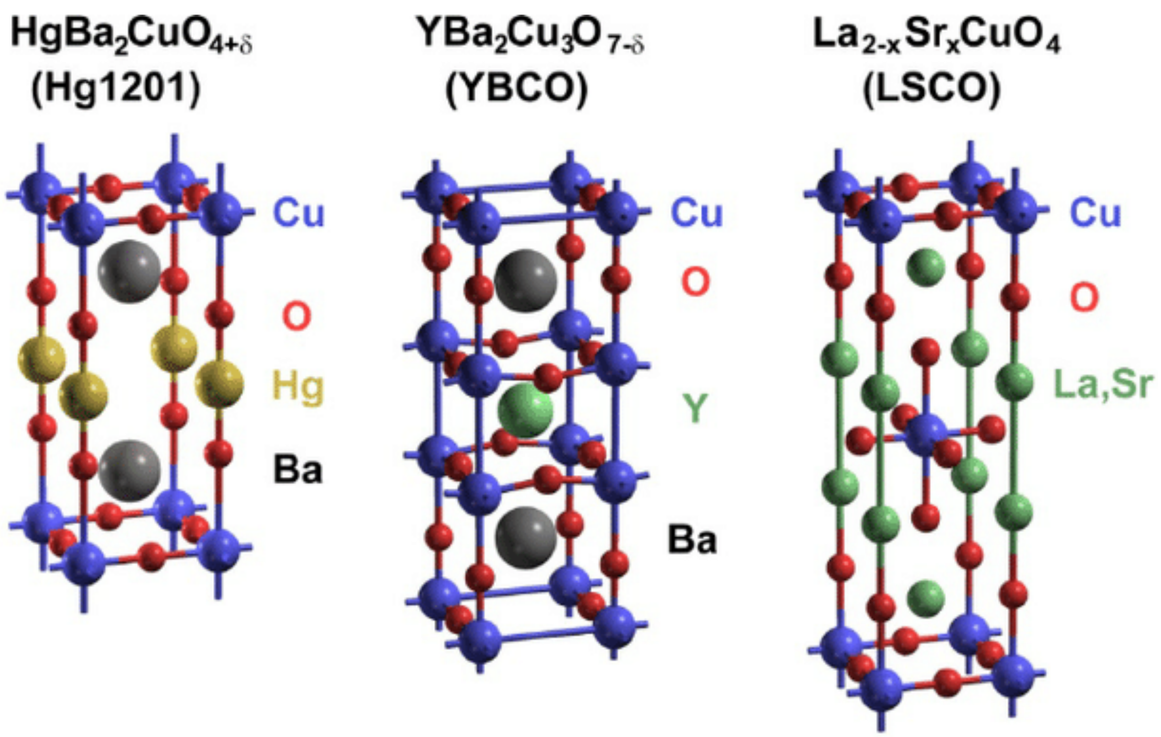

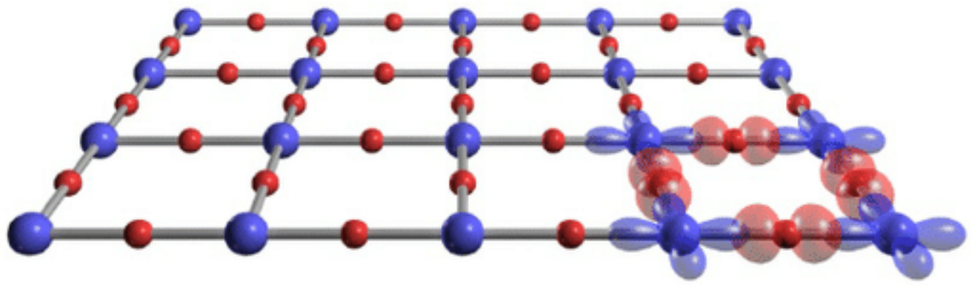

Keimer, Kivelson, Norman, Uchida, and Zaanen, *Nature* **518**, 179 (2015)

M. Platé *et al.*, PRL **95**, 077001 (2005)

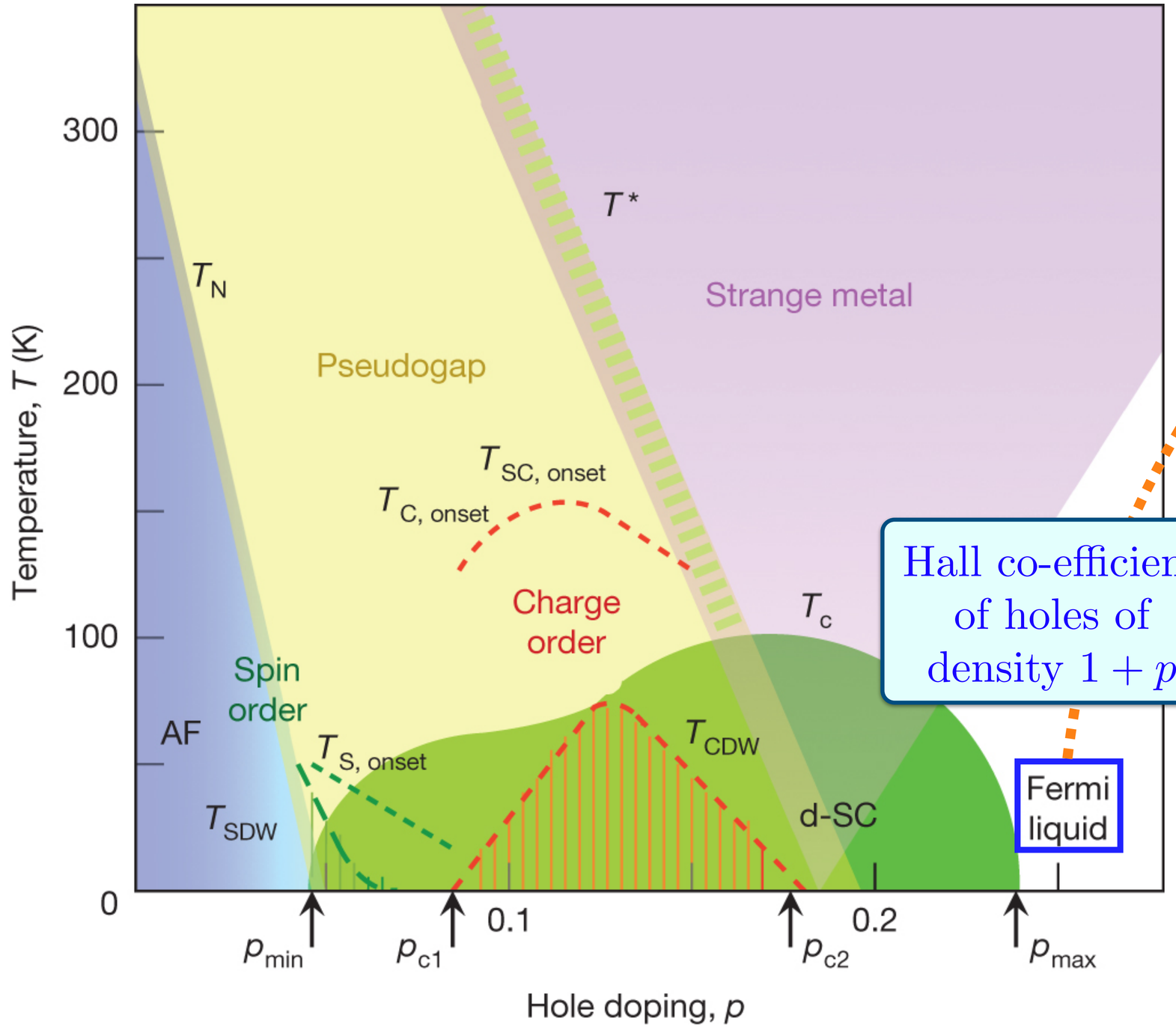

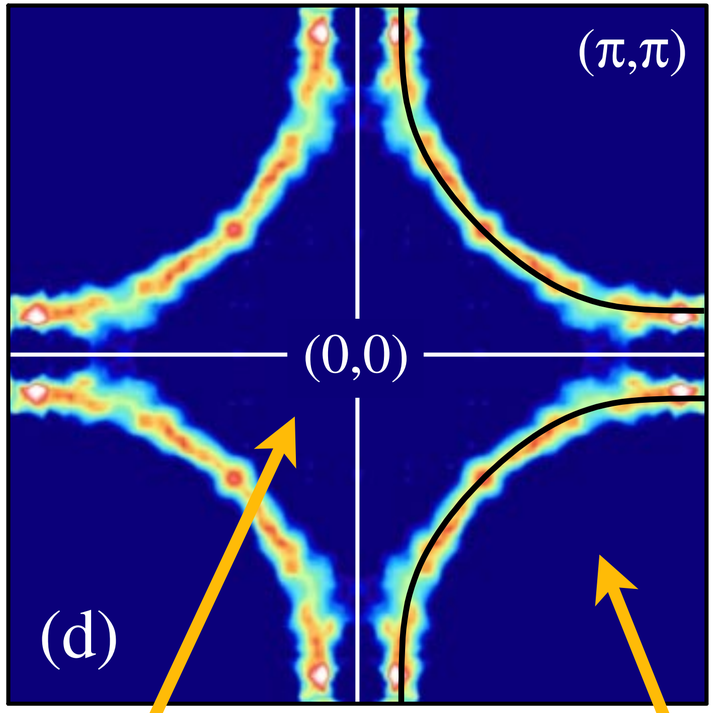

Hall co-efficient of holes of density $1 + p$

1-p electrons

1+p holes

Keimer, Kivelson, Norman, Uchida, and Zaanen, *Nature* **518**, 179 (2015)

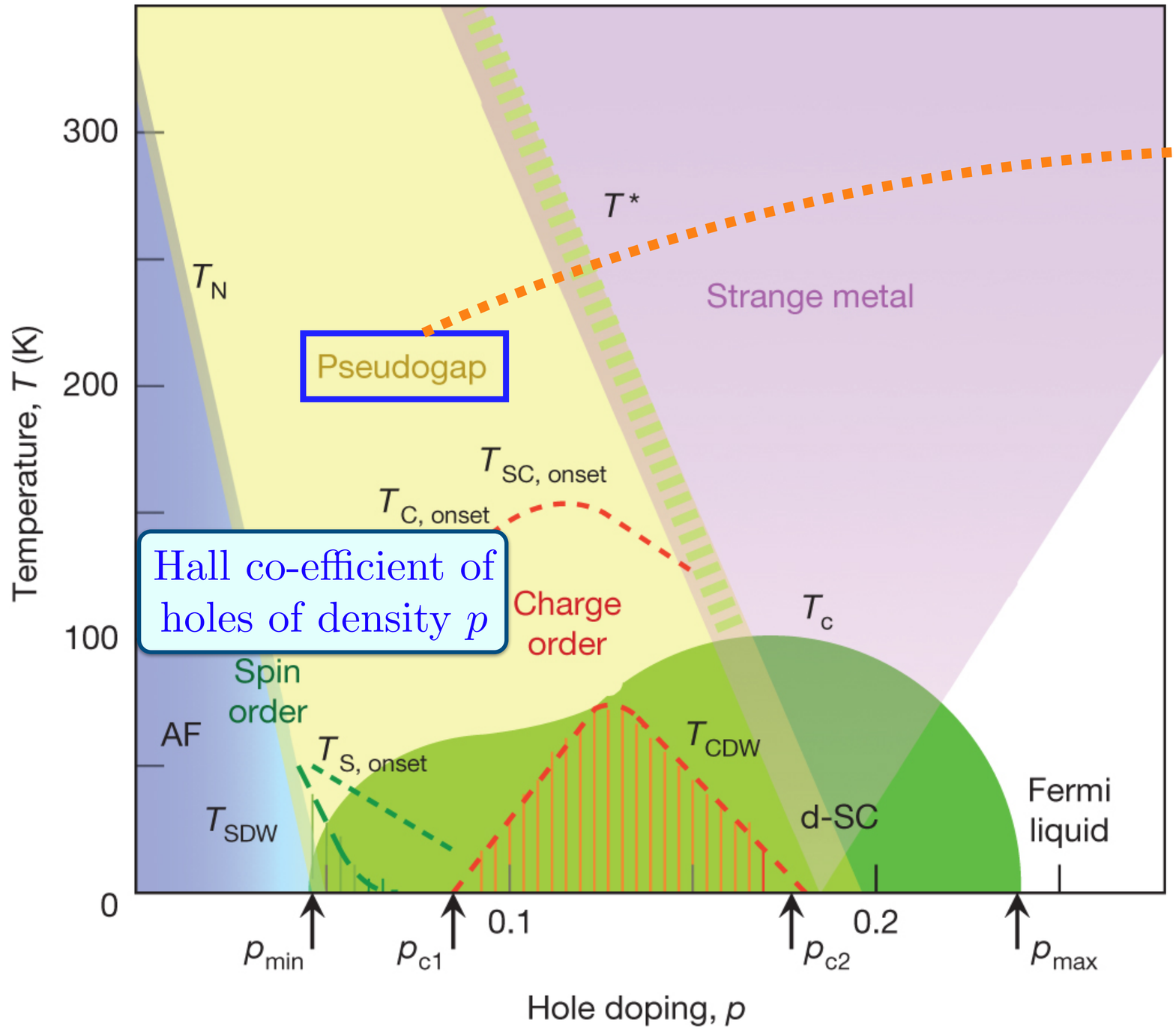

Kyle M. Shen *et al.*, Science **307**, 901 (2005)

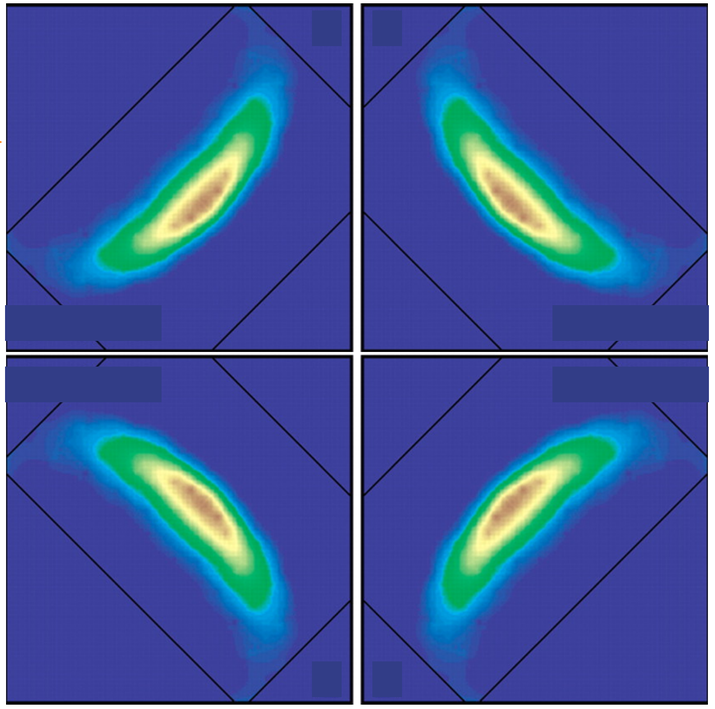

`Fermi arcs' ?

Observation of the Yamaji effect in a cuprate superconductor

Mun K. Chan[1] ✉, Katherine A. Schreiber[1], Oscar E. Ayala-Valenzuela[1], Eric D. Bauer[2], Arkady Shekhter[1] & Neil Harrison[1]

nature physics
arXiv:2411.10631
Published online: 16 September 2025

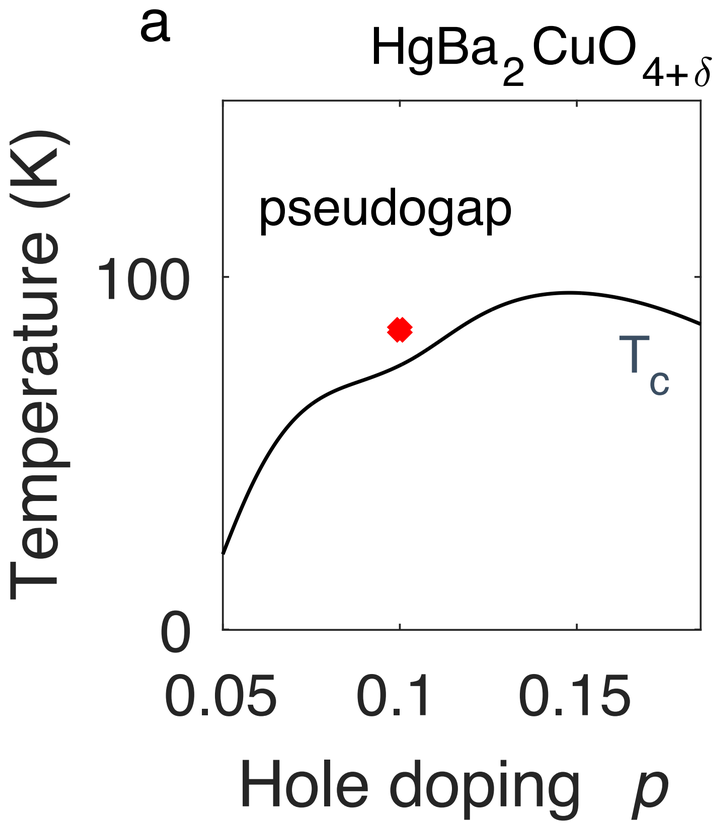

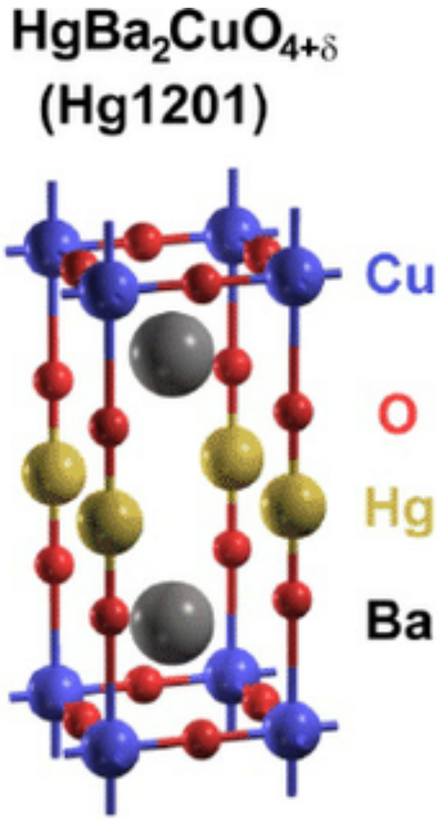

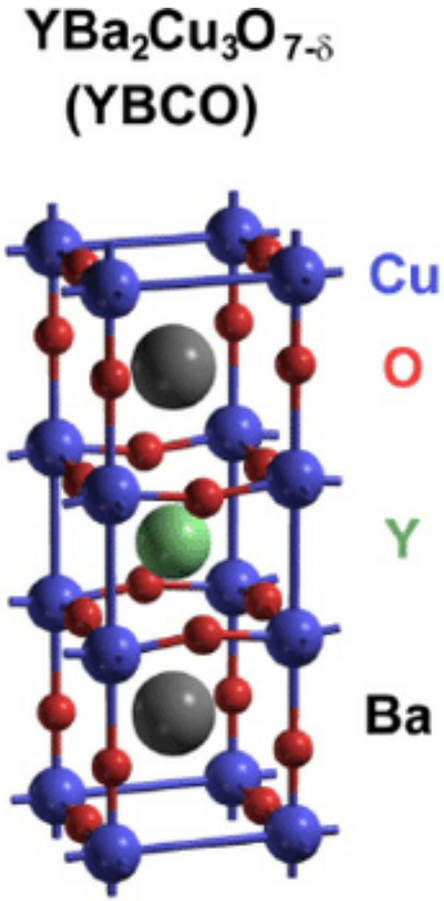

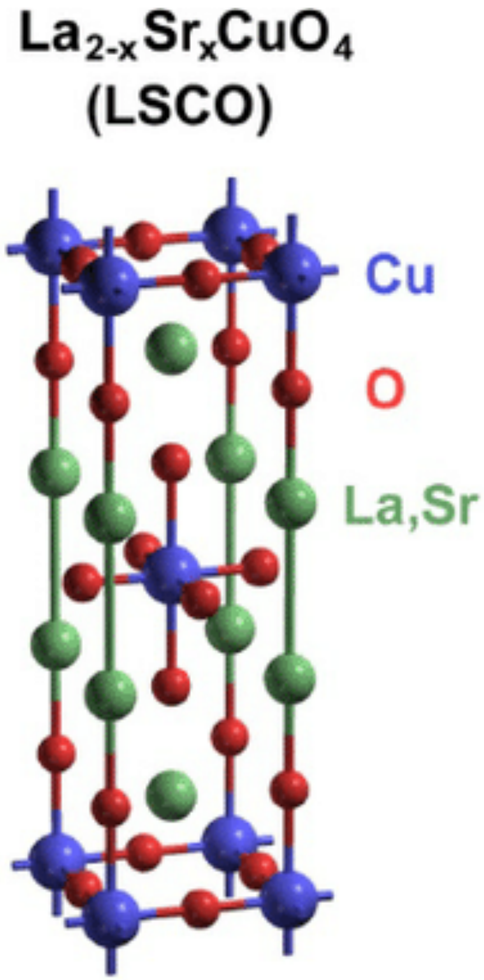

Observation of the Yamaji effect in a cuprate superconductor

Mun K. Chan[1] ✉, Katherine A. Schreiber[1], Oscar E. Ayala-Valenzuela[1], Eric D. Bauer[2], Arkady Shekhter[1] & Neil Harrison[1]

nature physics
arXiv:2411.10631
Published online: 16 September 2025

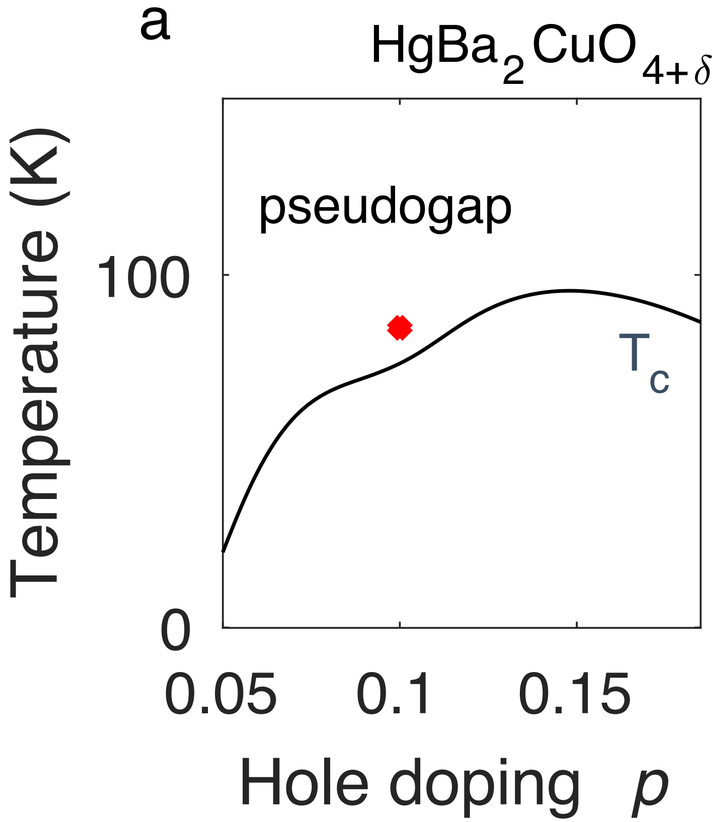

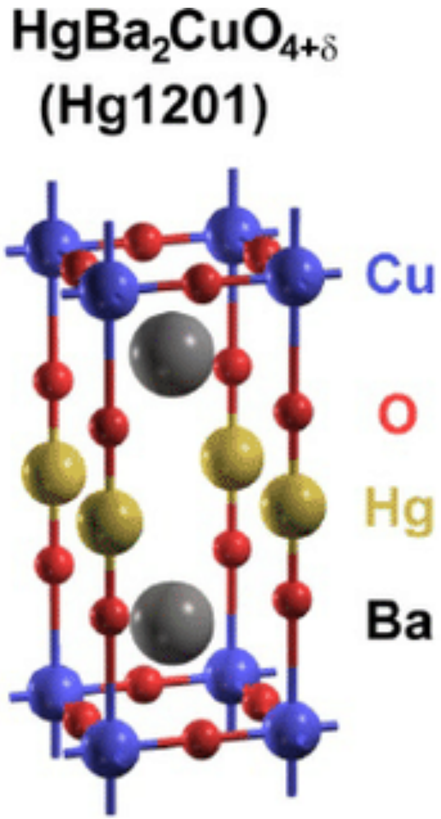

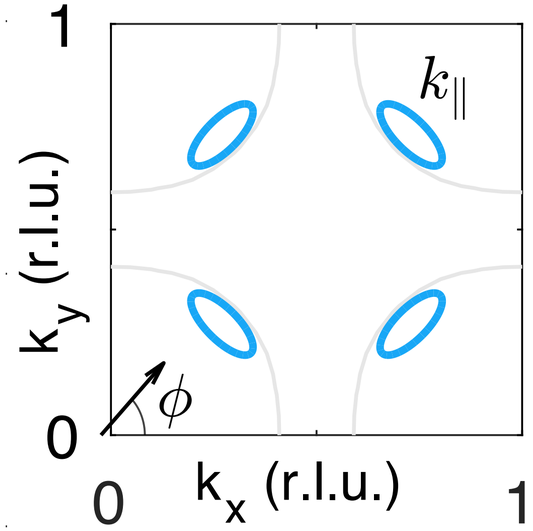

At the Yamaji angle, the orbits in the plane orthogonal to $\boldsymbol{B}$ have an area which is independent of momentum in the c direction, to first order in the hopping along the c direction.

K. Yamaji JPSJ **58**, 1520 (1989)

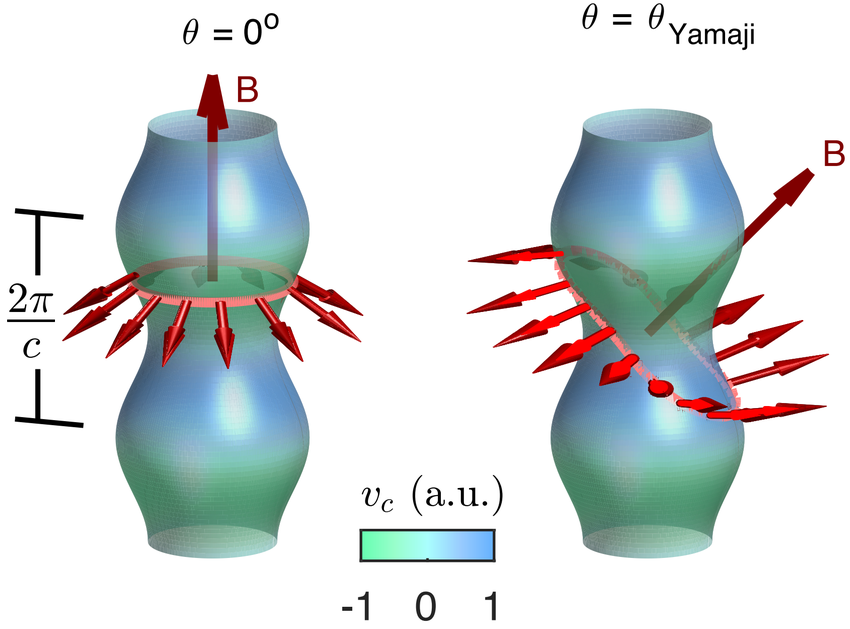

Observation of the Yamaji effect in a cuprate superconductor

Mun K. Chan[1] ✉, Katherine A. Schreiber[1], Oscar E. Ayala-Valenzuela[1], Eric D. Bauer[2], Arkady Shekhter[1] & Neil Harrison[1]

nature physics
arXiv:2411.10631
Published online: 16 September 2025

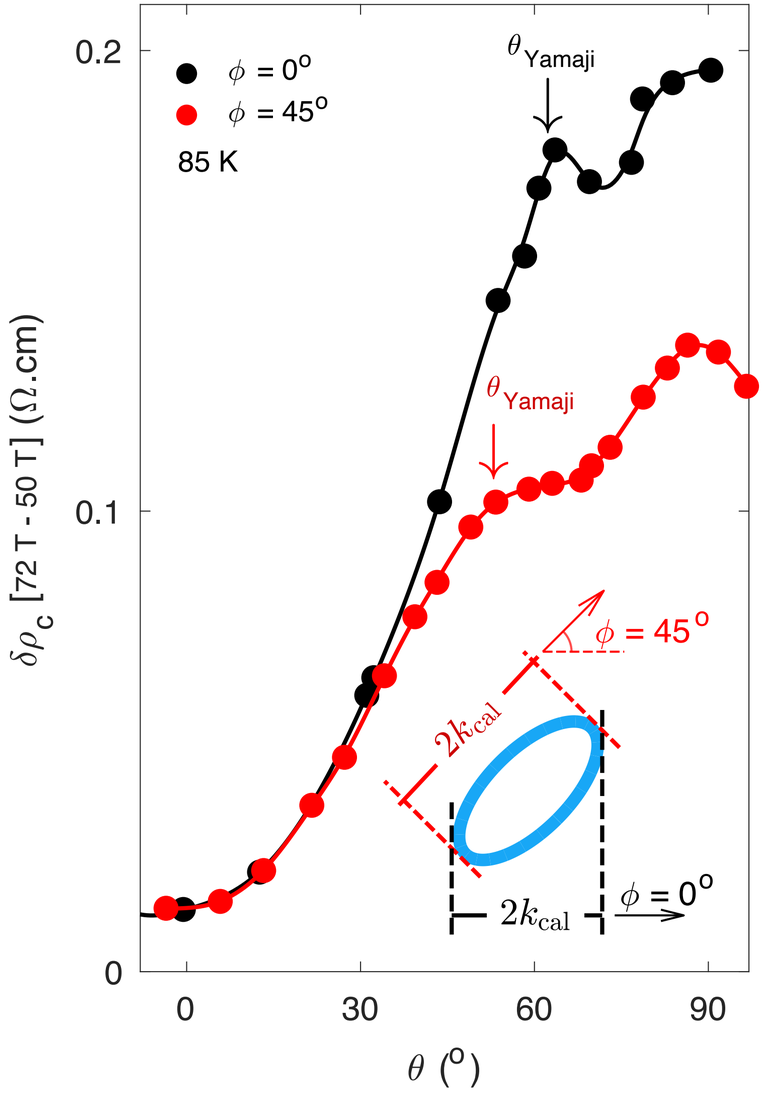

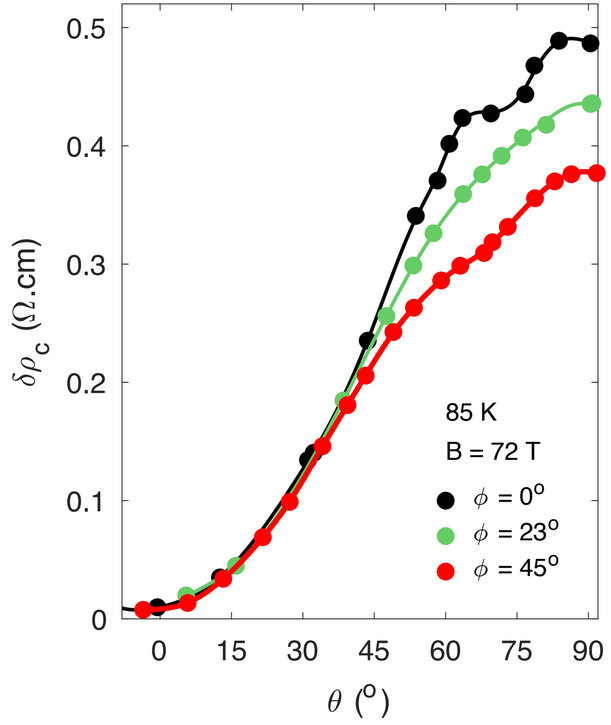

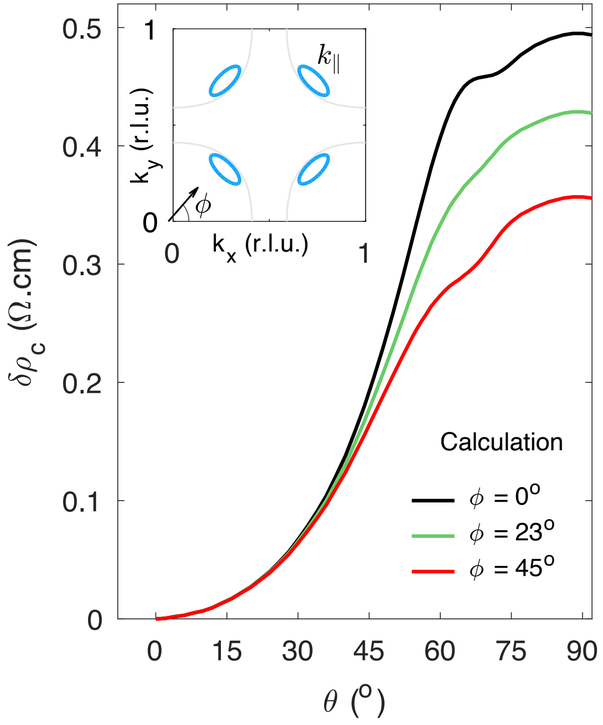

Doping
$p = 0.1$

"The small size of the pockets determined from the Yamaji effect is . . . approximately 1.3% of the Brillouin zone area"

Observation of the Yamaji effect in a cuprate superconductor

Mun K. Chan[1] ✉, Katherine A. Schreiber[1], Oscar E. Ayala-Valenzuela[1], Eric D. Bauer[2], Arkady Shekhter[1] & Neil Harrison[1]

nature physics
arXiv:2411.10631
Published online: 16 September 2025

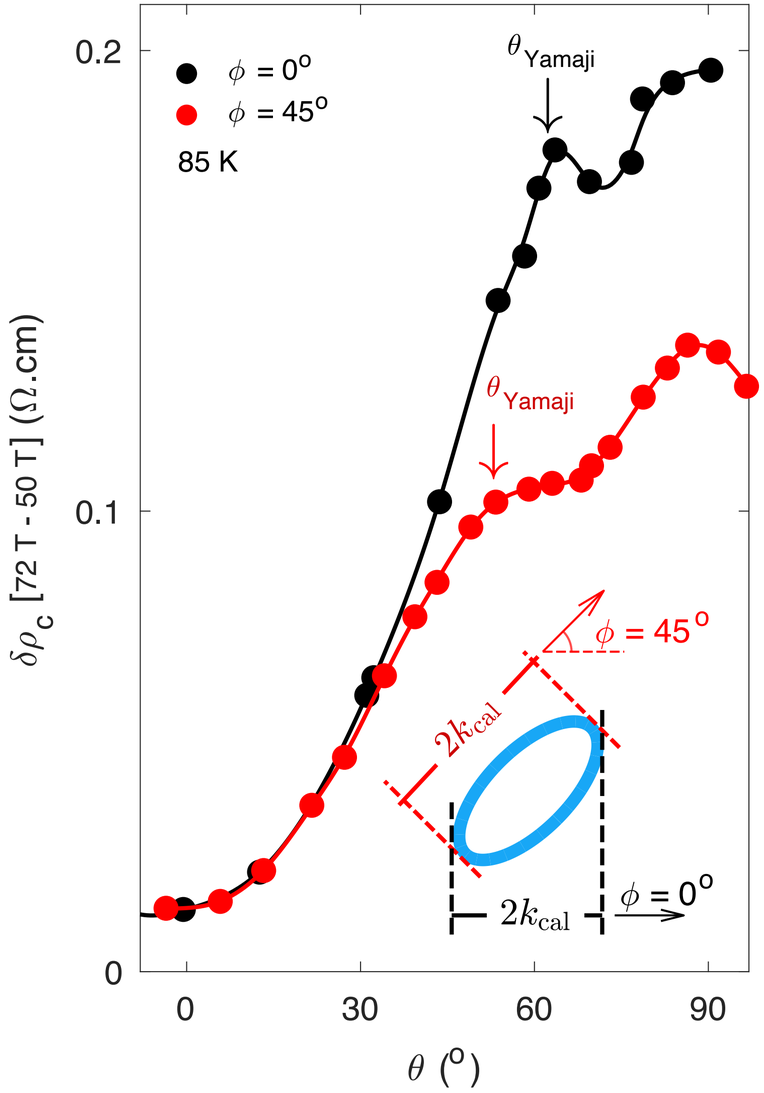

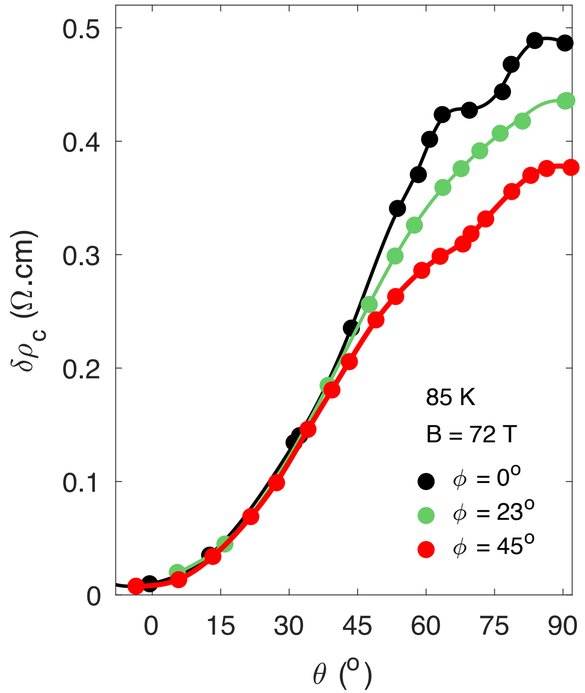

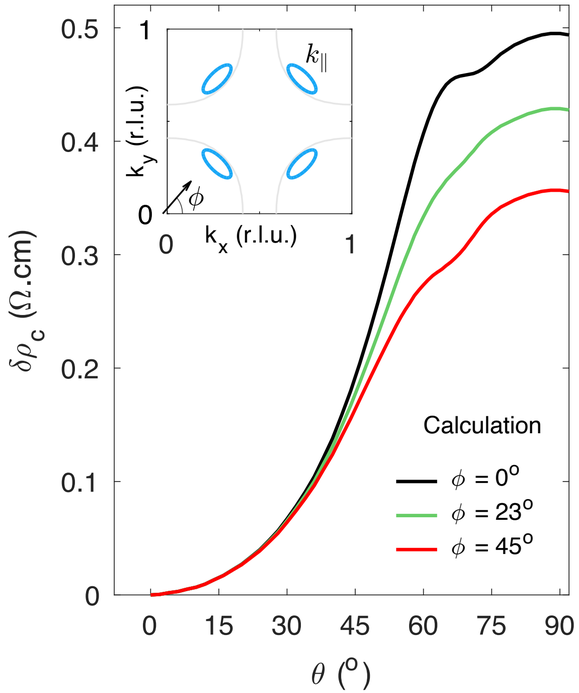

Doping
$p = 0.1$

"The small size of the pockets determined from the Yamaji effect is . . . approximately 1.3% of the Brillouin zone area"

FL* pocket fraction $= p/8 = 1.25\%$!

Fluctuating AF metal fraction $= p/4 = 2.5\%$. Yamaji effect requires correlated SDW order in the z direction, which is absent in $HgBa_2CuO_{4+\delta}$

($p/8$ also in YRZ ansatz, Peter Johnson photoemission, and Jenny Hoffman and Seamus Davis STMs; Stanescu-Kotliar)

Jing-Yu Zhao, S. Chatterjee, S. S., Ya-Hui Zhang, arXiv:2510.13943

Observation of the Yamaji effect in a cuprate superconductor

Mun K. Chan[1] ✉, Katherine A. Schreiber[1], Oscar E. Ayala-Valenzuela[1], Eric D. Bauer[2], Arkady Shekhter[1] & Neil Harrison[1]

nature physics
arXiv:2411.10631
Published online: 16 September 2025

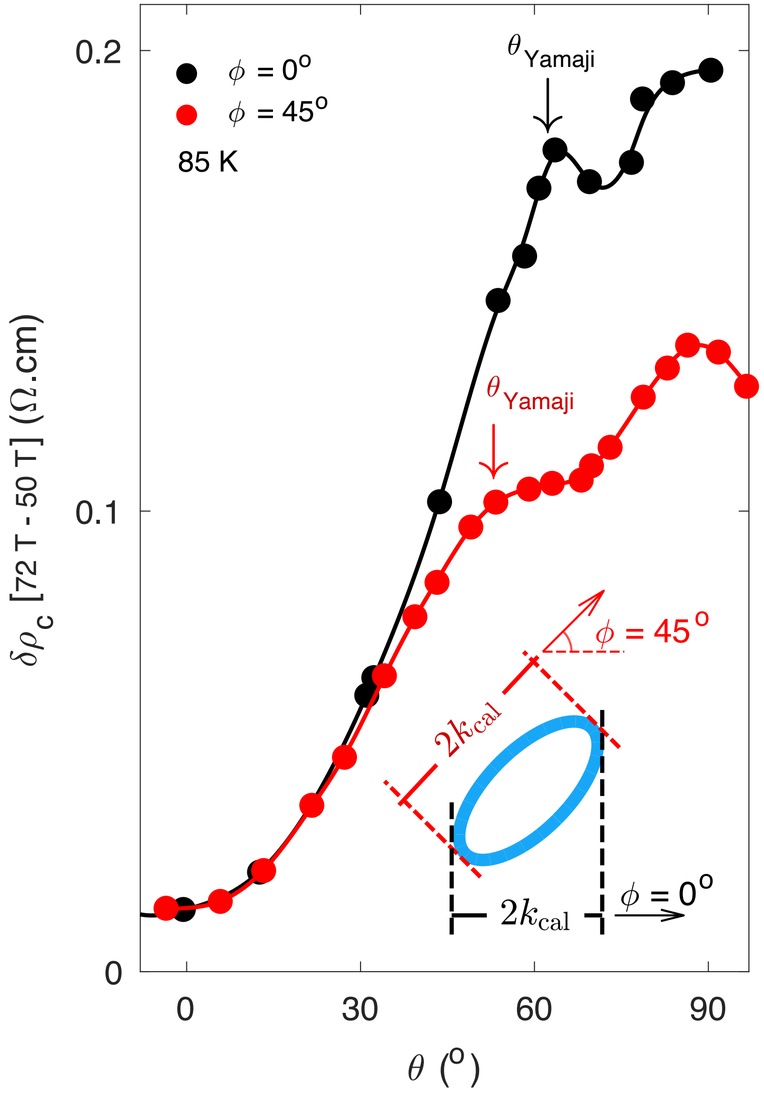

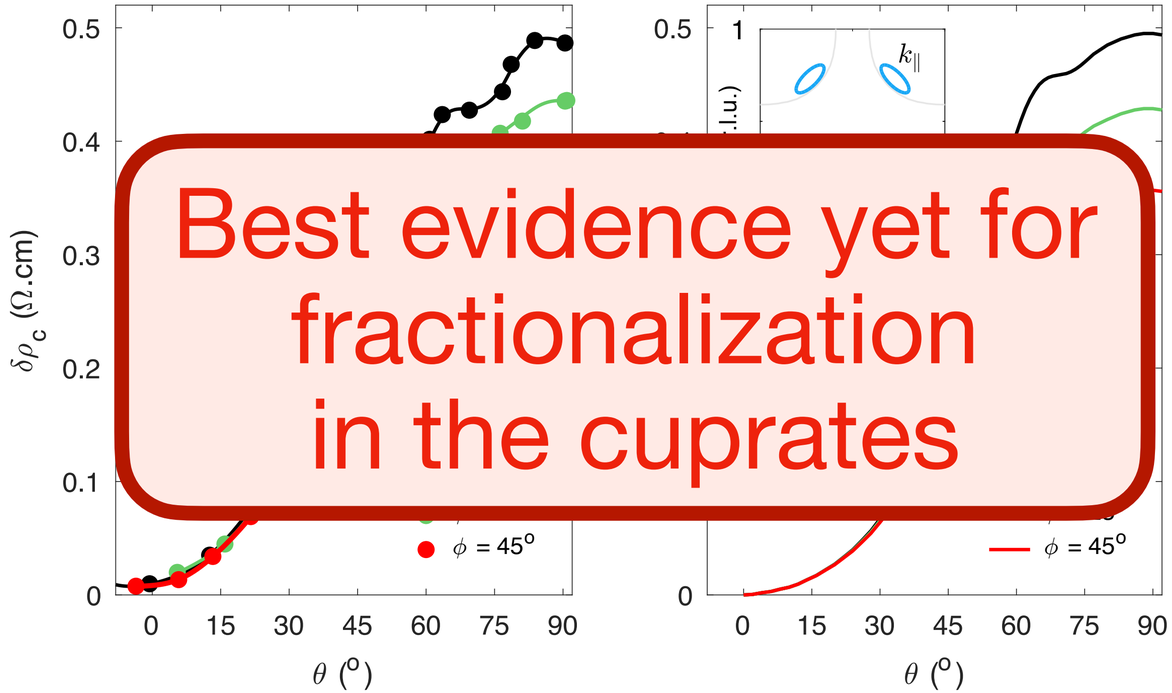

Best evidence yet for fractionalization in the cuprates

Doping $p = 0.1$

"The small size of the pockets determined from the Yamaji effect is . . . approximately 1.3% of the Brillouin zone area"

FL* pocket fraction $= p/8 = 1.25\%$!

Fluctuating AF metal fraction $= p/4 = 2.5\%$. Yamaji effect requires correlated SDW order in the z direction, which is absent in $HgBa_2CuO_{4+\delta}$

($p/8$ also in YRZ ansatz, Peter Johnson photoemission, and Jenny Hoffman and Seamus Davis STMs; Stanescu-Kotliar)

Jing-Yu Zhao, S. Chatterjee, S. S., Ya-Hui Zhang, arXiv:2510.13943

6. Fractionalized Fermi liquids (FL*)

Our motivation for studying quantum spin liquids has been to find a basis for a theory of the cuprate phase diagram. Christos *et al.* proposed [Christos et al., 2023] that the appropriate spin liquid was precisely that observed in various numerical studies of square lattice antiferromagnets: this is the spin liquid described by the $\mathbb{CP}^1$ theory of Section 1, which is dual to the SU(2) gauge theory of fermionic spinons in Section 3. The previous sections have shown that the theories of directly doping such spin liquids run into difficulties:

> Doping the $\mathbb{CP}^1$ spin liquid yields a holon metal state described in Section 4, which is a candidate for the pseudogap metal. However, as we discuss in Section 1, the holon metal is incompatible with recent angle-dependent magnetoresistance (ADMR) experiments [Fang et al., 2022, Chan et al., 2025].
>
> Doping the fermionic spin liquid can lead to a d-wave superconductor, as described in Section 5. However, the velocities of the nodal quasiparticles are nearly isotropic, with $v_F \sim v_\Delta$.

We now show that replacing the holon metal with another doped spin liquid phase, the fractionalized Fermi liquid (FL*), resolves both (and other) difficulties above. It agrees with the ADMR measurements in the pseudogap, and a confinement transition from FL* yields a

d-wave superconductor with anisotropic nodal velocities.

We begin by presenting the basic definition of the FL* state. Consider any system of $S = 1/2$ fermions of density ρ, with spin rotation invariance preserved. In the Fermi liquid (FL) state, Luttinger's argument [Luttinger, 1960] states that the fractional volume of the Brillouin zone enclosed by the Fermi surface should be $\rho/2$, modulo integers to account for filled bands. Oshikawa [Oshikawa, 2000] placed Luttinger's argument on a non-perturbative basis by related to an anomaly associated with translations and charge conversation. This is summarized in Fig. 22.

Fermi liquid

Spin-1/2 holes of density
$\rho = 1 + p$

Positive Hall coefficient
of carrier density ρ

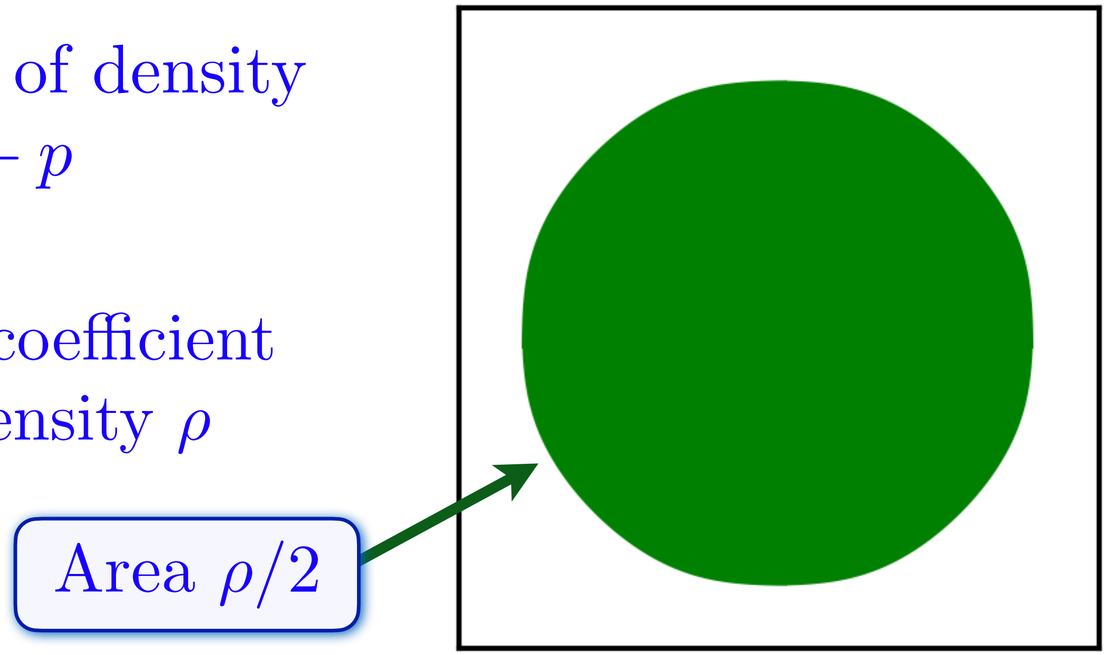

Luttinger, 1960: Area enclosed by the Fermi surface is the same as that for free fermions *with the same symmetry.*

Oshikawa, 2000: Area constrained by a 't Hooft anomaly of global U(1) and translations

Figure 22: Properties of the Fermi liquid (FL) state.

The idea of a 'fractionalized Fermi liquid' (FL*) was introduced in Refs. [Senthil et al., 2003, Senthil et al., 2004c], as a metallic state in which the Fermi surface did *not* obey the Luttinger constraint. In the simplest case, the fractional volume enclosed by the Fermi surface in FL* is $(\rho - 1)/2$. The central point [Senthil et al., 2004c, Paramekanti and Vishwanath, 2004, Qi and Sachdev, 2010, Sachdev et al., 2012, Bonderson et al., 2016, Else et al., 2021, Sachdev, 2023] was that it was possible to satisfy Oshikawa's anomaly by combining the anomaly of a Fermi surface (which contributes an amount equivalent to a density $\rho - 1$) with that of a fractionalized spin liquid (which contributes an amount equivalent to a density 1). It is trivially possible to shift ρ by an even integer by adding and removing filled bands, and the novelty is the shift in FL* by an odd integer. This is summarized in Fig. 23.

Fractionalized Fermi liquid (FL*)

Spin-1/2 holes of density
$\rho = 1 + p$

Positive Hall coefficient
of carrier density $\rho - 1$

Total area
$(\rho - 1)/2$

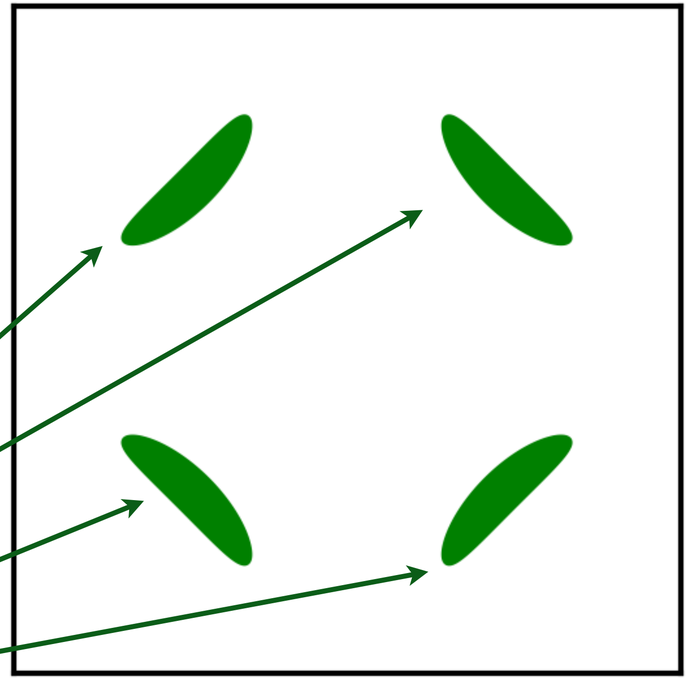

Oshikawa anomaly is satisfied by the sum of
spin liquid (1) and
Fermi surface anomalies $(\rho - 1)$

Figure 23: Properties of the fractionalized Fermi liquid (FL*) state.

6.1. FL* in single band models

Next, we describe here construction of the FL* phase in a single band model, such as the square lattice Hubbard model (possibly with additional short-range interactions) of interest for the cuprates. At the level of cartoon pictures, we illustrate the structure of the FL* and other states in Fig. 24 [Punk et al., 2015]. This figure describes three distinct metallic phases in a Hubbard time model with electron density $1 - p$. Recall that in the absence of a broken symmetry, the Luttinger constraint on hole Fermi surfaces is that they have a fractional area per spin of $(1 + p)/2$, relative to the area of the full square lattice Brillouin zone.

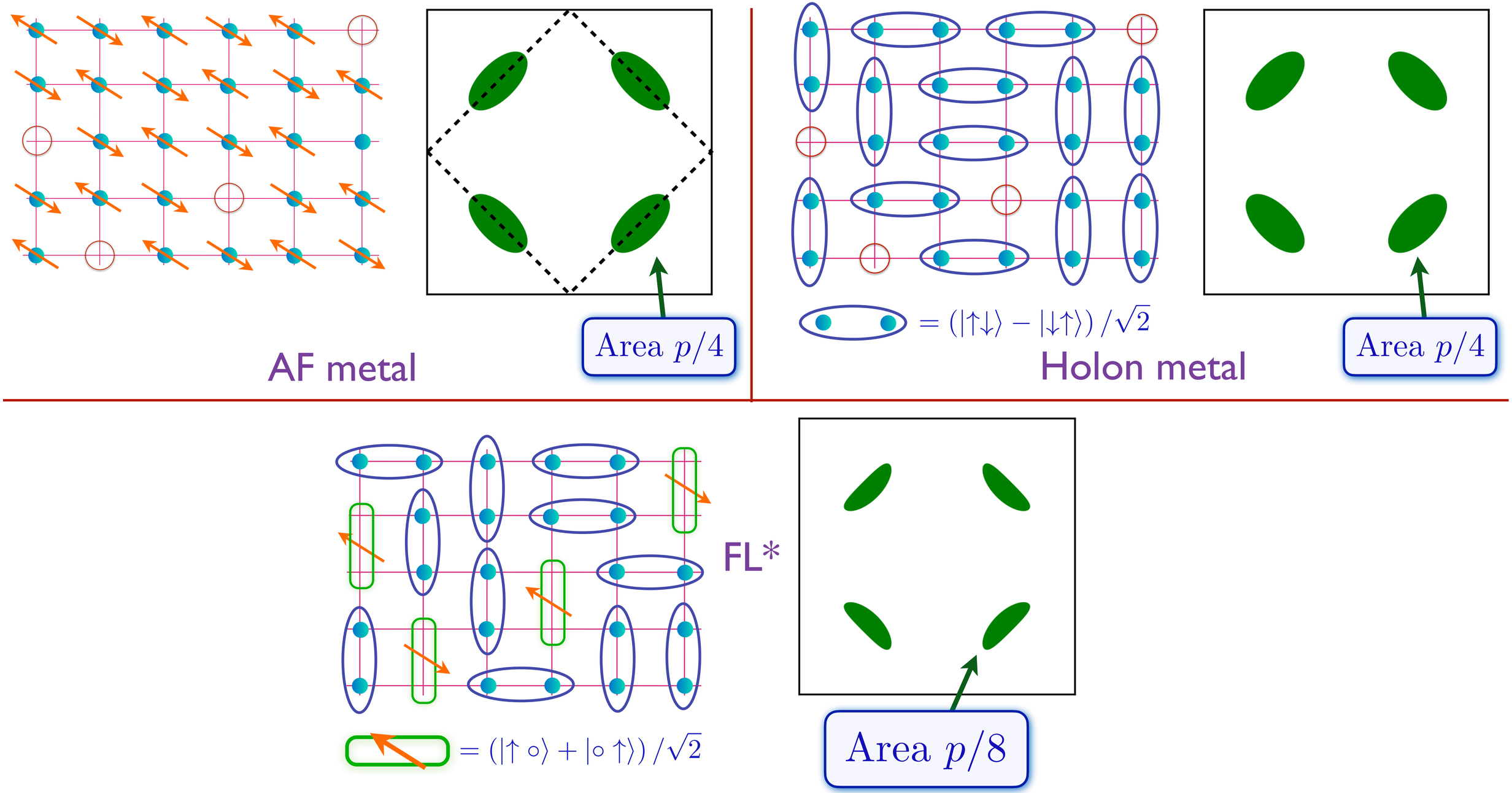

Figure 24: Cartoon pictures of different states of doped antiferromagnets; adapted from

Ref. [Punk et al., 2015]. The areas are those that would be measured by a probe such as quantum oscillation. The AF metal has long-range antiferromagnetic order, and the reduced Brillouin zone is shown with the dashed line. The other phases do not break any symmetries. The open circles are holons, and these are assumed fermionic in the holon metal. The green dimers represent bound states of holons and spinons. Note that all 3 states would show a Hall co-efficient of density p positively charged carries.

AF Metal. This is a state with antiferromagnetic long-range order, which we described in Section 1. We can understand the Fermi surface by considering free electrons moving in a background with the same symmetry *i.e.* in a background spin-dependent potential which has a modulation at the wavevector (π, π). This leads to the magnetic Brillouin zone boundary shown by the dashed line, and 4 hole pocket Fermi surfaces. Only two of these pockets are independent within the magnetic Brillouin zone. After accounting for a factor of 2 from spin, we conclude that the fractional area of each pocket is $p/4$. This Fermi surface area obeys the Luttinger constraint. Thermal fluctuations do not move Fermi surfaces, only broaden them, and so we expect that a fluctuating spin density wave state will also have pockets of area $p/4$ [Schmalian et al., 1998, Schmalian et al., 1999, Ye and Chubukov, 2023, Kokkinis and Chubukov, 2025].

Holon metal. This is a state with no broken symmetry, in which the electrons have paired

up in singlet bonds which resonate with each other. The dopants are realized by spinless mobile vacancies of charge $+e$, known as holons. The density of holons is p, and if the holons are fermions, they will form Fermi surfaces corresponding to spinless free fermions of density p. If there are four distinct Fermi surfaces in the Brillouin zone (as is the case in many computations), then the fractional area of each pocket will be $p/4$. Although this area is the same as that for the AF metal, the reason is very different. Now there is no broken symmetry, and the fermionic quasiparticles are spinless holons. This Fermi surface area does *not* obey the Luttinger constraint, and this is permitted because of the presence of the spin liquid. A systematic, gauge theoretic treatment of the holon metal state was presented in Section 4 and Refs. [Sachdev et al., 2009, Chowdhury and Sachdev, 2015a, Chowdhury and Sachdev, 2015b, Chatterjee et al., 2017, Wu et al., 2018, Scheurer et al., 2018, Sachdev, 2019, Sachdev et al., 2019, Wu et al., 2020, Bonetti and Metzner, 2022, Scholle et al., 2023], and it is relevant to ultracold studies of the Hubbard model on the Lieb lattice [Lebrat et al., 2024, Nikolaenko et al., 2025].

FL.* Finally, we turn to the metallic state of interest. The holon metal state also has spinon excitations, which can be created out of the ground state. Now imagine a situation in which each holons gains energy by binding with a spinon, so that the system can pay the price for creating the spinons. Then the ground state will change into one in

which the mobile charge carriers are holon-spinon bound states [Ribeiro and Wen, 2005, Kaul et al., 2007, Kaul et al., 2008, Qi and Sachdev, 2010, Lau et al., 2011b, Moon and Sachdev, 2011, Lau et al., 2011a, Mei et al., 2012, Punk and Sachdev, 2012, Punk et al., 2015, Feldmeier et al., 2018, Grusdt et al., 2018, Chiu et al., 2019, Grusdt et al., 2023, Schlömer et al., 2024, Nyhegn et al., 2025]. These bound states are always fermions with charge $+e$, spin $S = 1/2$, just like a hole. Treating these holes as free fermions, we conclude that the total area of the Fermi surface should be $p/2$. If there are 4 distinct pockets (as there in the computation below), then each pocket will have the distinctive area of $p/8$. This Fermi surface area also does *not* obey the Luttinger constraint.

We highlight key features of the single-band FL* state of Ref. [Punk et al., 2015] in Fig. 24. We will see that these features will also play a key role in the Ancilla Layer Model of Section 2, as we illustrate later in Fig. 29.

The electron quasiparticle of FL* is a (green) "dimer" in Fig. 24, a bound state of a spin and vacancy.

FL* has a background of spinon excitations obtained by breaking singlet bonds (the blue dimers) in Fig. 24.

Recent ADMR observations by Fang *et al.* [Fang et al., 2022] and Chan *et al.* [Chan et al., 2025] in the pseudogap metal and well modeled by hole pockets containing quasiparticles which can tunnel coherently between layers. This is not possible for the holon metals as the holons carry charges of distinct emergent gauge fields within each layer. In the AF metal coherent tunneling requires significant interlayer spin correlations, which are not observed [Tabis et al., 2014, Anderson et al., 2025], but could perhaps be induced by the applied magnetic field. The FL* quasiparticles are gauge neutral and can indeed tunnel coherently between layers. So even at the outset, these observations favor a FL* description of the pseudogap phase of the cuprates [Zhao et al., 2025].
Moreover, the observations of Chan *et al.* [Chan et al., 2025] also provide a quantitative correspondence with the FL* theory. Their observation of the Yamaji effect in the cuprate $HgBa_2CuO_{4+\delta}$ show pockets of a fractional area of 'approximately 1.3%' at a doping $p = 0.1$,

close to the value $p/8 = 1.25\%$ predicted for FL* [Senthil et al., 2003, Senthil et al., 2004c, Kaul et al., 2007, Qi and Sachdev, 2010, Nikolaenko et al., 2023, Zhao et al., 2025].

6.2. Layer construction with ancilla qubits

While much insight can be gained from the methods above, they fall short of providing a mean-field theory for the FL* phase, which could be used to study quantum phase transitions out of it. A suitable mean field theory can also lead to a trial wavefunction for the FL* state, which can be used for variational numerical computations and compared to cold atom observations [Koepsell et al., 2021, Müller et al., 2025, Shackleton and Zhang, 2024], as discussed in Section 4. To these ends, we now describe the Ancilla Layer Model (ALM) [Zhang and Sachdev, 2020b, Zhang and Sachdev, 2020a], which also easily ensures consistency with anomaly arguments.

We wish to have a mean-field theory which changes a large hole-like Fermi surface of area $(1+p)/2$ to small hole-like Fermi surfaces of total area $p/2$. The simplest way to achieve this in mean-field theory is to hybridize the large Fermi surface with another band at half-filling (as in the Kondo lattice, and was done by Yang-Rice-Zhang [Yang et al., 2006])—this leads to a Fermi surface of the needed area $(1+p+1)/2 \ (\text{mod } 1) = p/2$. But we are *not allowed* to add a single band at half-filling because it is not 'trivial' *i.e.* it is not anomaly-free, and its excitations cannot be integrated out because the extra band can only acquire a gap with a broken symmetry. On the other hand, we *are allowed* to add two bands at half filling each (or any even number of bands), because they can form a trivial insulator with a gap. After the first added band hybridizes with the physical electrons to yield the small Fermi surfaces, the

second added band is left decoupled, and it can form the spin liquid needed to satisfy the Oshikawa anomaly. This is the essence of the ALM.

We begin with a constructive derivation of the ALM starting from the familiar Hubbard model in Eq. (1), and proceeding to the paramagnon representation in Eq. (4). After some renormalization of the high energy states we give the paramagnon $\mathcal{P}$ some independent dynamics with a non-zero mass $m_{\mathcal{P}}$, and obtain its effective Lagrangian

$$\mathcal{L}[\mathcal{P}] = \sum_{\boldsymbol{i}} \left[\frac{m_{\mathcal{P}}}{2} \left(\partial_\tau \mathcal{P}_{\boldsymbol{i}}\right)^2 + \frac{3U}{8} \mathcal{P}_{\boldsymbol{i}}^2 \right] , \tag{123}$$

where the $\mathcal{P}^2$ term is as in Eq. (4). This is a paramagnon theory with 3 local harmonic oscillators on each site. Now we take steps different from conventional paramagnon approaches. The ground state of the paramagnon theory is obtained when all three oscillators are in the $n = 0$ state: $|0, 0, 0\rangle$. There is a triplet of first excited states:

$$|1, 0, 0\rangle \sim \mathcal{P}_{\boldsymbol{i}x} |0, 0, 0\rangle ; |0, 1, 0\rangle \sim \mathcal{P}_{\boldsymbol{i}y} |0, 0, 0\rangle ; |0, 0, 1\rangle \sim \mathcal{P}_{\boldsymbol{i}z} |0, 0, 0\rangle .$$

We can map this low energy spectrum to that of a pair of $S = 1/2$ ancilla spins with a mutual interaction $J_\perp \boldsymbol{S}_{1\boldsymbol{i}} \cdot \boldsymbol{S}_{2\boldsymbol{i}}$. By comparing the above matrix elements to those that couple the

singlet and triplet spin states states, we obtain the operator identification

$$\boldsymbol{\mathcal{P}_i} \sim \boldsymbol{S}_{1\boldsymbol{i}} - \boldsymbol{S}_{2\boldsymbol{i}} \,. \tag{124}$$

Inserting Eq. (124) into Eq. (4), we obtain the Hamiltonian of the ALM, $\mathcal{H}_{\mathrm{ALM}}$, which is a simple augmentation of a Kondo lattice Hamiltonian $\mathcal{H}_{\mathrm{KL}}$ by the layer of $\boldsymbol{S}_{2\boldsymbol{i}}$ spins

$$\begin{aligned}
\mathcal{H}_{\mathrm{ALM}} &= \mathcal{H}_{\mathrm{KL}} + J_\perp \sum_{\boldsymbol{i}} \boldsymbol{S}_{1\boldsymbol{i}} \cdot \boldsymbol{S}_{2\boldsymbol{i}} + \sum_{\boldsymbol{i}<\boldsymbol{j}} J_{\boldsymbol{ij}}\, \boldsymbol{S}_{2\boldsymbol{i}} \cdot \boldsymbol{S}_{2\boldsymbol{j}} \\
\mathcal{H}_{\mathrm{KL}} &= \sum_{\boldsymbol{i}<\boldsymbol{j}} J_{1,\boldsymbol{ij}}\, \boldsymbol{S}_{1\boldsymbol{i}} \cdot \boldsymbol{S}_{1\boldsymbol{j}} - \sum_{\boldsymbol{i},\boldsymbol{j}} t_{\boldsymbol{ij}}\, c^\dagger_{\boldsymbol{i}\alpha} c_{\boldsymbol{j}\alpha} + \sum_{\boldsymbol{i}} \frac{J_K}{2} \boldsymbol{S}_{1i} \cdot c^\dagger_{\boldsymbol{i}\alpha} \boldsymbol{\sigma}_{\alpha\beta} c_{\boldsymbol{i}\beta} \,.
\end{aligned} \tag{125}$$

This Hamiltonian is illustrated in the bottom half of Fig. 25.

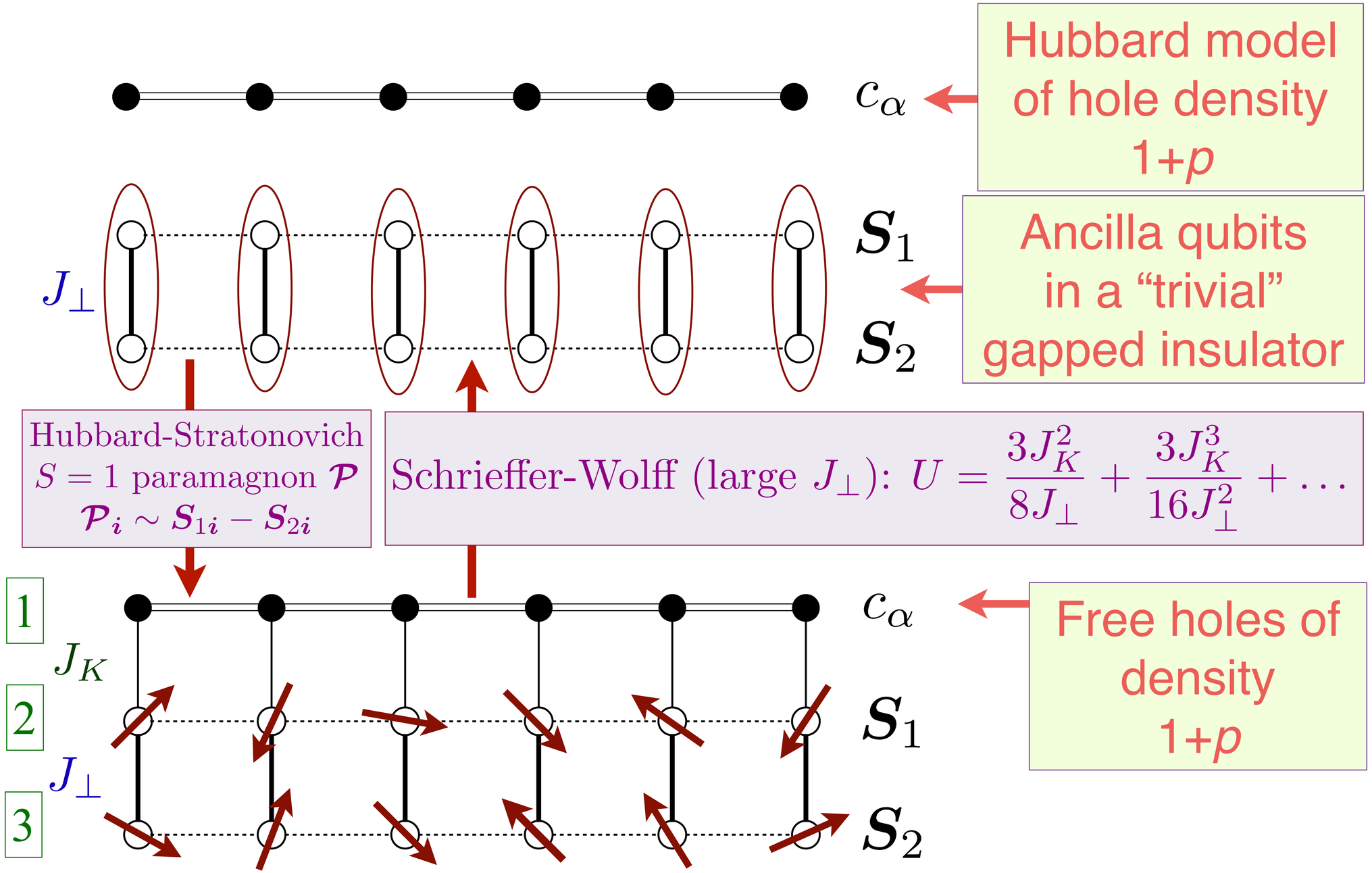

Figure 25: Illustration of the mapping from a single-band Hubbard model with decoupled ancilla qubits,

to a single band with free fermions coupled to a bilayer antiferromagnet. The Schrieffer-Wolff transformation is derived in Ref. [Nikolaenko et al., 2021], and the Hubbard-Stratonovich transformation is derived in Ref. [Mascot et al., 2022]. The layer numbers of the layer construction with ancilla qubits are indicated in the bottom picture.

So we see that the ancilla spins are simply the fractionalization of the familiar $S = 1$ paramagnon into a pair of $S = 1/2$ spins [Mascot et al., 2022]. The above derivation of the mapping to the ALM yields an additional ferromagnetic Kondo interaction between the electrons $c_{\boldsymbol{i}\alpha}$ and spins $\boldsymbol{S}_{2\boldsymbol{i}}$. Ferromagnetic Kondo couplings are expected to be irrelevant, and we will note this coupling again in Eq. (131). We have also explicitly included a direct exchange interaction between the $\boldsymbol{S}_{2\boldsymbol{i}}$ spins, as it will be important for our purposes below. Note that there is no Hubbard interaction U in $\mathcal{H}_{\mathrm{ALM}}$, and it has been replaced by the Kondo interaction J_K in $\mathcal{H}_{\mathrm{ALM}}$.
We discuss the phase diagram of $\mathcal{H}_{\mathrm{ALM}}$ shown in Fig. 26.

Fermi-volume-changing QPT in a single band model

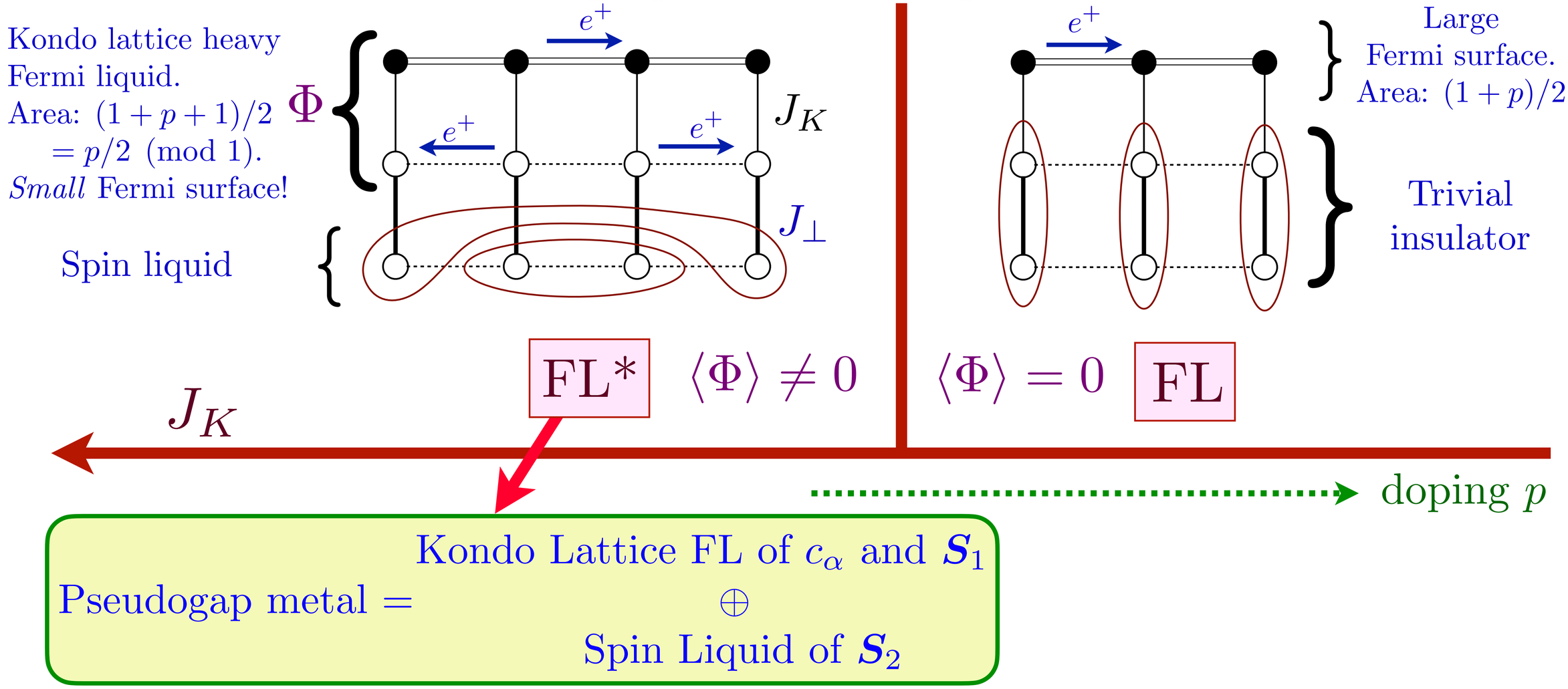

Figure 26: Phases of the Ancilla Layer Model. The noted areas are per spin. The phases are distinguished by the condensation of the boson Φ, which hybridizes the conduction electrons in the top

layer with the fermionic spinons in the middle layer.

At small J_K, the ancilla spins decouple into rung singlets, and we are back to a c_α state adiabatically connected to free electrons, which is the conventional Fermi liquid with a large hole pocket of area $(1+p)/2$.
At large J_K, we assume that the c_α electrons and $\boldsymbol{S}_1$ spins realize the commonly observed heavy Fermi liquid (FL) phase of $\mathcal{H}_{\rm KL}$. With the density of c_α equal to $1+p$, the total density of the 'large' Fermi surface is $2+p$. As a trivial filled band with density 2 can always be removed, we obtain 'small' Fermi surface associated with density p in the FL phase of $\mathcal{H}_{\rm KL}$. So the total area of hole pockets is $p/2$. While this is the Luttinger value for $\mathcal{H}_{\rm KL}$, it is *not* for $\mathcal{H}_{\rm ALM}$. The $\boldsymbol{S}_{2\boldsymbol{i}}$ have an effective ferromagnetic Kondo coupling to the conduction electrons c_α (mediated by the antiferromagnetic $J_\perp$ and the antiferromagnetic J_K), and so we can expect them to decouple from the top two layers. Indeed, we obtain a FL* phase for $\mathcal{H}_{\rm ALM}$ if the $\boldsymbol{S}_{2\boldsymbol{i}}$ layer forms a spin liquid, and the effects of $J_\perp$ in Eq. (125) can be treated perturbatively. This leads the identification in Fig. 26 of the FL* pseudogap metal with the combination of a Kondo lattice FL state of c_α and $\boldsymbol{S}_1$, and a spin liquid of $\boldsymbol{S}_2$.

6.3. Mean field theory of the cuprate pseudogap.

We can now obtain a mean-field theory of the pseudogap by extending the Kondo lattice mean-field theory to the Hamiltonian $\mathcal{H}_{\rm ALM}$ in Eq. (125).
We begin with the top two layers of electrons c_α and spins $\boldsymbol{S}_1$ in the ALM in Fig. 25. We proceed with parton decomposition of $\boldsymbol{S}_1$ in terms of the fermionic spinons $f_{1\alpha}$ as in Eq. (73)

$$\boldsymbol{S}_{1\boldsymbol{i}} = \frac{1}{2} f^\dagger_{1\boldsymbol{i}\alpha} \boldsymbol{\sigma}_{\alpha\beta} f_{1\boldsymbol{i}\beta} \,, \tag{126}$$

and obtain the mean-field fermion Kondo lattice Hamiltonian for the c_α and $f_{1\alpha}$:

$$\mathcal{H}_{\rm KLmf} = \sum_{\boldsymbol{i},\boldsymbol{j}} \left[-t_{\boldsymbol{ij}} c^\dagger_{\boldsymbol{i}\alpha} c_{\boldsymbol{j}\alpha} - t_{1,\boldsymbol{ij}} f^\dagger_{1\boldsymbol{i}\alpha} f_{1\boldsymbol{j}\alpha} \right] - \sum_{\boldsymbol{i}} (\Phi \, c^\dagger_{\boldsymbol{i}\alpha} f_{1\boldsymbol{i}\alpha} + \Phi^* \, f^\dagger_{1\boldsymbol{i}\alpha} c_{\boldsymbol{i}\alpha}) \,. \tag{127}$$

Here Φ is decoupling field of the J_K exchange interaction in Eq. (125), and is illustrated in Fig. 30. At the mean-field level, we can assume the $\boldsymbol{S}_2$ spin liquid remains decoupled, and important effects of this spin liquid will be discussed in Section 5.
When considered as a theory of the Kondo lattice model $\mathcal{H}_{\rm KL}$, the FL state corresponds to the condensation of the decoupling field Φ. On the other hand, on the Hilbert space of the full $\mathcal{H}_{\rm ALM}$, this same Φ condensed phase is the FL* state. This interesting inversion is highlighted in Fig. 27: the single band model has an 'inverted' Kondo lattice transition.

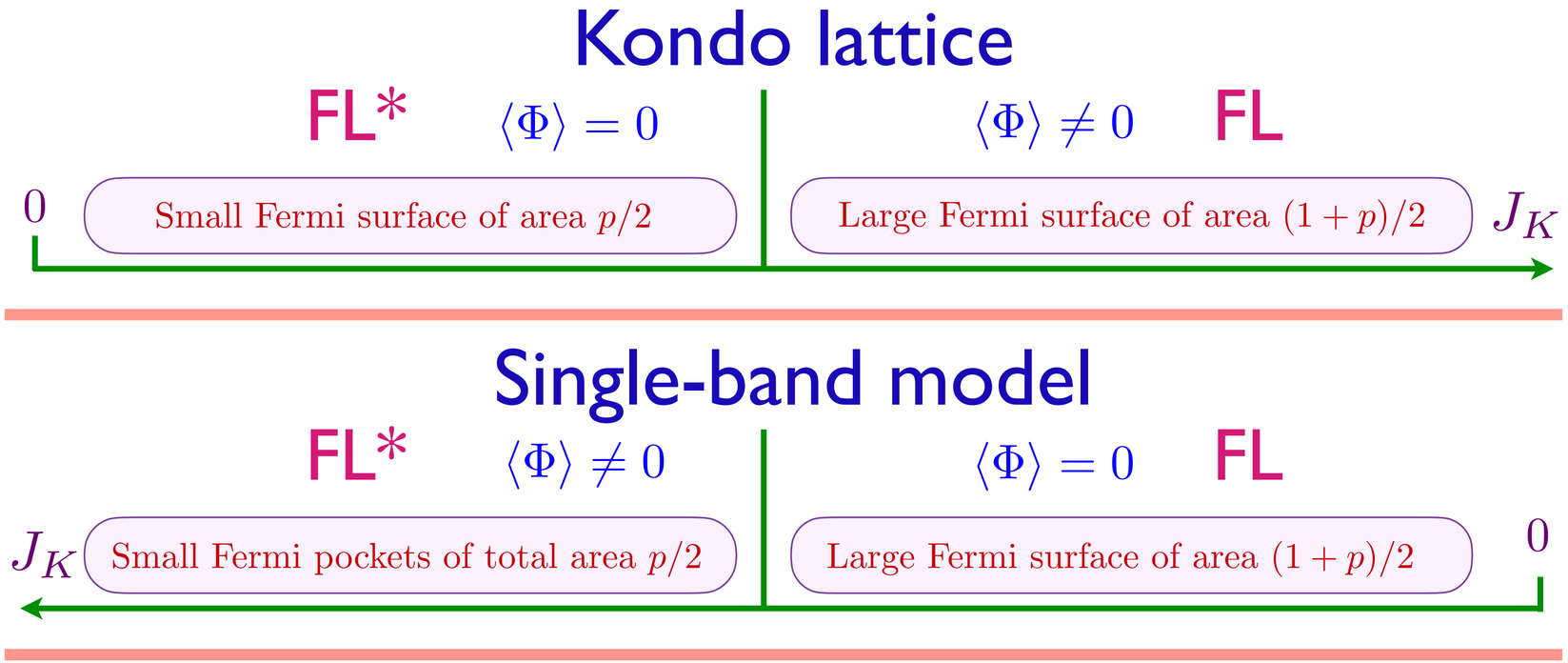

Figure 27: Comparison of the phases of the Kondo lattice model and the Ancilla Layer Model of the single band Hubbard model in Fig. 26. There is an inversion in the phase in which Φ is condensed.

The magnitude of Φ determines the value of the electronic gap in the anti-nodal region of the Brillouin zone (near momenta $(\pi, 0)$, $(0, \pi)$).

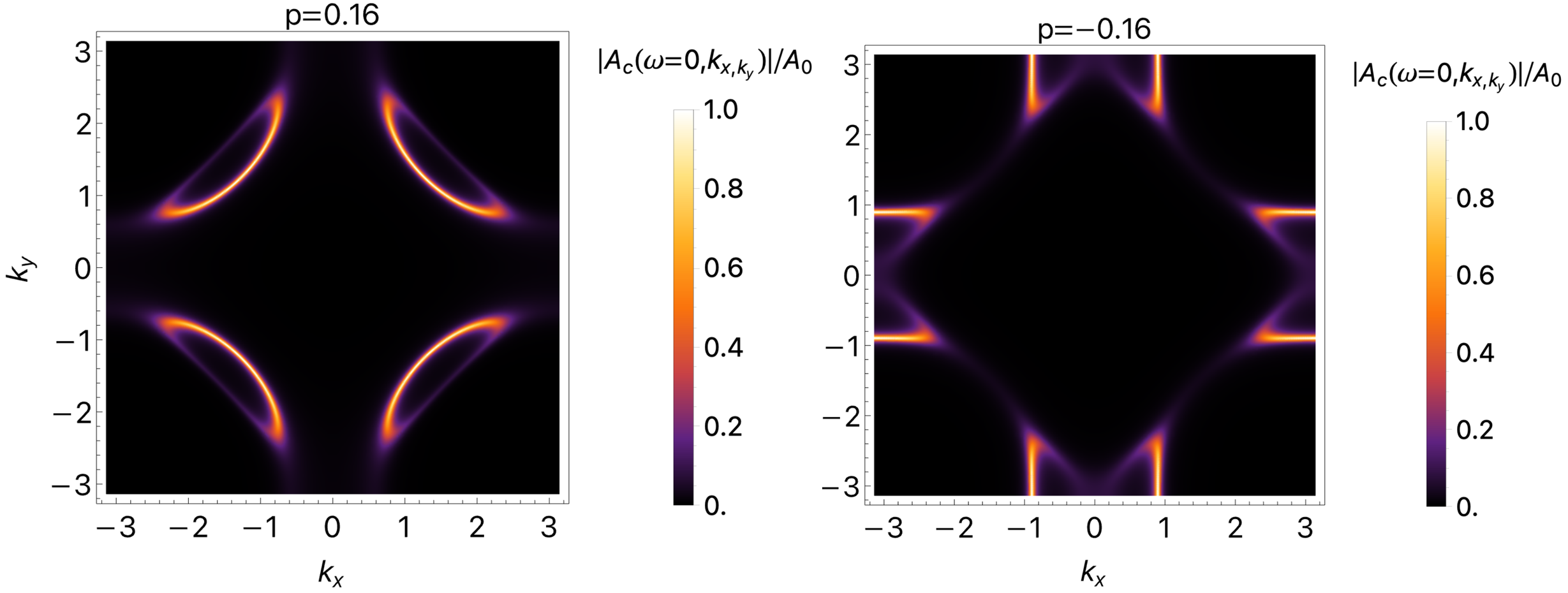

Figure 28: Spectral density of hole (left) and electron (right) pockets at $p = 0.16$ and $p = -0.16$ respectively in the FL* state. The fractional area of each hole pocket is $p/8$, and the fractional area of the electron pocket is $|p|/4$. Compared to Fig. 6 for the SDW state, the pocket areas have been halved in the FL* state.

Fig 28 shows the electron spectral density (as measured by photoemission) at zero frequency

for both the electron and hole pockets, computed by diagonalizing Eq. (127).
We can now present in Fig. 29 the close analogy between the FL* state obtained in the ALM and the state presented in Fig. 24 as highlighted in the box before the beginning of Section 2

> The electron quasiparticle of FL* is the hybridization of c_α and $f_{1\alpha}$ induced by Φ, which creates the bound state $\sim c_{\boldsymbol{i}\alpha} f^\dagger_{1\boldsymbol{i}\alpha}$ between a vacancy and a spin, analogous to the green dimers in Fig. 24.
>
> The background of spinons in FL* are obtained from the spin liquid of $\boldsymbol{S}_2$ spinons in the bottom layer, analogous the spinons obtained by breaking the blue dimers in Fig. 24. We will later represent these spinons by f_α via Eq. (129).

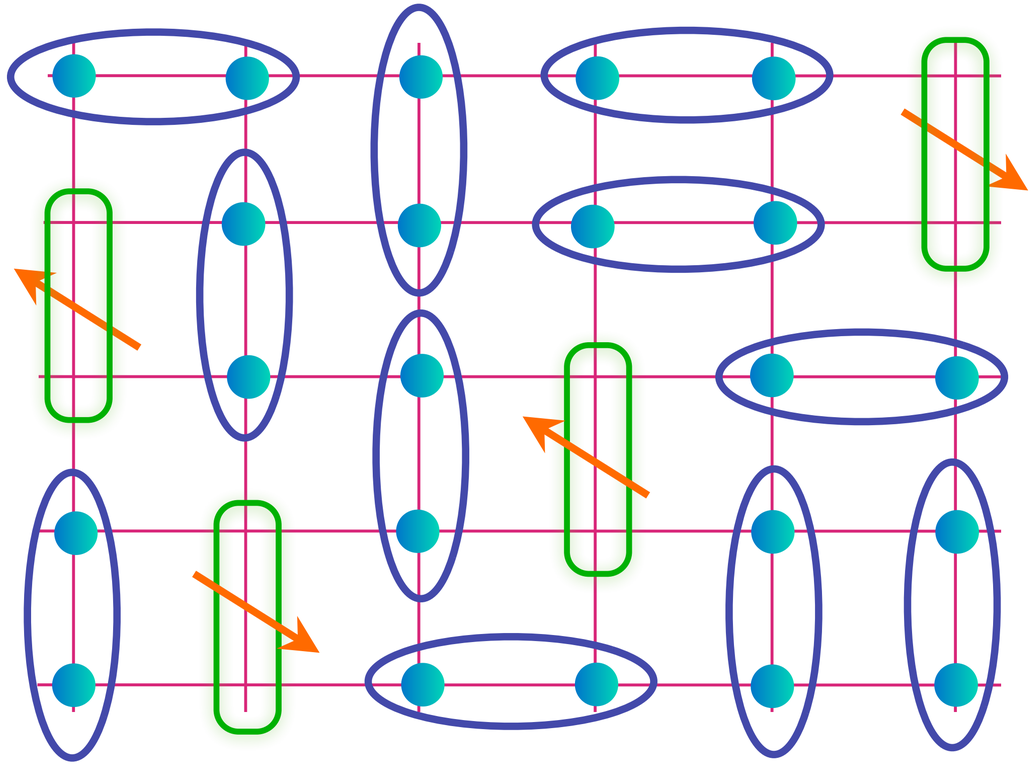

(a) FL* state on a square lattice (top view) of N sites and Np holes. This implies Np green dimers and $N(1-2p)/2$ blue dimers.

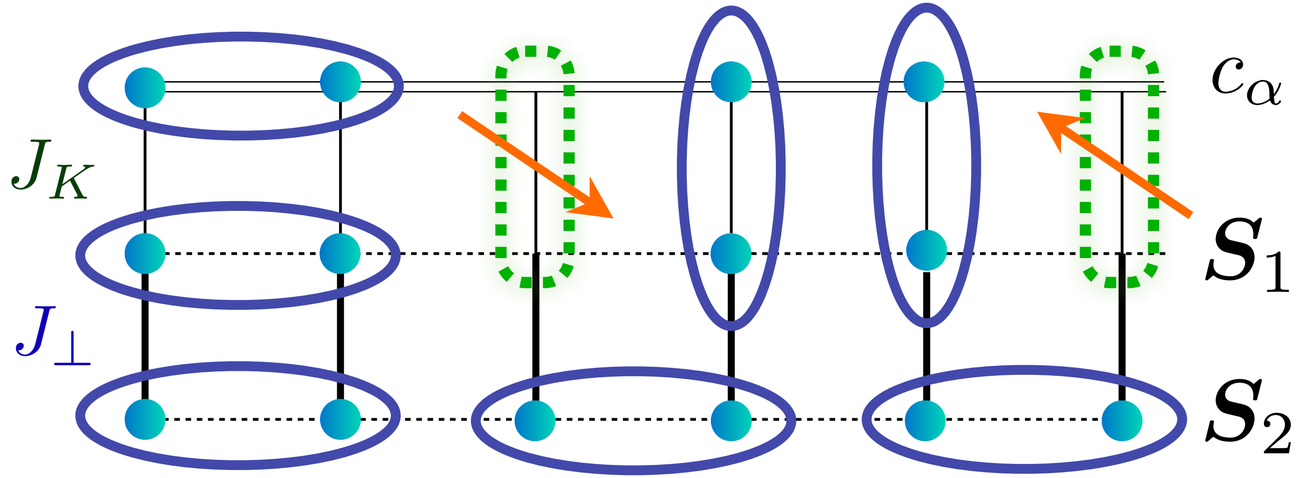

(b) FL* state of ancilla model with 3 square lattice layers (edge view) of $3N$ sites and Np holes. This implies Np green dimers and $N + N(1-2p)/2$ blue dimers.

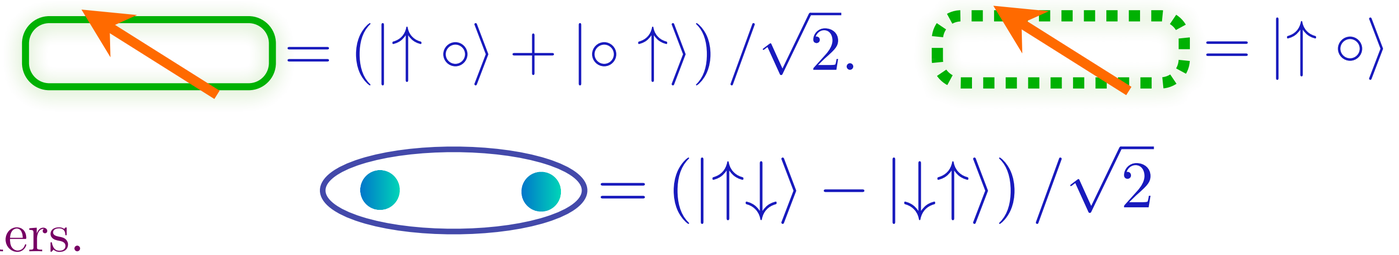

Figure 29: Comparison between (a) the quantum dimer theory of the square lattice FL* state [Punk et al., 2015] and the (b) ancilla layer theory. The dashed green dimer is the state $c_{i\alpha} f_{1i\alpha}^\dagger$ created by the hybridization Φ in the ALM. Note that the ALM has exactly N blue dimers more than the dimer model, and these extra dimers are the number in a trivial rung-singlet bilayer antiferromagnet.

A key observation is that the number of spin-singlet blue dimers in the ALM is exactly N more than in the dimer model of Fig. 24, while the number of green dimers is the same. This is acceptable because N spin singlets is precisely the number that can be accommodated in a trivial rung-singlet state of a bilayer antiferromagnet.

The connection in Fig. 29 shows that the ALM is, in a sense, 'minimal'. For a FL* mean field theory with both a small Fermi surface and spinons, we need the middle and bottom ancilla layers to provide the vacancy-spin and singlet valence bonds respectively. And a bonus, not available in the quantum dimer analysis of Ref. [Punk et al., 2015, Feldmeier et al., 2018] or other approaches [Ribeiro and Wen, 2005, Mei et al., 2012, Punk and Sachdev, 2012], is that it also provides a mean-field theory which captures the FL large Fermi when the bottom two layers are in a rung-singlet state.

6.4. Wavefunction for FL* and cold atom observations.

A separate mean-field approach is to work with variational wavefunctions. The ancilla layer method was the first to provide a variational wavefunction for the FL* phase of the single-band Hubbard model. This approach couples all three layers together in the proposed wavefunction [Zhang and Sachdev, 2020b]

$$\begin{aligned} |\mathrm{FL}*\rangle \;\; = \;\; & [\text{Projection onto rung singlets of } \boldsymbol{S}_1, \boldsymbol{S}_2] \\ & \bowtie |\text{Slater determinant of } (c, f_1)\rangle \\ & \otimes |\text{Spin liquid of } \boldsymbol{S}_2\rangle \; . \end{aligned} \tag{128}$$

Here f_1 is obtained from the parton decomposition of $\boldsymbol{S}_1$ in Eq. (126). Note that this wavefunction depends only upon the co-ordinates of the c electrons alone, as the co-ordinates of the f, f_1 fermions have been projected out. This wavefunction replaces the 'vanilla' Gutzwiller projected wavefunctions of the c electrons alone [Anderson et al., 2004] in the underdoped region. We see rather explicitly in Eq. (128) the expressivity of the layered construction [Rumelhart et al., 1986], allowing us to include both a small Fermi surface and a spin liquid in the same state.

The wavefunction Eq. (128) has been studied numerically in Refs. [Müller et al., 2025, Shackleton and Zhang, 2024, Zhou et al., 2024a], with the couplings in $\mathcal{H}_{\mathrm{KLmf}}$ treated as variational parameters. The results of

Refs. [Müller et al., 2025, Shackleton and Zhang, 2024] successfully capture the evolution of local, multi-point spin and charge correlations with doping as measured in cold atom experiments on the square lattice fermionic Hubbard model [Koepsell et al., 2021]. The results of Ref. [Zhou et al., 2024a] compare well with the exact diagonalization of Hubbard models in one and two dimensions.

6.5. SU(2) gauge theory of the onset of *d*-wave superconductivity from FL*

This section addresses the fate of the FL* pseudogap as the temperature is lowered, upon including the coupling to the $\boldsymbol{S}_2$ spin liquid in $\mathcal{H}_{\text{pseudogap}}$ in Eq. (132). This Hamiltonian specifically choses the π-flux spin liquid of Section 3 for the $\boldsymbol{S}_2$ layer. We will show that for this spin liquid there is a transition to a conventional BCS-type d-wave superconductor, with anisotropic nodal velocities for the Boboliubov quasiparticles, and $h/(2e)$ vortices.

Nevertheless the transition itself is not of the BCS type with a Cooper-pairing instability of a Fermi surface. Instead, the transition is driven by the confinement of the fractionalized excitations of the $\boldsymbol{S}_2$ spin liquid. We also find nearby instabilities to charge ordering, consistent with observations—see the review in Ref. [Bonetti et al., 2025] for more information.

We note here recent numerics which support the idea of the d-wave superconductor emerging from the doping-induced confinement of the π-flux spin liquid. As we have discussed in Section 3, the π-flux spin liquid is one description of the quantum-criticality between the Néel and VBS states. The numerical studies of Refs. [Jiang and Kivelson, 2021, Jiang et al., 2023] examined the J_1-J_2 square lattice antiferromagnet near the Néel-VBS transition, and indeed found d-wave superconductivity upon doping.

Now we return to the analysis of the pseudogap using the ALM in Eq. (125). In Section 3, we presented a mean field analysis in terms of decoupled Kondo lattice and spin liquid models. This section will couple them using the methods developed in Sections 2 and 5.

On the spin liquid layer of $\boldsymbol{S}_2$ spins we write a parton decomposition which parallels that in Eq. (73) and (126)

$$\boldsymbol{S}_{2\boldsymbol{i}} = \frac{1}{2} f^{\dagger}_{\boldsymbol{i}\alpha} \boldsymbol{\sigma}_{\alpha\beta} f_{\boldsymbol{i}\beta} \, . \tag{129}$$

Then the analysis of the exchange interactions within the $\boldsymbol{S}_2$ layer is precisely that in Section 3. W decouple the $J_{\boldsymbol{ij}}$ term in Eq. (125) to $\mathcal{H}_{SLf}$ in Eq. (87) realizing a π-flux state of the $\boldsymbol{S}_2$ spins with a SU(2) gauge field.
To couple this spin liquid to the Kondo lattice, we have to decouple the $J_\perp$ term coupling the f_1 and f spinons in Eq. (125). Given the SU(2) gauge structure of the $\boldsymbol{S}_2$ layer, it pays to decouple the $J_\perp$ term in a manner which keeps the SU(2) gauge invariance explicit. In fact, the needed decoupling field is precisely the boson $\mathcal{B}_{\boldsymbol{i}}$ introduced in Eq. (112). We also introduce a matrix fermion operator $\mathcal{F}_{1\boldsymbol{i}}$

$$\mathcal{F}_{1\boldsymbol{i}} \equiv \begin{pmatrix} f_{1\boldsymbol{i}\uparrow} & -f_{1\boldsymbol{i}\downarrow} \\ f^{\dagger}_{1\boldsymbol{i}\downarrow} & f^{\dagger}_{1\boldsymbol{i}\uparrow} \end{pmatrix} , \tag{130}$$

whose transformations under the symmetries in Eqs. (115,116,117) are the same as those of $\mathcal{C}_{\boldsymbol{i}}$. We summarize the gauge and symmetry properties in Table 2.

Field	Layer	Gauge	Global	
		SU(2)	SU(2)	U(1)
c or $\mathcal{C}$	1	$\mathbf{1}$	$\mathbf{2}_R$	-1
f_1 or $\mathcal{F}_1$	2	$\mathbf{1}$	$\mathbf{2}_R$	-1
f or $\mathcal{F}$	3	$\mathbf{2}_L$	$\mathbf{2}_R$	0
B or $\mathcal{B}$	$2 \leftrightarrow 3$	$\mathbf{2}_L$	$\mathbf{1}$	1

Table 2: Summary of gauge and global symmetry transformations for the fields of the ALM in the FL* phase. The representations of the SU(2) are indicated by their dimension; the subscripts L/R indicate whether the SU(2) acts by left/right multiplication in the matrix form of the field. The representations of the global U(1) is the electrical charge in units of e. For the fermions, the layer column indicates the layer number is Fig. 25. For the bosons, the layer column indicates the layers between which there is a Yukawa coupling to the fermions.

Then, from the $J_\perp$ term, symmetry considerations are sufficient to constrain the structure of the Yukawa term between B and the fermions [Christos et al., 2023], which follows from Eq. (113) and is illustrated in Fig. 30:

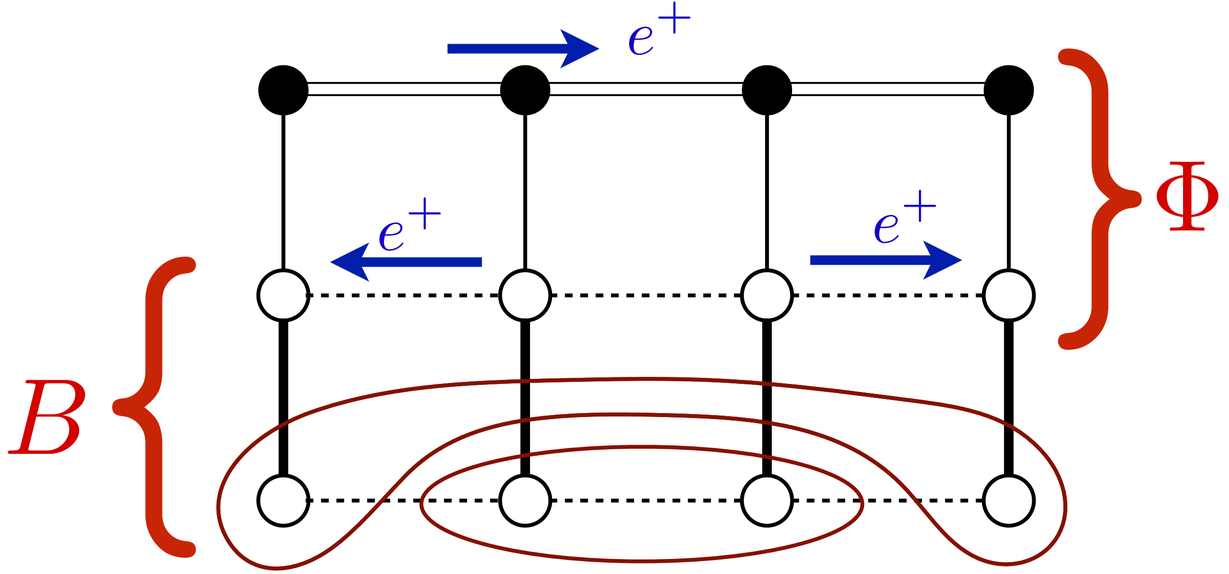

Figure 30: The two distinct Higgs fields in the ancilla layer theory of the single band Hubbard model. Φ hybridizes conduction electrons in the top layer with spinons in the middle layer. B couples the spinons of the bottom layer to the upper layers.

$$\begin{aligned}
\mathcal{H}_Y &= -\frac{1}{2}\sum_{\boldsymbol{i}}\left[i\,\mathrm{Tr}\left(\mathcal{F}_{1\boldsymbol{i}}^{\dagger}\mathcal{B}_{\boldsymbol{i}}^{\dagger}\mathcal{F}_i\right) + ig\,\mathrm{Tr}\left(\mathcal{C}_{\boldsymbol{i}}^{\dagger}\mathcal{B}_{\boldsymbol{i}}^{\dagger}\mathcal{F}_i\right) + \mathrm{H.c.}\right] \\
&= \sum_{\boldsymbol{i}}\Big[i\left(B_{1\boldsymbol{i}}f_{\boldsymbol{i}\alpha}^{\dagger}f_{1\boldsymbol{i}\alpha} - B_{2\boldsymbol{i}}\varepsilon_{\alpha\beta}f_{\boldsymbol{i}\alpha}f_{1\boldsymbol{i}\beta}\right) + \mathrm{H.c.} \\
&\qquad + ig\left(B_{1\boldsymbol{i}}f_{\boldsymbol{i}\alpha}^{\dagger}c_{\boldsymbol{i}\alpha} - B_{2\boldsymbol{i}}\varepsilon_{\alpha\beta}f_{\boldsymbol{i}\alpha}c_{\boldsymbol{i}\beta}\right) + \mathrm{H.c.}\Big]\,,
\end{aligned} \tag{131}$$

We have also included a Yukawa coupling to c_α from an allowed term $\sim \boldsymbol{S_{2i}} \cdot c^\dagger_{\boldsymbol{i}\alpha} \boldsymbol{\sigma}_{\alpha\beta} c_{\boldsymbol{i}\beta}$, which descends from the Kondo coupling noted below Eq. (124).
We can now collect all terms to write down the complete Hamiltonian needed for our analysis of the pseudogap metal, and its low temperature instabilities.

$$\mathcal{H}_{\rm pseudogap} = \mathcal{H}_{\rm KLmf} + \mathcal{H}_{SLf} + \mathcal{H}_Y + \mathcal{E}_2[B,U] + \mathcal{E}_4[B,U] \tag{132}$$

specified in Eqs. (127), (87), (131), (120). This Hamiltonian has 3 fermions c_α, $f_{1\alpha}$, f_α whose transformations under SU(2) gauge, spin rotation, and electromagnetic charge symmetries are in Eqs. (115), (116), (117), with $f_{1\alpha}$ transforming just like c_α.
The boson B couples the Kondo Lattice to the spin liquid on the bottom layer, with SU(2) gauge field $U_{\boldsymbol{ij}}$.
There is a remarkable similarity between Eq. (132), and the Weinberg-Salam theory of weak interactions [Christos et al., 2023]. Although the dispersions of the fermions and bosons have a lattice structure, the SU(2)$\times$ U(1) gauge structure (we treat the electromagnetic U(1) as global), and the Yukawa couplings between the Higgs and the fermions are similar, with the spinons mapping to neutrinos, and the electrons mapping to electrons.

6.6. Anisotropic velocities in the d-wave superconductor

FL→dSC

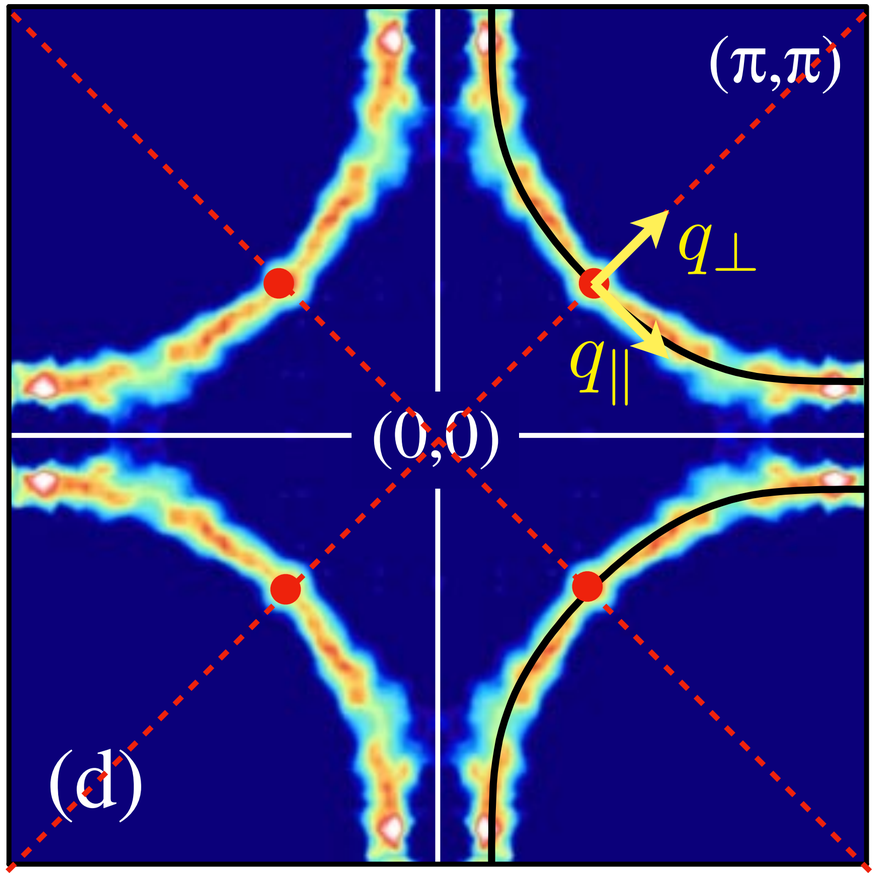

BCS/Bogoliubov quasiparticles
in a d-wave superconductor

$$E_{\boldsymbol{k}} = \left(\varepsilon_{\boldsymbol{k}}^2 + \Delta_{\boldsymbol{k}}^2\right)^{1/2}$$
$$\Delta_{\boldsymbol{k}} = \Delta_0 \left(\cos k_x - \cos k_y\right)$$

4 nodal points where

$$E_{\boldsymbol{k}_0+\boldsymbol{q}} = \left(v_F^2 q_\perp^2 + v_\Delta^2 q_\parallel^2\right)^{1/2}$$

with $v_F \gg v_\Delta$.

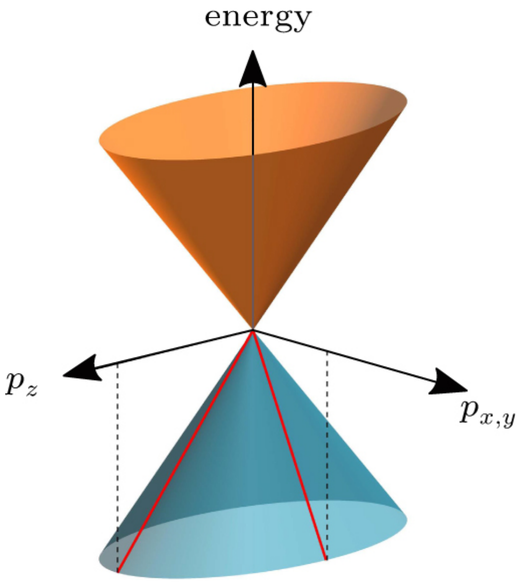

We now show how the problem of isotropic quasiparticle velocities, noted in Section 5, is resolved by the presence of the pocket Fermi surfaces described by $\mathcal{H}_{\mathrm{KLmf}}$ in Eq. (127). The discussion below is based on the detailed computations presented in Refs. [Chatterjee and Sachdev, 2016, Christos and Sachdev, 2024].

Given the pocket Fermi surfaces and spinons in the FL* normal state, we imagine imposing a BCS type pairing on the Fermi surface excitations. If the pairing is *d*-wave, it would lead to 8 nodal Bogoliubov points as shown in Fig. 31A. However this state also has the 4 nodal quasiparticles of the $\boldsymbol{S}_2$ spin liquid, associated with the dispersion in Fig. 18. So strictly speaking, this state remains fractionalized, and is *not* a conventional *d*-wave superconductor. It would be appropriate to call it d-SC*.

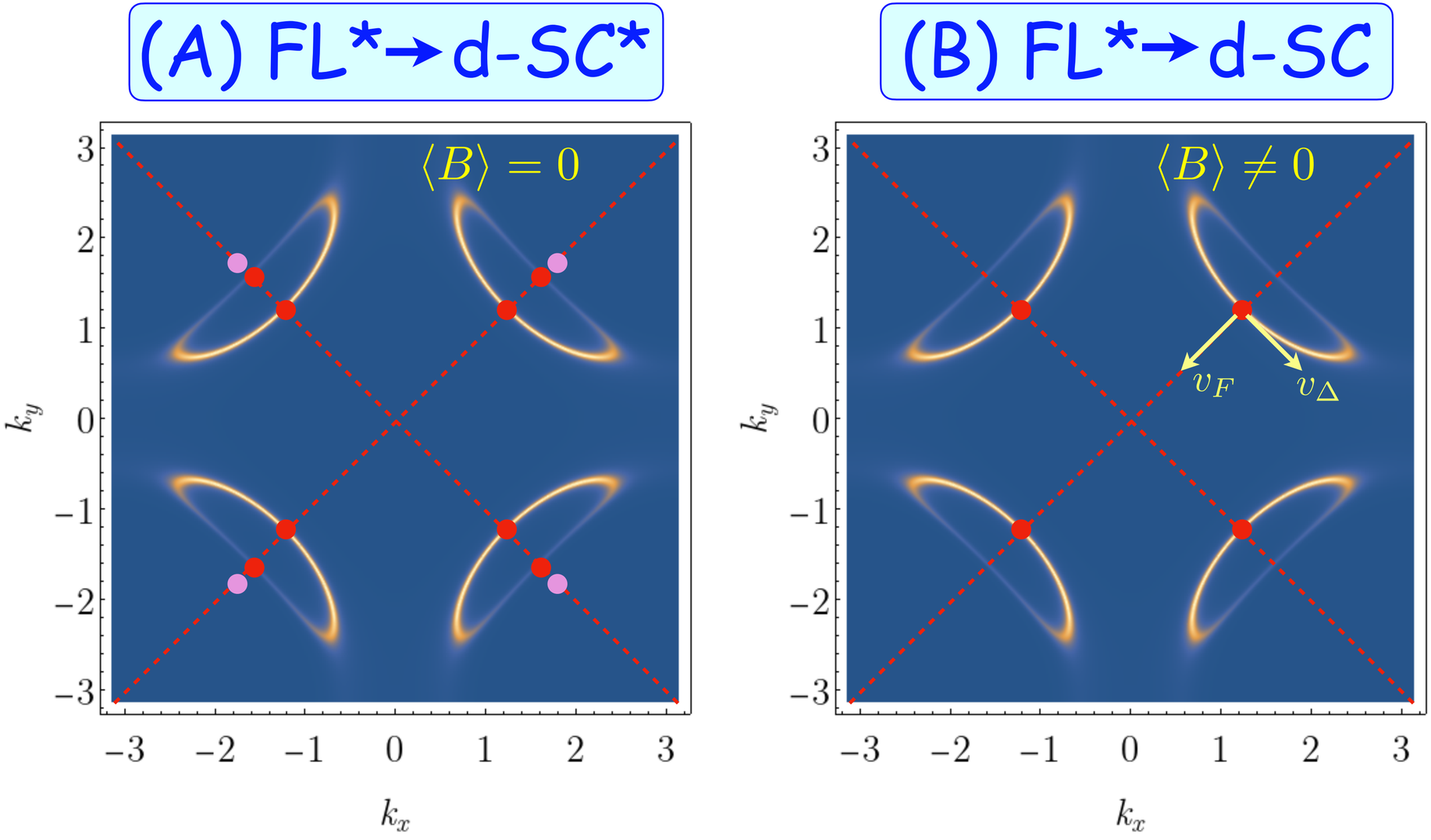

Figure 31: (A) Cooper pairing the Fermi surface quasiparticles in FL* leads to d-SC* state, with 8 nodal Bogoliubov quasiparticles (red), and 4 nodal spinons (pink). (B) Upon condensing B, the spinons mutually annihilate 4 of the Bogoliubov quasiparticles, leaving 4 Bogoliubov quasiparticles with

$v_F \gg v_\Delta$.

However, if we induce the pairing by the B condensate in Eq. (131), the SU(2) gauge field is higgsed. Morever, the Yukawa coupling allows the nodal quasiparticles of the $\boldsymbol{S}_2$ spin liquid to hybridize with the Bogoliubov quasiparticles of the pocket Fermi surfaces. The net result, sketched in Fig. 31B, is that the B condensate can enable the nodal points on the 'backsides' of the pocket Fermi surfaces to mutually annihilate with the spinons of the $\boldsymbol{S}_2$ spin liquid. We are then left with the 4 nodal quasiparticles on front sides of the pocket Fermi surfaces. The number of nodal points are the same as those obtained in conventional BCS theory from d-wave pairing of a Fermi liquid. These remaining nodal points are associated with pairing on the pocket Fermi surfaces, and these is no reason for their velocity to be isotropic (unlike the spinons).

The annihilation of the extra nodal points occurs via hybridization between the electrons and spinons within a mean-field band structure of $\mathcal{H}_{\mathrm{KLmf}} + \mathcal{H}_{SLf} + \mathcal{H}_Y$ in Eqs. (127), (81), and (131) . Furthermore, computations which diagonalize this Hamiltonian with B fixed and $U = 1$ do indeed yield anisotropic velocities similar to those observed. Unlike the situation in Section 5, the spinons do *not* become the Bogoliubov quasiparticles in the doped case; instead the spinons are needed to annihilate the extraneous Bogoliubov quasiparticles.

An interesting prediction can be made in the particular case of the electron-doped cuprates. In these materials, photoemission experiments have observed a normal state to superconductivity which is gapped near $(\pi/2, \pi/2)$ and has spectral weight only near electron pockets at the antinode [Armitage et al., 2002]. If d-wave superconductivity were to emerge as a BCS instability from such a normal state, the resulting superconductor should be gapped. However, the FL* theory yields a different prediction. Similar to how the spinon degrees of freedom emerge to annhilate with the backside pocket when B Higgs condenses in the hole-doped case, the Dirac node of the spin liquid will appear with a finite spectral weight near $(\pi/2, \pi/2)$ when B condenses, leading to a nodal superconductor. Such a prediction can be explored in future photoemission experiments in the electron doped cuprates [Xu et al., 2023] and could serve as an experimental test of the FL* theory.

The cuprate phase diagram

FL*

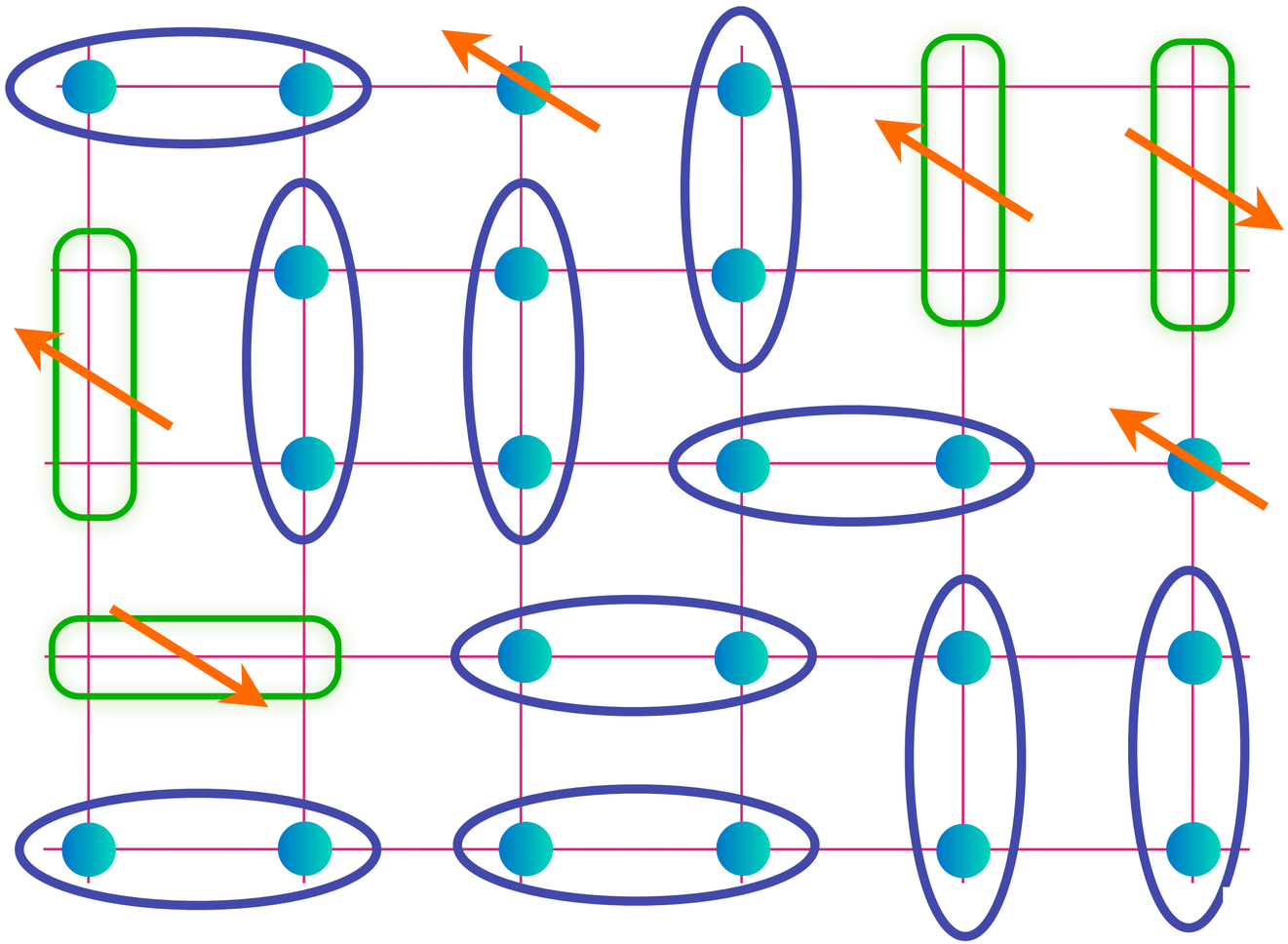

$= (|\uparrow\downarrow\rangle - |\downarrow\uparrow\rangle)/\sqrt{2}$

$= (|\uparrow\circ\rangle + |\circ\uparrow\rangle)/\sqrt{2}$

Ordinary metal

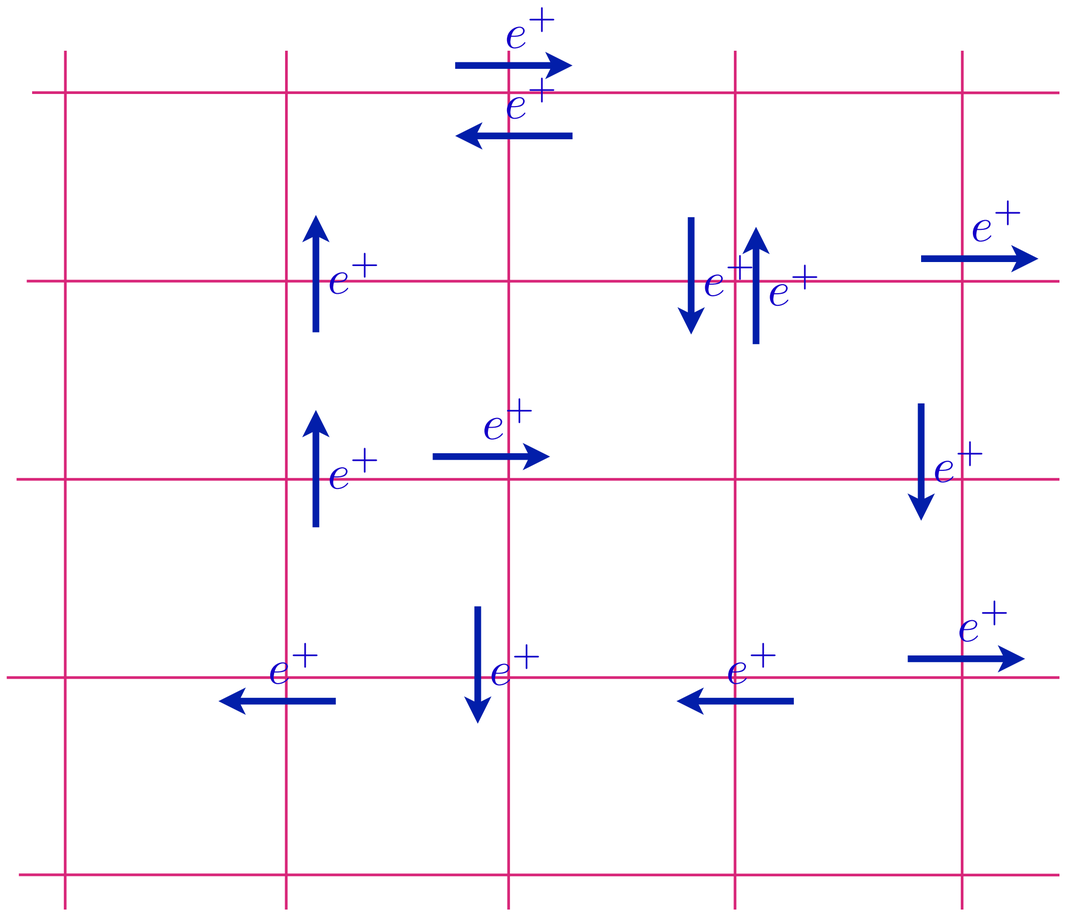

At large p, we obtain a gas of nearly free fermionic holes of density $1+p$ (relative to the filled band with 2 electrons per site)

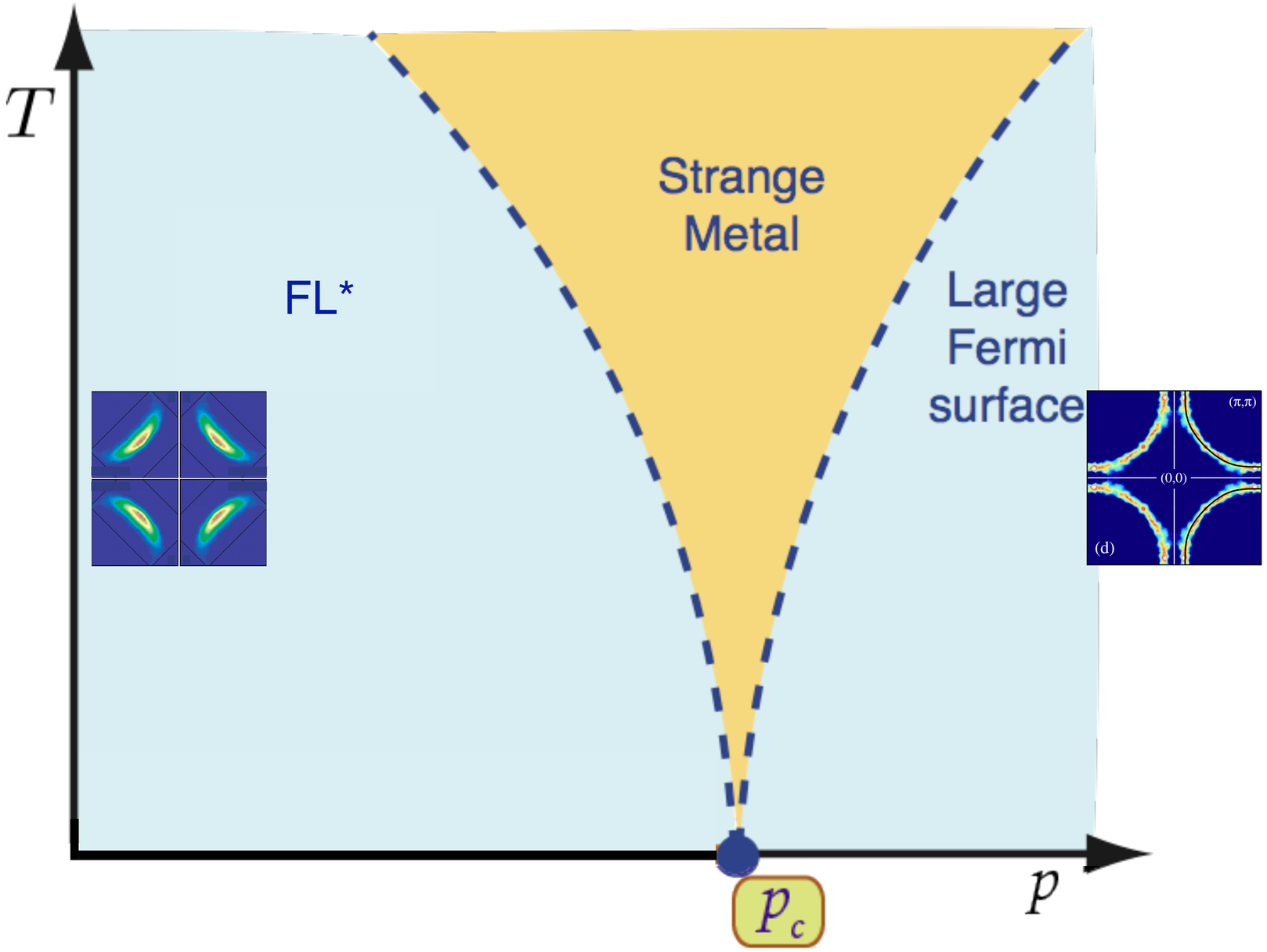

Quantum-criticality
of a quantum phase transition
between two metals
(FL* and FL) at $p = p_c$,
with no symmetry breaking.

Ya-Hui Zhang and S. S., PRR **2**, 023172 (2020)

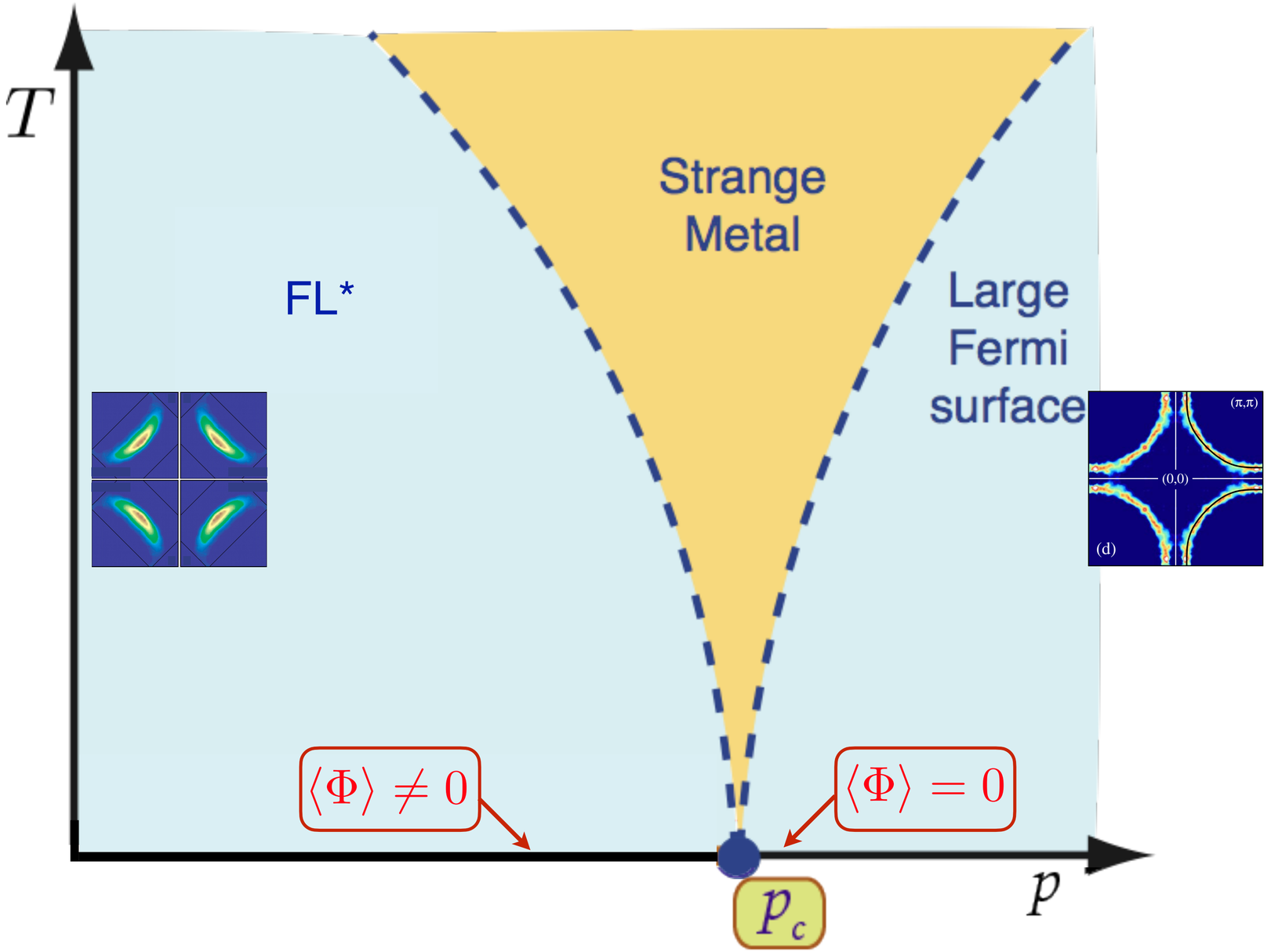

Quantum-criticality
of a quantum phase transition
between two metals
(FL* and FL) at $p = p_c$,
with no symmetry breaking.
Φ was the hybridization
between c and f_1 in theory of
hole pockets— it is
now a Higgs field.

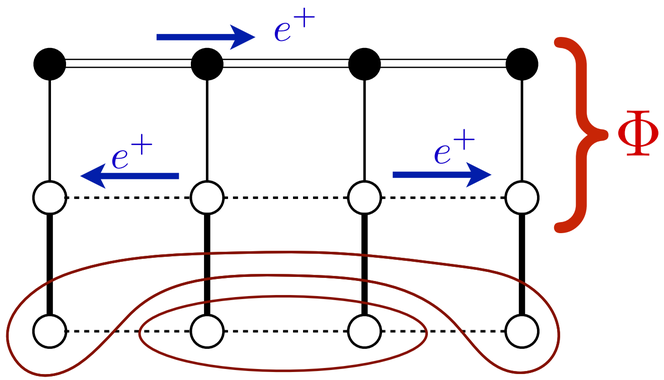

Ya-Hui Zhang and S. S., PRR **2**, 023172 (2020)

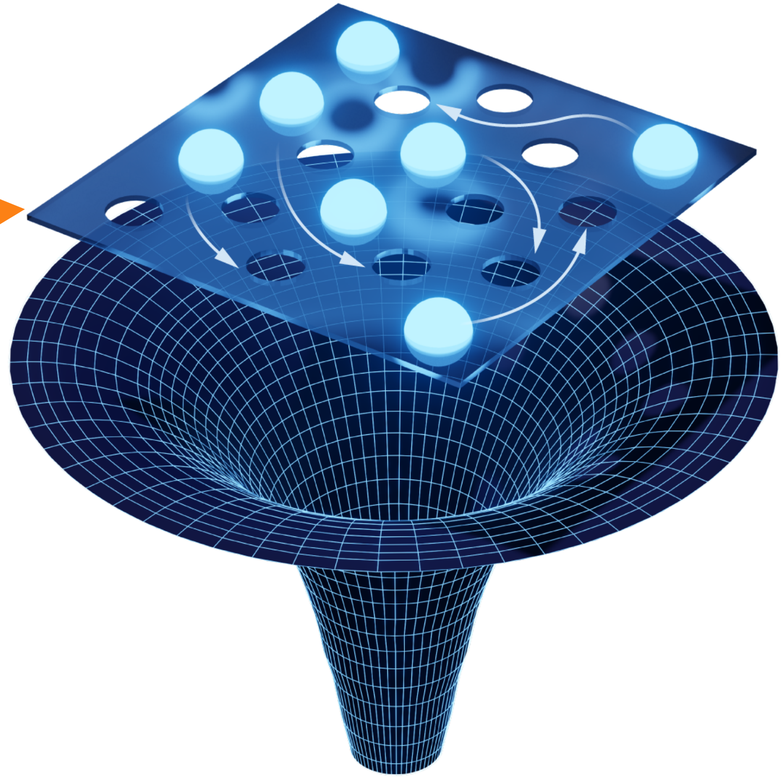

T

Strange Metal

FL*

Large Fermi surface

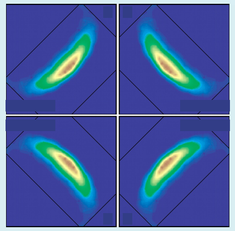

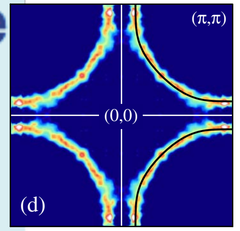

$\langle \Phi \rangle \neq 0$

$\langle \Phi \rangle = 0$

p_c

p

Explain with a local, two-dimensional extension of the Sachdev-Ye-Kitaev (SYK) model of mobile electrons, the 2D-Yukawa-SYK model with a spatially random Yukawa coupling between the large Fermi surface and Φ: a critical charge liquid

Aavishkar A. Patel, Haoyu Guo, Ilya Esterlis, S. S., *Science* **381**, 790 (2023)

Chenyuan Li, Aavishkar A. Patel, Haoyu Guo, Davide Valentinis, Jorg Schmalian, S.S., Ilya Esterlis, PRL **133**, 186502 (2024)

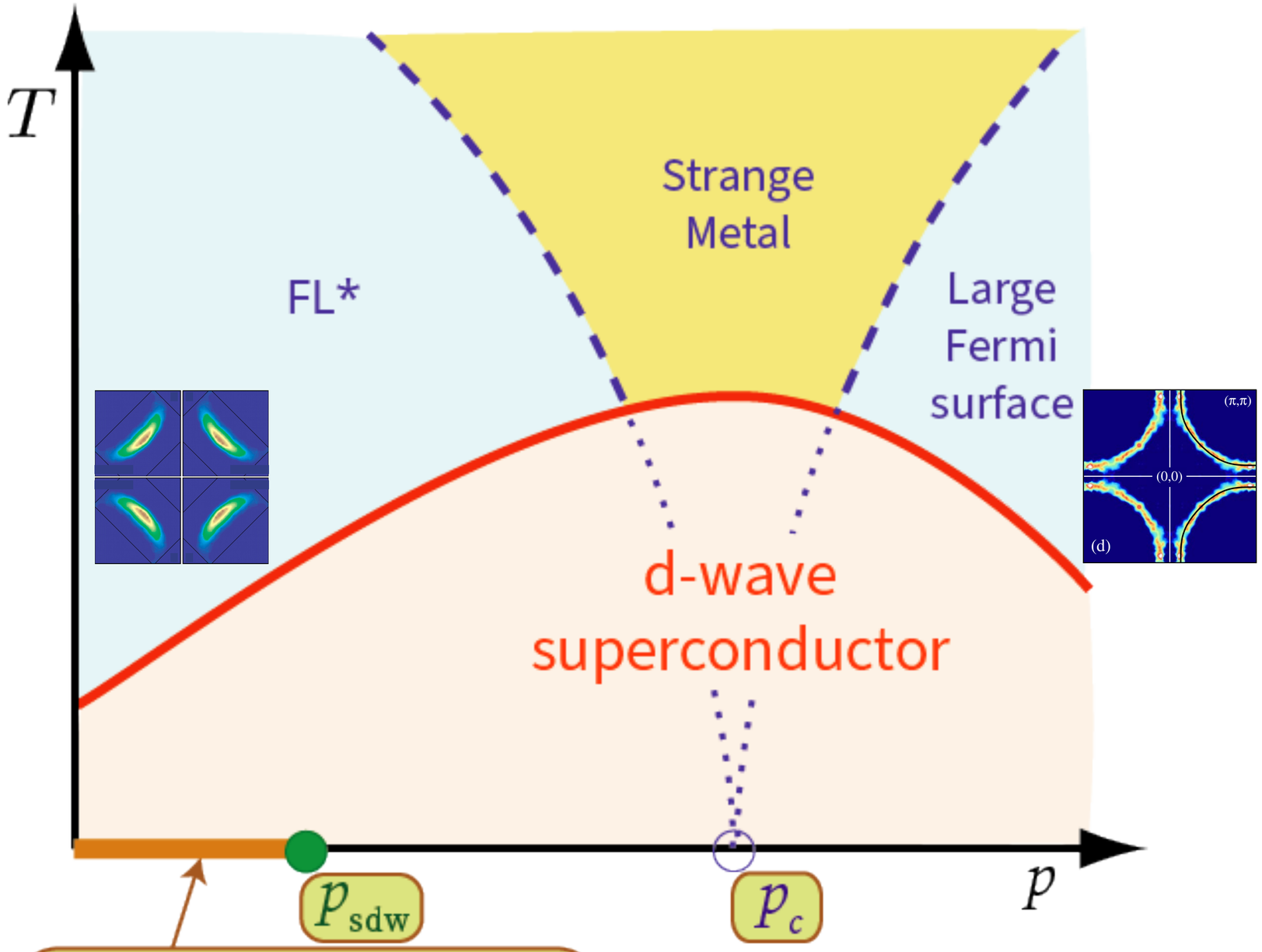

Quantum-criticality
of a quantum phase transition
between two metals
(FL* and FL) at $p = p_c$,
with no symmetry breaking.
Φ was the hybridization
between c and f_1 in theory of
hole pockets— it is
now a Higgs field.

Both metals lead to the same
d-wave superconductor at lower
temperatures, and so there is
transition at $p = p_c$ within the
superconducting state.

M. Christos, Zhu-Xi Luo, L. Shackleton, Ya-Hui Zhang,
M. S. Scheurer, and S. S., PNAS **120,** e2302701120 (2023)

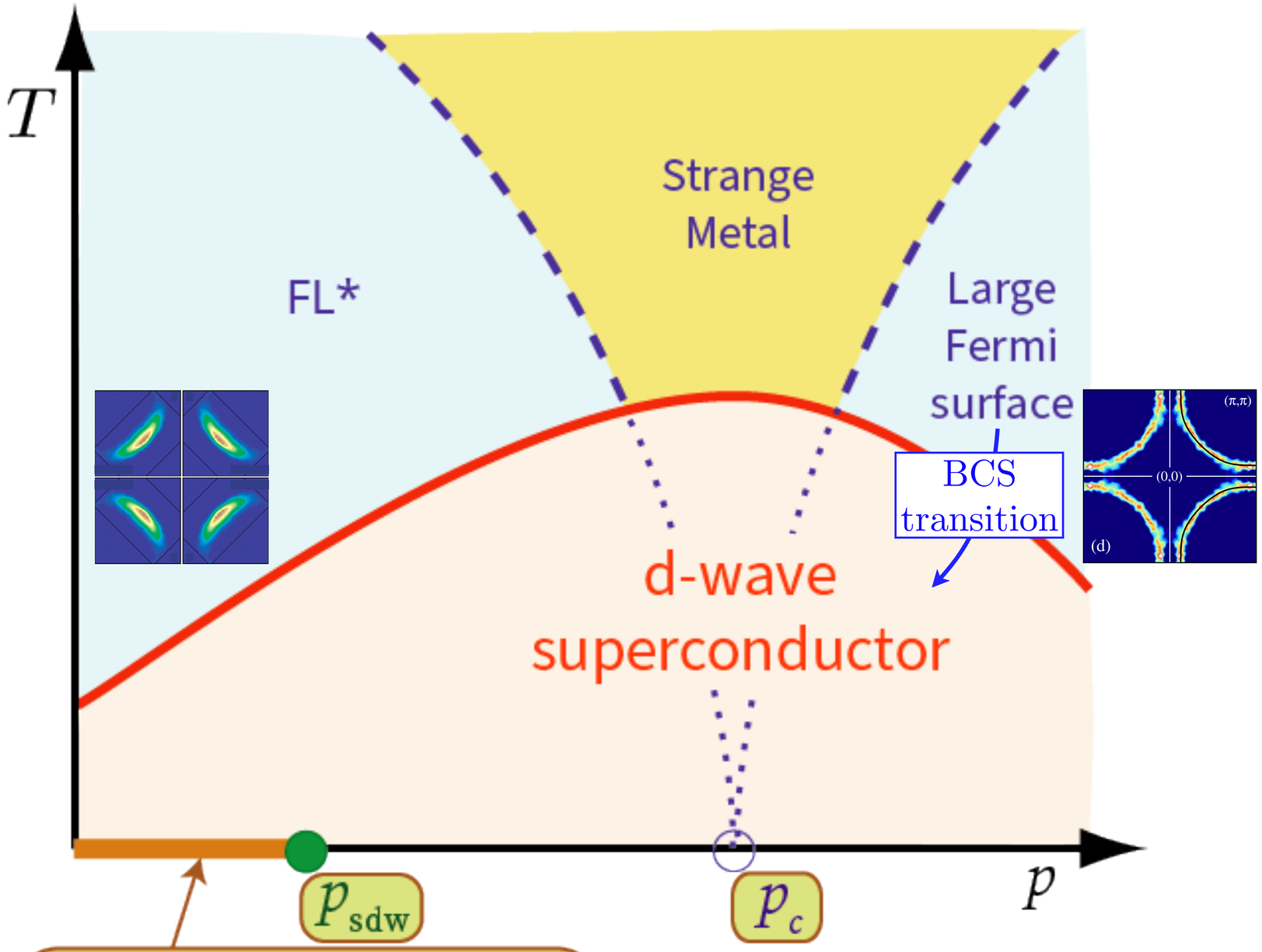

Quantum-criticality
of a quantum phase transition
between two metals
(FL* and FL) at $p = p_c$,
with no symmetry breaking.
Φ was the hybridization
between c and f_1 in theory of
hole pockets— it is
now a Higgs field.

Both metals lead to the same
d-wave superconductor at lower
temperatures, and so there is
transition at $p = p_c$ within the
superconducting state.

M. Christos, Zhu-Xi Luo, L. Shackleton, Ya-Hui Zhang,
M. S. Scheurer, and S. S., PNAS **120,** e2302701120 (2023)

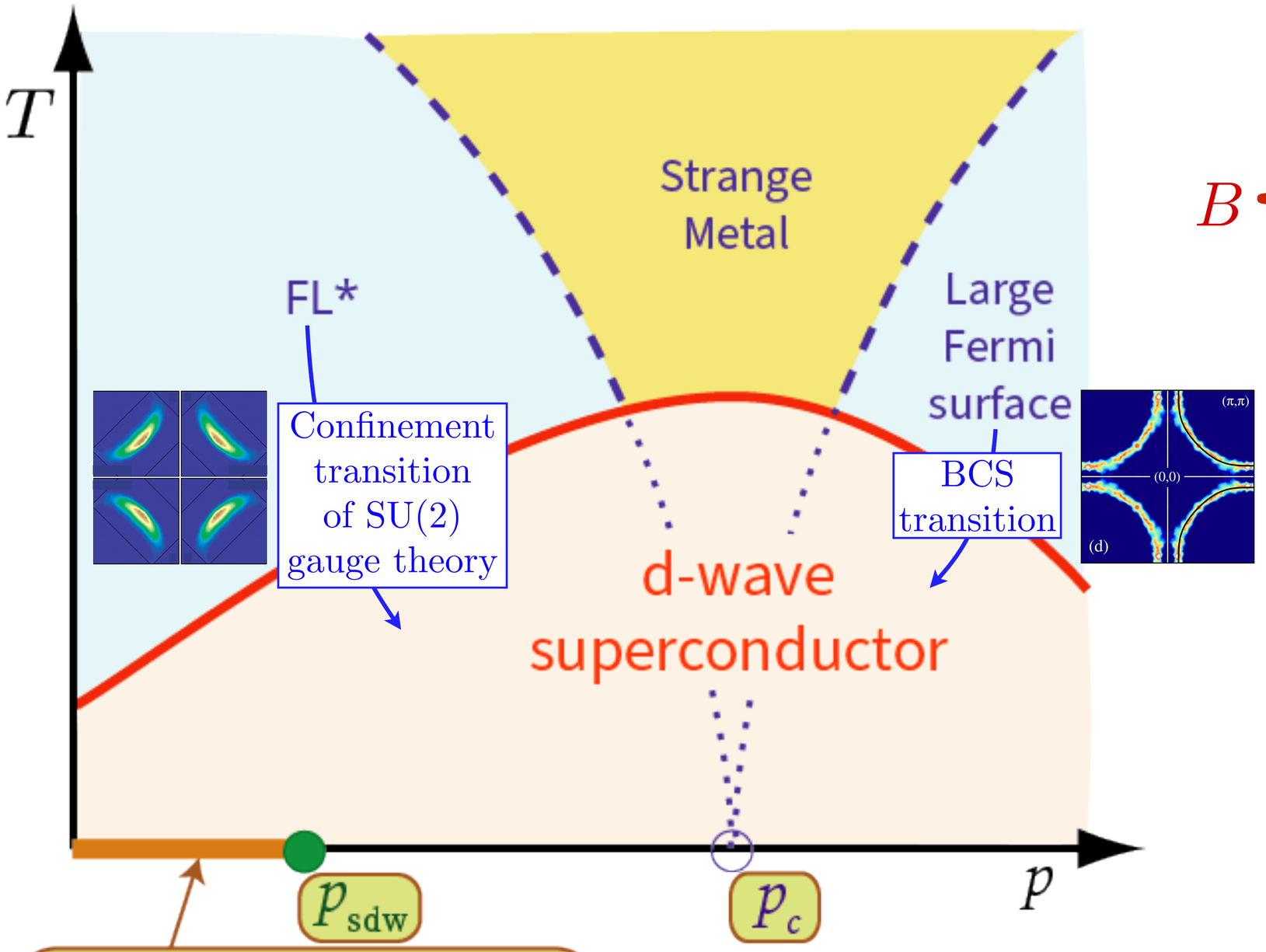

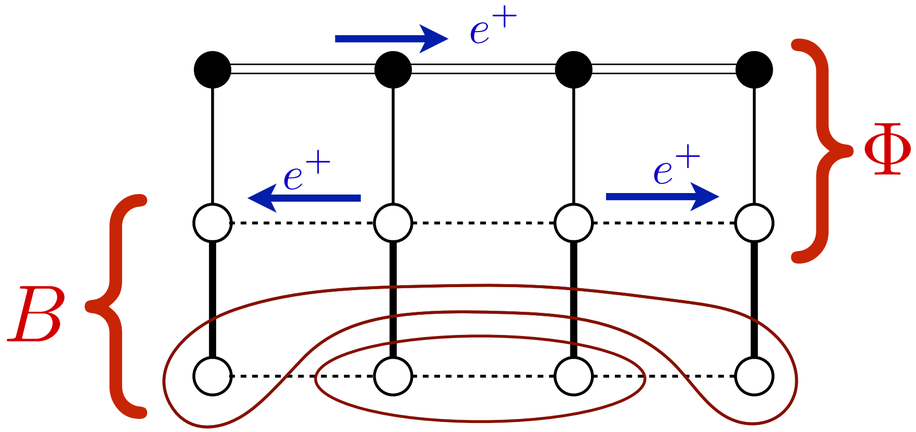

Condense B to Higgs SU(2) gauge field, and obtain BCS-like superconductor

Both metals lead to the same d-wave superconductor at lower temperatures, and so there is transition at $p = p_c$ within the superconducting state.

M. Christos, Zhu-Xi Luo, L. Shackleton, Ya-Hui Zhang, M. S. Scheurer, and S. S., PNAS **120,** e2302701120 (2023)

Doping an insulating antiferromagnet with holes of density p

FL*

Metal with density p of spin-1/2, charge $+e$ 'holes' (or 'magnetic polarons') and charge 0, spin-1/2 'spinons'

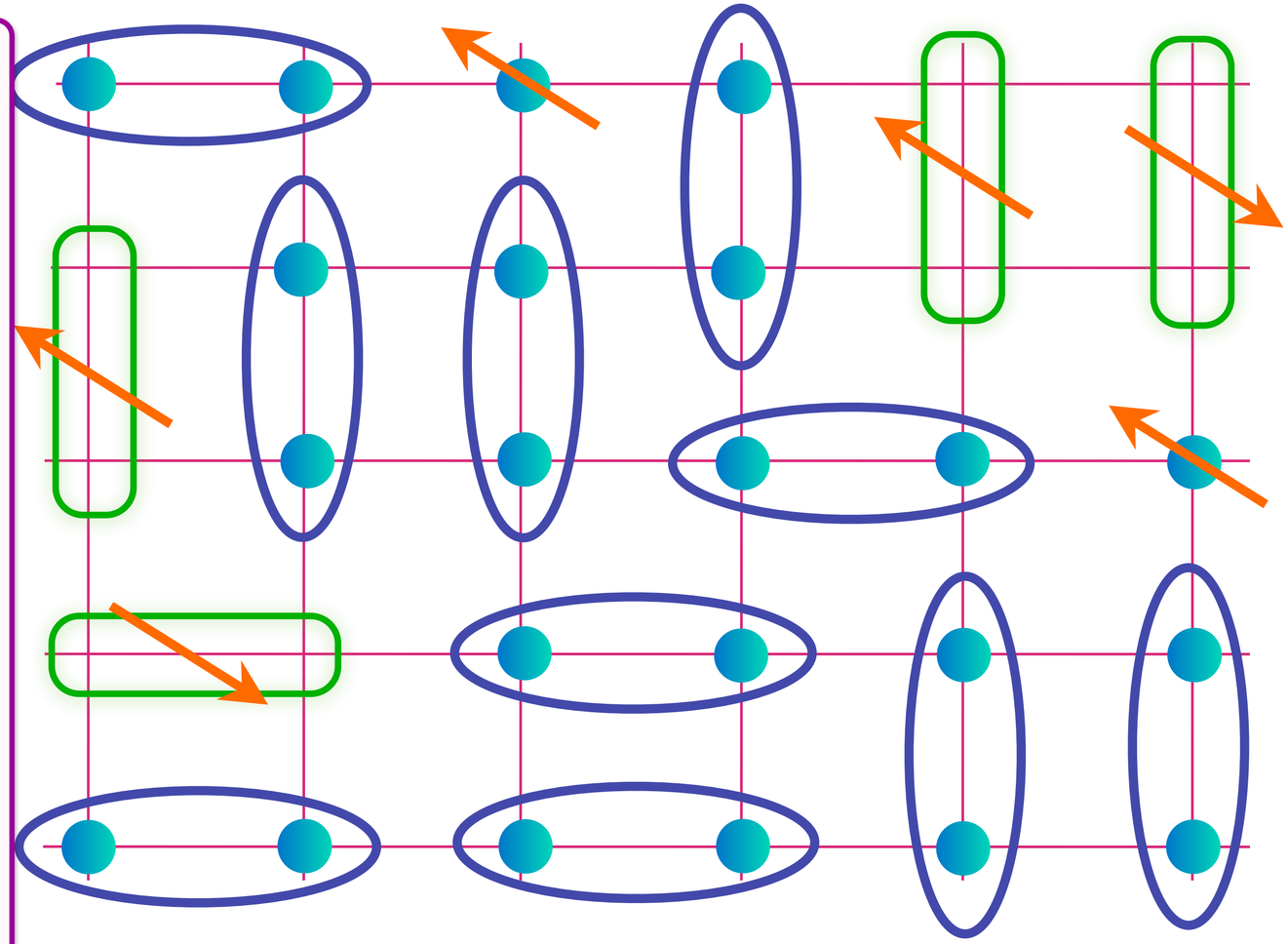

The d-wave superconductor is obtained by confining the SU(2) gauge field, and this exploits the pre-existing pairing in the blue dimers. Such a state is smoothly connected to the BCS d-wave superconductor.

$= (|\uparrow\downarrow\rangle - |\downarrow\uparrow\rangle)/\sqrt{2}$

$= (|\uparrow \circ\rangle + |\circ \uparrow\rangle)/\sqrt{2}$

Doping an insulating antiferromagnet with holes of density p

FL*

Metal with density p of spin-1/2, charge $+e$ 'holes' (or 'magnetic polarons') and charge 0, spin-1/2 'spinons'

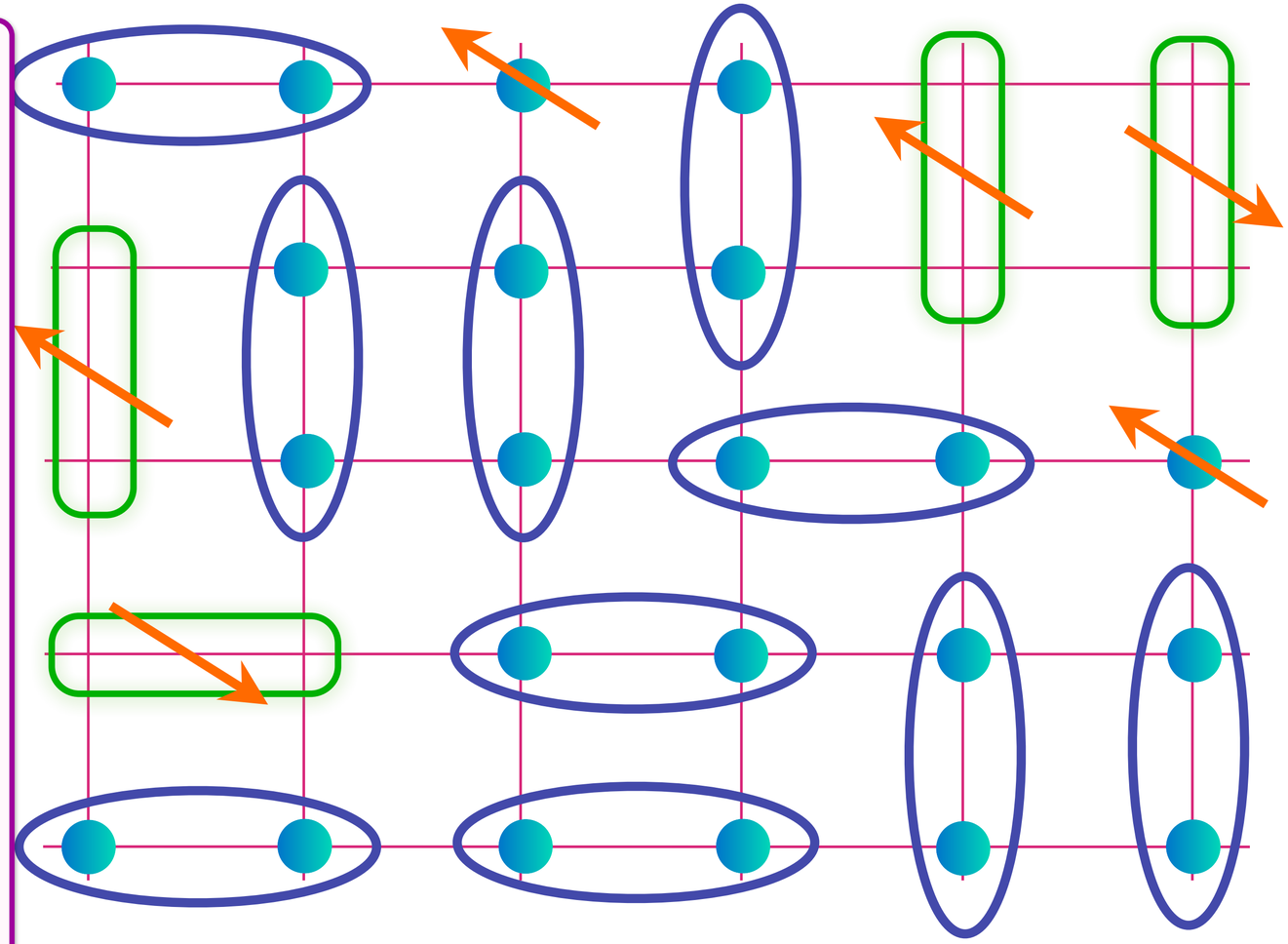

The d-wave superconductor is obtained by confining the SU(2) gauge field, and this exploits the pre-existing pairing in the blue dimers. Such a state is smoothly connected to the BCS d-wave superconductor.

Applying BCS pairing to the hole pockets (green dimers) yields a distinct SC* state, which is *not* smoothly connected to the BCS d-wave state.

$= (|\uparrow\downarrow\rangle - |\downarrow\uparrow\rangle)/\sqrt{2}$

$= (|\uparrow \circ\rangle + |\circ \uparrow\rangle)/\sqrt{2}$

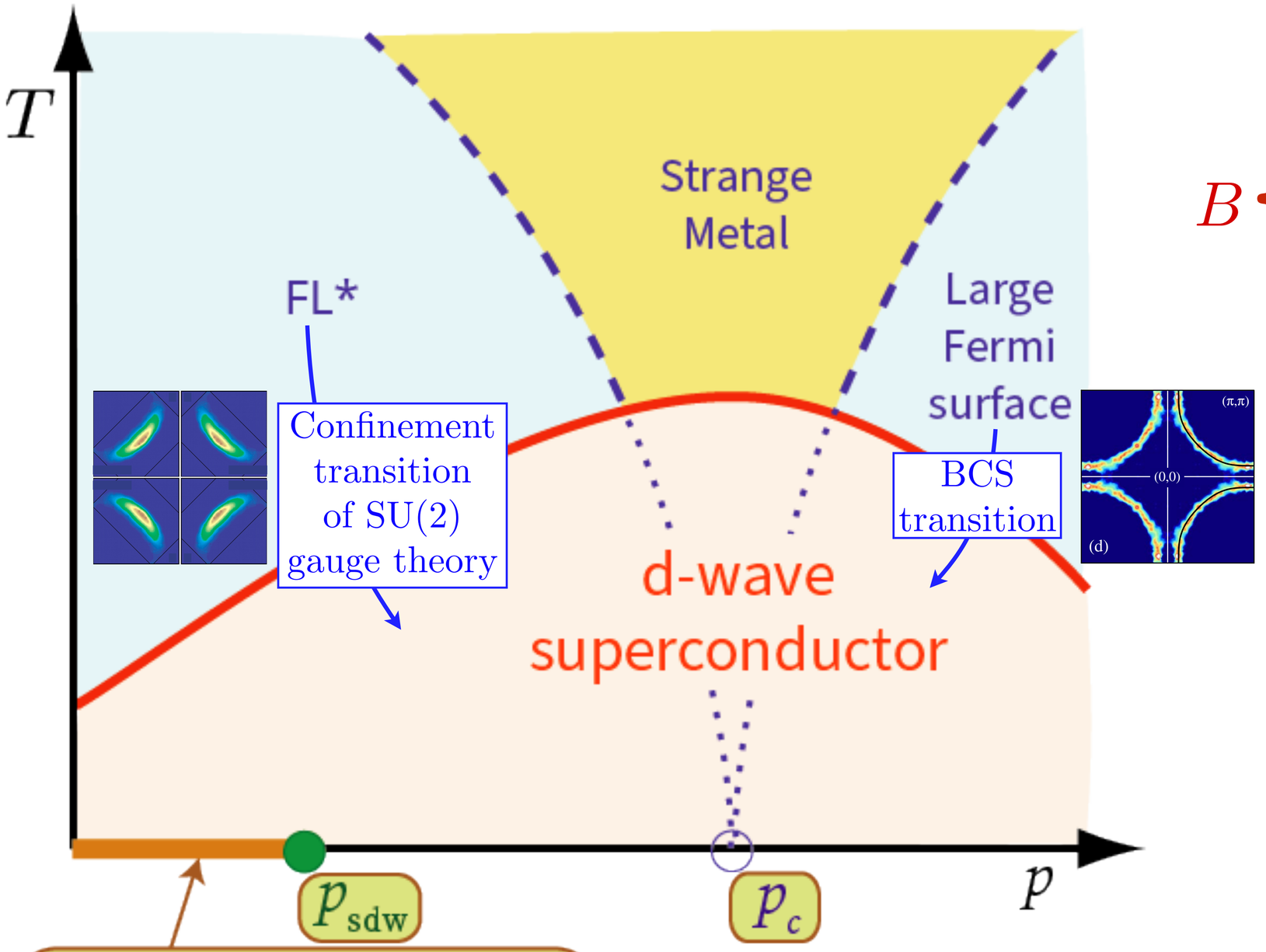

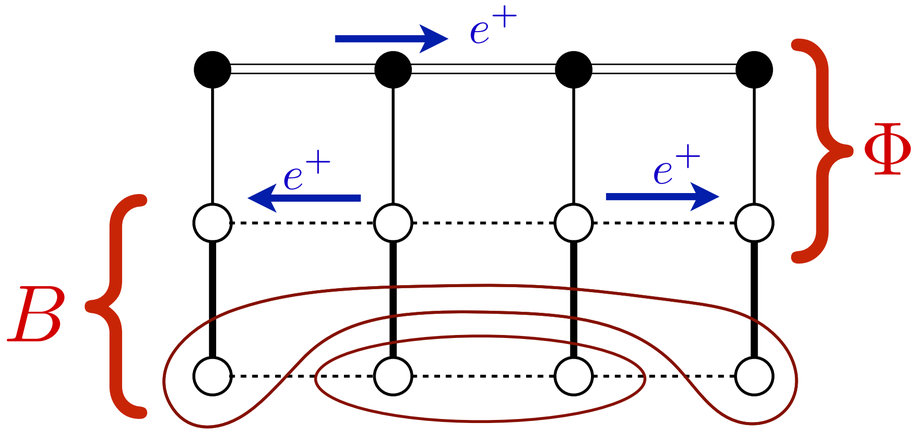

Condense B to Higgs SU(2) gauge field, and obtain BCS-like superconductor

Both metals lead to the same d-wave superconductor at lower temperatures, and so there is transition at $p = p_c$ within the superconducting state.

M. Christos, Zhu-Xi Luo, L. Shackleton, Ya-Hui Zhang, M. S. Scheurer, and S. S., PNAS **120,** e2302701120 (2023)

I thank Pietro Bonetti, Shubhayu Chatterjee, Maine Christos, Alexander Nikolaenko, Ya-Hui Zhang, and Jing-Yu Zhao for recent collaborations on the work reviewed here. This research was supported by NSF Grant DMR-2245246 and by the Simons Collaboration on Ultra-Quantum Matter which is a grant from the Simons Foundation (651440, S. S.).


Abanov, A. G. and Wiegmann, P. B. (2000).
Theta terms in nonlinear sigma models.
Nucl. Phys. B, 570:685–698.


Affleck, I. and Marston, J. B. (1988).
Large-n limit of the Heisenberg-Hubbard model: Implications for high-T_c superconductors.

Phys. Rev. B, 37:3774–3777.


Affleck, I., Zou, Z., Hsu, T., and Anderson, P. W. (1988).
SU(2) gauge symmetry of the large-U limit of the Hubbard model.
Phys. Rev. B, 38:745–747.


Alicea, J. (2008).
Monopole quantum numbers in the staggered flux spin liquid.
Phys. Rev. B, 78(3):035126.


Anderson, P. W., Lee, P. A., Randeria, M., Rice, T. M., Trivedi, N., and Zhang, F. C. (2004).
The physics behind high-temperature superconducting cuprates: the 'plain vanilla' version of RVB.
Journal of Physics Condensed Matter, 16(24):R755–R769.


Anderson, Z. W., Tang, Y., Nagarajan, V., Chan, M. K., Dorow, C. J., Yu, G., Abernathy, D. L., Christianson, A. D., Mangin-Thro, L., Steffens, P., Sterling, T., Reznik, D., Bounoua, D., Sidis, Y., Bourges, P., and Greven, M. (2025).
Gapped commensurate antiferromagnetic response in a strongly underdoped model cuprate superconductor.
npj Quantum Materials, 10(1):93.


Armitage, N. P., Ronning, F., Lu, D. H., Kim, C., Damascelli, A., Shen, K. M., Feng, D. L., Eisaki, H., Shen, Z.-X., Mang, P. K., Kaneko, N., Greven, M., Onose, Y., Taguchi, Y., and Tokura, Y. (2002).
Doping dependence of an *n*-type cuprate superconductor investigated by angle-resolved photoemission spectroscopy.
Phys. Rev. Lett., 88:257001.


Arovas, D. P. and Auerbach, A. (1988).
Functional integral theories of low-dimensional quantum Heisenberg models.
Phys. Rev. B, 38:316–332.


Assaad, F. F., Imada, M., and Scalapino, D. J. (1996).

Quantum Transition between an Antiferromagnetic Mott Insulator and $d_{x^2-y^2}$ Superconductor in Two Dimensions.
Phys. Rev. Lett., 77(22):4592–4595.


Bonderson, P., Cheng, M., Patel, K., and Plamadeala, E. (2016).
Topological Enrichment of Luttinger's Theorem.
arXiv e-prints.


Bonetti, P. M., Christos, M., Nikolaenko, A., Patel, A. A., and Sachdev, S. (2025).
Critical quantum liquids and the cuprate high temperature superconductors.


Bonetti, P. M., Christos, M., and Sachdev, S. (2024).
Quantum oscillations in the hole-doped cuprates and the confinement of spinons.
Proceedings of the National Academy of Sciences, 121:e2418633121.


Bonetti, P. M. and Metzner, W. (2022).
SU(2) gauge theory of the pseudogap phase in the two-dimensional Hubbard model.
Phys. Rev. B, 106(20):205152.


Borejsza, K. and Dupuis, N. (2004).

Antiferromagnetism and single-particle properties in the two-dimensional half-filled Hubbard model: A nonlinear sigma model approach.
Phys. Rev. B, 69(8):085119.


Cai, X., Han, Z., Li, Z.-X., Kivelson, S. A., and Yao, H. (2024).
Quantum spin liquid from electron-phonon coupling.
arXiv e-prints, page arXiv:2408.04002.


Cai, X., Li, Z.-X., and Yao, H. (2021).
Antiferromagnetism Induced by Bond Su-Schrieffer-Heeger Electron-Phonon Coupling: A Quantum Monte Carlo Study.
Phys. Rev. Lett., 127(24):247203.


Cai, X., Li, Z.-X., and Yao, H. (2022).
Robustness of antiferromagnetism in the Su-Schrieffer-Heeger Hubbard model.
Phys. Rev. B, 106(8):L081115.


Chan, M. K., Schreiber, K. A., Ayala-Valenzuela, O. E., Bauer, E. D., Shekhter, A., and Harrison, N. (2025).
Observation of the Yamaji effect in a cuprate superconductor.

Nature Physics, 21(11):1753–1758.


Chatterjee, S. and Sachdev, S. (2016).
Fractionalized Fermi liquid with bosonic chargons as a candidate for the pseudogap metal.
Phys. Rev. B, 94(20):205117.


Chatterjee, S., Sachdev, S., and Scheurer, M. (2017).
Intertwining topological order and broken symmetry in a theory of fluctuating spin density waves.
Phys. Rev. Lett., 119(22):227002.


Chen, B.-B., Zhang, X., Wang, Y., Sun, K., and Meng, Z. Y. (2024).
Phases of (2 +1)D SO(5) Nonlinear Sigma Model with a Topological Term on a Sphere: Multicritical Point and Disorder Phase.
Phys. Rev. Lett., 132(24):246503.


Chester, S. M. and Su, N. (2024).
Bootstrapping Deconfined Quantum Tricriticality.
Phys. Rev. Lett., 132(11):111601.


Chiu, C. S., Ji, G., Bohrdt, A., Xu, M., Knap, M., Demler, E., Grusdt, F., Greiner, M., and Greif, D. (2019).
String patterns in the doped Hubbard model.
Science, 365(6450):251–256.


Chowdhury, D. and Sachdev, S. (2015a).
Higgs criticality in a two-dimensional metal.
Phys. Rev. B, 91(11):115123.


Chowdhury, D. and Sachdev, S. (2015b).
The Enigma of the Pseudogap Phase of the Cuprate Superconductors.
In Jedrzejewski, J., editor, *Quantum criticality in condensed matter*, 50th Karpacz Winter School of Theoretical Physics, pages 1–43. World Scientific.


Christos, M., Luo, Z.-X., Shackleton, L., Zhang, Y.-H., Scheurer, M. S., and Sachdev, S. (2023).
A model of *d*-wave superconductivity, antiferromagnetism, and charge order on the square lattice.
Proc. Nat. Acad. Sci., 120(21):e2302701120.


Christos, M. and Sachdev, S. (2024).
Emergence of nodal Bogoliubov quasiparticles across the transition from the pseudogap metal to the d-wave superconductor.
npj Quantum Materials, 9(1):4.


Christos, M., Shackleton, L., Sachdev, S., and Luo, Z.-X. (2024).
Deconfined quantum criticality of nodal d -wave superconductivity, Néel order, and charge order on the square lattice at half-filling.
Physical Review Research, 6(3):033018.


Chubukov, A. V., Sachdev, S., and Senthil, T. (1994a).
Quantum phase transitions in frustrated quantum antiferromagnets.
Nucl. Phys. B, 426:601–643.


Chubukov, A. V., Senthil, T., and Sachdev, S. (1994b).
Universal magnetic properties of frustrated quantum antiferromagnets in two dimensions.
Phys. Rev. Lett., 72:2089–2092.


Coleman, P. and Andrei, N. (1989).
Kondo-stabilised spin liquids and heavy fermion superconductivity.

Journal of Physics: Condensed Matter, 1(26):4057.


Dagotto, E., Fradkin, E., and Moreo, A. (1988).
SU(2) gauge invariance and order parameters in strongly coupled electronic systems.
Phys. Rev. B, 38:2926–2929.


Dupuis, N. (2002).
Spin fluctuations and pseudogap in the two-dimensional half-filled Hubbard model at weak coupling.
Phys. Rev. B, 65(24):245118.


Else, D. V. and Senthil, T. (2021).
Strange Metals as Ersatz Fermi Liquids.
Phys. Rev. Lett., 127(8):086601.


Else, D. V., Thorngren, R., and Senthil, T. (2021).
Non-Fermi Liquids as Ersatz Fermi Liquids: General Constraints on Compressible Metals.
Physical Review X, 11(2):021005.

Fang, Y., Grissonnanche, G., Legros, A., Verret, S., Laliberté, F., Collignon, C., Ataei, A., Dion, M., Zhou, J., Graf, D., Lawler, M. J., Goddard, P. A., Taillefer, L., and Ramshaw, B. J. (2022).
Fermi surface transformation at the pseudogap critical point of a cuprate superconductor.
Nature Physics, 18(5):558–564.

Feldmeier, J., Huber, S., and Punk, M. (2018).
Exact Solution of a Two-Species Quantum Dimer Model for Pseudogap Metals.
Phys. Rev. Lett., 120:187001.

Feng, C., Xing, B., Poletti, D., Scalettar, R. T., and Batrouni, G. G. (2022).
Phase Diagram of the Su–Schrieffer–Heeger–Hubbard model on a square lattice.
Physical Review B, 106(8):L081114.

Ferrari, F. and Becca, F. (2020).
Gapless spin liquid and valence-bond solid in the J_1-J_2 Heisenberg model on the square lattice: Insights from singlet and triplet excitations.
Phys. Rev. B, 102(1):014417.

Fradkin, E. (2025).

Intertwined Orders and the Physics of High Temperature Superconductors.
Particles, 8(3).


Fradkin, E., Kivelson, S. A., and Tranquada, J. M. (2015).
Colloquium: Theory of intertwined orders in high temperature superconductors.
Reviews of Modern Physics, 87(2):457–482.


Götz, A., Assaad, F. F., and Costa, N. C. (2024a).
Tuning the order of a deconfined quantum critical point.
arXiv e-prints, page arXiv:2412.17215.


Götz, A., Beyl, S., Hohenadler, M., and Assaad, F. F. (2022).
Valence-bond solid to antiferromagnet transition in the two-dimensional Su-Schrieffer-Heeger model by Langevin dynamics.
Phys. Rev. B, 105(8):085151.


Götz, A., Hohenadler, M., and Assaad, F. F. (2024b).
Phases and exotic phase transitions of a two-dimensional Su-Schrieffer-Heeger model.
Phys. Rev. B, 109(19):195154.


Grusdt, F., Demler, E., and Bohrdt, A. (2023).

Pairing of holes by confining strings in antiferromagnets.
SciPost Physics, 14(5):090.


Grusdt, F., Kánasz-Nagy, M., Bohrdt, A., Chiu, C. S., Ji, G., Greiner, M., Greif, D., and Demler, E. (2018).
Parton Theory of Magnetic Polarons: Mesonic Resonances and Signatures in Dynamics.
Physical Review X, 8(1):011046.


Han, Z. and Kivelson, S. A. (2023).
Resonating Valence Bond States in an Electron-Phonon System.
Phys. Rev. Lett., 130(18):186404.


Hayward, L. E., Hawthorn, D. G., Melko, R. G., and Sachdev, S. (2014).
Angular fluctuations of a multi-component order describe the pseudogap regime of the cuprate superconductors.
Science, 343:1336.


Hering, M., Sonnenschein, J., Iqbal, Y., and Reuther, J. (2019).
Characterization of quantum spin liquids and their spinon band structures via functional renormalization.

Phys. Rev. B, 99(10):100405.


Huh, Y., Fritz, L., and Sachdev, S. (2010).
Quantum criticality of the kagome antiferromagnet with Dzyaloshinskii-Moriya interactions.
Phys. Rev. B, 81(14):144432.


Huh, Y., Punk, M., and Sachdev, S. (2011).
Vison states and confinement transitions of $\mathbb{Z}_2$ spin liquids on the kagome lattice.
Phys. Rev. B, 84(9):094419.


Jaefari, A., Lal, S., and Fradkin, E. (2010).
Charge-density wave and superconductor competition in stripe phases of high-temperature superconductors.
Phys. Rev. B, 82(14):144531.


Jalabert, R. A. and Sachdev, S. (1991).
Spontaneous alignment of frustrated bonds in an anisotropic, three-dimensional Ising model.
Phys. Rev. B, 44:686–690.


Jiang, H.-C. and Kivelson, S. A. (2021).
High Temperature Superconductivity in a Lightly Doped Quantum Spin Liquid.
Phys. Rev. Lett., 127(9):097002.


Jiang, H.-C., Kivelson, S. A., and Lee, D.-H. (2023).
Superconducting valence bond fluid in lightly doped eight-leg t -J cylinders.
Phys. Rev. B, 108(5):054505.


Kaul, R. K., Kim, Y. B., Sachdev, S., and Senthil, T. (2008).
Algebraic charge liquids.
Nature Physics, 4:28–31.


Kaul, R. K., Kolezhuk, A., Levin, M., Sachdev, S., and Senthil, T. (2007).
Hole dynamics in an antiferromagnet across a deconfined quantum critical point.
Phys. Rev. B, 75(23):235122.


Koepsell, J., Bourgund, D., Sompet, P., Hirthe, S., Bohrdt, A., Wang, Y., Grusdt, F., Demler, E., Salomon, G., Gross, C., and Bloch, I. (2021).
Microscopic evolution of doped Mott insulators from polaronic metal to Fermi liquid.
Science, 374(6563):82–86.

Kokkinis, E. K. and Chubukov, A. V. (2025).
Pseudogap in electron-doped cuprates: thermal precursor to magnetism.
arXiv e-prints, page arXiv:2505.11727.

Lau, B., Berciu, M., and Sawatzky, G. A. (2011a).
Computational approach to a doped antiferromagnet: Correlations between two spin polarons in the lightly doped CuO_2 plane.
Phys. Rev. B, 84(16):165102.

Lau, B., Berciu, M., and Sawatzky, G. A. (2011b).
High-Spin Polaron in Lightly Doped CuO_2 Planes.
Phys. Rev. Lett., 106(3):036401.

Lebrat, M., Kale, A., Haldar Kendrick, L., Xu, M., Gang, Y., Nikolaenko, A., Bonetti, P. M., Sachdev, S., and Greiner, M. (2024).
Ferrimagnetism of ultracold fermions in a multi-band Hubbard system.
arXiv e-prints, page arXiv:2404.17555.

Lee, J. and Sachdev, S. (2015).
Wess-Zumino-Witten Terms in Graphene Landau Levels.

Phys. Rev. Lett., 114(22):226801.


Lee, P. A. (2014).
Amperean Pairing and the Pseudogap Phase of Cuprate Superconductors.
Physical Review X, 4(3):031017.


Lee, P. A., Nagaosa, N., and Wen, X.-G. (2006).
Doping a Mott insulator: Physics of high-temperature superconductivity.
Rev. Mod. Phys., 78:17–85.


Liu, W.-Y., Poilblanc, D., Gong, S.-S., Chen, W.-Q., and Gu, Z.-C. (2024).
Tensor network study of the spin-1/2 square-lattice J_1-J_2-J_3 model: Incommensurate spiral order, mixed valence-bond solids, and multicritical points.
Phys. Rev. B, 109(23):235116.


Lu, Y.-M., Cho, G. Y., and Vishwanath, A. (2017).
Unification of bosonic and fermionic theories of spin liquids on the kagome lattice.
Phys. Rev. B, 96:205150.


Luttinger, J. M. (1960).

Fermi Surface and Some Simple Equilibrium Properties of a System of Interacting Fermions.
Phys. Rev., 119:1153–1163.


Mascot, E., Nikolaenko, A., Tikhanovskaya, M., Zhang, Y.-H., Morr, D. K., and Sachdev, S. (2022).
Electronic spectra with paramagnon fractionalization in the single-band Hubbard model.
Phys. Rev. B, 105(7):075146.


Mei, J.-W., Kawasaki, S., Zheng, G.-Q., Weng, Z.-Y., and Wen, X.-G. (2012).
Luttinger-volume violating Fermi liquid in the pseudogap phase of the cuprate superconductors.
Phys. Rev. B, 85(13):134519.


Moon, E. G. and Sachdev, S. (2011).
Underdoped cuprates as fractionalized Fermi liquids: Transition to superconductivity.
Phys. Rev. B, 83(22):224508.


Müller, T., Thomale, R., Sachdev, S., and Iqbal, Y. (2025).
Polaronic correlations from optimized ancilla wave functions for the Fermi-Hubbard model.

Proceedings of the National Academy of Science, 122(20):e2504261122.


Nahum, A., Serna, P., Chalker, J. T., Ortuño, M., and Somoza, A. M. (2015).
Emergent SO(5) Symmetry at the Néel to Valence-Bond-Solid Transition.
Phys. Rev. Lett., 115(26):267203.


Nie, L., Sierens, L. E. H., Melko, R. G., Sachdev, S., and Kivelson, S. A. (2015).
Fluctuating orders and quenched randomness in the cuprates.
Phys. Rev. B, 92(17):174505.


Nikolaenko, A., Bonetti, P. M., Kale, A., Lebrat, M., Greiner, M., and Sachdev, S. (2025).
Canted magnetism and Z_2 fractionalization in metallic states of the Lieb lattice Hubbard model near quarter filling.
Phys. Rev. B, 112(4):045129.


Nikolaenko, A., Tikhanovskaya, M., Sachdev, S., and Zhang, Y.-H. (2021).
Small to large Fermi surface transition in a single band model, using randomly coupled ancillas.
Phys. Rev. B, 103(23):235138.


Nikolaenko, A., von Milczewski, J., Joshi, D. G., and Sachdev, S. (2023).

Spin density wave, Fermi liquid, and fractionalized phases in a theory of antiferromagnetic metals using paramagnons and bosonic spinons.
Phys. Rev. B, 108(4):045123.


Nomura, Y. and Imada, M. (2021).
Dirac-Type Nodal Spin Liquid Revealed by Refined Quantum Many-Body Solver Using Neural-Network Wave Function, Correlation Ratio, and Level Spectroscopy.
Physical Review X, 11(3):031034.


Nyhegn, J. H., Knakkergaard Nielsen, K., Balents, L., and Bruun, G. M. (2025).
Spin-charge bound states and emerging fermions in a quantum spin liquid.
arXiv e-prints, page arXiv:2507.02508.


Oshikawa, M. (2000).
Topological Approach to Luttinger's Theorem and the Fermi Surface of a Kondo Lattice.
Phys. Rev. Lett., 84:3370.


Pandey, H., Christos, M., Bonetti, P. M., Shanker, R., Nikolaenko, A., Sharma, S., and Sachdev, S. (2025).

Thermal SU(2) lattice gauge theory of the cuprate pseudogap: reconciling Fermi arcs and hole pockets.
arXiv e-prints, page arXiv:2507.05336.


Paramekanti, A. and Vishwanath, A. (2004).
Extending Luttinger's theorem to $\mathbb{Z}_2$ fractionalized phases of matter.
Phys. Rev. B, 70(24):245118.


Pépin, C. and Freire, H. (2023).
Charge order and emergent symmetries in cuprate superconductors.
Annals of Physics, 456:169233.


Punk, M., Allais, A., and Sachdev, S. (2015).
A quantum dimer model for the pseudogap metal.
Proc. Nat. Acad. Sci., 112:9552.


Punk, M. and Sachdev, S. (2012).
Fermi surface reconstruction in hole-doped t-J models without long-range antiferromagnetic order.
Phys. Rev. B, 85(19):195123.


Qi, Y. and Sachdev, S. (2010).
Effective theory of Fermi pockets in fluctuating antiferromagnets.
Phys. Rev. B, 81(11):115129.


Ran, Y. and Wen, X.-G. (2006).
Continuous quantum phase transitions beyond Landau's paradigm in a large-N spin model.


Read, N. and Sachdev, S. (1989).
Valence-bond and spin-Peierls ground states of low-dimensional quantum antiferromagnets.
Phys. Rev. Lett., 62:1694–1697.


Read, N. and Sachdev, S. (1990).
Spin-Peierls, valence-bond solid, and Néel ground states of low-dimensional quantum antiferromagnets.
Phys. Rev. B, 42:4568–4589.


Read, N. and Sachdev, S. (1991).
Large N expansion for frustrated quantum antiferromagnets.
Phys. Rev. Lett., 66:1773–1776.


Ribeiro, T. C. and Wen, X.-G. (2005).
New Mean-Field Theory of the $tt't''J$ Model Applied to High-T_c Superconductors.
Phys. Rev. Lett., 95(5):057001.


Rumelhart, D. E., Hinton, G. E., and Williams, R. J. (1986).
Learning representations by back-propagating errors.
Nature, 323(6088):533–536.


Sachdev, S. (1992).
Kagome and triangular-lattice Heisenberg antiferromagnets: Ordering from quantum fluctuations and quantum-disordered ground states with unconfined bosonic spinons.
Phys. Rev. B, 45:12377–12396.


Sachdev, S. (2019).
Topological order, emergent gauge fields, and Fermi surface reconstruction.
Rept. Prog. Phys., 82(1):014001.


Sachdev, S. (2023).
Quantum Phases of Matter.
Cambridge University Press, Cambridge, UK, 1 edition.


Sachdev, S. and Jalabert, R. (1990).
Effective lattice models for two-dimensional antiferromagnets.
Modern Physics Letters B, 04(16):1043–1052.


Sachdev, S., Metlitski, M. A., and Punk, M. (2012).
Antiferromagnetism in metals: from the cuprate superconductors to the heavy fermion materials.
Journal of Physics Condensed Matter, 24(29):294205.


Sachdev, S., Metlitski, M. A., Qi, Y., and Xu, C. (2009).
Fluctuating spin density waves in metals.
Phys. Rev. B, 80(15):155129.


Sachdev, S., Metlitski, M. A., Qi, Y., and Xu, C. (2009).
Fluctuating spin density waves in metals.
Phys. Rev. B, 80:155129.


Sachdev, S., Scammell, H. D., Scheurer, M. S., and Tarnopolsky, G. (2019).
Gauge theory for the cuprates near optimal doping.
Phys. Rev. B, 99(5):054516.


Sachdev, S. and Vojta, M. (1999).
Translational symmetry breaking in two-dimensional antiferromagnets and superconductors.
J. Phys. Soc. Jpn **69**, *Supp. B, 1.*


Scheie, A. O., Ghioldi, E. A., Xing, J., Paddison, J. A. M., Sherman, N. E., Dupont, M., Sanjeewa, L. D., Lee, S., Woods, A. J., Abernathy, D., Pajerowski, D. M., Williams, T. J., Zhang, S.-S., Manuel, L. O., Trumper, A. E., Pemmaraju, C. D., Sefat, A. S., Parker, D. S., Devereaux, T. P., Movshovich, R., Moore, J. E., Batista, C. D., and Tennant, D. A. (2024).
Proximate spin liquid and fractionalization in the triangular antiferromagnet $KYbSe_2$.
Nature Physics, 20(1):74–81.


Scheurer, M. S., Chatterjee, S., Wu, W., Ferrero, M., Georges, A., and Sachdev, S. (2018).
Topological order in the pseudogap metal.
Proc. Nat. Acad. Sci., 115(16):E3665–E3672.


Scheurer, M. S. and Sachdev, S. (2018).

Orbital currents in insulating and doped antiferromagnets.
Phys. Rev. B, 98(23):235126.


Schlömer, H., Schollwöck, U., Bohrdt, A., and Grusdt, F. (2024).
Kinetic-to-magnetic frustration crossover and linear confinement in the doped triangular t −J model.
Phys. Rev. B, 110(4):L041117.


Schmalian, J., Pines, D., and Stojković, B. (1998).
Weak Pseudogap Behavior in the Underdoped Cuprate Superconductors.
Phys. Rev. Lett., 80(17):3839–3842.


Schmalian, J., Pines, D., and Stojković, B. (1999).
Microscopic theory of weak pseudogap behavior in the underdoped cuprate superconductors: General theory and quasiparticle properties.
Phys. Rev. B, 60(1):667–686.


Scholle, R., Bonetti, P. M., Vilardi, D., and Metzner, W. (2023).
Comprehensive mean-field analysis of magnetic and charge orders in the two-dimensional Hubbard model.

Phys. Rev. B, 108(3):035139.


Schulz, H. J. (1990).
Effective action for strongly correlated fermions from functional integrals.
Phys. Rev. Lett., 65:2462–2465.


Senthil, T., Balents, L., Sachdev, S., Vishwanath, A., and Fisher, M. P. A. (2004a).
Quantum criticality beyond the Landau-Ginzburg-Wilson paradigm.
Phys. Rev. B, 70(14):144407.


Senthil, T. and Fisher, M. P. A. (2006).
Competing orders, nonlinear sigma models, and topological terms in quantum magnets.
Phys. Rev. B, 74(6):064405.


Senthil, T., Sachdev, S., and Vojta, M. (2003).
Fractionalized Fermi Liquids.
Phys. Rev. Lett., 90(21):216403.


Senthil, T., Vishwanath, A., Balents, L., Sachdev, S., and Fisher, M. P. A. (2004b).
Deconfined Quantum Critical Points.
Science, 303:1490–1494.

Senthil, T., Vojta, M., and Sachdev, S. (2004c).
Weak magnetism and non-Fermi liquids near heavy-fermion critical points.
Phys. Rev. B, 69(3):035111.

Shackleton, L. and Sachdev, S. (2025).
Sign-problem-free effective models of triangular lattice quantum antiferromagnets.
Phys. Rev. B, 111(7):075101.

Shackleton, L. and Zhang, S. (2024).
Emergent polaronic correlations in doped spin liquids.
arXiv e-prints, page arXiv:2408.02190.

Shraiman, B. I. and Siggia, E. D. (1988).
Mobile Vacancies in a Quantum Heisenberg Antiferromagnet.
Phys. Rev. Lett., 61:467–470.

Song, X.-Y., He, Y.-C., Vishwanath, A., and Wang, C. (2020a).
From spinon band topology to the symmetry quantum numbers of monopoles in Dirac spin liquids.
Phys. Rev. X, 10(1):011033.

Song, X.-Y., He, Y.-C., Vishwanath, A., and Wang, C. (2020b).
From spinon band topology to the symmetry quantum numbers of monopoles in Dirac spin liquids.
Phys. Rev. X, 10(1):011033.

Song, X.-Y., Wang, C., Vishwanath, A., and He, Y.-C. (2019).
Unifying description of competing orders in two-dimensional quantum magnets.
Nature Communications, 10:4254.

Tabis, W., Li, Y., Tacon, M. L., Braicovich, L., Kreyssig, A., Minola, M., Dellea, G., Weschke, E., Veit, M. J., Ramazanoglu, M., Goldman, A. I., Schmitt, T., Ghiringhelli, G., Barišić, N., Chan, M. K., Dorow, C. J., Yu, G., Zhao, X., Keimer, B., and Greven, M. (2014).
Charge order and its connection with Fermi-liquid charge transport in a pristine high-T_c cuprate.
Nature Communications, 5:5875.

Takahashi, J., Shao, H., Zhao, B., Guo, W., and Sandvik, A. W. (2024).
SO(5) multicriticality in two-dimensional quantum magnets.
arXiv e-prints, page arXiv:2405.06607.


Tanaka, A. and Hu, X. (2005).
Many-Body Spin Berry Phases Emerging from the π-Flux State: Competition between Antiferromagnetism and the Valence-Bond-Solid State.
Phys. Rev. Lett., 95(3):036402.


Wang, C., Nahum, A., Metlitski, M. A., Xu, C., and Senthil, T. (2017).
Deconfined quantum critical points: symmetries and dualities.
Phys. Rev. X, 7(3):031051.


Wang, H.-X., Jiang, Y.-F., and Yao, H. (2025).
Robust *d*-wave superconductivity from the Su-Schrieffer-Heeger-Hubbard model: Possible route to high-temperature superconductivity.
Science Bulletin, 70(14):2260–2265.


Wen, X. G. (1991).
Mean-field theory of spin-liquid states with finite energy gap and topological orders.
Phys. Rev. B, 44:2664–2672.


Wen, X.-G. and Lee, P. A. (1996).
Theory of Underdoped Cuprates.

Phys. Rev. Lett., 76(3):503–506.


Whitsitt, S. and Sachdev, S. (2016).
Transition from the Z_2 spin liquid to antiferromagnetic order: Spectrum on the torus.
Phys. Rev. B, 94(8):085134.


Wietek, A., Capponi, S., and Läuchli, A. M. (2024).
Quantum Electrodynamics in 2 +1 Dimensions as the Organizing Principle of a Triangular Lattice Antiferromagnet.
Physical Review X, 14(2):021010.


Wu, W., Scheurer, M. S., Chatterjee, S., Sachdev, S., Georges, A., and Ferrero, M. (2018).
Pseudogap and Fermi-Surface Topology in the Two-Dimensional Hubbard Model.
Phys. Rev. X, 8(2):021048.


Wu, W., Scheurer, M. S., Ferrero, M., and Georges, A. (2020).
Effect of van Hove singularities in the onset of pseudogap states in Mott insulators.
Phys. Rev. Res., 2:033067.


Xing, B., Chiu, W., Poletti, D., Scalettar, R. T., and Batrouni, G. G. (2021).

Quantum Monte Carlo Simulations of the 2D Su-Schrieffer-Heeger Model.
Physical Review Letters, 126(1):017601.

Xu, K.-J., Guo, Q., Hashimoto, M., Li, Z.-X., Chen, S.-D., He, J., He, Y., Li, C., Berntsen, M. H., Rotundu, C. R., Lee, Y. S., Devereaux, T. P., Rydh, A., Lu, D.-H., Lee, D.-H., Tjernberg, O., and Shen, Z.-X. (2023).
Bogoliubov quasiparticle on the gossamer fermi surface in electron-doped cuprates.
Nature Physics, 19(12):1834–1840.

Xu, X. Y. and Grover, T. (2021).
Competing Nodal *d*-Wave Superconductivity and Antiferromagnetism.
Phys. Rev. Lett., 126(21):217002.

Yang, K.-Y., Rice, T. M., and Zhang, F.-C. (2006).
Phenomenological theory of the pseudogap state.
Phys. Rev. B, 73(17):174501.

Ye, M. and Chubukov, A. V. (2023).
Crucial role of thermal fluctuations and vertex corrections for the magnetic pseudogap.
Phys. Rev. B, 108(8):L081118.

Zhang, Y.-H. and Sachdev, S. (2020a).
Deconfined criticality and ghost Fermi surfaces at the onset of antiferromagnetism in a metal.
Phys. Rev. B, 102(15):155124.

Zhang, Y.-H. and Sachdev, S. (2020b).
From the pseudogap metal to the Fermi liquid using ancilla qubits.
Physical Review Research, 2(2):023172.

Zhao, J.-Y., Chatterjee, S., Sachdev, S., and Zhang, Y.-H. (2025).
Yamaji effect in models of underdoped cuprates.
arXiv e-prints.

Zhou, B., Jin, H.-K., and Zhang, Y.-H. (2024a).
Variational wavefunction for Mott insulator at finite U using ancilla qubits.
arXiv e-prints, page arXiv:2409.07512.

Zhou, Z., Hu, L., Zhu, W., and He, Y.-C. (2024b).
SO(5) Deconfined Phase Transition under the Fuzzy-Sphere Microscope: Approximate Conformal Symmetry, Pseudo-Criticality, and Operator Spectrum.

Physical Review X, 14(2):021044.